Advanced InSAR methodologies to study subsidence and fracturing caused by groundwater withdrawal in Valley of Mexico

Von der
Fakultät Architektur, Bauingenieurwesen und Umweltwissenschaften
der Technischen Universität Carolo-Wihelmina
zu Braunschweig

zur Erlangung des Grades einer
Doktor-Ingenieurin (Dr.-Ing.)
genehmigte

Dissertation

von
Gabriela Llanet SILES
geboren am 12.01.1986
aus Jujuy, Argentinien

Eingereicht am: 3 November 2014

Disputation am: 15 Januar 2015

Berichterstatter: Univ.-Prof. Dr.-Ing. habil. Wolfgang Niemeier

Dr. Penelope Lopez-Quiroz

Univ.-Prof. Dr. sc. Antje Schwalb

2015

Acknowledgments

Firstly, I would like to thank my principal advisor Prof. Wolfgang Niemeier who provided me with support, guidance and encouragement during the three years of my doctorate studies. I am very thankful to Dr. Penelope Lopez-Quiroz from the Centro de Geociencias of the UNAM for her time and supplying the data that made possible this investigation. I really appreciate her help, patience and expertise given from the other side of the Atlantic. Many thanks go also to her colleagues in the Centre of Geociencias who cooperate with some ideas and data for this research. Of course, thanks Hind! Without your help this Mexican adventure would not have been started.

Special thanks to Prof. Schwalb for agreeing to be my third supervisor and participation in my defence committee. I owe thanks also to Prof. Empelmann and Prof. Meon who also were part of my committee team. Additionally, I want to thanks to the IGP peers, particularly the present and former GIS team who help me to improve my knowledge in that area. This acknowledgment also extends to Dr.-Ing. B. Riedel for his constructive criticism to improve this work.

I express my gratitude to the German Academic Exchange Service (DAAD) for providing financial support for this research. Thanks to the European Spatial Agency (ESA) for the SAR data and to INEGI, CONABIO and other Mexican organizations to make relevant information available to the public. Likewise, my gratitude to Andy Hooper and his team who open their MTI code (StaMPS/MTI) to the research community, and also to the DORIS developers. Thanks to JPL for the ROIPAC software, and to the USGS and DEOS for the SRTM and Orbit data, respectively.

I am immensely thankful to my loved family in Argentina whose support and motivation were the motor that propel me to continue this tough trip. I extend my thanks to my friends for being their when I needed it the most. Last but not least, I would like to thank Thierry for his patience and unconditional support particularly in the difficult times throughout this long long journey.

Table of Contents

Zusammenfassung

Radarfernerkundungstechniken sind gut geeignet um Deformationsprozesse zu studieren. Insbesondere seit der Verfügbarkeit der SAR Interferometrie wurde bereits mit den standardmäßigen und multi-temporalen Konfigurationen eine Vielzahl von Anwendungen im Hinblick auf das Monitoring von Deformationen realisiert. Beispielsweise wurden die Setzungen in Mexico City mit konventionellen und multi-temporalen Methoden erfasst; allerdings wurde bis jetzt keine komplette Charakterisierung und detaillierte zeitliche Analyse der Landbesiedelung im gesamten Tal von Mexiko, die das Seebett von fünf ehemaligen Seen (Chalco, Xochimilco, Texcoco, Xaltocan und Zumpango) beinhaltet, durchgeführt. In dieser Arbeit wurde die Bodensenkungen und die dazugehörigen Boden-Brüche im Tal von Mexiko mit Hilfe der Small Baseline Methode von StaMPS kartiert und analysiert.

Die dazugehörige Inversionsmethode wurde im Detail studiert und interpretiert und dieser Algorithmus auf Basis der geologischen Information so angepasst, dass die Ergebnisse als räumliche Referenz dienen können. Dieser erweiterte Algorithmus wurde durch den Vergleich mit existierenden Ergebnissen aus dem südlichen Tal validiert. Das „Unwrapping“ und die Qualität der Zeitreihen wurden mit statistischen Verfahren bewertet. Die Ergebnisse zeigen, dass der vorgestellte Algorithmus sich ausreichend an das Untersuchungsgebiet anpasst.

Detaillierte Analysen von ERS- und ENVISAT-Daten mit konventionellem und multitemporalem InSAR für die Zeiträume von 1999-2000 und von 2002-2010 wurden erstmals im Norden des Talbereiches von Mexico durchgeführt. Dieses Gebiet umfasst das Cuautitlan-Pachuca Sub-Basin, wo nur wenige in-situ Vergleichsmessungen verfügbar waren.

Sowohl die städtischen als auch die ländlichen Bereiche erfahren Bodensenkungen. Große Setzungsraten wurden besonders in dicht bevölkerten Gebieten gefunden oder in Bereichen mit beträchtlicher Wasserentnahme zur Feldbewässerung. Die Zeitreihen im nördlichen und südlichen Teil des Tals von Mexiko wurden verwendet, um die Auswirkungen der GW-Entnahme auf wichtige Infrastrukturprojekte zu bewerten, z.B. den *Tunel Emisor Oriente*, den Gran Canal del Desagüe, Eisenbahnen und Straßen. Zusätzlich bieten diese Zeitreihen essentielle Informationen für die Stadtplanung, sowie das Abfall- und Wasser-Management.

Als weiterer Schwerpunkt wurde die Flexibilität des verwendeten InSAR Algorithmus genutzt, um nichtlineare Verformung zu identifizieren und eine Methode zur Lokalisierung von Boden-Bruchzonen zu entwickeln und um ihre Dynamik zu verstehen. Die Lage der mit dieser Methode identifizierten Bruchzonen stimmt mit existierenden Aufzeichnungen von Bruchaktivitäten überein. Die Bruchauslösemechanismen werden an den Stellen diskutiert und bewertet, an denen deutliche Beschleunigungen oder Verzögerungen erkannt wurden. Der vorgestellte Ansatz zur Identifikation der Brüche stellt nützliche und wertvolle Informationen für die Verbesserung der Schadenskarten in diesem Gebiet dar und unterstützt den Entscheidungsprozess im Katastrophenmanagement. Zusätzlich kann die Kenntnis über die Lage der Bruchzonen die Grundwasserströmungsmodelle für die Bewertung und Überwachung von potenziellen Kontaminationsquellen verbessern. Ebenso können die InSAR Ergebnisse zu einem besseren Verständnis der Aquifer-Dynamik führen und Antworten zur zeitlichen Entwicklung der auftretenden Fließspannungen geben, um daraus nachhaltige Wasserentwicklungspläne ableiten zu können.

Abstract

Radar remote sensing techniques are well suited for deformation studies. Particularly, since the emergence of SAR interferometry, its standard and multi-temporal configurations have been widely used in a variety of applications for deformation monitoring. The Mexico City subsidence, for example, has been mapped using both the conventional and multi-temporal methods; however, no complete characterization and detailed temporal analysis of the land settlement in the entire Valley of Mexico, covering the lakebed of the five ancient lakes (Chalco, Xochimilco, Texcoco, Xaltocan and Zumpango) has been performed until now. In this work, we mapped and analysed the subsidence and associated earth fissuring in the Valley by exploiting, for the first time, the *Small Baseline* method from StaMPS.

The inversion methodology was studied in detail and interpreted, and the algorithm was adjusted to select a spatial reference on the basis of the surface geology information. This extended algorithm was assessed by comparing the results obtained with existing ones particularly over the southern Valley. Furthermore, unwrapping and quality of the times series were analysed using maps of system misclosure. Our results indicate that the proposed algorithm adapts adequately to the study area.

Detailed ERS and ENVISAT conventional and multi-temporal InSAR (MTI) analysis for the 1999-2000 and 2002-2010 periods, respectively, were performed for the first time on the northern Valley of Mexico encompassing part of the Cuautitlan-Pachuca sub-basin, where a few in situ measurements were available.

Both urban and rural areas are experiencing subsidence, and rapid rates were found in densely populated areas or where sizeable volumes of water are used for crop irrigation. Time series in both, the northern and southern part of the Valley were used to evaluate the impact of the subsidence on important infrastructure such as the *Tunel Emisor Oriente,* railways and roads. Furthermore, they provide essential information for urban planning, waste and water management.

As second main aspect, the flexibility of the proposed InSAR algorithm to identify points undergoing non-linear deformation, and where probably other approaches may fail, was exploited to develop a methodology that contributes to the location of soil fractures and to the understanding of their dynamics. Fissure-prone zones identified by this method, effectively coincided with existing records of ground failures. The fracture trigger mechanisms are furthermore discussed and evaluated where notable acceleration or deceleration is found. The proposed soil fracture identification approach provided useful and valuable information for improving the vulnerability maps in the area and assisting the decision-making process in disaster management. Additionally, earth fissuring zonation may ameliorate groundwater flow models for evaluation and monitoring of potential contamination sources. Equally, better knowledge of the aquifer dynamics and responses to the applied stresses through time can be achieved by using InSAR outcomes, in turn aiding and tailoring plans for sustainable development of groundwater resources.

Chapter 1

Introduction

The immoderate consumption of natural resources for different purposes is leading to their depletion worldwide. For example, water, a vital and essential element for livelihood and development of regular activities (e.g., agriculture, industry, mining), has become one of the most vulnerable resources in many countries. Crowded metropolis such as Mexico City strongly depend on groundwater for water supply (Rodríguez-Castillo and Rodríguez-Velázquez 2006). Moreover, the continuous rapid demographic growth in these cities along with uncontrolled urban sprawl over potential natural groundwater recharge zones, negatively affect the groundwater storage compounding the water scarcity problem.

In the Valley of Mexico, the extensive groundwater withdrawal has led to the reduction of the groundwater levels, causing dehydration of the clayey deposits and their subsequent non-recoverable consolidation and compaction. The major related effect is the subsidence, which has critical social, economic and environmental consequences. Ground sinking and the associated soil fracturing influence and even destroy urban infrastructure (e.g., subway and network systems, colonial and modern structures). It is certainly a challenging issue for sustainable city development. Furthermore, drainage systems are impacted and important water leaks occur. Thus, precise surveys and continuous surveillance of these phenomena are neccesary.

Satellite remote sensing techniques represent a valuable tool for studying and monitoring this and other earth processes (e.g., volcanic and tectonic) that affect the Valley. SAR interferometry, both in its conventional and multi-temporal configurations (Berardino et al. 2002; Ferretti et al. 2001), has been successfully employed around the world for ground deformation monitoring due to excessive water withdrawal (Amelung et al. 1999; Herrera et al. 2009; Ng et al. 2012; Tomás et al. 2005).

Different interferometric synthetic aperture radar (InSAR) approaches have been applied in Mexico City, already demonstrating their potential for land subsidence detection and its supervision, particularly in the southern part (Strozzi and Wegmüller 1999; Strozzi et al. 2003; Cabral-Cano et al. 2008; Lopéz-Quiroz et al. 2009; Osmanoglu et al. 2010; Yan et al. 2012; Chaussard et al. 2014). Global positioning system (GPS) measurements have also been performed (Cabral Cano et al. 2008; Osmanoglu et al. 2010); however, this technique measures deformation only at a few discrete points. In contrast, the higher spatial coverage by InSAR provides more information about the phenomenon where GPS measurements are not available.

Discrepancies between the different multi-temporal interferometric methods employed up to now over Mexico City have been attributed to various factors (different periods of study and sensors, a priori deformation model assumptions). In addition, some of these approaches may fail to detect significant subsidence in low coherent areas (such as vegetated or cropping lands) and/or areas where non-linear deformation occurs. Hence, the exploitation of a specific approach that allows measuring subsidence where others fail, and the comparison of achievable results to those obtained by other algorithms motived part of this research. The Small Baseline Subset (SBAS) module from the Stanford Method for Persistent Scatterers (StaMPS) (Hooper 2008; Hooper et al. 2012; Hooper et al. 2007; Hooper et al. 2004) was proposed and slightly adjusted to include an appropriate spatial reference for the time series inversion. The inversion strategy provided by StaMPS was studied in detail, and other methods were also analysed.

Moreover, as previously stated, most studies have concentrated on the southern part of the Valley; nonetheless none them presented a complete and detailed evaluation of the subsidence and soil fracturing in the northern part, where important engineering projects are carried out (e.g., Tunel Emisor Oriente) and others are planned (e.g., artificial water recharge, new Mexico Airport). Part of this investigation is extensively focused on this area.

Earth fissures are common hazards that appear and propagate affecting several zones in the entire Valley. Several studies based on ground measurements have been performed, e.g., Cerca et al. (2010), Ovando-Shelley et al. (2012), Méndez et al. (2008a), proving relevant but point-wise or local data. Because soil fractures, once produced, are irreversible and continue to spread (Carreón-Freyre et al. 2011), their monitoring and updated mapping is demanding. In this research, a methodology for aiding the identification and understanding of ground failure is presented. This approach is based on the non-linear information observed in the InSAR time series. Thereby, we emphasized that the algorithm appraisal and adjustment is primarily important for that purpose. The location of fissure-prone areas effectively coincides with data compiled from existing records. The latter indicates a good capability of the methodology presented here.

The current regional subsidence and associated soil fracturing analysis on Valley of Mexico by means of InSAR can aid the improvement of vulnerability maps, particularly in the northern area. Contributions from this investigation can be used to support the development of rural and urban engineering projects, as well as water and waste management strategies.

1.1 Research Objectives

This thesis primarily aimes to contribute to risk and hazard assessment in the entire Valley of Mexico by exploiting a specific and adapted interferometric open source code and by developing a methodology for identification of areas prone to ground failures, likewise providing useful information to urban planning, waste and water management. The main objectives are summarized below:

- Study, interpretation and adaptation of a specific multi-temporal interferometric approach (StaMPS)
- Assessment of a MTI method not previously applied (to our knowledge) to subsidence studies in the entire Valley of Mexico
- Exploration of the capabilities and flexibilities of the method explored, particularly in areas where other approaches might fail
- Analysis and investigation of subsidence related processes that may be revealed by anomalies in the deformation time series

- Temporal and spatial (particularly to the northern part of the Valley) extension of the subsidence, evaluation and impact on local infrastructure.
- Identification, monitoring and forecast of areas prone to fissuring by an InSAR-based post-proccesing tool
- Analysis of the complex mechanisms involved in the earth fissuring process affecting the Valley

1.2 Outline of this research

This investigation is organized in nine chapters. In the first chapter the structure and objectives of this work are outlined.

In Chapter 2 and 3 some principles of SAR focusing and interferometric processing are presented. Description of interferometric geometry and distortion is given, as well as details about the interferometric phase components and unwrapping methods used in this thesis.

Chapter 4 gives a review of the MTI methods, focusing principally on the SBAS approaches. In Chapter 5 the proposed MTI algorithm is studied in detail. Specially, the SBAS inversion method, which differs from the previous one (López-Quiroz et al. 2009) applied to the southern Valley of Mexico, is analysed and interpreted by using geodetic concepts. The selection of temporal reference is evaluated based on an uncertainty analysis, and the extension of the algorithm for inclusion of an appropriate reference area is introduced. The latter is further discussed in Chapter 7.

Interaction between the groundwater extraction, subsidence and related effects are presented in Chapter 6. A brief geo-hydrological overview of the study area is provided. Subsidence evolution and consequences using available literature was investigated. Furthermore, some measures to reduce hydraulic problems in the Valley of Mexico are described and discussed.

Chapter 7 presents the StaMPS algorithm assessment, influence of the spatial and temporal references and results for the period 2002-2010. Futhermore, impact of subsidence on important local infrastructure is evaluated based on InSAR outcomes. The estimated time series and the detected non-linear component are explored to study the soil fracturing process near the volcanic edifice of the Peñon del Marques. Part of the content of this Chapter was presented at the *2nd Joint International Symposium on Deformation Monitoring (JISDM)* (Siles et al. 2013).

Chapter 8 explores the proposed interferometric method in the northern Valley of Mexico where to our knowledge no previous detailed MTI analysis was performed. Correlation between subsidence and water content is evaluated along the TEO, and ground ruptures affecting certain areas are inferred from average velocities. The methodology for detection of fissure-prone areas is described and possible trigger mechanisms are examined. Some results presented in this chapter were shown at the *Geomonitoring Tagung 2015* (Siles et al. 2015) and submitted to *Natural Hazards*. Other methodologies and outcomes given here will be submitted to *Remote Sensing*.

Findings of this research are summarized in Chapter 9, including as well possible future directions to explore.

Chapter 2

Synthetic Aperture Radar

Since the advent of the satellite era there has been an increased development in the space-oriented technology. Its usage for different applications has significantly developed.

Among the radar (radio detection and ranging) techniques, the synthetic aperture radar (SAR) was an important breakthrough. The SAR technology was born in 1951 by the hand of Carl Wiley while he was working on a correlation guidance system (Wiley 1985). The idea of the SAR system is basically to synthetize the large antenna used in the Real Aperture Radar (RAR) and to profit from the Doppler Effect to achieve high resolution images. This technique has experienced an extraordinary evolution regarding sensors, configuration, imaging resolution, and it has become a powerful tool for a numberless of uses of different nature (e.g., Moon et al. 2010 ; Shimada et al. 2010; Reale et al. 2011; Kerbaol and Collard 2005; Mathieu et al. 2003; Holah et al. 2005; Kurosu et al. 1995; Kim et al. 2008; Vachon et al. 1994; Eldhus et 1996; Skriver et al. 2000; Cao et al. 2009; Dierking and Busche 2006).

In this chapter basics of SAR are briefly described, first introducing the system historical development and sensors.

2.1 History and general characteristics

The SAR introduced a new generation of radar techniques and remote sensing imaging. This echo-mode array imaging system has an extensive field of commercial and military applications from topographic imaging to geo-hazard assessment and underground exploration passing through monitoring of historical buildings, thematic mapping and atmosphere studies. This is an active radar which emits microwaves in a very short period of time and receives the backscattered signal from an object (Curlander and McDonough 1991). Due to the high velocity of the satellite (~ 7.5 km/s), the signal is received several times during its path. The objective remains in the radars beam during several minutes and it is observed by the satellite from its different positions on its path. This is equivalent to a prolonged length of the antenna, and that is why the SAR system is said to virtualize the behaviour of a very large antenna (see Figure 2-1).

This coherent imaging system profits from the Doppler effect which is the result of the movement of the satellite along its path, to achieve a very high azimuthal resolution which is one, if not the most, important characteristic of this radar system. Two objects slightly separated in the azimuthal direction, i.e. parallel to the flight direction, can be distinguished due to their different Doppler shifts, which stems from their different relative velocities with respect to the satellite.

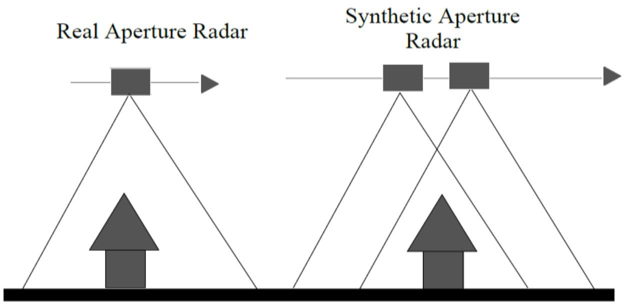

Figure 2-1 To the left the real antenna Aperture and to the right the synthetic aperture created by the combined backscattering echoes.

The satellite receives back the Doppler echoes, which are then subjected to a complex procedure (i.e. synthetic processing; see section 2.3) to get the level 1 SAR image.

The first civilian mission that used the SAR system was the american SEASAT (Jordan 1980), which was launched in 1978 and was an inspiration for other SAR missions. After SEASAT, two other Shuttle missions of one week duration each were performed by NASA: SIR-A and SIR-B (Cimino et al. 1986). Many other SAR orbital systems propelled since the first mission: the ALMAZ by the USSR[1], the SIR-C/X SAR (Jordan et al. 1991), which was launched in cooperation between the NASA[2], DARA[3] and ASI[4], ERS-1/2 and ENVISAT missions by the European Space Agency (ESA), and the ALOS project carried out by the JAXA. In 1995, the canadian RADARSAT-1 (Raney et al. 1991) was put into orbit with a service projected to last 5 years, however it operated until 2012. At the present, the ongoing operational SAR satellites of TerraSAR-X (Werninghaus et al. 2007), RADARSAT-2 (Hillman et al. 2011), Cosmo-SKY (Torre and Capece 2011) and ALOS-2 (Kankaku et al. 2013) along with currently planned SAR missions (e.g. SENTINEL; Attema et al. 2008) represent the availability of SAR data for several years at X- (3 cm), C- (6 cm), and L-band (24cm) wavelengths (see Table 2-1).

Satellite	Country	Year	Band	Wavelength (cm)	Polarization	Incident Angle (°)
SEASAT	USA	1978	L_band	23.5	HH	23.5
SIR-A	USA	1981	L_band	23.5	HH	23.5
SIR-B	USA	1984	C_band	23.4	HH	16-65
ERS-1/2	Europe	1991/95	C_band	5.25	VV	23
ALMAZ	USSR	1991	S_band	10	HH	30-60
JERS-1	Japan	1992	L_Band	23.5	HH	35
SIR-C/X-SAR	USA	1994	L_Band	23.5	HH,HV,VH,VV	48- Multi angle pointing capability
			C_band	5.8	HH,HV,VH,VV	
	Germany/Italy		X_band	3.1	VV	
RADARSAT-1	Canada	1995	C_band	5.3	HH	20-50
SRTM	USA	2000	C_band	5.6	HH+VV	30-60
	Germany		X_band	3		54
ENVISAT	Europe	2002	C_band	5.2	HH,HV,VH,VV	15-45
TERRASAR-X	Germany	2007	X_band	3.1	HH,HV,VH,VV	15-60
RADARSAT-2	Canada	2007	C_Band	5.5	HH,HV,VH,VV	18-50
ALOS PALSAR-1	Japan	2006	L_band	23.6	HH,VV,HV,VH	8-60
ALOS PALSAR-2	Japan	2014	L_band	22.9	HH,VV,HV	8-70
					HH+HV	
					VV+VH	
					HH+HV+VV+VH	

Table 2-1 Earth observing SAR satellites

---

[1] Union of Soviet Socialist Republics
[2] National Aeronautics and Space Administration
[3] Deutsche Agentur für Raumfahrtangelegenheiten
[4] Agenzia Spaziale Italiana

Even though there are some differences between these sensors such as polarization, resolution, frequency and other characteristics, the underlying operation concept used by each of them is the same and is based on the Doppler effect for achieving high resolution.

It is important to highlight that the potential of a SAR sensor to detect ground or objects' movement depends largely on the wavelength. The shorter the wavelength, the better is the resolution and its capability to identify motion. On the other hand, if the surface is covered by vegetation, the underlying dynamics cannot be efficiently unveiled when using larger frequencies (e.g., TerraSAR-X) because of their lower penetration depth capacity. In that case, an L-band radar sensor (e.g., ALOS; see also Table 2-1) might be more suitable, since its longer wavelength can penetrate the vegetation better and it can receive the reflected signal from the target object underneath. The same concept can be applied in a rugged mountainous area, where the L-band can produce better results, in terms of coherence, than an X- or C-band.

2.2 SAR spaceborn system

The interferometric synthetic aperture radar (InSAR) and its multi-temporal configurations are main techniques used in this thesis. However, fundamental concepts regarding the SAR geometry and processing need first to be assimilated. Moreover, the SAR focusing is the starting point of the methodology applied in this work, since the available raw SAR data (see Chapters 7 and 8) must be transformed into Single Look Complex (SLC) images before performing the standard and time series InSAR procedures. Buckley (2000) was used as the main reference for description of the focusing steps. Further details can also be found in Curlander and McDonough (1991).

2.2.1 Doppler Effect

The SAR system has the capability to reach a very high azimuthal resolution by using the Doppler effect. The SAR satellite emits energy within the microwave part of the spectrum and then it receives back. The backscatterer signal is then processed by a complex process to get the SLC image.

The Doppler effect consists of the wavelength variation from a signal emitted or received from any object. By using this effect it is possible to study the movement of a target by analyzing the wavelength variation of the received signal with respect to the emitted one. Thanks to this, it is possible to know the velocity of the target observed by the satellite and to identify whether the target moves towards or away from the satellite.

Considering a source emitting waves at a frequency f_s receding from an observer at a velocity v, the observed frequency f_0 is (e.g., Chen 2011):

$$f_o = \left[\frac{1-(v/c)}{1+(v/c)} \right]^{1/2} f_s \tag{2.1}$$

where c represents the speed of light. Let us now regard the velocity of the satellite as V_{SAR}. For $V_{SAR} << c$, (v^2/c^2) approaches 0, and then the difference f_D between the emitted f_s and the received frequency f_o can be estimated as

$$f_D = 2\frac{V_{SAR}}{c} f_s. \qquad (2.2)$$

If more than one object is observed by the satellite, they can be discriminated in the along-track direction because of their different Doppler characteristics, which result from their different relative movements with respect to the satellite (see Figure 2-2).

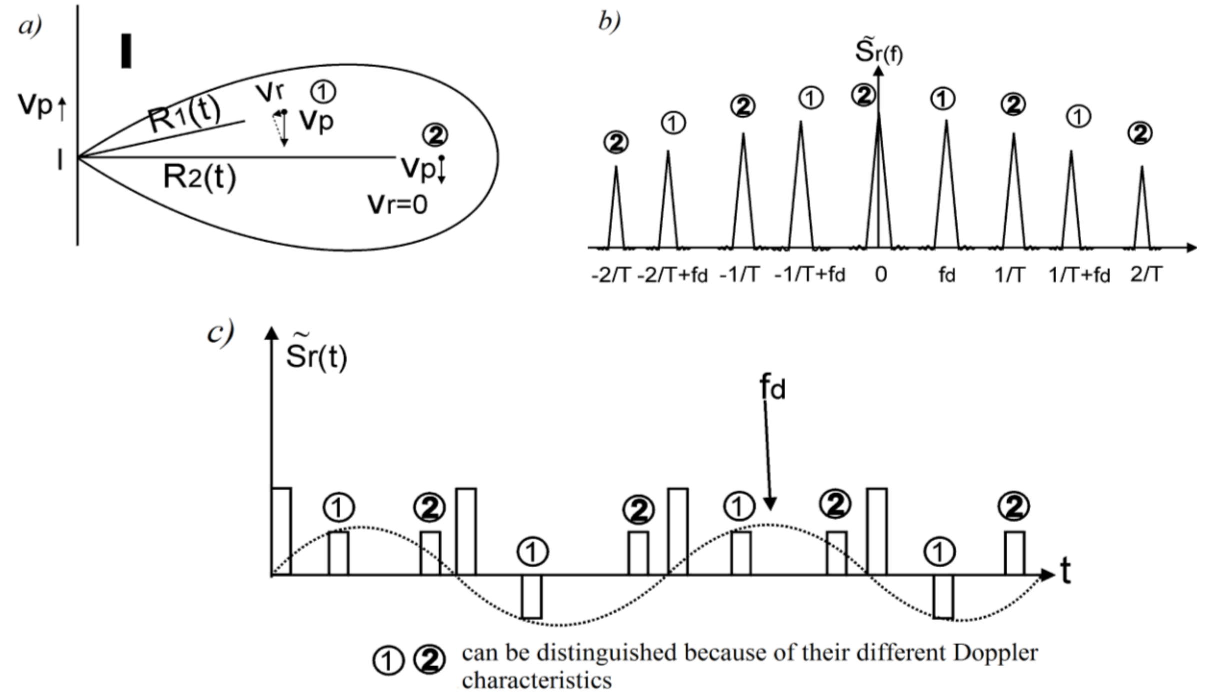

Figure 2-2 *a*) Representation of objects 1 and 2 in the satellite footprint (finite broadside irradiated area). R_1 and R_2 are the range distance of object 1 and 2, respectively, at a certain time t. V_r and V_p are the velocities in the range and azimuth direction, respectively. V_r=0 when the target moves in (or parallel to) the azimuth direction. *b*) The frequency spectrum showing the Doppler frequencies of the targets 1 and 2**.** *c*) Signal signature of elements 1 and 2 in the time domain. The dashed line represents the Doppler frequency (adapted from Broquetas and Camps 2000).

The Doppler frequency variation for each ground point observed by the SAR satellite is unique (Chan and Koo 2008); its precise estimation affects directly the SAR imaging results because SAR relies on precise phase and Doppler measurements for obtaining fine resolution imaging.

2.2.2 SAR Geometry and resolution

The SAR spaceborn system consists on a satellite moving at a height H and at a constant velocity V_{SAR}. Figures 2-3*a* and *b* show the geometry of the SAR system.

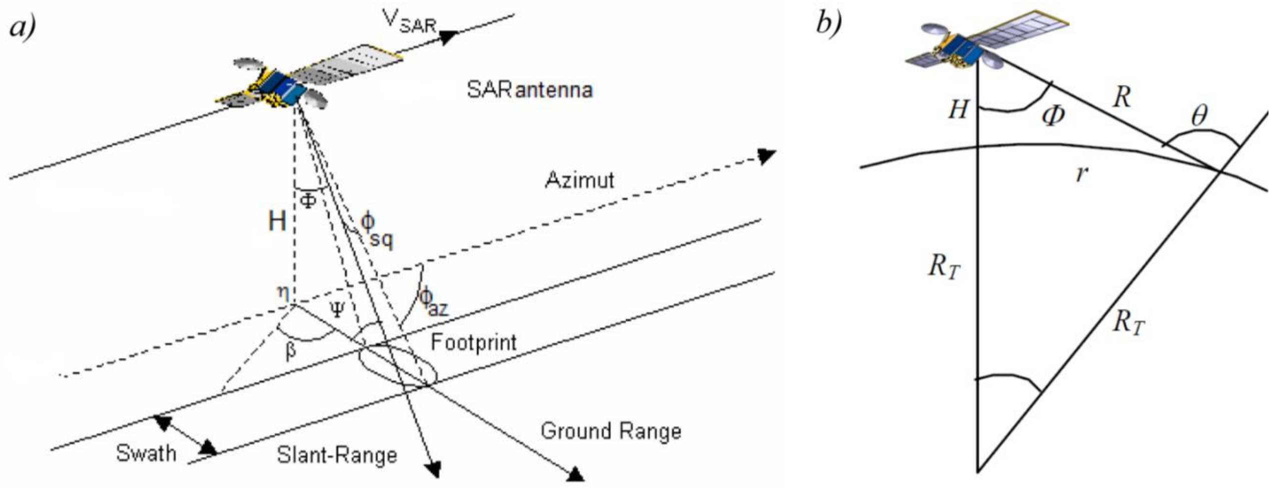

Figure 2-3 *a)* Imaging Geometry of the SAR system. Due to the spacecraft V_{SAR} the pulses illuminated a swath parallel to the satellite track. The footprint is indicated by the ellipsoidal form. *b)* Geometry of incident angle (adapted from Di Masso Cervera 2007).

Two main directions characterize the SAR geometry: the azimuth or line of flight direction, also known as along-track direction, and the range or across track direction. We refer to the farthest portion of the radar image as the far range, and to the closest as near range. The slant range is the distance from the satellite to the object, while the ground range is defined as the direction of the side-looking radar image as projected onto the nominally horizontal reference plane. The zero-Doppler direction is also very important and indicates the line in which the Doppler frequency is equal to zero.

Other elements that describe the SAR geometry are the nadir, the incident, look and the squint angles. The nadir, represented by η in Figure 2-3*a*, is the projection of the satellite onto the earth. The angle between the radar line of sight (LOS) and the local vertical with respect to the geoid is the incident angle Φ. This element has an important influence in the radar backscattering and the appearance of objects on the imaginary caused by topographic effects (see section 2.2.2). In general, reflectivity from distributed scatterers decreases with increasing incident angles.

The look angle θ, referred to in the literature as elevation angle, is defined as the angle between the vertical of the antenna to the ground and the transmitted ray at the point of incidence. θ increases from the far range and is the complement of the depression angle β.

A geometrical element that plays a crucial role in the focusing process is the squint angle ϕ_{sq}, which is the angle between the across track (range) and the squint mode look direction or in other words, the direction corresponding to the non-zero Doppler plane. This angle appears when the antenna is steered away from the zero-Doppler direction (Hanssen 2001). Its complement, when imaging in a normal SAR position, is the azimuth angle $\phi_{az,}$ which is the angle between the azimuth direction and the across direction (Henderson and Lewis 1998). In ideal the case, the squint and azimuth angle will be 0° and 90°, respectively; nevertheless, the antenna point forward or/and backward from the perpendicular position what results in values larger than those expected.

These elements, main components of the SAR geometry, are essential not only in the synthetic procedure, but also in InSAR and the multi-temporal processing (see Chapters 3, 4 and 5). Furthermore, concepts such as azimuthal and range resolution need to be introduced as are they are relevant when considering the sensibility of the different SAR sensors to identify the target objects. The minimum distance in range direction, in which two elements or targets can be separated or discriminated is defined as the range resolution and depends on the duration of the emitted pulses. The range resolution R_r can be expressed in terms of the slant range R_r or ground range R_g as (Curlander and McDonough 1991)

$$R_r = \frac{c}{2B_r} \tag{2.3}$$

$$R_g = \frac{R_r}{sen\Phi} \tag{2.4}$$

where B_r is the bandwidth and Φ is the incident angle. The component ($sen\ \Phi$) in equation (2.4) indicates that there is a loss of resolution between the slant range and ground range. For a pulse or chirp compression technique, the effective resolution improves to 9.6 m, which translated to the ground range correspond to 25 meters (Curlander and McDonough 1991).

The Doppler bandwidth B_{dop} , on the other hand, determines the azimuth resolution R_{az} of the focused SAR image (Raney 1998)

$$B_{dop} = \frac{2\beta_a V_{SAR}}{\lambda}, \tag{2.5}$$

$$R_{az} = \frac{V_{SAR}}{B_{dop}} \tag{2.6}$$

being β_a the azimuth bandwidth of the antenna and V_{SAR} the relative spacecraft velocity. By combining equations (2.5) and (2.6), and considering a very long distance L_a and $B_{dop}=\lambda/L_a$, the azimuth resolution R_{az} can be written as

$$R_{az} = \frac{L_a}{2}. \tag{2.7}$$

This simple expression tells us that the resolution for the SAR system is more or less haft of the antenna and independent from the height. The latter indicates that the same resolution could be achieved using aircrafts at different altitude or any spaceborn SAR system. If we compare this equation to that of the RAR system (Franceschetti and Lanari 1999)

$$R_{RAR} = \frac{R\lambda}{L_a}, \tag{2.8}$$

the length of the antenna L_a is in the denominator while in the case of SAR is in the numerator. This means that for achieving a high resolution in azimuth with a RAR system we would need a very large antenna, which is impractical in the reality. Note also that the SAR azimuthal resolution is independent from the wavelength, in comparison to the RAR azimuthal resolution R_{RAR}.

2.3 Synthetic processing: focusing

Thanks to the SAR processing it is possible to combine coherently the echoes that the SAR antenna receives (i.e. they are linearly combined after a phase shift correction which is induced by the motion; Barbarrosa and Farina 1994). By matching the Doppler frequency variations and demodulating by adjusting the frequency variation in the return echoes from each point on the ground, a high-resolution image (i.e. SLC or a level 1 SAR product) is obtained (see Figure 2-4).

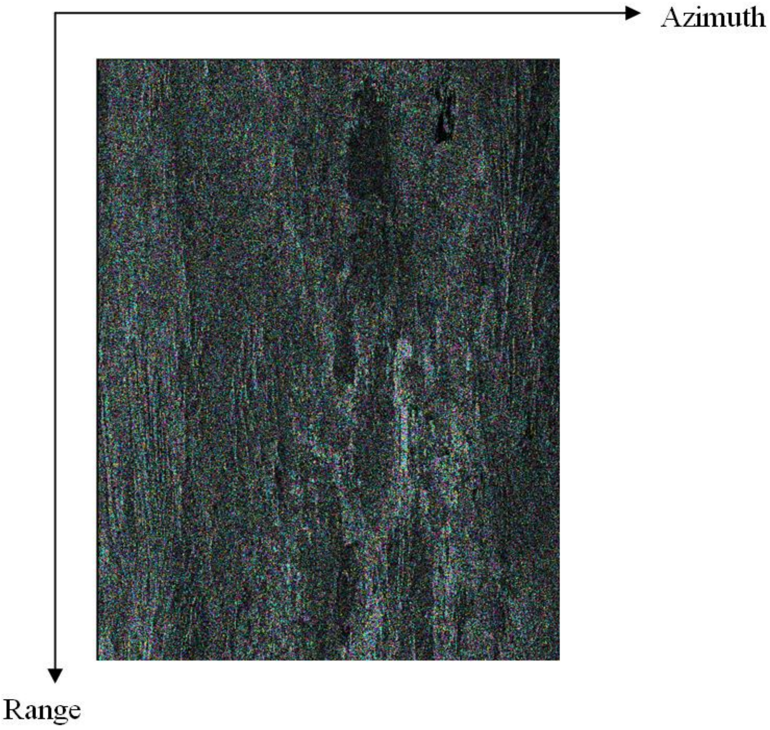

Figure 2-4 Example of SLC image acquired over northern Valley of Mexico processed using the ROIPAC focusing algorithm.

There are several SAR focusing algorithms, e.g. the range-Doppler algorithm, the chirp scaling algorithm and the wavenumber domain processing (Bamler 1992). In this work the range-Doppler processor provided by the Repeat Orbit Interferometry Package (ROIPAC) developed by the Jet Propulsion Laboratory (JPL) of NASA (Rosen et al. 2004) was applied.

The SAR processing entails several steps before reaching the final SLC. Figure 2-5 shows the simplified flow chart of the focusing procedure.

The first step is to read the parameters required for the SAR focusing, which are contained in the header file. The necessary parameters for further processing steps are depicted in Table 2-2.

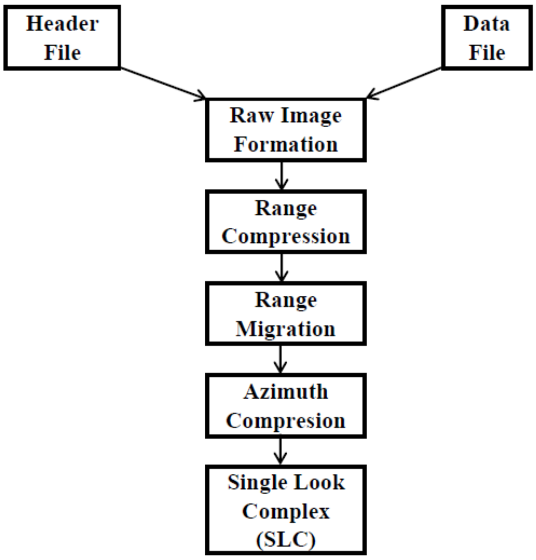

Figure 2-5 Flowchart showing the main steps of the SAR focusing process

	ERS	ENVISAT	Unit
Pulse Repetition interval	595.27	605.17	Microseconds
Pulse repetition frequency	1679.9	1652.41569	Hertz
Sampling frequency	18.962	19.20	Megahertz
Pulse length	37.12	27.17	Microseconds
Chirp slope	418.91	588.74	Gigahertz/second
Wavelength	5.6666	5.62356	centimetre
Carrier frequency	5.29	5.331004	Gigahertz
Bandwith	15.55	16.00	Megahertz

Table 2-2 Parameters necessary for the SAR processing for two type of sensors: ERS and ENVISAT (both used in this work).

After reading in the necessary parameters and a block of data, the range compression can be performed. The latter step involves convolution of the raw data with the estimated range reference function (RRF), which is a replica of the transmitted radar pulse that is correlated with each row of the raw SAR data. This can be performed by a complex multiplication in the range frequency domain. For that purpose the RRF is transformed into the Fourier domain using a Fast Fourier Transformation algorithm and then multiplied by the one-dimensional Fourier converted raw data. Finally, the product is transformed back to the time domain to complete the range compression procedure.

The estimation of the Doppler centroid f_{DC} is an important part of the processing and must be determined before the Cell migration correction and the Azimuth compression are carried out (see Figure 2-5). The Doppler centroid can be defined as the Doppler-shift of a target positioned in the antenna boresight direction (Madsen 1989). In the ideal case (i.e. normal SAR configuration) the Doppler Centroid would be zero, however, the antenna is squinted because the Earth rotates while satellite orbits leading to larger values. To estimate the Doppler Centroid, usually the Doppler is first modeled as a linear function of the slow time *s*. In this work the clutterlock operation (automatic estimation of the f_{DC}) together with the correlation Doppler estimator (Madsen 1989) was employed.

In the case of two SAR signals forming an interferometric pair, the azimuth spectral filtering can be applied to compensate the decorrelation from different Doppler centroids between the two images (see Chapter 3). Other strategy consists on processing the data in the same Doppler centroid. Nevertheless, this procedure conduces to errors in one or both images being process with deviation with respect to the real Doppler history.

After f_{CD} estimation, the range-compressed point target response is distributed over several range bins as the target is imaged in slow time in the operation known as Range Migration. The shape of the migration path is calculated from the precise orbital information, and the range migration correction is accomplished by shifting the bin cell in the range direction with a value

$$DR(s) = R(s) - R_c \tag{2.9}$$

where

$$R(s) - R_c = -\frac{\lambda f_{DC}}{2}(s - s_c) - \frac{\lambda f_R}{4}(s - s_c)^2 \tag{2.10}$$

being f_{R} is the Doppler rate, s slow time and s_c the slow time when the target is in the center of the beam. Equation (2.11) indicates that more significate range migration occurs at longer wavelengths.

Following the cell migration correction, the azimuth energy is aligned vertically in the computer memory and the azimuth compression is then performed. This step consists of focusing the data in azimuth by accounting for the phase shift of the target as it moves through the aperture. For this purpose are necessary: the generation of a matched filter, a look extraction with weighting and the performance of the inverse discrete Fourier transform.The azimuth math filter is explained in detailed in Curlander and McDonough 1991.

Azimuth compression is a convolution of the range-compressed, range-migrated data with the azimuth reference function. This procedure can be efficiently carried out in the Doppler frequency domain by a complex multiplication of the azimuth reference function Doppler spectrum with the range-compressed range-migrated data. Finally, the product is inverse Fourier transformed to provide the focused image (i.e. SLC).

Because the SLCs are affected by speckle (i.e. variance of the image; Henderson and Lewis 1998), a very dominating factor in SAR imaginary that could be very useful but also can be seen as a problem, an optional procedure can be applied: multi-looking. This filtering procedure reduces the speckle at the expense of the resolution. It consists of averaging independent sub-images or looks of the same area, which are formed during the SAR processing by partitioning the frequency in the azimuth domain, process that is equivalent to a linear filter applied to smooth the image after detection (Henderson and Lewis 1998). The number of looks (typically 3 or 4) is usually selected such that the azimuth pixel size approximately equals that of the ground range pixel size.

2.4 Geometrical Distortion

Depending on the varying incident angle, the SAR image can be affected by geometrical distorsion such as layover, foreshortening and shadow (detailed description can be found in Henderson and Lewis 1998).

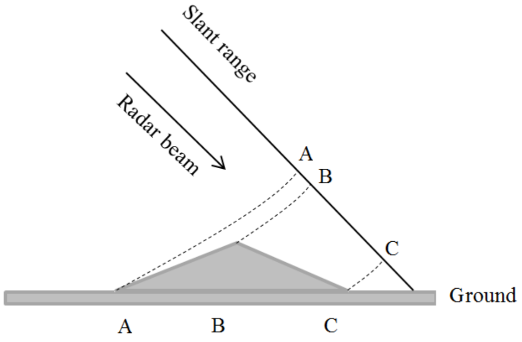

Figure 2-6 Example of forshortening effect

Foreshortening appears when the radar beam reaches a slope facing towards the satellite, effect that is translated into the SAR image as shortened slope (Figure 2-6). This effect depends on the relation between the incident angle and the mountain slope and can be lessened by imaging at large incident angles.

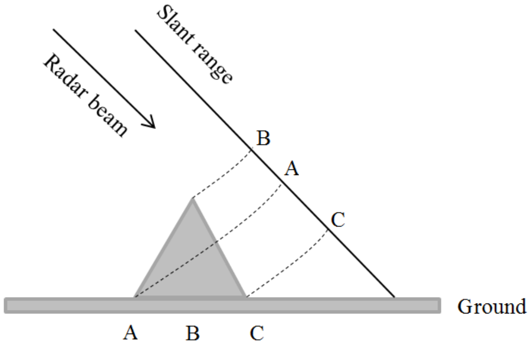

Figure 2-7 Example of layover effect: point B appears before point A in slant range

The layover, is another geometric distortion affecting the SAR imaging and it ocurrs when the return signal from the top of a feature (e.g., a mountain) is received before the signal from the bottom (see Figure 2-7). This effect might difficult the interpretation of an image, as each pixel may contain scattering contributions from more than one area in the scene (Henderson and Lewis 1998). Layover is generally severe for small incident angles and in mountainous regions.

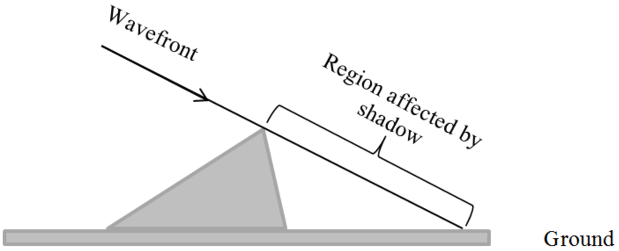

Figure 2-8 Radar shadowing. The area affected with would appear in the image as a dark zone.

The shadowing effect happens because of the side-looking geometry. Areas affected by shadow will appear as dark areas in the image (see Figure 2-8). A possible solution to imaging these regions is by looking them from the opposite side. However, available data in both directions is not always available.

Chapter 3

SAR Interferometry

The SAR technology has brought with it the development of several approaches with powerful applications. InSAR is one of the most significant advances for deformation studies.

The term interferometry comes from interference, which in physics refers to the interaction of two front waves that could be destructive or constructive. A destructive interference takes place when the waves involved move in an opposite direction or are out of phase. On the other hand, in constructive interference, the waves that interact have the same frequency and travel in the same direction. In the case of radar interferometry, the principle behind is the same: two fronts of microwaves interact coherently (i.e. phase and amplitude are received and preserved). This type of interferometry is also known as multiplicative interferometry.

In InSAR the coherent cross-multiplication of two SAR input signals is performed to get essential information for topographic mapping and change detection applications with sub-centimeter accuracy.

The first experiments with radar interferometry dated back to 1969 for planetary mapping of Venus. However, the original SAR interferometric application was performed in 1971 by the USA military in order to get elevation from phase difference images (Henderson and Lewis 1998). In 1986, Zebker and Goldstein showed their first results from an experiment using a single-pass antenna airborne interferometry, digital processing and coherent multiplicative interferometry (Zebker and Goldstein 1986). Their outcomes were interferograms, complex images in which each resolution element contains the amplitude and the phase information (Hanssen 2001). Gabriel and Goldstein (1988) and Li and Goldstein (1990) demonstrated, using the SIR-B and SEASAT data, respectively, that interferometry could also be applied with spaceborn data acquired over several days. Since then, the usage of SAR interferometry extended into different application areas such as topographic mapping (Bamler et al. 1996), deformation monitoring (Ferretti et al. 1999 ; Gabriel et al. 1989; Strozzi et al. 2003; Usai and Hanssen 1997; Zhong et al. 2010), thematic (Geudtner et al. 1996; Rosen et al. 1996 ; Roth et al. 1997; Wegmüller et al. 1995 ; Zebker and Villasenor 1992) and atmospheric delay studies (Hanssen 2001; Jolivet et al. 2011).

While the SAR interferometry applications sprawled, new interferometric configurations appeared. Moreover, strategies for coping with different constraints of the interferometric processing were developed. The differential SAR interferometry (D-InSAR), for example, which stands for three-pass or four-pass interferometry allows solving the deformation phase in cases where the topographic effect masks it. However, this configuration must still deal with some problems regarding decorrelation, atmospheric effects and loss of coherence. In an endeavour to solve these problems the so called multi-temporal InSAR (MTI) techniques were raised. Chapters 4 and 5 focus on the latter techniques.

3.1 Interferogram Formation

The SAR technology allows the acquisition of valuable information about earth processes; however, SAR data can be exploited at a maximum when combined. The interferometric SAR configuration uses this idea to extract meaningful information for detecting changes in the ground surface or to map the topography captured during the satellite path.

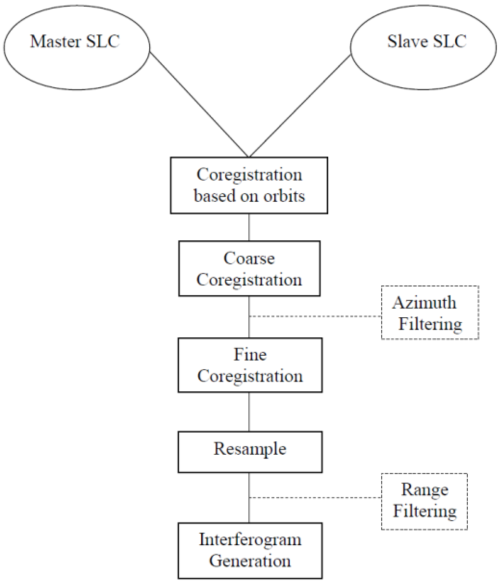

Figure 3-1 Simplified flowchart of the SAR interferometry processing. The processes connected by dashed lines are considered as optional steps in the processing. The extraction of the topographic phase in not included.

The interferometric method involves several steps for the formation of the interferogram, which is a complex image. Coregistration and resampling are necessary for the generation of the complex interferogram (see Figure 3-1). Filtering procedures can be included in the processing.

Coregistration is one of the main steps in the interferogram generation. It comprises matching two images in the geometry of one of them; this insures that the position of one pixel in an image corresponds to the position of the same pixel in the other image.

The images are referred to as master and slave, generally corresponding to the acquisitions during the first and second path of the satellite, respectively, looking at the same target.

Two categories of coregistration must be carried out to reach sub-pixel accuracy: coarse and fine. However, a primary coregistration using the information of the slave and master orbits is usually performed with a precision of 30 pixels. Subsequently, the coarse coregistration is done to determine offsets in the azimuth and the range directions between the images with an accuracy of the order of a pixel. The correlation can be computed in the space or in the spectral domain. Following the coarse coregistration, an azimuth filter in the master spectrum could be applied to filter out the part of the spectrum that does not overlap that of the slave, which is a consequence of their different Doppler centroid frequencies.The same can be done for the slave image too.

Afterwards, the fine coregistration needs to be done. The offset vectors that align the slave image to the master are computed with sub-pixel accuracy for the tie points in the master. This task can be achieved by using methods such as cross-correlation (Li and Goldstein 1990) in space (or in the spectral domain) or oversampling (Rufino et al. 1996), which avoids aliasing of spectrum. Other methods for coregistering are based on the signal to noise ratio (SNR) calculated in the frequency domain of the interferogram (Gabriel and Goldstein 1988).

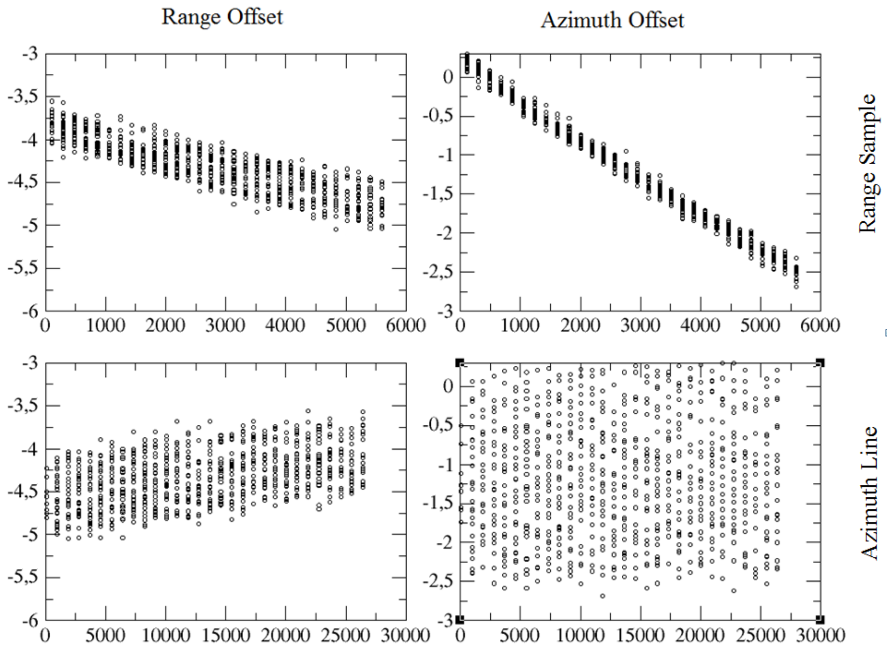

Figure 3-2 Example of offsets estimated for an ENVISAT interferogram covering the northern part of the Valley of Mexico with a perpendicular baseline of 385 m and a temporal baseline of 35 day. Output from the coregistration step of the ROIPAC software.

An optional step to prevent from undersampling during resampling is the oversampling in range and azimuth. Usually, a factor of 2 is sufficient to produce high quality interferograms.

Once the oversampled images are aligned, the resample or interpolation process must be completed to place the points of the slave in their corresponding positions in the master grid with a sub-pixel precision. Interpolators such as the nearest neighbor, linear interpolation, cubic convolution kernel, truncated sinc or raised cosine can be applied to resample the slave onto the master's grid. Optionally, after this step range filtering can be used to reduce the noise in the interferogram caused by slightly different viewing angles during the two different passes of the satellite or because images from different sensors are used.

Finally, the complex multiplication between the resampled master and slave can be computed to form the interferogram.

For the case of deformation studies the topography extraction could be deemed as an additional step after the interferogram generation. For that purpose, a digital elevation model (DEM) can be created from the available SAR data or downloaded from an exterior source (e.g., from the shuttle radar topography mission (SRTM); Farr and Kobrick 2000). On the other hand, this step could define the D-InSAR technique, which can be considered as a branch of the conventional InSAR.

3.2 Interferometric phase

Mathematically, the complex interferogram computed from multiplication of the master complex image y_1, by the conjugate complex slave y_2^*, resampled on the geometry of the first image can be expressed as

$$y_1 y_2^* = |y_1| e^{j\phi_1} |y_2| e^{-j\phi_2} = |y_1||y_2| e^{j(\phi_1 - \phi_2)} = |y_1||y_2| e^{j(\phi_{\text{int}})} \tag{3.1}$$

where ϕ_1 and ϕ_2 are the phases of the master and the slave, respectively, and ϕ_{int} represents the interferometric phase (see Figure 3-3).

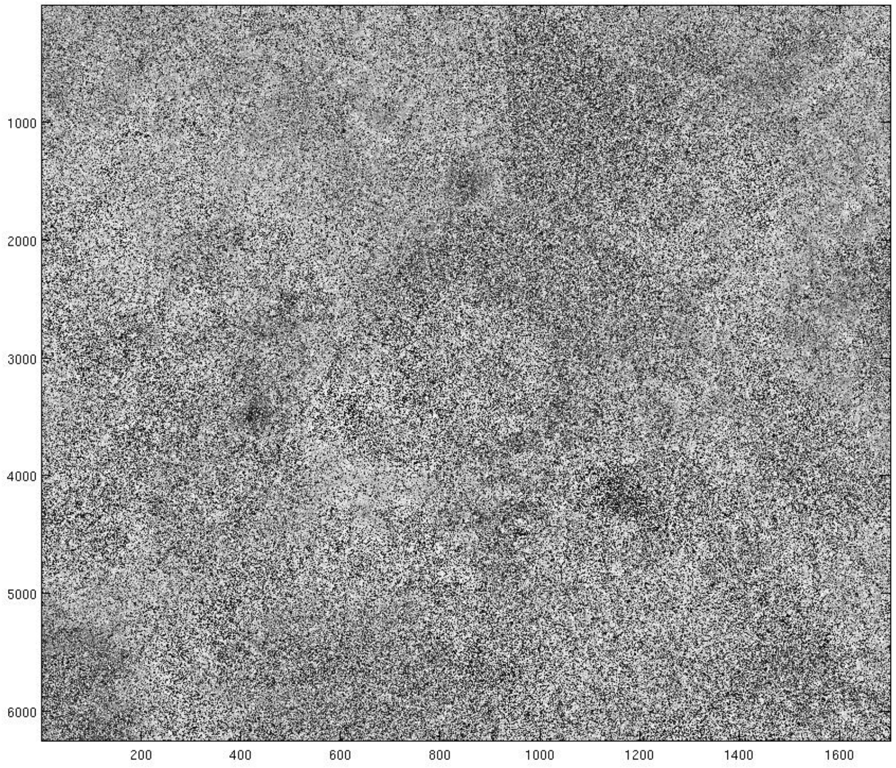

Figure 3-3 Phase ϕ_{int} of a raw interferogram calculate form ENVISAT images over part of the Cuautitlán-Pachuca subbasin

ϕ_{int} can be expressed as a function of the changes in the length path and the scattering characteristics of the resolution cell,

$$\phi_{\text{int}} = \phi_M - \phi_S = -\frac{4\pi}{\lambda}\Delta R \tag{3.2}$$

where λ is the wavelength and ΔR is the difference in range which can be expressed approximately as

$$\Delta R = B\sin(\theta - \alpha) \tag{3.3}$$

being B the baseline, θ the look angle and α the angle respect to the local normal. The minus sign in equation (3.2) appears because the phase delay ϕ_{int} increases while ΔR decreases.

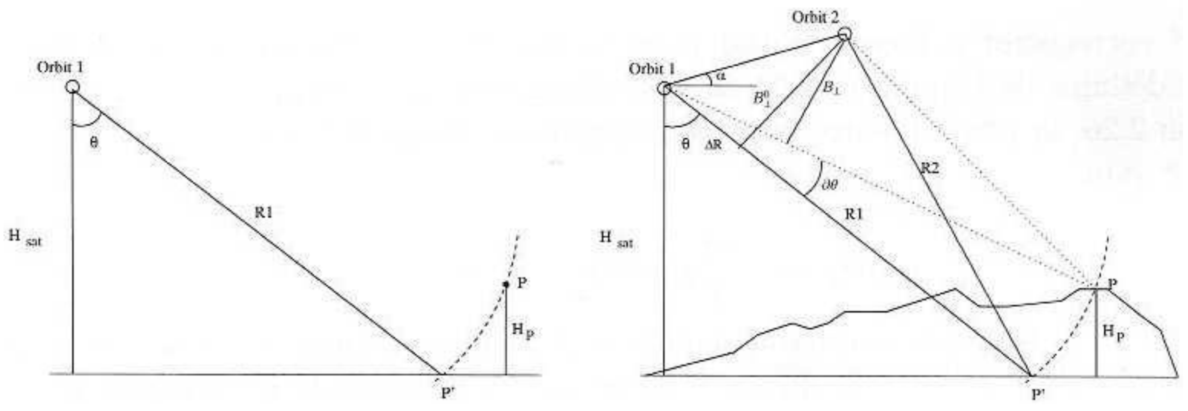

Figure 3-4 Single-pass and interferometric configuration. a) In this case, points P (at a certain height H_p) and P' (on the reference body) at a certain distance R from a SAR sensor cannot be solved from one SAR image. b) Interferometric case: two SAR sensors observed the target from different look angles. The physical separation of the satellites is given by the baseline B, being $B_\perp$ the perpendicular component. The height H_p can, now, be solved by using the satellite height H_{sat} and the range R_1 (adapted from Hanssen 2001).

If between the two passes of the satellite no changes are experienced in the earth surface then point P in Figure 3-4b would stay in the same position. In this case, equation (3.2) can be express as (Rodriguez and Martin 1992; Hooper 2006)

$$\phi \approx \frac{4\pi}{\lambda} B\left(\sqrt{1-\frac{{H_p}^2}{R^2}}\cos\alpha - \frac{H_p}{R}\sin\alpha\right) \tag{3.4}$$

where the H_p represents the high above the reference ellipsoid , and this indicates that the phase is only due to the topography (Rodriguez and Martin 1992).

3.3 Components of the interferometric phase

The phase of the interferogram contains information coming from different sources. Considering all the elements that contribute to the signal, the interferometric phase ϕ_{int} can given as (Hooper et al. 2004)

$$\phi_{\text{int}} = \phi_{flat} + \phi_{topo} + \phi_{defo} + \phi_{atm} + n \tag{3.5}$$

where ϕ_{flat} represents the phase of the flat earth caused by the reference ellipsoid, ϕ_{topo} corresponds to the topography, ϕ_{defo} due to the changes in ground surface observed in LOS, ϕ_{atm} is due to the atmospheric delay and *n* contains the noise due to the variability in the scattering, thermal noise and coregistration errors.

3.3.1 *Flat earth phase*

This component is due to difference in altitude of the points targets respect to a reference surface. It can be computed as

$$\phi_{flat} = -\frac{4\pi}{\lambda}\frac{B_\perp \Delta R}{R\tan\theta} \tag{3.6}$$

where the perpendicular baseline $B_\perp$ is estimated using the precise orbits. For the estimation of this phase the coordinates of the satellite in the master and slave position and the point observed are computed on the reference surface (usually the WGS84 ellipsoid). The effect of this component appears in the interferogram as long wavelength features.

3.3.2 *Topographic phase*

The influence of the topography in the interferometric phase can be expressed as a function of the perpendicular baseline $B_\perp$, the high information Δh contained in the digital elevation model, the wavelength λ and the look angle θ

$$\phi_{topo} = \frac{4\pi}{\lambda R}\frac{B_\perp \Delta h}{\sin\theta}. \tag{3.7}$$

This equation tells us that, for certain look angle, the larger the perpendicular baseline $B_\perp$, the larger the influence of the topography. This factor must be taken into account when trying to monitor changes. In that case, interferograms with perpendicular baselines smaller than 400 meters (for ERS and ENVISAT) are preferable.

3.3.3 *Atmospheric phase*

The SAR signal is affected by atmospheric artifacts which effect is usually referred to as atmospheric phase delay (APS). The APS is one of the main factor limiting the accuracy of InSAR when monitoring changes in the surface (Hanssen 2001, Zebker 1997).

The atmospheric component includes the effects coming from the interaction with the ionosphere and the troposphere. However, the later restricts the most the sub-centimeter accuracy that could be achieved by the repeat-pass interferometry.

Ionosphere effects occur because of the radioviolet radiation and the energetic solar electrons of solar and magnetospheric origin (Hanssen 2001). For the correction of the ionospheric delay we can compute the Total Electron Content (TEC), which is the integral of electron density in a 1 m^2 column along the signal transmission path. In navigation systems such as the Global positioning System (GPS), this component can be eliminated by using the ionosphere-free combination of carrier phase or the code pseudo ranges measured in two frequencies. Part of the remaining ionospheric terms can be eliminated by using the combination of three coherent frequencies. Similar to the GPS, in InSAR an identical ramp of TEC in both SAR images would be canceled in the interferogram. In general, the identification of ionospheric effects in SAR interferograms results particularly difficult (Hanssen 2001).

For the tropospheric correction two constituents must be considered: the turbulent tropospheric delay and the vertical stratification. The correction of the former, which is the predominant component of the atmospheric phase delay, represents a challenge for both GPS and InSAR techniques. The main source of the turbulent delay is the water vapor, which causes heterogeneities in the refractivity during the SAR acquisitions. The contribution of this signal is present in both, flat and mountainous terrains.

The second or vertical component of the atmospheric phase is the result of different refractivity profiles during the acquisitions and it affects steep regions (Hanssen 2001). Considering a mountainous region and a troposphere in hydrostatic equilibrium, the stratified atmospheric effect could be corrected by using its inverse proportional relation with the topographic elevation (Massonet and Feigl 1998).

Efforts have been made to improve the correction of this component since its total effect could be 10s of cm (Liu et al. 2009). The use of meteorological data for the correction coming from in-situ stations or GPS information have been applied in many studies (Löfgren et al. 2010; Onn and Zebker 2006; Williams et al. 1998; Webley et al. 2002). Nevertheless, a large number of meteorological or GPS stations are necessary for an accurate estimation of the atmospheric delay, implying high operation costs.

Weather models alone or combined with the interferometric phase of non-deforming areas have been also used for the correction of APS component that correlates the topography (Cavalie et al. 2007; Delacourt et al. 1998; Doin et al. 2009; Puysségur et al. 2007 ; Wicks et al. 2002).

Maps of tropospheric heterogeneities have been successfully produced by employing the data from MODerate resolution Imaging Spectrometer (MODIS) (Li et al. 2005) or MEdium Resolution Imaging Spectrometer (MERIS) onboard ENVISAT (Li et al. 2006a; Li et al. 2006b) sensors. However, the limitations of the MODIS reside on non-simultaneity of SAR acquisition and for both, MODIS and MERIS on the calibration and cloud coverage.

Other strategies imply the use of filtering to smooth the atmospheric component in time series InSAR (Ferretti et al. 2001; Berardino et al. 2002; Schmidt and Bürgmann 2003).

All these methods have improved the estimation and correction of the APS, however, none of them have achieved its complete elimination from the interferometric phase, either for mapping topography purposes or deformation analysis.

3.3.4 Noise phase

One way to measure the phase noise affecting the quality of the interferogram could be by computing the complex coherence (e.g., Hanssen 2001)

$$\gamma = \frac{E\left\{y_1 y_2^*\right\}}{\sqrt{E\left\{|y_1|^2\right\} E\left\{|y_2|^2\right\}}}, \qquad 0 \le \gamma \le 1. \tag{3.8}$$

Influences from several sources of decorrelation can also be independently estimated and used later to compute their combined effect.

The geometrical decorrelation (γ_{geo}) in an interferogram, caused by different incident angles between acquisitions, can be estimated as a function of the critical baseline $B_\perp$ (Hanssen 2001)

$$\left|\gamma_{geo}\right| = \begin{cases} \frac{B_{\perp,crit} - B_\perp}{B_{\perp,crit}}, & \left|B_\perp\right| \le B_{\perp,crit} \\ 0, & \left|B_\perp\right| > B_{\perp,crit} \end{cases}, \tag{3.9}$$

where $B_{\perp,crit}$ is

$$B_{\perp,crit} = \lambda(B_R / c)R_1 \tan(\theta_{inc} - \varsigma) \tag{3.10}$$

In equation (3.10) B_R represents the bandwidth equal to the spectral shift between the SAR acquisitions and ζ the topographic slope.

In order to decrease the effect of the geometric decorrelation, the formation of interferograms with perpendicular baselines smaller than the critical one is desirable.

The temporal decorrelation (γ_{temp}) produced by changes in the electrical characteristics of the scatterers between the first and the second acquisition can be reduced by the selection of relatively short time spans between the satellite paths. Nevertheless, this is also depends on the conditions of the area under study and the phenomenon observed.

Another source of the decorrelation comes from different Doppler centroids (γ_{DC}) between the acquisitions. This effect can be reduced by the application of filtering in the spectrum domain or by processing the raw data images at the mean Doppler centroid frequency (see also Chapter 2).

The noise produced by the penetration of the radar wave in the scattering medium is cause of decorrelation (γ_{vol}). The influence of the thermal noise (γ_{themal}) also affecting the interferogram quality, can be derived from the estimated SNR of a specific system (Zebker et al. 1994).

Part of the noisy phase is due to the errors from the coregistration and resampling steps during the interferogram formation. Thus, the algorithms for those processes should be carefully selected in order to diminish this source of noise.

Considering these noise terms, the total decorrelation can be computed as (Zebker and Villasenor 1992),

$$\gamma_{tot} = \gamma_{geo} \cdot \gamma_{DC} \cdot \gamma_{vol} \cdot \gamma_{thermal} \cdot \gamma_{temp} \cdot \gamma_{proc} \cdot \tag{3.11}$$

3.4 Unwrapping

Unwrapping represents the key step in the InSAR processing for retrieval of both height information for Digital Elevation Model (DEM) generation, and magnitude of displacement for deformation studies. This process consists on adding to each measured interferometric phase ϕ_{int} the correct number of integer cycles p

$$\psi = \phi_{\text{int}} + 2\pi p. \tag{3.12}$$

The number of cycles p must be such that ψ (wrapping function) $\in [-\pi,\pi)$ (see Figure 3-5).

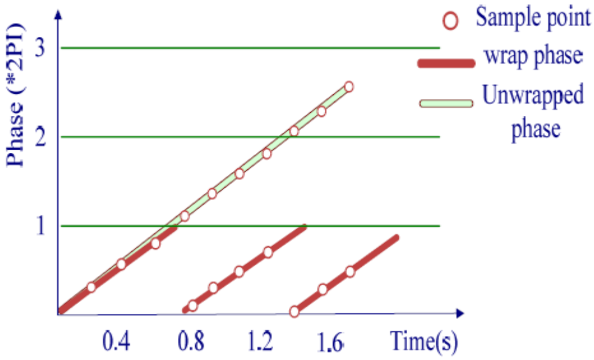

Figure 3-5 Example of the ideal case where the interferometric phase is completely restored to the real phase after unwrapping (from Pan and Gan 2008). Note that in this case no errors are assumed in the interferometric data.

The integration of phase differences from a reference point is the simplest way of carrying out the phase unwrapping. If all differences between neighboring pixels are within one-half cycle (π radians) this procedure could be carried out straightforward and the selection of any reference points should conduce to the same result. However, this is not always the case for all the pixels, and discontinuities (i.e. phase variations between neighbor pixels) are usually larger than π. This causes inconsistences or residues leading to different unwrapping outcomes depending on the reference points selected and the path followed.

The discontinuities in an interferogram are consequence of layover or forshortening effects (see Chapter 2), decorrelation or high deformation gradients affecting the study area. Various algorithms have been developed in order to solve this problem. Broadly, we can divide the phase unwrapping algorithms into three groups: path following methods such the Goldstein's branch cut method (Goldstein et al. 1988), the norm algorithms (Ghiglia and Romero 1994; M.D. Pritt 1994; Pritt 1996) including the minimum L_p norm algorithm and the optimal estimation methods, such as network flow model (Chen 2001) and kalman filter models (Krämer 1989; Liu et al. 2010; Loffeld et al. 2008; Osmanoglu et al. 2009).

In this work the Goldstein's branch-cut algorithm, embedded in the ROIPAC software and the Statistical-cost, Network-flow Algorithm for Phase Unwrapping (SNAPHU) developed by Chen and Zebker (2000), are employed. Besides, the 3D method proposed by Hooper (2010) is exploited and its performance analysed.

Branch cut method (Goldstein et al. 1988)

The basic idea of the branch cut method or L-0 method is to unwrap the phase along a selected path that conduce to a self-consistent solution. For that purpose, first, it is necessary to compute the residues (Figure 3-6; Goldstein et al. 1988). The residues are due to different sources of errors such as thermal noise, speckle, high phase gradients, and topographic effects. In order to reduce these components, multi-looking filtering can be applied to the image, nevertheless, this implies also to coarsen the spatial resolution. Filtering, on the other hand, reduces the residues in any given image, making possible the selection of appropriate cuts (Goldstein et al. 1988).

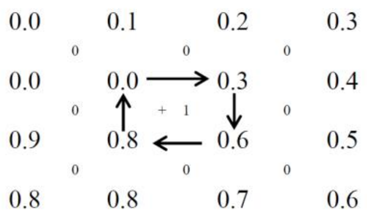

Figure 3-6 Residues from an example of wrapped phase array .Wrapped phase values (in cycles) are represented by large numbers. The small numbers are the results of the clockwise wrapped gradient loop integrals (adapted from Goldstein et al. 1988).

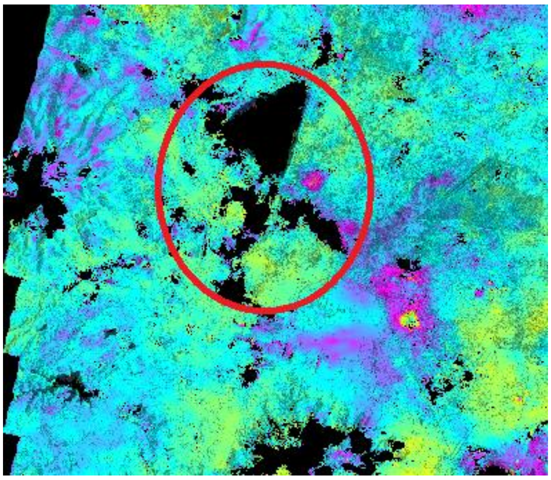

Figure 3-7 Unwrapped interferogram using the Branch Cut algorithm. The red circle indicates an example of a low coherence area that was not unwrapped. A lake and cropping lands are within the circle.

The identified plus and minus residues in the filtered image are connected forming cuts that grow in a treelike manner. The cuts are constructed in such a way that the integration path avoids encircle net residues. From various tests performed using the branch-cut algorithm it was observed that this approach works quite well in coherent areas (see Figure 3-7); however, it tends to fail in areas of low coherence or low SNR where the cuts close themselves, conducing to unsatisfactory results.

SNAPHU (Chen and Zebker 2000)

This unwrapping method takes advantage of the maximum a posteriori probability (MAP) concept for finding the most likely unwrapped solution from the observations: the input interferogram measuring surface topography, deformation or smooth generic data.

Chen (2001) poses phase unwrapping as a MAP problem and exploits generalized nonlinear cost functions. These functions, which reflect the theoretical relationships between unwrapped phase and the observed wrapped phase, image intensity and interferogram coherence, are derived while trying to achieve accurate solutions during the minimization of the L_p-norm. Depending on the subject of study (deformation or topography) different MAP cost functions are derived for different phase statistics.

In a certain way, this algorithm has advantages of the L_2 and L_0 algorithms. In areas where discontinuities are not expected (high coherent areas) MAP cost functions depend on the local correlation and are similar to the L_2 functions. On the other hand, in regions affected by discontinuities due to, e.g. large displacements, the cost functions are similar to those of the L_0 strategies.

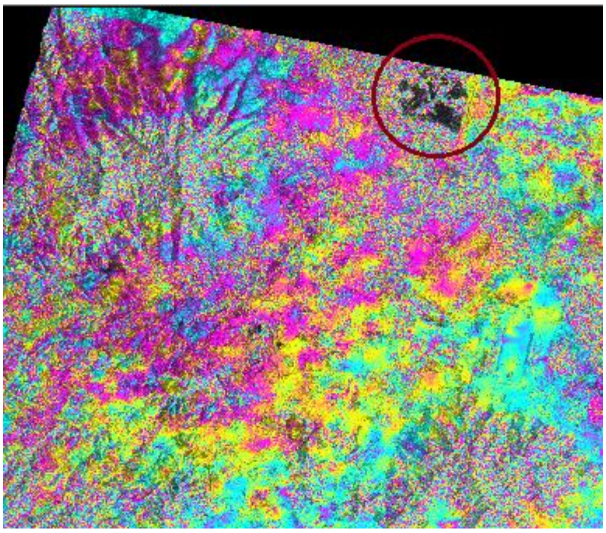

Figure 3-8 Area of poor coherence unwrapped by SNAPHU. Note that the encircled area (in red) corresponding to a lake has been unwrapped.

In general, this algorithm yields to precise results for deformation and topographic mapping. However, some irregularities have been also observed when unwrapping the phase in areas of poor or no coherence exists such as in water bodies (see Figure 3-8).

Spatio-temporal unwrapping method (Hooper 2010)

The quality of the deformation time series obtained in MTI techniques depends on the effective elimination of components that mask the signal of interest (i.e. deformation in this work), but principally on the performance of the unwrapping procedure for estimation of the integer phase-cycle ambiguities.

Hooper (2010) proposed a new unwrapping method using the spatial-correlated information of the signal. He assumes that the phase difference between nearby pixels tends to be less than half a cycle because the contribution from the components spatially correlated is small. From this hypothesis, he establishes the unwrapping as a MAP problem similar to Chen (2001).

The algorithm uses SNAPHU for unwrapping the data in space. However, because the data sets are sparse, SNAPHU cannot be directly applied and a resampling method is first required to reduce the irregular grid to a regular one (Figure 3-9).

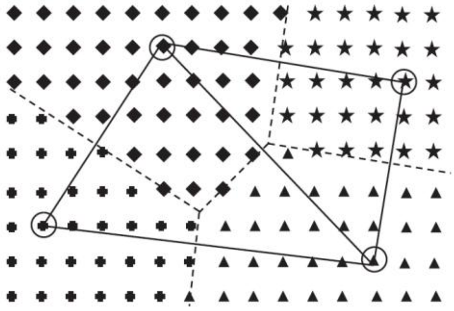

Figure 3-9 Reduction from irregular to a regular grid used by SNAPHU (from Agram 2010).

After interpolation, the phase difference between non interpolated neighboring grid cells is computed for each interferogram and then low-pass filtered in time. The filtered values are then unwrapped under the Nyquist assumption. Probability density function (PDF) for the unwrapped phase difference between neighboring grid cells in each interferogram are built using the outcomes from the previous step.

For non-zero phase differences between neighboring interpolated cells from the same phase measurement, the PDF is zero. Otherwise, the PDF is the normalize product of a Gaussian PDF and a comb function, which is used to ensure that the unwrapped phase is equal to the wrapped phase plus an integer number of cycles *p*. These PDFs are employed for derivation of the cost functions, and the optimization routines of SNAPHU are used to maximize the total joint probability density (Hooper 2010). Detailed description of this unwrapping method can be found in Hooper (2010).

As a remark, Lopez-Quiroz et al. (2009) also took advantage of the existing unwrapping approaches (SNAPHU and Branch Cut) and designed a methodology to help the unwrapping procedure. For this purpose, they used the stable pattern of the deformation observed for a particular period of the year (i.e. dry period), and estimated the average deformation rate using the best five interferograms corresponding to that “season”. This information is later used to reduce the number of fringes and thus make easier the unwrapping. This method was applied to Mexico City, but can be extended to other areas presenting similar characteristics such as high deformation gradients.

Chapter 4

Advanced InSAR methods for time series analysis

4.1 InSAR versus MTI methods

The conventional InSAR and its 3-and 4-pass configuration (D-InSAR) represent a powerful tool for detection and monitoring of displacements. They have been successfully applied in deformation studies due to active volcanism (Pritchard and Simons 2002), co-seismic motions (Simons et al. 2002; Zebker and Rosen 1994), post-seismic motions (Jacobs et al. 2002; Pollitz et al. 2001), mining and groundwater induced deformation (Amelung et al. 1999), and creeping faults (Bürgmann et al. 2000; Ryder and Bürgmann 2008). However, this technique still has limitations for certain applications and under conditions that make it fails or conduces to untrustworthy results. In zones characterized by lush vegetation, ice-melting processes or other phenomena that induce changes in the scattering properties, the interferogram quality is degraded. The level of deterioration depends as well on the length of the spatial separation between the antennas i.e. geometric baseline, which if too long notably reduces the SNR, and if too short decreases the sensitivity of InSAR for phase difference measurement. Detailed studies regarding the spatial baseline effect have been presented by Li and Goldstein (1990) and Rodriguez and Martin (1992) too. Different viewing angles between acquisitions can also negatively impact the interferogram because the signals do not fully correlate (Zebker and Villasenor 1992). In addition, differences in Doppler frequencies due to different squint angles add decorrelation. The latter, can in principle be diminished by azimuth and range filtering. Nevertheless, there are critical values for the temporal and spatial baselines and the difference in Doppler beyond which the signals completely decorrelate and the result is useless in standard interferometry applications.

The phase difference between two SAR radar images is also affected by the APS. Methods for the elimination or reduction of the APS and the orbital fringes were presented in Chapter 3. Normally, because the magnitude of the orbital residuals is very small they cannot be discerned from the atmospheric delay in the interferometric signal.

In order to cope with the limitations of the classic InSAR technique, MTI approaches have been developed. Basically, these procedures take advantage of the available large SAR data sets and combine them to finally retrieve information of the signal behaviour in time. They can be widely classified into two algorithm groups which are optimized for different scattering models: Permanent Scatterer Interferometry (PSI) and SBAS approaches. Pixels with scattering properties remaining stable in time and when observed from different angles, defined as persistent scatterers (PS), are the goal of the PSI. In the case of the SBAS methods, multiple-master interferograms are formed, unwrapped and then inverted to retrieve incremental phase displacements.

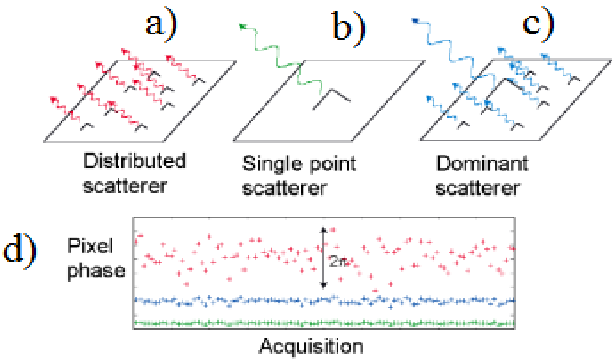

Figure 4-1 Various scattering models for the a SAR resolution cell (from Agram 2010): a) the mechanisms for distributed scatterer, b) ideal case of a single scatterer and c) patch depicting the case of a dominant scatterer. The graphic in the bottom (d) shows the variation of the phase versus the acquisition number for the different models. Scatterers phase is randomly distributed within [-π,π]. Stability is observed for the single point and dominant scatterrer patterns.

The variation of the scattering properties within a resolution cell depends mainly on the behaviour of the scatterer/s embedded in the image pixel. Figure 4-1 presents three models for which the scattering properties behave in a different manner.

Supposing all scatterers contribute the same to the interferometric phase, then the SNR can be improved by averaging neighboring cells (multi-looking) at expenses of the resolution. This way, the random component of the phase of each scatterer is cancelled, leaving the average phase of the multi-looked pixel. This model corresponds to the principle used in the SBAS methods (Figure 4-1a). Since the SBAS algorithms rely on the unwrapped phase, the multi-looking process must be carried out prudently because a full resolution image can be more robustly unwrapped than when applying filtering (Hooper 2008).

If only one scatterer would contribute to the interferometric phase (Figure 4-1b), the backscatter signal would vary little in the time and the ground displacement could be estimated without errors (Agram 2010). This is rarely the case and most of the time the resolution cells present various scatterers with a similar strength, or among the scatterers there is one contributing the most to the signal.

In the case of a dominant scatterer, its contribution prevails over the others and the pixel would be characterized by a stable signal (Figure 4-1c). In this case the displacement of the scatterer can be determined directly from the interferometric phase.

4.2 Permanent Scatterer Interferometry

By using statistics the PS are identified in the PSI methods. There are two main algorithms developed for the identification of the PS pixels: amplitude based (Ferretti et al. 2001) and phase stability-based methods (e.g., Hooper et al. 2004; Hooper et al. 2007).

The idea of these methods is to identify the stable phase targets in an image to either estimate the magnitude of displacement affecting an area or refine DEMs. The computation of differential interferograms with a common master acquisition is required.

In principle, coherence maps could be also used for the identification of the coherent pixels (Ferretti et al. 2001). However, factors such as topographic, orbital and atmospheric effects could make a stable target look as noisy in the coherence map, and thus the selection of PS based on the coherence would limit the analysis. Moreover, the spatial and temporal decorrelation would restrict the pair of interferograms to be formed for generation of profitable coherence maps for the PS detection. Nevertheless, coherence maps are still useful for a preliminary PS selection.

4.2.1 Amplitude-based method (Ferretti et al. 2001)

This method evaluates the amplitude values A of the pixels to identify stable targets. From this criterion, only pixels showing very stable amplitude in time are selected as PS candidates (PSC).

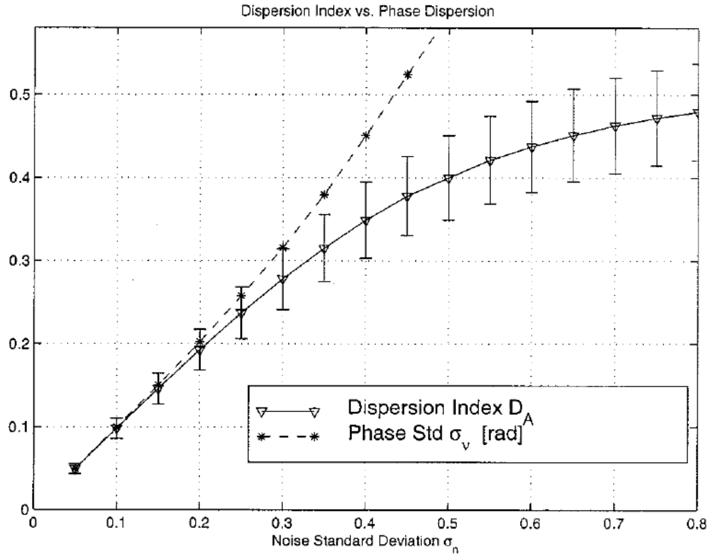

Figure 4-2 Mean values of D_A plotted for each value of σ_n, with error bars representing the dispersion. Phase standard deviations s_v are also plotted. The graphic suggest that small values of D_A are good estimates of the phase dispersion (from Ferretti et al. 2001).

For high SNR selected pixels, the distribution of amplitude values *f*(A) approaches the Gauss distribution and then the amplitude variance could be express as (Ferretti et al. 2001):

$$\sigma_A \simeq \sigma_{n_R} = \sigma_{n_I} \tag{4.1}$$

where σ_R , σ_I are the variance of the real and complex part of the noise, respectively. From this expression the phase dispersion can be estimated as (Ferreti et al. 2001),

$$\sigma_v \simeq \frac{\sigma_{n_I}}{g} \simeq \frac{\sigma_A}{\mu_A} \triangleq D_A \tag{4.2}$$

where μ_A is the mean amplitude and σ_A is the standard deviation of the amplitude for each pixel. Then, the D_A, defined as the dispersion index (Ferreti et al. 2001) is a measure of the phase stability for pixels with high SNR. PSCs are initially selected for D_A under a certain threshold, which usually is under 0.25 (Figure 4-2; Ferretti et al. 2001).

Once most probably PSs are selected and the APS correction is performed, initially rejected PSs can be identified by analyzing their time series phase and they can be included in the final deformation map. This method was successfully employed in deformation studies over built-up areas, but its capability tends to critically decrease in natural terrains (Hooper et al. 2004).

Other methods have also been developed based on the Ferretti et al. (2001) model. Colesanti et al. (2003) improved the method to cope with the non-linear motion and Lyons and Sandwell (2003) used the scattering amplitude which is the inverse of D_A for the PSC recognition. The Interferometric Point Target Analysis (IPTA) method developed by Werner et al. (2003) extends the original method proposed by Ferretti et al. (2001) to non-urban areas. This method exploits the temporal and spatial characteristics of the target embedded in the interferometric signal. Crosetto et al. (2003) and Adam et al. (2004) also employed the amplitude information for PS recognition.

4.2.2 Phase stability-based method (Hooper et al. 2004; Hooper et al. 2007)

This algorithm is based on the phase characteristics and allows the detection of stable pixels in areas where amplitude based algorithms may fail. By using this approach a larger density of PS is found in certain areas (e.g., vegetated, cropping lands) in comparison to the Ferretti et al. (2001) approach.

Contrary to other PSI algorithms, this method uses only the spatially correlated nature of the deformation and no a priori assumptions about its temporal behaviour are done. Moreover, this method have been proved to work also with a few number of SAR acquisitions (e.g., 5 images; Hooper et al. 2004). Detailed description of the method is presented in Chapter 5.

4.3 Small Baseline methods

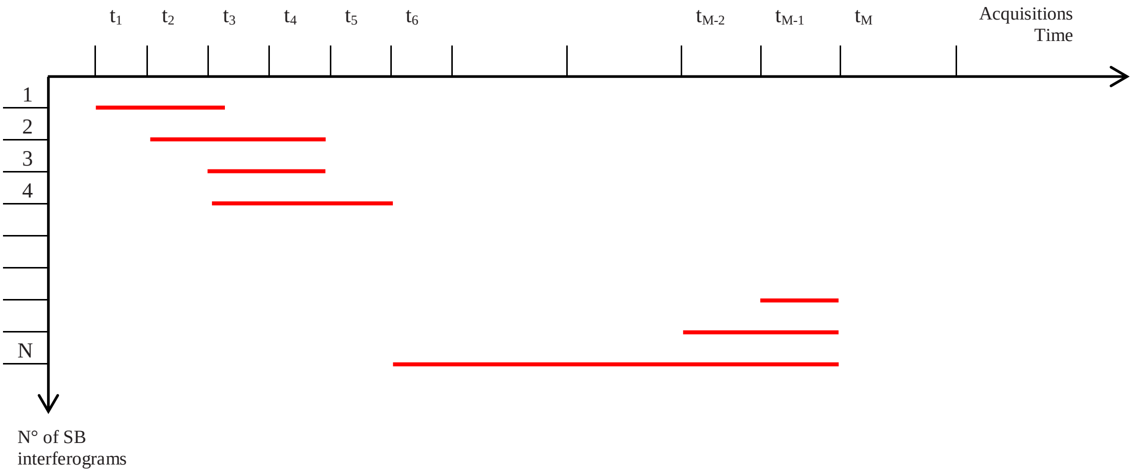

Figure 4-3 Example of SAR data combination for generation of SB interferograms**.**

The ground scattering model in the small baseline approaches consists of resolution elements containing no dominant scatterer. Within these methods, the application of spectral filtering in azimuth and range would increase the SNR helping the identification of PS. On the other hand, as the MTI techniques rely on the ability of the unwrapping, which can be carried out more efficiently in full resolution images, the application of filtering (multi-looking) could affect the quality of the SBAS time series.

The simplest form of the SBAS technique based on staking interferograms was first presented by Sandwell and Price (1998). Some algorithms were later developed (Agram et al. 2013; Berardino et al. 2002; Hetland et al. 2012; Hooper 2008; Lanari et al. 2004; Schmidt and Bürgmann 2003) taking advantage of the available large sets of SAR data and their proper combination for generation of mean displacement maps and deformation time series. In this work we proposed the StaMPS SBAS algorithm developed by Hooper (2008), which was adapted for selection of an appropiate spatial reference for the time series inversion.

Roughly speaking, all SBAS methods are based on the inversion of unwrapped D-InSAR interferograms with small perpendicular and temporal baselines (see Figure 4-3). One important difference between them resides on the use of different inversion methods: singular Value Decomposition (SVD) (Berardino et al. 2002), minimization of the L_1 norm (Lauknes et al. 2011) and constrained Least Squares (LS) (López-Quiroz et al. 2009; Schmidt and Bürgmann 2003). In the following some of these approaches are presented focusing on their inversion methods. Study of the algorithms presented below, allows a better interpretation and comparison with the inversion method employed in this work. Moreover, the sources of discrepancies between our results and existing ones (see Chapter 7) can be better determined.

4.3.1 Usai (2003)

By using a redundant number of observations contained in the overlapping interferograms, the approach proposed by Usai (2003) allows not only to bring back the evolution of deformation but also to reduce the effects of processing errors and decorrelation noise. Basically, the procedure consists of:

- Coregistration of all the images to a selected master database so that each ground element correspond to the correct pixel in each interferogram
- Generation and unwrapping of the differential interferograms
- Inversion of the system consisting on the unwrapped phases. Phase-unwrapping errors are identified by forming close loops in time of the deformation maps (Usai 2003).

The system to be solve can be written as

$$y = \mathbf{A}x \qquad , \quad \mathbf{Q_y} = \sigma^2 \mathbf{Q} \tag{4.3}$$

where **A** is the design matrix, x and y represents the unknown incremental phases and the observed unwrapped phase, respectively. $\mathbf{Q}_{\mathrm{y}}$ is the covariance matrix of the observations and **Q** that of the parameters, while σ is the variance factor.

The solution of system (4.3) is estimated as

$$\hat{x} = (\mathbf{A}^{\mathrm{T}}\mathbf{A})^{-1}\mathbf{A}^{T} y \tag{4.4}$$

$$\mathbf{Q}_{\hat{x}} = (\mathbf{A}^{T}\mathbf{A})^{-1}. \tag{4.5}$$

An iterative strategy is used to further improve the results. Consequently, the updated system to be solved is

$$\begin{pmatrix} y_1 \\ y_2 \end{pmatrix} = \begin{pmatrix} \mathbf{A}_1 \\ \mathbf{A}_2 \end{pmatrix} x. \tag{4.6}$$

And the new estimation of the unknown is expressed as

$$\hat{x}_2 = \hat{x}_1 + \mathbf{Q}_{\hat{x}_1}\mathbf{A}_2^T(\mathbf{I} + \mathbf{A}_2\mathbf{Q}_{\hat{x}_1}\mathbf{A}_2^T)^{-1}(y_2 - \mathbf{A}_2\hat{x}_1) \tag{4.7}$$

$$\mathbf{Q}_{\hat{x}_2} = \mathbf{Q}_{\hat{x}_1} - \mathbf{Q}_{\hat{x}_1}\mathbf{A}_2^T(\mathbf{I} + \mathbf{A}_2\mathbf{Q}_{\hat{x}_1}\mathbf{A}_2^T)^{-1}\mathbf{A}_2\mathbf{Q}_{\hat{x}_1}. \tag{4.8}$$

where x_1 is estimated in the first iteration. This method includes in the inversion the addition of data between two disjoint data sets by interpolation.

4.3.2 Berardino et al. (2002)

This method uses the SVD method for connecting independent groups of interferograms. The approach includes the estimation of the topographic error and the deformation time series are filtered for removal of the APS. The approach is applied only to coherent points in order to exclude the noisy ones that would negatively affect the phase unwrapping. Let us now present some details of their method.

Being

$$\boldsymbol{\phi}^T = \left[\phi(t_1),\ldots,\phi(t_N)\right]$$

the vector of the N unknown unwrapped incremental phases for a generic pixel and

$$\boldsymbol{\delta\phi}^T = \left[\delta\phi_1,\ldots,\delta\phi_M\right]$$

the deformation vector of the pixel containing the M observed differential phases, where for each j-interferogram with master IE and slave IS the phase is

$$\delta\phi = \phi(\mathrm{t}_{\mathrm{IE_j}}) - \phi(\mathrm{t}_{\mathrm{IS_j}}), \qquad \mathrm{IE_j} > \mathrm{IS_j}, \forall \mathrm{j} = 1,\ldots,\mathrm{M} \tag{4.9}$$

the model that relates the observations with the unknowns can be express as (Berardino et al. 2002)

$$\mathbf{A}\boldsymbol{\phi} = \boldsymbol{\delta\phi} \tag{4.10}$$

with **A** the N-by-M design matrix that describes the interferometric system.

The design matrix is composed by ones and minus ones depending if the coefficient correspond to the master (t_{IE}) or slave (t_{IS}), respectively, or ceros otherwise.

Because in most cases, some subsets do not overlapped in time or in space, **A** is a rank deficient matrix and system (4.10) cannot be inverted straight forward. For solving this problem, the SVD method is proposed for the inversion insuring the minimum length norm among all the possible LS solutions (Lanari et al. 2004). By using this strategy, the solution can be presented as

$$\hat{\boldsymbol{\phi}} = \mathbf{A}^{+}\boldsymbol{\delta\phi} \qquad \textit{with} \qquad \mathbf{A}^{+} = \mathbf{V}\mathbf{S}^{+}\mathbf{U}^{\mathbf{T}} \tag{4.11}$$

with **A**+ the pseudo-inverse and **U** and **V** orthogonal matrices M-by-M and N-by-M, respectively. However, this procedure introduces some discontinuities in the deformation time series; thus instead of using the unknown vector of incremental phases $\boldsymbol{\phi}$, the vector of mean phase velocities $\boldsymbol{v}$ and a new design matrix **B** are replaced in system (4.10),

$$\mathbf{B}\boldsymbol{v} = \boldsymbol{\delta\phi} \tag{4.12}$$

where each B(*i*,*k*) element is,

$$B(i,k) = \begin{cases} t_{k+1} - t_k & \textit{for } IS_j + 1 \le k \le IE_j, \qquad \forall j=1,\ldots,M \\ 0 & \textit{otherwise} \end{cases} . \tag{4.13}$$

Because the derivation of the cumulative phases $\boldsymbol{\phi}$ is not direct, and additional step is required to recover them. If extra information regarding the nature of the deformation is known, then it can be introduced into the model like

$$\boldsymbol{v} = \mathbf{M}\,\boldsymbol{p} \tag{4.14}$$

where **M** is the coefficient matrix describing the parameters of the velocity model. By introducing this expression into system (4.12) then

$$\mathbf{BM}\,\boldsymbol{p} = \boldsymbol{\delta\phi}. \tag{4.15}$$

Considering a cubic model for the displacement, for each i-generic pixel it can be written as

$$\phi(t_i) = \bar{v}.(t_i - t_0) + \frac{1}{2}\bar{a}.(t_i - t_0)^2 + \frac{1}{6}\Delta\bar{a}.(t_i - t_0)^3 \tag{4.16}$$

with $\bar{v}$ representing the mean velocity, $\bar{a}$ the mean acceleration and $\Delta\bar{a}$ the mean acceleration variation. By using model (4.16) the linear system can be formed with M equations and four unknowns: $\bar{v}$, $\bar{a}$, $\Delta\bar{a}$ plus the residual height error Δz

$$[\mathbf{AM}, \mathbf{c}]\mathbf{x} = \boldsymbol{\delta\phi} \tag{4.17}$$

where **M** is a N-by-4 matrix and

$$c^T = \left[\left(4\pi/\lambda\right)/\left(B_{\perp 1}/r_1 \sin\theta_1\right),\ldots,\left(4\pi/\lambda\right)/\left(B_{\perp M}/r_M \sin\theta_M\right)\right] \tag{4.18}$$

proportional to the residual DEM errors and **A** is the design matrix of the cumulative phase change values.

By solving system (4.17) the residual topography errors and the temporal low-pass components of the deformation are estimated. The estimated residual topography errors and the low-pass elements are subtracted from each interferogram to reduce the fringe patterns that could have affected the quality of the unwrapping in the first estimation.

After that, a new unwrapping procedure is applied to the residual-wrapped phases. Subsequently, the subtracted low-pass component is added back, and finally the SVD-based inversion is applied. The atmospheric artifacts are filtered in the time series following a similar procedure described in Ferretti et al. (2001). The estimated topography errors in the first step can be also used to refine the DEM.

4.3.3 Schmidt and Bürgmann (2003)

Schmidt and Bürgmann (2003) apply a linear inversion to a set of interferograms to obtain the range change time series. The method allows the detection of non-linear deformation.

This approach was applied to interferograms with spatial baselines no longer than 200 m to ensure small topographic errors. In order to get the differential interferograms, an external DEM (SRTM-30 m) was used to remove the topography from the interferometric phase. Finally, after orbital corrections, filtering and unwrapping, the incremental displacement was retrieved using the following model

$$\mathbf{G}\boldsymbol{m}=\boldsymbol{d} \tag{4.19}$$

being **G** the design matrix that link the vector of the observed unwrapped phases **d** and the vector **m** of the unknown incremental range changes.

System (4.19) is solved using the SVD to find the generalized inverse of **G** and the final range change time series can be constructed using **m** such that

$$\phi_{i\,j}=\sum_{k=i}^{j-1} m_k . \tag{4.20}$$

In order to diminish the atmospheric effect a smoothing function based on finite difference approximation is introduced into system (4.19)

$$\begin{bmatrix} \mathbf{G} \\ \gamma^2 \frac{d}{dt} \end{bmatrix} \boldsymbol{m}=\begin{bmatrix} \boldsymbol{d} \\ 0 \end{bmatrix} \tag{4.21}$$

being γ the smoothing factor and chosen for that study equal to 0.14 to minimize both, the residual sum of squares given by

$$\left| \boldsymbol{d} - \mathbf{G}\boldsymbol{m} \right|_2 \tag{4.22}$$

and the atmospheric delays.

4.3.4 Cavalie et al. (2007)

In this method a series of short baseline (SB) interferograms are combined to retrieve the temporal evolution of the phase change. No model a priori of the deformation is introduced and the atmospheric artifacts are estimated within the inversion procedure by introducing a temporal smoothing as another constraint similar to Schmidt and Bürgmann (2003). In addition, an extra term is considered which is proportional to the perpendicular baseline to limit the effects of the high errors. The system used for the inversion is expressed as,

$$\begin{pmatrix} \boldsymbol{d}' \\ 0 \end{pmatrix}=\begin{pmatrix} \mathbf{G}' & \boldsymbol{b}' \\ \gamma^2 \omega_i \frac{d}{dt^2} & 0 \end{pmatrix} \cdot \begin{pmatrix} \boldsymbol{m} \\ e_{dem} \end{pmatrix} \tag{4.23}$$

where **b** represents the perpendicular baseline vector, e_{dem} coefficient of proportionality between the phase and the baseline due to DEM errors, **d’, G’** and **b**’ are weighted by the matrix **W** as,

$$\boldsymbol{d}'=\mathbf{W}\boldsymbol{d} \tag{4.24}$$

$$\mathbf{G}'=\mathbf{WG} \tag{4.25}$$

and

$$\boldsymbol{b}'=\mathbf{W}\boldsymbol{b}. \tag{4.26}$$

γ is the smoothing coefficient that weights the minimum curvature (d/dt^2), with a five-point finite difference scheme centered on each i-acquisition date.

The weight elements $\omega_{i,}$ are the temporal weights of the smoothing operator. They are selected to be equal to the average difference in time Δt_i for which APS removal for widely spaced acquisitions is not negligible and ground motion is not allowed to vary too much (Cavalie et al. 2007). The magnitude of the γ factor is chosen to decrease the influence of the random APS but attempting to keep most of the signal of interest.

4.3.5 López-Quiroz et al. (2009)

They map the spatial and temporal patterns of the Mexico City subsidence using the SBAS method, selecting interferograms with temporal baseline lower than 9 months and perpendicular baselines lower than 500 meters. The atmospheric phase contribution due to the troposphere vertical stratification is corrected by using its correlation with elevation. In their method, the unambiguous phase is retreiverd by applying an iteratively unwrapping method that decreases the unwrapping errors, improving the quality of the final unwrapped interferograms. The SVD method is first proposed for finding the inverse generalized and find the solution of the system (4.19). However, the application of the SVD method set to zero the incremental phase changes between successive acquisitions. This is because some groups of independent images do not overlap in time or in space for the given configuration (López-Quiroz et al. 2009). Therefore, a constrained-LS-based solution for inverting the interferometric system is proposed.

Considering a quadratic behaviour for the cumulative phase delays ϕ_k^l

$$\phi_k^l = a_t^l(t_k - t_1) + b_t^l(t_k - t_1)^2 + e^l B_\perp^k + c_t^l \tag{4.27}$$

being eB the residual height error correlated with the perpendicular baseline $B_\perp$, the system to be solved by means of LS is (López-Quiroz et al. 2009)

$$\begin{bmatrix} d_1^l \\ \vdots \\ d_k^l \\ \vdots \\ d_{N_l}^l \\ 0 \\ \vdots \\ 0 \end{bmatrix} = \left[\begin{array}{c} \begin{bmatrix} \\ \quad \mathbf{G} \quad \\ \\ \end{bmatrix} \begin{bmatrix} 0 & 0 & 0 & 0 \\ \vdots & \vdots & \vdots & \vdots \\ 0 & 0 & 0 & 0 \end{bmatrix} \\ \gamma \cdot \begin{bmatrix} 0 & \cdots & 0 & \cdots & 0 & 0 & 0 & -B_\perp^1 & -1 \\ 1 & \ddots & & & \vdots & -(t_2 - t_l) & -(t_2 - t_l)^2 & -B_\perp^2 & -1 \\ \vdots & \ddots & 0 & & 0 & & & & \vdots \\ \vdots & & \ddots & \ddots & \vdots & & & & \vdots \\ 1 & \cdots & \cdots & 1 & 0 & -(t_{M_l} - t_l) & -(t_{M_l} - t_l)^2 & -B_\perp^{M_l} & -1 \end{bmatrix} \end{array}\right] \cdot \begin{bmatrix} m_1^l \\ \vdots \\ \vdots \\ m_{M_l}^l \\ a_t^l \\ b_t^l \\ e_t^l \\ c_t^l \end{bmatrix} \tag{4.28}$$

where the weight γ is small enough to ensure that for ($\mathbf{G}^T\mathbf{G}$) invertible the constraint does not affect the subsidence time series and only when the matrix product is singular is applied. By profiting from this strategy, López-Quiroz et al. (2009) eliminate the noise generated by the SVD method affecting the preliminary map of subsidence. Note that the proposed idea follows that of Schmidt and Bürgmann (2003).

An alternative SBAS inversion method (Hooper 2008) is presented in Chapter 5, testing as well the SVD and WLS-SVD methods over the same study area but now only using stable pixels, previously selected to the unwrapping.

4.3.6 Lauknes et al. (2011)

This method takes advantage of the L_1-norm cost functions to solve the SBAS equation system, combined with reweighted LS to achieve more accurate time series than those estimated with the L_2 norm. In order to increase the spatial sampling, the selection of the PS is based on the same coherence threshold proposed by Lanari et al. (2007). Like any other SBAS algorithm, it relies on the unwrapping availability; however, their approach leads to a better robustness with respect to the unwrapping errors because the L_1-norm cost functions are more tolerant to outliers (Lauknes et al. 2011). The linear system in this approach is expressed as,

$$\mathbf{B}\boldsymbol{v} = \boldsymbol{\delta\phi}' + \boldsymbol{n} \tag{4.29}$$

where **B** is the design matrix, $\boldsymbol{\delta\phi}'$ is the vector of the topography corrected unwrapped phase values, $\boldsymbol{v}$ is the coefficient vector and $\boldsymbol{n}$ the residual vector to be minimized.

By assuming a full-rank matrix **B** the solution of system (4.29) is

$$\boldsymbol{(}\mathbf{B}^{\mathbf{T}}\mathbf{W}\boldsymbol{(}k\boldsymbol{)}\mathbf{B}^{\mathbf{T}}\boldsymbol{)}\boldsymbol{v(}k+1\boldsymbol{)} = \mathbf{B}^{\mathbf{T}}\mathbf{W}\boldsymbol{(}k\boldsymbol{)}\boldsymbol{\delta\phi}' \tag{4.30}$$

with

$$\mathbf{W}(k) = diag\left\{ \left| n_i \right|^{-1} \right\}_{i=0}^{M-1} \tag{4.31}$$

The **W**(k) is the weighing matrix at the k–th iteration, M represents the number of multi-looked interferograms. In case of **B** being an ill-posed matrix, the pseudoinverse of ($\mathbf{B}^T\mathbf{B}$) can be computed using the SVD method.

4.3.7 Summary and general comparison

The methods presented above enable to find the solution of the SBAS interferometric system, which usually is ill-posed. These approaches propose alternative strategies to overcome the normal singularly of the design matrix, some of them estimating at the same time the effect of various factors such as residual topography and APS. None of them can be considered better than the other; on the contrary, elements from these algorithms can be combined to optimize even more the solution of the target system. Nevertheless, limitations of each method should also be taken into account. For example, the interpolation methodology proposed by Usai (2003) may work correctly if a priori information of the deformation is known, which is not always available. The latter might be especially critical if large and frequent temporal gaps between successive acquisitions exist. Thus, this method maybe more appropriate for cases in which a dense temporal data sampling is available and most interferometric pairs overlap in time. The use of the SVD method, on the other hand, may solve the problem of missing links from the mathematical point view by connecting the independent subsets. Nevertheless, the application of this method may cause variations that cannot be explained from the physical point of view, as reported by Usai (2003). Thus, certain assumptions or reformulations need to be introduced into the original system to reduce these discontinuities and produce an acceptable solution from the physical perspective (Usai 2003; Berardino et al. 2002). The use of Weighted Least Squares (WLS) can certainly improve the solution as demonstrated by Lauknes et al. (2011) and in this study (see Chapter 7); nonetheless, the weights selection should be carefully evaluated since their inappropriate choice could significantly bias the final outcomes, and thus their interpretation.

From the literature, it seems that the employment of constrained LS provide a more accurate solution than the SVD for certain interferometric systems. For the Mexico City subsidence study the proposed combined SVD-constrained LS gave better results; however, the use of a full-rank matrix with a “controlled point” selected based on an uncertainty analyses yield to comparable results over the same area as shown in Chapter 7.

Chapter 5

Specific method for deformation studies in Mexico: StaMPS

In the last years, several scientific and commercial software packages have been established for carrying out the InSAR processing and exploit at a maximum the information that can be derived by combining SAR acquisitions. Even though traditional interferometric software represents a powerful tool for SAR processing, they are not able to solve the limitations of the conventional InSAR. This boosted the extension of the InSAR techniques and the emergence of new MTI algorithms. StaMPS, a software package that has been developed partially at the Stanford University, the University of Iceland and Delft University of Technology, uses an optimized algorithm for detection of PS (Hooper et al. 2004; Hooper et al. 2007) which has been proved to work in areas subjected to high decorrelation. Different from the approach proposed by Ferretti et al. (2001), this method does not introduce any hypothetical model a priori of the deformation and only its spatial correlation is used for retrieval of displacement.

In the case of the amplitude based approaches for detection of PS, the presumption of a deformation model, limits the selection of pixels to those with high SNR. However, high coherent areas where these algorithms works well, are not always subject of study and phase stability based algorithms such as the here proposed result valuable.

StaMPS includes a SBAS method (Hooper 2008) that works with full resolution SAR images and operates over the so called slowly decorrelated filtered (SDFP) pixels; a PS-SBAS merged approach (Hooper 2008) is incorporated as well. StaMPS is quite extensive when talking about applications. The PS and SBAS methods are enhanced to detect, monitor and study deformation phenomena affecting not only urban but also non-urban areas and terrains undergoing non-linear events, such as in the Valley of Mexico.

In this Chapter principal characteristics of the proposed MTI algorithm are presented. Hooper et al. (2004), Hooper et al. (2007), Hooper (2008) and Hooper (2010) and are the main references used in the description of StaMPS. The inversion method is analyzed in detail, the extension of algorithm for the inclusion of an appropriate spatial reference for the present application is introduced and the temporal reference selection is justified by considering an uncertainty evaluation.

5.1 Coregistration step

General steps of the interferometric process were already presented in Chapter 3. Here, the particular coregistration algorithm applied by StaMPS and which is a crucial step in the interferogram formation is briefly described. This method has been reported to provide better results in comparison with other methodologies, especially in areas affected by high decorrelation (Sousa et al. 2011), such as considerable surface in northern Valley of Mexico.

StaMPS works together with the Delft object-oriented radar interferometric software (DORIS; Kampes et al. 2003) for the generation of the interferogram. Notwithstanding, the coregistration method employed by DORIS tends to fails for interferograms with larger temporal and perpendicular baselines or Doppler centroids. In order to overcome with these limitations, StaMPS incorporates a new amplitude based coregistration method. This algorithm estimates the offsets between the images, in positions where the correlation is good. Once the offsets are computed, mapping functions are used to align the acquisitions respect to the “master” image, which is selected so that the sum decorrelation is minimized (Hooper et al. 2007). In StaMPS these mapping functions are estimated by means of WLS inversion in the following way.

A generic pixel is map to the “master” grid using of a polynomial function express as (Hooper et al. 2007)

$$f_x^m(x^m, y^m) = a_{00}^m + a_{10}^m x^m + a_{01}^m y^m + a_{11}^m x^m y^m + \ldots + a_{pq}^m (x^m)^p (y^m)^q + \ldots \qquad (5.1)$$

where x and y denote the coordinates of the pixel in azimuth and range, respectively. Initially, the coefficients for the functions *f*(x,y) between two images m and n are first estimated to later help the computation of the offsets between each image and the “master”.

Considering Δx_m^0, Δy_m^0 offsets between the image m and the master 0 and $\Delta x_m^n, \Delta y_m^n$ the offsets between image m and another image n , the relation between them can be express as

$$\Delta x_{m,k}^n = \Delta x_{m,k}^0 - \Delta x_{n,k}^0 \qquad (5.2)$$

$$\Delta x_{m,k}^n = f_x^m(x_k^m, y_k^m) - f_x^n(x_k^n, y_k^n) \qquad (5.3)$$

being k the point where the cross-correlation is computed using a certain window size, usually 64 pixels and with oversample factor of 2.

In the case of very coherent pixels, Δx_m^0 is possible to estimate directly at many points, which is not always the case. Thus, StaMPS proposes a coregistration strategy that allows solving the problem.

By using WLS adjustment the coefficients of the mapping functions *f*(*x*,*y*) for image m and n can be found simultaneously by solving the system (Hooper et al. 2007)

$$\begin{bmatrix} \vdots \\ \Delta\hat{x}_{m,i}^n \\ \Delta\hat{x}_{m,i+1}^n \\ \vdots \end{bmatrix} = \begin{bmatrix} \cdots & & & \cdots & & & & \cdots \\ \cdots & 1 & x_i^m & y_i^m & \cdots & -1 & -x_i^n & -y_i^n & \cdots \\ \cdots & 1 & x_{i+1}^m & y_{i+1}^m & \cdots & -1 & -x_{i+1}^n & -y_{i+1}^n & \cdots \\ \cdots & & & \cdots & & & & \cdots \end{bmatrix} \begin{bmatrix} a_{00}^m \\ a_{10}^m \\ a_{01}^m \\ . \\ . \\ a_{00}^n \\ a_{10}^n \\ a_{01}^n \\ . \end{bmatrix}. \qquad (5.4)$$

Because, each acquisition must be aligned to the “master”, the coefficients of the mapping function between each image and the master must be estimated. For that purpose, the Δx^0 and Δy^0 are estimated by using the functions $f_x(x,y)$ and $f_y(x,y)$, already determined and the coefficients for the mapping function between the master and the acquisition m are then calculated in azimuth and range. Each image is then resample to the “master” coordinate system, using a raised cosine interpolation kernel of 12 points and finally the interferograms are generated by differencing the phase of each image to the “master” phase. This coregistration approach is used for the single master (PSI) and multi-master SAR image combination (SBAS).

5.2 PSI: stable pixels selection

The task of the PSI algorithms is to identify those pixels dominated by a single scatterer in order to extract the phase information contained in the interferometric phase. The StaMPS algorithm selects the PS based on a phase stability analysis, which makes it a powerful tool over the amplitude based methods (Adam et al. 2005; Colesanti et al. 2003; Crosetto et al. 2003; Ferretti et al. 2001), because of the heigher PS density achieved.

Low SNR pixels can actually contained a stable scatter; however, due to changes in the scattering properties of the surrounding scatterers within the same resolution cell, the target pixel is characterized by a noisy phase. While amplitude dispersion algorithms would weed this pixel, StaMPS would consider it in the PS analysis, which primarily involves two steps: a) amplitude phase discrimination, and b) phase-stability selection.

5.2.1 *A priori amplitude-based selection*

Even though StaMPS uses a phase stability analysis for selection of the final PSs, in order to minimized the initial selection of improbable PS, and thus reduce the data processing time, it incorporates an amplitude based measurement for the initial PS discrimination. The dispersion index D_A (Ferretti et al. 2001) is used for that task. The D_A threshold in StaMPS is usually set higher than the value proposed by Ferretti et al. (2001), selecting in this way, pixels that are less probable to be PSs. Once the initial PSC are selected, they are submitted to the phase stability analysis. An additional step is also included to analyze pixels with a higher D_A threshold than the one initially established.

5.2.2 *Phase stability-based selection*

The interferometric phase is masked by many components: atmosphere, topography, orbit ramp, noise. By using an external DEM and orbital information the topographic and orbital contributions can be extracted. Then, the differential phase in the interferogram can be express as (Hooper et al. 2004),

$$\phi_{\mathrm{int}} = \phi_{def} + \Delta\phi_{\in} + \phi_{atm} + \Delta\phi_{orb} + n \tag{5.5}$$

where now $\Delta\phi_{\in}$ and $\Delta\phi_{orb}$ are the height and geometrical residuals due to the use of an inaccurate topographic model and imprecise orbit information, respectively. ϕ_{atm} is the atmospheric effect between the two passes and n, the noisy term due to different decorrelation sources. The noise component of the phase is the key point for the PS selection as it contains the variability of the phase characteristics, or clutter, we are interested on. In fact, in StaMPS PS pixels are those whose n is small enough to allow signal detection (Hooper et al. 2007). In order to analyze the noise component the first four terms in equation (5.5) need to be subtracted. For that purpose, StaMPS uses the fact that all the terms in equation (5.5) are spatially correlated or correlated with the baseline, except for the noise term (see Table 5-1). By using this information, spatial and temporal filters are applied to estimate the first terms and subtract them from the phase leaving only the noise n (for more details about the filters see Hooper et al. 2007). This procedure is carried out in an iterative way until the estimated $\phi_{n,x,i}$ values converge. In our study case this happened after 5 or 6 iterations.

	Component	Spatial Properties	Temporal Properties
$\phi_{def,x,i}$	Deformation	Low freq	Low freq
$\phi_{atm,x,i}$	Atmosphere	Low freq	High freq
$\Delta\phi_{orb,x,i}$	Orbital errors	Low freq	High freq
$\phi_{n,x,i}$	Scatterer noise	High freq	High freq
$\phi_{\in,x,i}$	DEM Error	High freq	Correlated with baseline

Table 5-1 Spectral characteristics for the observed interferometric phase for an i-PS pixel (adapted from Hooper 2006).

First, a band-pass filter is combined with a low-pass filter an applied in the frequency domain. By doing this, the spatially correlated part of (5.5) is estimated and subtracted, leaving the uncorrelated components of the phase ϕ^u (Hooper et al. 2007)

$$W\left\{\psi_{x,i}-\tilde{\psi}_{x,i}\right\}=W\left\{\phi^u_{D,x,i}+\phi^u_{A,x,i}+\phi^u_{S,x,i}+\Delta\phi^u_{\theta,x,i}+\phi^u_{n,x,i}\right\}. \tag{5.6}$$

Because the deformation, atmospheric and orbitals components have a very low frequency (i.e. long wavelength) in the space domain, their uncorrelated parts are expected to be so small that they can be replaced with a term δ. Considering $\Delta\phi^u_{\theta,x,i}$ approximately the same for each interferogram, this term can be estimated from equation (5.6) in the sense of LS. This is possible because is the only term that correlates with the perpendicular baseline. Introducing the term δ into equation (5.6) and subtracting the estimated $\Delta\phi^u_{\theta,x,i}$ gives

$$W\left\{\psi_{x,i}-\tilde{\psi}_{x,i}-\Delta\hat{\phi}^u_{\theta,x,i}\right\}=W\left\{\phi^u_{n,x,i}+\delta'_{x,i}\right\}. \tag{5.7}$$

From (5.7) a measure of the phase stability γ_x can be derived (Hooper et al. 2007; Hooper et al. 2004)

$$\gamma_x=\frac{1}{N}\left|\sum_{i=1}^{N}\exp\left\{\sqrt{-1}(\psi_{x,i}-\tilde{\psi}_{x,i}-\Delta\hat{\phi}^u_{\theta,x,i})\right\}\right|, \tag{5.8}$$

where N is the number of interferograms. If $\phi^u_{n,x,i}$ is very small and δ approximately zero, γ_x is an indicator of the noise level, and thus can be used to decide whether or not the pixel is a PS (Hooper et al. 2007). As we can see from equation (5.8), the values of γ depend on the filtering settings used for determining $\tilde{\psi}_{x,i}$, thus, their evaluation is important (see also Chapter 7).

Once the phase analysis for each pixel is done, those more probably to be a PS are selected using a threshold determined by the fraction of false positives (non-PS pixels) that are deemed acceptable (Hooper et al 2007). Pixels which appear as PS only in certain interferograms and those dominated by adjacent pixels are also rejected.

The probability function of each pixel belonging to the group of PS can be accurately calculated by using the dispersion index D_A and the temporal coherence γ_x due to the existence of correlation between the amplitude variance and the phase stability. This function is used to finally determine a γ– threshold (γ_{thres}) such that the fraction of pixels being non-PS pixels is equal to a certain value q (see Hooper et al. 2007 for details). Hooper et al. (2007) found an empirical relation between γ_{thres} and D_A so that

$$\gamma_{thres}=kD_A, \tag{5.9}$$

where k is a constant. It follows then that for a k estimated in the sense of LS adjustment, pixels for which $\gamma_x > kD_{A,x}$ are labelled as PSs.

5.3 SBAS approach

StaMPS incorporates a SBAS method (Hooper 2008) that introduces a new index for initial selection of stable pixels. The targets of this SBAS algorithm are the SDFP pixels, as defined by Hooper (2008). The phase of these pixels, filtered in azimuth and in range to reduce the effect of noise, decorrelates little over short time intervals (Hooper 2008). In order to retrieve the incremental phase changes from the SDFP pixels, a WLS inversion, using the QR decomposition and a covariance matrix based on the noise information of each SB interferogram is employed.

5.4 Slowly-Decorrelating Filtered Phase pixel selection

As in the PSI method, the selection of SDFP pixels in the SBAS is based on their phase characteristics. Nevertheless, Hooper (2008) introduces a new parameter, the amplitude difference dispersion $D_{\Delta A}$ for the initial selection of PS, which differs from the traditional dispersion index D_A (Ferretti et al. 2001). This initial selector for pixels was proved to work better in cases where spectral filtering was applied to the SB interferograms. After the pixels are selected by the $D_{\Delta A}$, the phase stability analysis is carried out similarly to that for the PS (Hooper et al. 2007), but the probability functions are computed using the $D_{\Delta A}$ index instead of D_A.

The difference dispersion index is defined as (Hooper 2008)

$$D_{\Delta A} \equiv \frac{\sigma_{\Delta A}}{\mu_A} \tag{5.10}$$

where the $\sigma_{\Delta A}$ is the standard deviation of the difference in amplitude between the master and the slave and μ_A is the mean amplitude. This dispersion measure is derived from the phase statistics of Gaussian scatterers. For more details regarding the statistical analysis refer to Hooper (2008). As previously stated, this measure is similar to the dispersion amplitude D_A. In fact, there are relations between these variables that can be established depending if the filtering is applied or not.

After the initial pixel selection is carried out, the coherence similar measure γ_x, is employed for the phase stability analysis (see section 5.2).

5.5 Inversion: interpretation, spatial reference and error propagation analysis

The SBAS methods differ mainly in the way they perform the inversion of the unwrapped phases for unveiling the behaviour of the deformation time series (see Chapter 4). The method proposed here makes no assumption about the temporal behavior of the deformation (Hooper et al. 2004). In addition, it is important to emphasize that by using the suggested algorithm we operate on single-look interferograms, thus benefiting from: a) processing the data at the highest possible resolution b) the ability to unwrap the phase more robustly in three dimensions (Hooper 2008). On the other hand, the constraint SBAS approach, previously applied over southern Mexico City (López-Quiroz et al. 2009) applied multi-looking, possibly limiting the detection of important deformation in certain areas of high deformation gradients due to undersampling (Massom and Dan 2006).

The unwrapping procedure must be done to retrieve the unambiguous phase that is later inverted to give the phase at each acquisition time with respect to a certain instant and a reference area (i.e. non deforming areas or point). The final deformation and the atmospheric components of the signal can be extracted by the application of temporal and spatial filtering to the estimated cumulated phase.

In this section the SBAS inversion method of StaMPS is presented. First, some details of the model and the matrix system are described; afterwards, the inversion method is explained. Some geodetic concepts are adapted for interpretation of the SBAS inversion strategy, and the algorithm is extended to consider an adequate spatial reference for the northern and southern Valley of Mexico (see also Chapter 7), necessary for correct estimation of the time series used in the methodology for the identification of fracture-prone zones (see Chapter 8).

5.5.1 Inversion model and its components

Initially N full-resolution SB interferograms are generated from the M single-look SAR images acquired at chronological times ($t_1,\dots,t_M$). Each acquisition is assumed to interfere with at least another image. This implies that each SB subset is composed by a minimum of two acquisitions.

The unwrapped phase of a generic pixel in the k-SB interferograms from SAR acquisitions at times t_A, t_B, after flattening and topographic correction, can be express as (Hooper et al. 2004)

$$\phi_{\mathrm{int}\,k} = \phi(t_A) - \phi(t_B) \approx \phi_{def,k} + \phi_{atm,k} + \phi_{orb,k} + \Delta\phi_{topo} + n_k \qquad ,with \;\; t_A > t_B \qquad (5.11)$$

where

- $\phi_{def,\,k}$ is the phase change due to the ground displacement in the satellite LOS direction between the acquisition times t_A y t_B ,
- $\phi_{atm,k}$ is the phase due to differential atmospheric delay between the two passes,
- $\phi_{orb,k}$ is the residual phase due to orbit inaccuracies,
- $\Delta\phi_{\mathrm{DEM}}$ represents residual DEM errors and
- n_k is the phase noise.

StaMPS assumes that the terms $\phi_{k,\,def}$, $\phi_{k,atm}$, $\phi_{k,orb}$, of equation (5.11) are spatially correlated (see also Table 5-1), the residual heights $\Delta\phi_{\mathrm{DEM}}$ are partially spatially correlated and the noise n_k is spatially uncorrelated with a Gaussian Distribution.

The goal is to extract the time-dependant deformation signal from the SB interferograms. Therefore, the model that relates the phase increments $\boldsymbol{\phi}$ between SAR acquisitions and the InSAR data needs to be solved. This relation can be express by the following mathematical model

$$\mathbf{G}\boldsymbol{\phi} = \zeta \,, \qquad with\; E(\boldsymbol{\phi}) = 0; \qquad \Sigma_{\zeta} = \sigma_0^2\mathbf{Q} \qquad (5.12)$$

where

- **G** represents the design matrix depending on the available set of SB interferograms ,
- $\boldsymbol{\phi}$ refers to the unknown phase increments for each PS pixel between the M chronologic times ,
- ζ contains the observations ϕ_{int}, i.e. the phase information of each pixel in the N SB interferogram.

The first part of (5.12) is called the functional model, whereas the second part is known as the stochastic model. The latter is composed by the a priori covariance matrix of the observations

$\mathbf{\Sigma}_{\zeta}$, σ_0^2 the variance and **Q** the cofactor matrix. The structure of $\mathbf{\Sigma}_{\zeta}$ is discussed in the section 5.5.3.

Each row and column of the design matrix **G** corresponds to the interferograms and the acquisition days, respectively. It is a N-by-M matrix constructed from equation (5.11) such that

$$\forall i = 1,\ldots,N$$
$$\mathbf{G}(i,j) = \begin{cases} 1 & if \quad \phi(t_j)_i = \phi(t_A)_i \\ -1 & if \quad \phi(t_j)_i = \phi(t_B)_i \quad with\ j = 1,\ldots,M\,. \\ 0 & otherwise \end{cases} \tag{5.13}$$

For example for $\phi_{\text{int}1}=\phi\,(t_1)_1-\phi\,(t_3)_1$, $\phi_{\text{int}\,2}=\phi\,(t_2)_2-\phi\,(t_4)_2$ and $\phi_{\text{int}\,3}=\phi\,(t_3)_3-\phi\,(t_6)_3$ **G** would have the following form

$$\mathbf{G} = \begin{bmatrix} +1 & 0 & -1 & 0 & 0 & 0 & \cdots \\ 0 & +1 & 0 & -1 & 0 & 0 & \cdots \\ 0 & 0 & +1 & 0 & 0 & -1 & \cdots \\ \cdots & & \cdots & & & & \cdots \end{bmatrix}. \tag{5.14}$$

5.5.2 *Importance of the reference area selection*

The problem is to solve the system (5.12), i.e. to estimate the unknown phase increments $\boldsymbol{\phi}$. This is usually done by LS approaches; however, in order to derive the deformation time series, before inverting (5.12), the unwrapped phases of the SB interferograms must be first adjusted relative to an area where no deformation is expected.

The reference phase ϕ_{ref} is computed for each interferogram by averaging the phase of the H selected reference pixels such that

$$\overline{\phi}_{ref,\text{int}k} = \tfrac{1}{H}\sum_{l=1}^{H}\phi^{l}_{ref,\text{int}k}\,. \tag{5.15}$$

Then, for each PS the computed average reference phase ϕ_{ref} is subtracted from their original phase ϕ_{int}. For the l-pixel in the k-SB interferogram,

$$\phi'^{l}_{\text{int}k} = \phi^{l}_{\text{int}k} - \overline{\phi}^{l}_{ref,\text{int}k}\,. \tag{5.16}$$

Once the phases are spatially referred to the non-deforming area, the new functional model is then given by

$$\mathbf{G}\boldsymbol{\phi} = \boldsymbol{\zeta}'. \tag{5.17}$$

Normally, the reference area (or point) is selected based on in-situ measurements that provide information about stable or non-deforming zones. However, this data is no always available (as in my case) and thus geological and other information about the dynamics of the area of study need to be compiled to choose a suitable spatial reference for the time series inversion. For this purpose, the algorithm was extended to select an appropriate reference based on the geology and geotechnical information. Note from equation (5.17), this reference has a direct impact in the quality of the time series and influence the interpretation of the results. More details about the reference area selection are given in Chapter 7.

In the following, the structure of the covariance matrix Σ_{ζ} used for solving the inversion system is presented and investigated.

5.5.3 Estimation of Covariance matrix of the observations

Because the a priori covariance matrix $\mathbf{\Sigma}_\zeta$ for solving system (5.17) or (5.12) it is usually unknown, a scale factor is introduced and two new matrices are derived from the covariance matrix: the cofactor matrix $\mathbf{Q}_\zeta$ and the weight matrix **P**.

$$\mathbf{Q}_\zeta = \frac{\Sigma_\zeta}{\sigma_0^2} \tag{5.18}$$

$$\mathbf{P} = \sigma_0^2\, \Sigma_\zeta^{-1} \tag{5.19}$$

In the StaMPS approach the covariance matrix $\mathbf{\Sigma}_\zeta$,that characterizes the interferometric phases, is constructed based on the noise information of each SB interferogram. Assuming that the variance of each interferogram is given by their estimated noise variance, the stochastic model can be expressed as

$$\mathbf{P} = \sigma_0^2\, \Sigma_n^{-1} \tag{5.20}$$

where $\mathbf{\Sigma}_n$ is the estimated covariance matrix of the phase noise. In order to compute $\mathbf{\Sigma}_{n,}$, the noise component n_k of equation (5.11) needs first to be estimated for each pixel in the SB interferograms.

Considering that the noise term n is spatially non-correlated, it can be estimated for each SDFP pixel in the k-SB interferograms by applying a high-pass filter. The spatially correlated components of the signal such as deformation ϕ_{def}, atmosphere ϕ_{atm} and the residual heights $\Delta\phi_{\mathrm{DEM}}$ are obtained by band pass filtering the complex signal of the surrounding pixels ($\phi_{sc,\mathrm{int}\,k}^l$).

The high–pass filter is then performed by subtracting the filtered phase $\phi_{sc,k}$ from the original phase ϕ_{int} k . The result contains the non-spatially correlated residual heights ($\Delta\phi_{nsc,DEM}^l$). After removing the later term an estimator for the phase noise term n for each PS can be found

$$\phi_{\mathrm{int}\,k}^l - \phi_{sc,\mathrm{int}\,k}^l = \Delta\phi_{nsc,DEM}^l + n_k^l \tag{5.21}$$

$$\hat{n}_k^l = \phi_{\mathrm{int}\,k}^l - \phi_{sc,\mathrm{int}\,k}^l - \Delta\phi_{nsc,DEM}^l\,. \tag{5.22}$$

The noise estimator and its variance depend on the filtering settings. Assuming that the noise follows a Gaussian distribution, its covariance matrix can be computed as

$$\mathbf{\Sigma}_n = \tfrac{1}{X-1}\left[\boldsymbol{\mu}^T\boldsymbol{\mu}\right] \tag{5.23}$$

being $\boldsymbol{\mu}$ a (X-by-N)-matrix. The covariance matrix $\mathbf{\Sigma}_n$ is a symmetric matrix with dimensions (N-by-N) and is composed in the following way

$$\Sigma_n(i,k) = \begin{cases} \tfrac{1}{x-1}\sum_{i=1}^{X}(n_i^l - \bar{n}_i)^2 & \forall i = k, \quad with \quad i,k = 1,\ldots,N \\ \\ \tfrac{1}{X-1}\sum_{i=1}^{X}(n_i^l - \bar{n}_i)^2 (n_k^l - \bar{n}_k)^2 & \forall i \neq k, \quad with \quad i,k = 1,\ldots,N \end{cases}\,. \tag{5.24}$$

being $\bar{n}$ the mean noise for a generic interferogram computed as

$$\bar{n} = \tfrac{1}{X}\sum_{l=l}^{X} n^{l}. \qquad (5.25)$$

Because we are interested on the relative weight between the observations rather than on the absolute phase variance, σ_0^2 =1 can be assumed and equation (5.20) turns into,

$$\mathbf{P} = \Sigma_n^{-1}. \qquad (5.26)$$

After the phases are spatially referenced to the non-deforming area and the observations are weighted, system (5.17) can be solved.

In general, the WLS method optimizes the adjustment if the weights are distributed according to their magnitude; however, if the observations are not correctly weighted the quality of the results can be deteriorated because this method is more sensible to the outliers. In StaMPS the noise information is used in the inversion. Interferograms with larger baseline would be expected to receive less weight than those with shorter ones because they are more affected by decorrelation; nevertheless, basing the selection of weights only on the length of the geometrical (or temporal) baselines may not be always correct since even interferograms with shorter baselines can be seriously affected by atmospheric and/or other effects. To evaluate whether the selected weights optimize the results, a comparative analysis using unweighted LS (ULS) and WLS-SVD methods is considered. The latter analysis is presented in Chapter 7.

5.5.4 Numerical method for inversion

There are many numerical methods that can be used for solving system (5.12) or (5.17). Decompositions provide a numerically stable way to solve a system of linear equations and to invert a matrix. Additionally, they provide an important tool for analyzing the numerical stability of a system.

Depending on the set of SB interferograms generated from the available SAR acquisitions, **G** can or cannot be rank deficient. Normally, **G** is a rank deficient matrix due to the fact that usually the acquisitions belong to “independent subsets” (Casu et al. 2006), i.e. there are some subsets of images that are not overlapping in time or space. In this case, ($\mathbf{G}^{T}\mathbf{G}$) is singular and there is no unambiguous solution for the interferometric system. Several inversion approaches (Bernardino et al. 2002; Lanari et al. 2004) proposed the SVD, which diagonalizes the matrix **G** using two orthonormal matrices and allows to find the pseudoinverse $\mathbf{G}^{+}$, to give the solution to the SBAS system. Despite the SVD method enables to find a correct solution from the mathematical viewpoint, it might be necessary to radically change the formulation of the problem itself in order to have physically sound solution (Usai 2003). In this work the QR regularization method which is numerically more stable, much faster and better conditioned than SVD for full-rank cases, is utilized. The algorithm can be further adapted for rank deficient systems, by using a modified Gram-Schmidt approach; however, in this case, the SVD would be more stable.

The main question to be answered is: how to apply the QR decomposition in case **G** is rank-deficient, without drawing on the modified Gram-Schimidt method?

By making an analogy to the geodetic Datum poblem the rank defiency of the design matrix **G** can be geometrically interpreted as a defect in the configuration of a geodetic network. Let us now think our SB network as a geodetic one, with a defect d. Being **G** (N x M) -dimensional, the rank defect *d* can be defined as (Niemeier 2008)

$$d = rank(\mathbf{G}) - M. \qquad (5.27)$$

In the field of Geodesy, the Datum or zeroth-order design problem (Grafared 1994) is overcome by using concepts such as

a) selection of motionless points as a reference/control, or
b) projection of the system into a free solution, where all network points are selected as datum (Free Net Adjustment or Inner Constraints).

Here, the case for which the configuration defect of the SB network is one (d=1) is analysed and a) is proposed as a solution. We set as a "reference point" an image corresponding to a certain instant t_{ref}, implying $\phi(t_{\mathrm{ref}})=0$ for the SB interferograms containing the selected reference image. By making the later, we handle now with $\mathbf{G}_{fr}$, a Nx(M-1) full rank design matrix. In this way, system (5.17) can be solved by means of the LS method, profiting as well from the attributes of the **QR** factorization, which enables a faster processing time than the SVD but also more important, provides a stable solution of the inversion system.
Considering the decomposition of the coefficient matrix $\mathbf{G}_{fr}$ as

$$\mathbf{G}_{fr} = \mathbf{QR} \tag{5.28}$$

with **Q** an orthogonal matrix and **R** an upper triangular matrix and replacing (5.28) into (5.17) the new system can be written as

$$\mathbf{QP}\boldsymbol{\phi} = \boldsymbol{\zeta}'. \tag{5.29}$$

Since **Q** is orthogonal (i.e. $\mathbf{Q}^{\mathrm{T}} = \mathbf{Q}^{-1}$), we can apply the following

$$\mathbf{R}\boldsymbol{\phi} = \boldsymbol{a} \tag{5.30}$$

with

$$\boldsymbol{a} = \mathbf{Q}^T\boldsymbol{\zeta}'. \tag{5.31}$$

In order to find the unknown $\boldsymbol{\phi}$, the L_2 norm of the difference between **Rm** and **a**, containing the measurements is minimized

$$\left|\mathbf{R}\boldsymbol{\phi} - \boldsymbol{a}\right|_2 = \boldsymbol{min}. \tag{5.32}$$

Then, the solution of (5.30) is

$$\boldsymbol{\phi} = (\mathbf{R}^T\mathbf{PR})^{-1}\mathbf{R}^T\mathbf{Pa}, \tag{5.33}$$

$$\textstyle\sum_{\phi} = (\mathbf{G}_{fr}{}^T\mathbf{PG}_{fr})^{-1}. \tag{5.34}$$

where $\boldsymbol{\Sigma}_{\phi}$ is the covariance matrix of the mean estimated phases $\boldsymbol{\phi}$. The estimated $\boldsymbol{\phi}$ contains the deformation time series for each stable pixel.

5.5.5 Uncertainty analysis: influence of the temporal reference

Error propagation analysis is useful to identify the influence of various sources of error that may bias the SBAS results. Here, the influence of the temporal reference in the deformation time series is studied by an uncertainty appraisal.
If we consider the phase change between two acquisitions, ignoring other components than the deformation, equation (5.11) for a generic pixel can be written as

$$\phi_{\mathrm{int}} = \phi(t_A) - \phi(t_B) \approx \phi_{def} \tag{5.35}$$

or expressed as a function of the range change ΔR in LOS

$$\phi_{\mathrm{int}\,R} = \phi(t_A) - \phi(t_B) \approx \frac{4\pi}{\lambda}\Delta R. \tag{5.36}$$

According to the motion equation, the velocity can be express as

$$\Delta v = \frac{\Delta R}{\Delta t}, \tag{5.37}$$

being Δt the time interval in which the displacement ΔR occurs. By clearing ΔR up from (5.37) and replacing it into (5.36) we get the following expression

$$\phi_{\text{int}} = \frac{4\pi}{\lambda}\Delta v \Delta t. \tag{5.38}$$

From (5.38) the velocity can be express as a function of time span Δt and the phase change ϕ_{int}

$$\Delta v = \frac{\lambda}{4\pi}\frac{\phi_{\text{int}}}{\Delta t}. \tag{5.39}$$

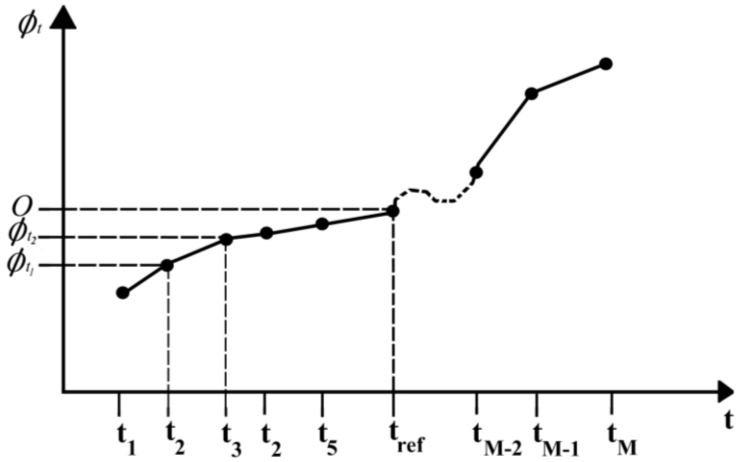

Figure 5-1 Estimated cumulated phase change ϕ vs. time acquisitions t for a generic pixel

Considering the entire period of study (see Figure 5-1) the average velocity of a generic target pixel can be estimated as

$$\bar{v}_{PS} = \frac{\lambda}{4\pi}\frac{\sum_{i=1}^{M-1}\phi_{\text{int},i}}{\sum_{i=1}^{M-1}\Delta t_i} \tag{5.40}$$

with

$\phi_{\text{int},i} = \phi_{t_i+1} - \phi_{t_i}$, the phase change between acquisition at t_i and t_{i+1}, and
$\Delta t_i = t_{i+1} - t_i$, the time span between instants t_i and t_{i+1}.

Note that the cumulative phase change must be referenced to a certain acquisition time, usually selected attempting to reduce the total decorrelation (see Chapter 3).
Now, taking a look at equation (5.32), there is more than one reference acquisition that can minimize the residuals between the model and the observations. In order to investigate how the temporal reference influences the quality of the final time series, error propagation analysis is proposed.
To obtain the uncertainties of the velocity Δv between two successive acquisitions, we applied the error propagation law to equation (5.39)

$$\sigma_{\Delta v}^2 = \left(\frac{\partial \Delta v}{\partial \phi_{\text{int}}}\right)^2 \sigma_{\phi_{\text{int}}}^2 + \left(\frac{\partial \Delta v}{\partial \Delta t}\right)^2 \sigma_{\Delta t}^2 \tag{5.41}$$

$$\sigma_{\Delta v}^2 = \left(\frac{\lambda}{4\pi\Delta t}\right)^2 \sigma_{\phi_{\text{int}}}^2 + \left(\frac{\lambda}{4\pi}\frac{\phi_{\text{int}}}{\Delta t^2}(-1)\right)^2 \sigma_{\Delta t}^2 \tag{5.42}$$

$$\sigma_{\Delta v}^2 = \left(\frac{\lambda}{4\pi\Delta t}\right)^2 \sigma_{\phi_{\text{int}}}^2 + \left(\frac{\lambda}{4\pi}\frac{\phi_{\text{int}}}{\Delta t^2}\right)^2 \sigma_{\Delta t}^2. \tag{5.43}$$

Note that for this simple analysis ϕ_{int} and Δt are considered as independent variables and thus, their correlation is zero. Assuming that there is no error in the acquisition time t then it follows that $\sigma_{\Delta t}^2 = 0$. Hence, (5.43) can be express as

$$\sigma_{\Delta v}^2 = \left(\frac{\lambda}{4\pi\Delta t}\right)^2 \sigma_{\phi_{\text{int}}}^2. \tag{5.44}$$

The expression above indicates that the magnitude of uncertainty of Δv depends on $(\sigma_{\phi_{\text{int}}} / \Delta t)$. The term Δt between successive acquisitions can be considered as a constant, and $\sigma_{\Delta v}$ depends on the propagation of uncertainties of the term ϕ_{int}.

Let us now estimate the variance of the deformation $\sigma_{\phi_{\text{int}}}^2$. The phase changes between three successive acquisitions t_1, t_2 and t_3 can be computed as

$$\phi_{\text{int}1} = \phi_{t_2} - \phi_{t_1} \tag{5.45}$$

$$\phi_{\text{int}2} = \phi_{t_3} - \phi_{t_2}. \tag{5.46}$$

Clearing up ϕ_{t2} from (5.45) and substitute into (5.46) we get the phase change ϕ_{int2} as a function of ϕ_{int1}, ϕ_{t1} and ϕ_{t3}

$$\phi_{\text{int}2} = \phi_{t_3} - \phi_{\text{int}1} - \phi_{t_1}. \tag{5.47}$$

Considering a new acquisition at instant t_4, the same procedure can be applied to ϕ_{int3} so that

$$\phi_{\text{int}3} = \phi_{t_4} - \phi_{t_3} \tag{5.48}$$

$$\phi_{\text{int}3} = \phi_{t_4} - \phi_{\text{int}2} - \phi_{\text{int}1} - \phi_{t_1}. \tag{5.49}$$

If we repeat this process for the $(M–1)$ phase change we obtain

$$\phi_{\text{int}M-1} = \phi_{t_M} - \sum_{i=1}^{M-2} \phi_{\text{int}i} - \phi_{t_1}. \tag{5.50}$$

By applying the propagation law to equation (5.50) and considering the phases as independent variables, the variance for the (M-1)-phase change between successive acquisitions can be then given as

$$\sigma_{\phi_{\text{int}M-1}}^2 = \sigma_{\phi_{t_M}}^2 + \sum_{i=1}^{M-2} \sigma_{\phi_{\text{int}i}}^2 + \sigma_{\phi_{t_1}}^2. \tag{5.51}$$

If we consider the first acquisition as the temporal reference (i.e. $t_{ref} = t_1$) it happens that $\sigma_{\phi_{t_1}}^2 = 0$ and (5.51) transforms into

$$\sigma_{\phi_{\text{int}M-1}}^2 = \sigma_{\phi_{t_M}}^2 + \sum_{i=1}^{M-2} \sigma_{\phi_{\text{int}i}}^2. \tag{5.52}$$

For the case for which the reference corresponds to the image acquired at the middle of the study period, equation (5.51) is written as follows

$$\sigma_{\phi_{\text{int}M-1}}^2 = \sigma_{\phi_{t_M}}^2 + \sum_{i=M/2}^{M-2} \sigma_{\phi_{\text{int}i}}^2 + \sigma_{\phi_{t_{M/2}}}^2. \tag{5.53}$$

Because the term $\sigma_{\phi_{t_{M/2}}}^2$ corresponds to phase variance of the reference image, it is set to zero and equation (5.53) turns into

$$\sigma^2_{\phi_{\mathrm{int}\,M-1}} = \sigma^2_{\phi_{t_M}} + \sum_{i=M/2}^{M-2} \sigma^2_{\phi_{\mathrm{int}\,i}} . \tag{5.54}$$

Note that the amount of addends in equation (5.51) doubles that of equation (5.53). Thus, a temporal reference, approximately corresponding to the middle of the period under analysis may optimize the quality of the deformation time series (see also Chapter 7). However, we emphasize that to optimally reduce the decorrelation that can affect the quality of the final time series, minimization of other variables (i.e. Doppler and perpendicular baselines) needs to be considered as well. Moreover, atmospheric artifacts in the master image may propagate affecting the quality of the interferograms, hence climate conditions of the study area (e.g., distribution of rainy and wet seasons) should be taken into account when selecting the temporal reference to avoid (or at least reduce) the propagation of this effect into the interferograms.

In conclusion, the adaptation of StaMPS for selection of an appropriate reference area and the proposed uncertainity analysis for selecting the temporal reference (considering as well the factors described above) seems to provide accurate and comparable results to existing ones over the Valley of Mexico, as shown in Chapter 7. Particularly in the northern area, where information about local dynamics is scarse, the extension for selection of a reference area based on the (available) geology, helped the correct estimation of the deformation time series which are used in the ground rupture zonation methodology (Chapter 8).

Chapter 6

The Valley of Mexico: interaction between groundwater withdrawal and subsidence

Up to now the technical concepts proposed for the Mexico Valley deformation (i.e. subsidence and associated effects) investigation have been described. Here the subject matter is tackled from a multidisciplinary perspective to better understand the complex phenomena affecting the target area.

Water supply has become a critical issue in many countries during the last decades. Mexico represents a very well-known example. The Metropolitan Area of the Valley of Mexico (ZMVM, by its acronym in spanish) and particularly Mexico City, where 20% of the total Mexican population is located, have been experiencing an accelerated demographic growth (period 1960-2010 from 1.4 to 15.1 million of habitants in Mexico State and from 3.1 to 8.8 million of habitants in the Federal District (DF); INEGI 2013). These incredible rates have been accompanied with the increment in the demand of public services such as fresh drinking water and better wastewater and drainage systems. In order to satisfy the water needs, water extraction practices have become exhaustive, conducing to the overexploitation of many aquifers, especially those embedded in the Mexico Basin.

The increasing pumping rates and the spread of the water wells within the Valley of Mexico (referred to as the Valley hereafter) have led to the regional lowering of the piezometric levels[5], producing loss of the pore pressure and compaction of the clay-rich deposits that compose the lacustrine plain where the City is built. Moreover, the sprawl of urban areas over potential recharge zones and the significant evapotranspiration (76%) that characterize this area, compromise the natural replenishment of the aquifer. Subsidence and its associated effects (e.g., ground failures and flooding), which are the major consequences of this situation, have repercussions on infrastructure, drainage systems and pipelines.

Most urban and non-urban areas of the Valley are affected by ground sinking rates that vary according to the soil constitution, ground water extraction rates and the clay-rich deposits thickness. Furthermore, subsidence is exacerbated by loading of soil due to urban constructions. This phenomenon has evolved to the extent that it has reached up to 13.5 m in some places of the Valley (Perez 2010). Thus, there is an urgent need to, if not revert water-related problems at least mitigate the ground settlement effects. The integration of different areas of science is essential to improve the critical situation the Valley of Mexico and other regions are undergoing. Geological and hydrological information of the area needs to be compiled and studied and current water management policies examined to address the land subsidence and related problems as a comprehensive study.

In this Chapter the actual situation in the Valley of Mexico is addressed from different viewpoints. Furthermore, main geo-hydrological, stratigraphic and geotechnical characteristics of the entire Valley are given, and subsidence and its effects described. This information results relevant for the spatial reference selection in the multi-pass InSAR study

---

[5] The piezometric level is the level of the water to which water in a system would rise in a piezometer (instrument to measure pressure) (Spellman 2008). The groundwater level is an indicator of the total energy available to move groundwater through an aquifer (Taylor and Alley 2002).

and aids the interpretation of the temporal and spatial deformation pattern (see Chapter 7 and 8). Additionally, some water policies are given and discussed.

6.1 General Description

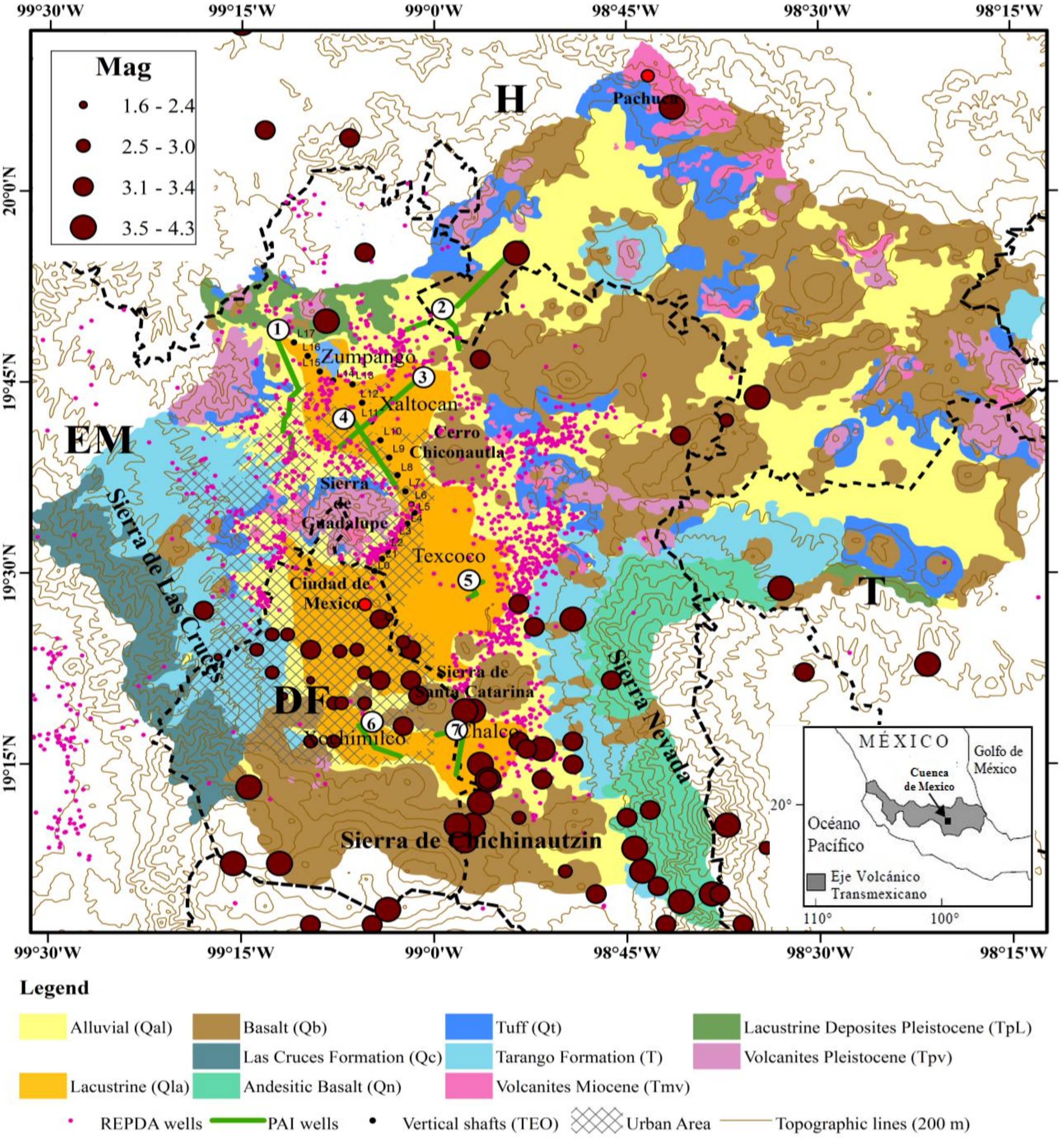

Figure 6-1 Geological map of Mexico Basin (based on Carrera-Hernandez and Gaskin 2007) . Main features of the Basin (mountainous ranges and lakes) are represented. The seven branches of the Pozos de Accion Inmediata (PAI) wells are shown: Teoloyucan (1), Tizayuca-Pachuca (2), Los Reyes-Ferrocarril (3), Los Reyes-Ecatepec (4), Texcoco-Peñon (5), Tlahuac-Nezahuacoyotl (6) and Mixquic-Santa Catarina (7). Epicentre of the seismic movements occurred during the 2006-2014 period are depicted as well (the magnitude correspond to the Richter scale) (from SSN 2014). The dashed black line indicates the state division (DF: Federal District, EM: Mexico State, H: Hidalgo, P: Puebla and T: Tlaxcala). The black rectangle in the small inset figure (adapted from Carreón-Freyre et al. 2006) to the lower right outlines the area of research in Mexico.

The Valley of Mexico belongs to the Trans Mexican Volcanic Belt (TMVB) and it encompasses Mexico City, which is the most important cultural, economic and industrial centre (see Figure 6-1). This Valley, located in the western part of the Mexico Basin which is situated at an average altitude of 2240 meters above see level (m.a.s.l) and has a surface of 9600 km^2, is surrounded by several mountainous ranges and volcanoes that reach up to 5500 m.a.s.l. The Sierra de Guadalupe, Sierra de Las Cruces and the Sierra Nevada can be found to the north, west and east, respectively (see Figure 6-1). The intensive volcanic activity to the South gave rise to the Sierra de Chichinautzin which effectively closed the Basin (~ 600000 years ago). The latter zone represents the most important natural recharge area of the Basin because of its high permeable basaltic rock (Lesser 1992).

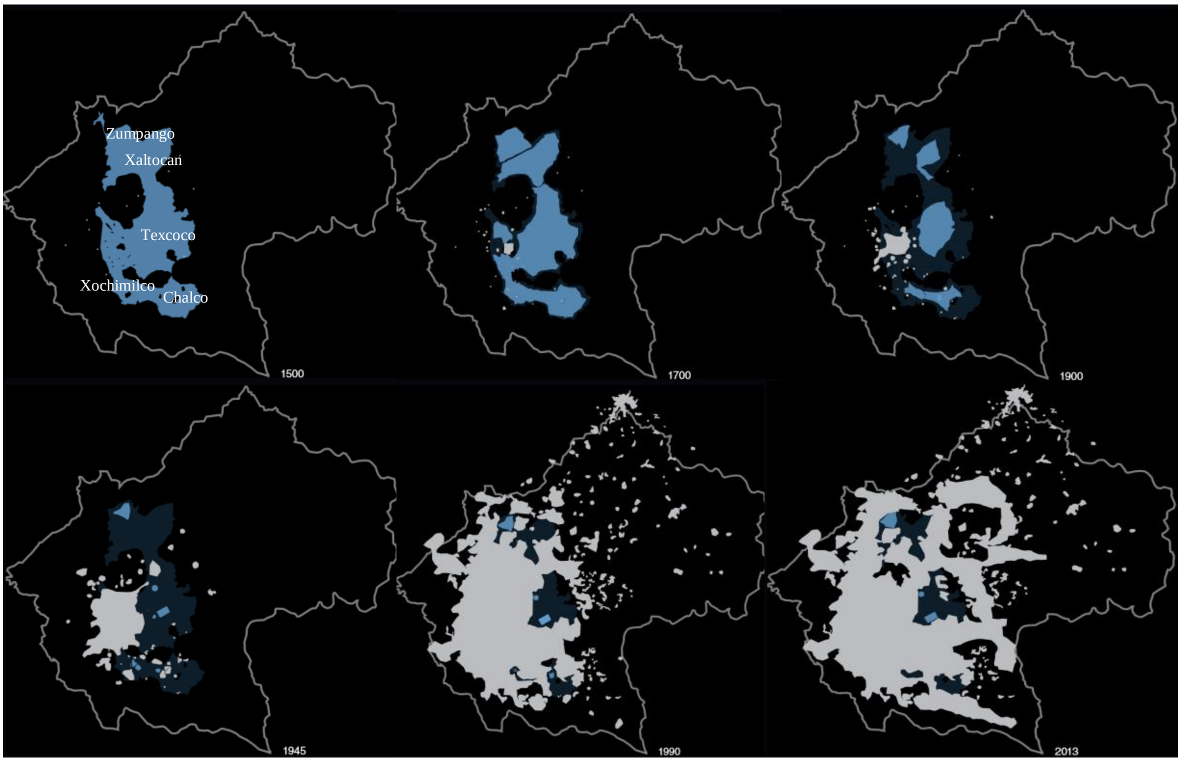

Figure 6-2 Evolution of the urban sprawl (in grey) and lakes surface (in light blue the remaining lake area and in dark blue the ancient lakebed zone) in the Valley of Mexico from 1500 to 2013 (adapted from Camarillo et al. 2013). Location of the five main lakes (Chalco, Xochimilco, Texcoco, Zumpango and Xaltocan) is represented. In 2013 most lakes appeared extinguished; only part of the Zumpango and the former Texcoco (now Nabor Carrillo) remains.

The plain where the Valley of Mexico is located was originally a system of five major lakes (Zumpango, Xoltacan, Texcoco, Chalco and Xochimilco). The Chalco and Xochimilco, located to the south of Sierra de Catalina are fresh-water lakes while Zumpango, Xoltacan and Texcoco are salt-water lakes.

The increasing drainage infrastructure (to reduce flooding) and the water exploitation during the last century, which continues up to now, have conduced to the almost complete disappearance of the lakes (see Figure 6-2).

From the geological point view, the Valley is characterized by volcanic materials such as pyroclastics and lava flows intercalated between alluviums and covered by lacustrine clays in the middle of the plateau. This disposition of the materials results from the volcanic events and sedimentation processes.

The mean precipitation for the region is 640 mm (CONAGUA 2009) and the rainy season normally covers from May to October. The highest peaks usually occur in July and August and they tend to be more intense to the south of the Valley. Regarding the water vapour, it varies temporally and spatially. Moreover, the orography that characterizes the south of the Valley might contribute to the higher frequency of precipitations than in the north, making the former region more humid than the latter area. Furthermore, the yet existing lakes (e.g.,

Zumpango, Nabor Carrillo- former Texcoco) and artificial dams modify the micrometeorology (e.g., albedo, temperature , wind direction) of the Valley (GDF and SMA 2006).
The mean annual temperature for the area varies between 12°C and 18 °C (GDF and SMA 2005).

6.2 Geology

6.2.1 Geotechnical, geological and stratigraphic configuration in the Valley

The area of study is characterized by hills and mountains of volcanic origin and by the presence of normal faults. According to the geotechnical classification three main units can be distinguished in the area (Gobierno del Distrito Federal 2004). Moreover, certain geological formations from Cretaceous to the Quaternary age within these units can be found:

i)Zone I-Foothills: is constituted by very compact and heterogeneous volcanic soils and lava flows with the presence of caves and caverns. Within this unit we can find predominantly the following formations:

- Tarango Formation (Tpt): continental material consisting of tuff, piroclastic material, lahars, lava flows, volcanic pumice stones and soil (Mooser and Molina 1993). These materials are extended to the base of the alluvial deposits on piedmont hillsides of the mountains located to the western and eastern part of the Valley. It also appears in other areas of the Basin.
- Tuff (Qt): consists of volcanic extrusive rocks from andesitic to dasitic composition and non-consolidated pyroclastic sequences. It appears discordantly overlying volcanic rocks from the Miocene- Pliocene (Vazquez and Jaimes 1989) and also discordantly covered by Quaternary units (Vazquez and Jaimes 1989).
- Las Cruces Formation (Qc): is composed by three strata volcanoes and pyroclastic deposits, oriented NNW and SSE and decouple the Mexico Basin from the Rio Lerma. The highest thickness of this formation reaches up 990 meters (Vazquez and Jaimes 1989). The volcanism from the Late Pliocene had given origin to this unit.
- Quaternary Basalts (Qb): appear interstratified with the lacustrine (Qla) and the alluvial (Qal) deposits (Mooser and Molina 1993). They present high permeability values due to the large number of fractures that affect them, providing an adequate route for aquifer recharge (Carrera-Hernandez and Gaskin 2007).
- Andesitic Basalts (Qn): constitute the high mountains of the Basin and lie above the Tarango Formation. They can also be found at the bottom of the Sierra de las Cruces and are composed of tuff, pumice and lahar (Mooser and Molina 1993). Highly consolidated clays from the Pliocene limit this formation (Mooser and Molina 1993).
- Miocene Vulcanite (Tmv): extrusive rocks from the middle and late Miocene that are distributed in small areas and are usually covered by younger volcanic materials. They originated from the volcanic activities related to the subduction of the Cocos Plate (Mooser and Molina 1993).
- Vulcanites Oligocene (Tv): can be found in few places within the Mexico Basin such as in the Sierra del Tigre and the Sierra de Tlaixpan (Texcoco). Like most structures from this age, they present faults with NNW direction.

ii)Zone II-Transition: is mainly formed by alluvial (Qal) (sand, silt, gravel and clay intercalated with conglomerate) and deep deposits of rock found at ~ 20m in depth. At the center of the plain, the alluvial deposits (Qal) appears interbedded with lava flow and layers of fine sand, clay and volcanic breccia, whereas at the edge of the plain, lava flows are interlayered with silts (Vazquez and Jaimes 1989). These deposits reach a maximum thickness of 800 m in the southern part of the Basin. Most of the water extraction wells are located in this unit (Carrera-Hernandez and Gaskin 2007).

According to the volume of clastics and the frequency of the deposits that constituted this unit, there are two transition zones: interstratified and abrupt (see Figure 6-3; Castillo-Guerrero 2012).

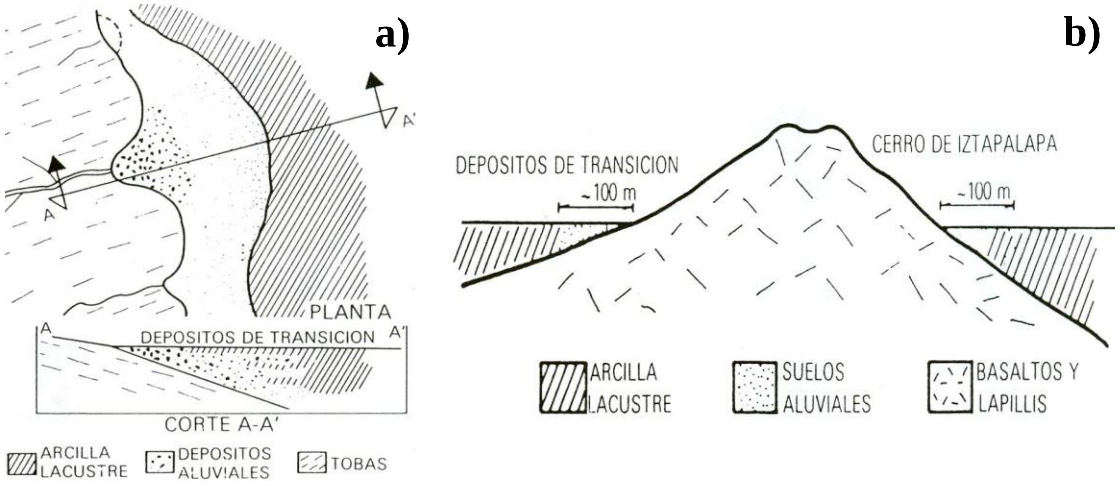

Figure 6-3 a) Interstratified transition: occurs in soils that were originated at the piedmont of the foothills (former lakes shore). Soils in these areas are similar to deltas that have extended until the clays of the ancient Texcoco Lake. The lacustrine clay intercalates with sand and gravels of the rivers; the thickness of the transitional deposits varied according to the dominant climate of the geologic age (from Castillo-Guerrero 2012). b) Abrupt transition**:** In these configurations, the presence of the alluvial deposits at the base of the volcanic structures is scarce and thus, the lacustrine clays are almost in direct contact with the rock (from Castillo-Guerrero 2012)**.**

iii) Zone III- Lacustrine (lakebeds of the now extinct lakes): is formed principally by clay deposits (Qla) of high compressibility and sandy beds. This unit extends from the Zumpango to the Chalco lake. It overlies or is inter-bedded with alluvial deposits which are characterized by heterogeneous sequences and sand (Huizar Alvarez et al. 2003).

The superficial lacustrine clay of zone III tends to be thinner in the north of the Valley and to increase their thickness to the south (Mooser and Molina 1993); this distribution is relevant for analysis of the subsidence since a clear correlation exists between the magnitude of accumulated subsidence and the thickness of the superficial clay layers (Auvinet Guichard and Moises 2011) (see also Chapters 7 and 8).

From the stratigraphic point view, four substrata can be distinguished within zone- III (Figure 6-4; Ovando-Shelley et al. 2013):

- Artificial fills: mainly archaeological debris, as the uppermost materials.
- Surface crust: consisting of dried low plasticity silty clays.
- Upper clay formation: having the most compressible soils; it is interspersed with six thin sand layers.
- Hard layer: appears at an average depth of about 40 m, formed by sands, gravely sands and thin lenses of softer silty clays
- Lower clay formation: second clay formation, about 10 m thick.
- Deep Deposits: very consistent silts and sandy silts interspersed with hard clays appear at the base of the stratigraphic column.

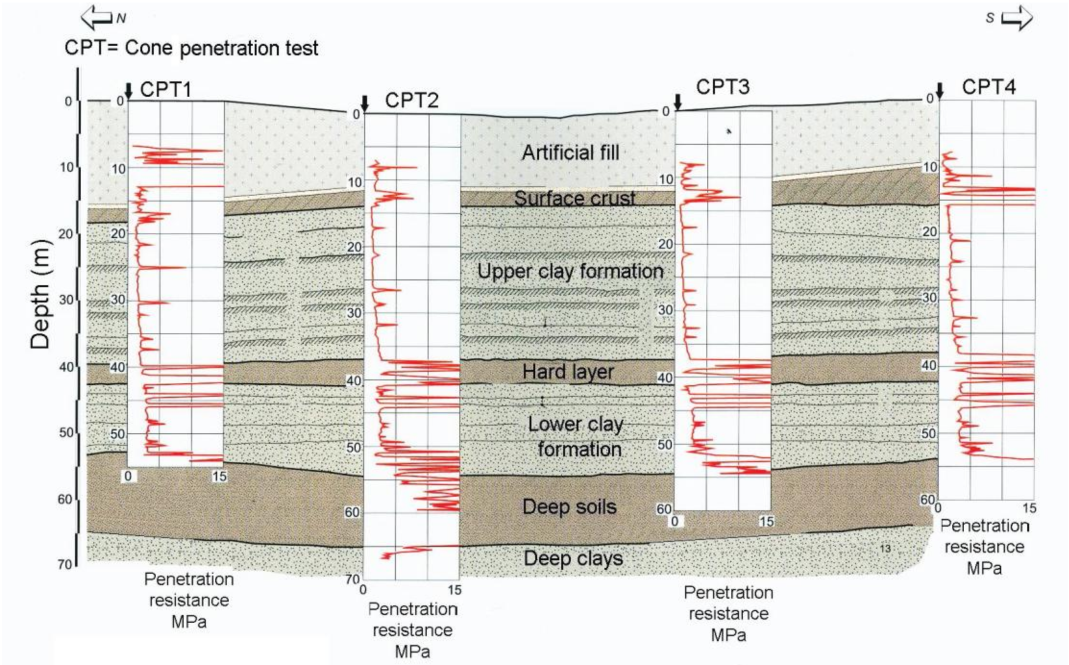

Figure 6-4 Stratigraphic cross section (from Ovando-Shelley et al. 2013).

6.2.2 *Regional structural geology in Mexico Basin*

The structural geology of the Mexico Basin is related to the tectonic and the intense volcanic activity from the beginning of the Tertiary, and that continued during the Pleistocene (Vazquez and Jaimes 1989).

Figure 6-5 Fault systems in Mexico Basin (from Marin-Cordova et al. 2004).

These volcanic events contributed to the formation of the endorreic Mexico Basin, which was filled by volcano clastic materials deposited in layers in a lake environment.

Several volcanic structures resulted from the volcanic activity such as the Popocatepetl, Iztaccihuatl, el Ajusco and Xitle. Moreover, several regional systems of fractures and faults identified by various scientists (e.g., Mooser 1975, Marín Córdova et al. 2004, De Cserna et al. 1988) can be found in the region (see Figure 6-5).

Affected Civil Infrastructure	Neotectonic Faults
Area of El Caracol, solar evaporator	F-9 and Distensive Axis
Azcapotzalco Avenue	F-8 and Distensive Axis
National Avenue	F-11
Highway Mexico-Pachuca	F-11
Lecheria-Texcoco road branch	F7- and F8
Calzada Ignacio Zaragoza and Peñon del Marques	F-6
Central Avenue at Nezahuacoyotl and Ecatepec	F7- and F8
Iztapalapa Avenue	F7- and F8
Benito Juarez International Airport	F-8
Nabor Carrillo Lake	F-8
Xico	F-5
Chalco	F-4

Table 6-1 Civil constructions within the Valley of Mexico affected by geological structures (adapted from Marin-Cordova et al. 2004).

Mooser (1975) refers to the presence of four main geological features within the Mexico Basin, separated by grabens oriented NE-SW: Cuautitlán, Peñones, Central and Oaxtepec. On the other hand, Marín-Córdova et al. (2004) defined sixteen NE-SW faults delimiting fifteen blocks (see Figure 6-5; Marín-Córdova et al. 2004), indicating that they belong to various grabens: faults F-12 and F-13 related to the Cuautitlán graben, faults F-8 and F-9 associated to the Peñones graben while faults F-6 and F-7, and F-4 and F-5 to the Central and Oaxtepec grabens, respectively. Particularly, the Cuautitlan graben in the north of the Valley, connecting the Zumpango and the Pachuca areas, presents a vertical component in the subsurface according to Huizar Alvarez (1996), which may compound the subsidence and the fracturing processes in this area (see also Chapter 8).

The structural geological study by Marin-Cordova et al. (2004) suggests that the alignment of the main NE - SW transtentional faults and the location of fractured areas indicate a NW-SE axis that joins the Popocatépetl volcano and the Tequisquiac-Huehuetoca zone, including the area of the former Texcoco Lake and the thermal zone of Peñón de los Baños. They have also pointed out that the presence of dams in the eastern slope of the Las Cruces range could have been affected by normal or strike-slip faults. Note that faulting model proposed by Marin-Cordova et al. (2004) is very regular; nevertheless, natural processes in general tend to be complex and variable, and thus the fault system in Figure 6-5 should be considered as a general representation of the actual faulting geometry.

The reactivation of the described regional structures in the Basin by tectonics or other forces can cause subsidence and represents considerable risk for the infrastructure and the population. Several urban structures reported to be affected are organized in Table 6-1(Marin-Cordova et al. 2004).

6.3 Hydrology of the Valley of Mexico

Within the Mexico Basin, a subsystem of aquifers which can be defined from the geological and hydrological viewpoint (Lesser 1992), can be found (see Figure 6-6). Here a brief description of the subsystems is presented, equally considering main hydraulic characteristics of the materials that constitute the aquifer units. Particularly, characteristics of the lacustrine deposits where the subsidence problem primarily occurs are presented and history of the piezometry and pumpage in the Basin is given as well. The later description is principally based on the study carried out by Carrera-Hernandez and Gaskin (2007).

6.3.1 Aquifer system

According to the administrative division (DOF 2009), seven aquifers can be identified within the Mexico Basin: Metropolitan Area of Mexico City (ZMCM), Chalco-Amecameca, Texcoco, Apan Cautitlán-Pachuca, Soltepec and Tecocomulco (see Figure 6-6). Most of these aquifer systems are constituted by three main units: two aquitards and a main aquifer. Here, general characteristics of each aquifer encompassed within the ZMVM (and the entire area of study) are presented.

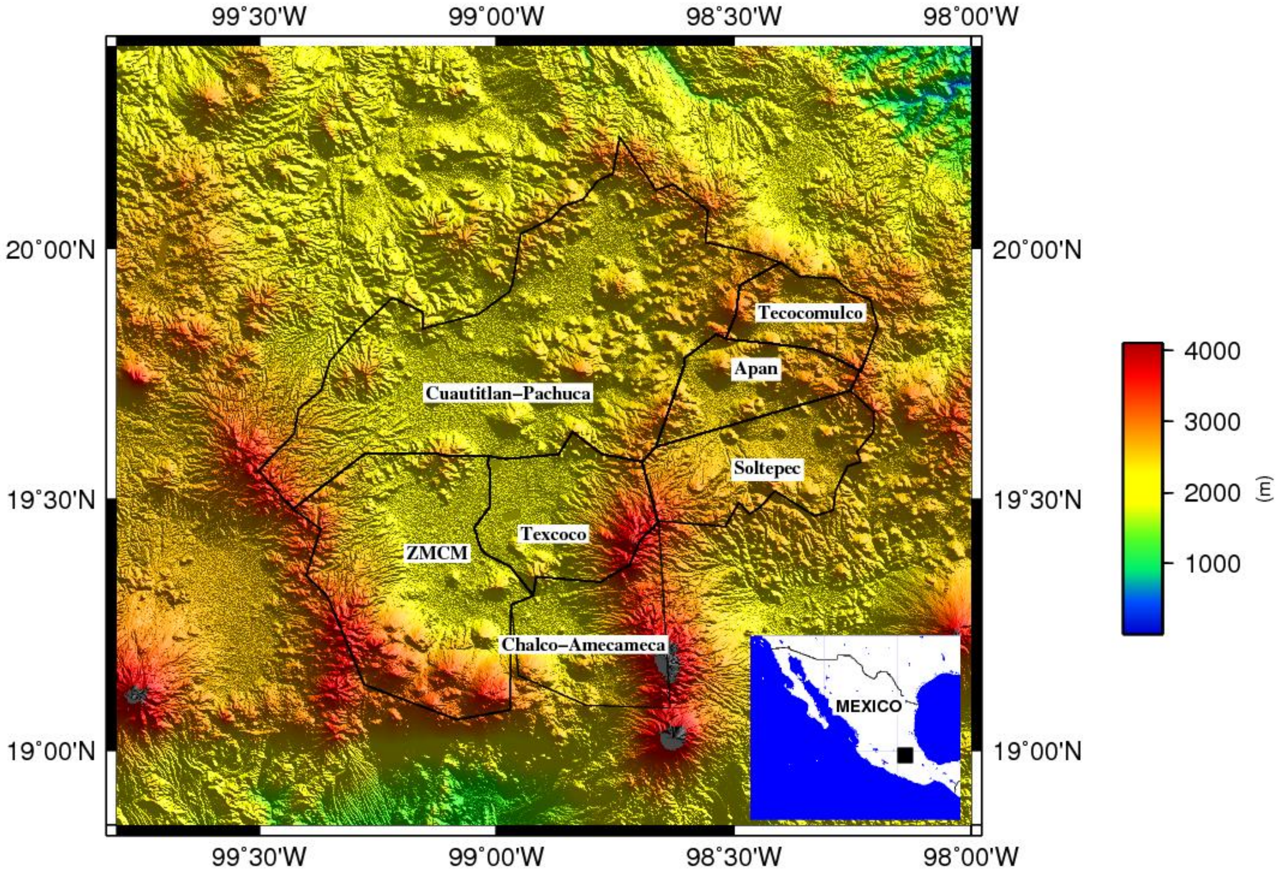

Figure 6-6 Aquifer system of the Mexico Basin (adapted from DOF 2009). Limits of the aquifer are indicated by black lines. The aquifers of ZMCM, Texcoco, Chalco-Amecameca and Cuautitlan-Pachuca are part of the ZMVM system. The rectangle in the small inset figure to the lower right outlines the location of the Mexico Basin.

Aquifer ZMCM: composed by three main units characterized by highly variable hydrodynamic parameters (Escolero Fuentes et al. 2009):

- Upper Aquitard: clayey unit of lacustrine origin characterized by a variable thickness, low permeability and great heterogeneity.

- Main aquifer (Granular unit): constituted by alluvial deposits, piroclasts, the Tarango Formation and bodies of basaltic and andesitic composition. This unit has a variable thickness being generally larger than 200 m.
- Tepozteco Formation (lower aquitard): a pyroclastic sequence located underneath the main aquifer. Thickest deposits can be found to the south (up to 600 m) and thinner to the north (around 100-200 m). The fractured volcanic rocks can reach up to 2000 m in depth, decreasing to the margins of the Valley.

Due to the irregular distribution of the clayey material, it is considered a semi confined aquifer (CONAGUA 2002a), i.e. there is a water exchange between the aquitards and the aquifer (Leyva Suarez 2010).

Most of the rocks that constitute the ZMCM are permeable specially the Quaternary basalts (Qb) of the Sierra de Chichinautzin which represents the most important recharge area. In the Sierras de Las Cruces and Guadalupe the recharge occurs mainly thanks to the presence of fractures.

Aquifer Cuautitlan-Pachuca: located to the north of the Valley of Mexico. This aquifer system includes two aquitards, a main aquifer (upper aquifer) and a lower aquifer (Huizar Alvarez et al. 2003):

- Aquitards: the upper aquitard is constituted by heterogeneous sequences of lacustrine deposits (Qla) while the lower aquitard by the Mexcala-Mendez unit. Between them the main aquifer is located. The lacustrine units cover partially the mixed fissured-granular unit of the main aquifer. The deposits of this unit cover an area that extends from Zumpango until the north of the Texcoco Lake, where it reaches a thickness up to ~ 400 m.
- Upper aquifer: Alluvial (Qla), the Tarango Formation (T) and volcanic rocks are part of the aquifer system. It contains two subunits: the mixed fissured granular unit and the Fissured unit.
- Lower aquifer or Basement: the limestone rocks of the Cretaceous are considered to form this unit.

The main groundwater flow comes from Pachuca, gradually added to the flows from the Sierra de Tepotzotlan and Sierra de las Cruces (Escolero Fuentes et al. 2009).

Texcoco Aquifer: has an area of 983 km^2 and shelters a population of more than 2800000 habitants (CONAGUA and OCAVM 2011). This aquifer, characterized by materials of low permeability, is communicated with the Cuautitlan-Pachuca aquifer to the north through the permeable materials of the Tarango Formation and the alluvial materials, and it is linked with the ZMCM through the common alluvial and lacustrine deposits present in both units. The natural groundwater flows occurs in EW direction, from the Sierra Nevada to the lacustrine plain; however, due to its overexploitation, the flow direction have been partially inverted (Escobar Villagran 2010). Between 2005-2009 several depression cones were identified in the aquifer area reaching up to 6-19 m lowering (CONAGUA and OCAVM 2011). Drawdown rates of 1.21 m/yr were found for the period 1968-2009 (CONAGUA and OCAVM 2011).

Aquifer Chalco-Amecameca: located to the south of the Valley of Mexico and it covers an area of 1393 km^2. Its hydrological units are similar to the rest of the Valley and consist of (Escolero Fuentes et al. 2009):

- Aquitard: Lacustrine sediments .Thin stratified aquifers are located within the aquitard structure (Huizar Álvarez 1993).
- Main Aquifer: Alluvial deposits and the Tarango Formation.
- Lower Aquifer: fractured vulcanites of the Miocene.

- Basement: vulcanites of the Oligocene and limestone of the Cretaceous.

The permeability of the sedimentary sequence of the aquifer presents a great variability mainly due to the presence of the heterogeneous granular material. This aquifer is considered to be semi confined, changing to unconfined (i.e. bounded by a free shallow water in contact with air and atmospheric pressure; Batu 1998) towards the edges (CONAGUA 2002b).

It is connected to the north with the Texcoco aquifer and to the east with the aquifer of ZMCM through common lacustrine and alluvial deposits.

According to CONAGUA (2002c) the overexploitation of this aquifer is of 22.17 Mm^3/year, and the depression of piezometric level reaches up to 0.99 m/yr.

Lithostratigraphic units	**Horizontal Hydraulic Conductivity (m/s)**	**Coefficient of specific storage(m^{-1})**	**Permeability Degree**
Quaternary lacustrine clays	10^{-9} to 10^{-7}	5E^{-2}	2
Quaternary Alluvial deposits (gravels and sands)	5.8E^{-6} to 5.2 E^{-3}	3.1E^{-7} to 9.4E^{-5}	5
Quaternary volcanic rocks of basaltic composition (lava flows, lapilli and ashes)	1.7 E^{-5} to 2.3 E^{-2}		7
Tarango formation (tuff, volcanic agglomerates and breccia)	2.0E^{-6} to 1.0E^{-4}		4
Andesitic volcanic rocks from the Pliocene and Quaternary(lava flows, tuff and fractured volcanic breccia)			6
Basaltic and andesitic volcanic rocks	1.4E^{-5} to 5.8E^{-3}		3
Stratified sequence from the lower Pliocene (tuff, volcanic breccia and agglomerate of andesitic composition)	1.2E^{-6} to 3.6 E^{-4}	1.2E^{-7} to 1.73 E^{-4}	4
Andesitic volcanic rocks from the lower Pliocene	4.4E^{-6} to 1.0E^{-4}	4.4E^{-6} to 1.4 E^{-4}	4
Lacustrine deposits of the lower Pliocene(clay and silts)			1
Volcanic rocks of the Miocene (tuff, fractured breccia and agglomerates)			1
Oligocene volcanic riolitic and basaltic (tuff, breccia and agglomerate)			1

Table 6-2 Main characteristics of the materials that constitute the aquifer system of the Valley of Mexico (adapted from Armendariz Fierro 2011). A Permeability degree equal to 1 indicates that the material is impermeable. Materials high permeable are those with a Permeability degree of 7.

6.3.2 General hydraulic characteristics

The material and rocks that constitute the geo-hydrological units of the Valley of Mexico present different hydraulic characteristics, particularly their permeability, transitivity and their transmission coefficient varies significantly. Knowledge about the different hydraulic parameters of the materials that constituted the aquifer system is paramount to understand the groundwater flow dynamics and the soil deformation responses to their variations. Moreover, they have a decisive influence on the designing of rainwater infiltration devices. Principal materials and their hydraulic properties are depicted in Table 6-2, especially considering the horizontal hydraulic conductivity[6], coefficient storage[7] and the permeability degree[8]. We observe that the high hydraulic conductivity corresponds to the volcanic rocks and alluvial

---

[6] Flow of a unit volume of water per day under a unit hydraulic gradient through a unit cross-sectional area at prevailing temperatures (ASCE 1996)

[7] May be defined as the volume of water that is released from or taken into storage per unit surface area of a confined aquifer or a confined aquifer layer per unit change in hydraulic head (Batu 1998).

[8] The permeability if the capacity of a geologic material for transmitting a fluid, in other words ease with which a fluid will pass through a porous medium. The degree of permeability depends upon the size and shape of the openings and the extent of interconnections. It is related to the permeability coefficient and the hydraulic conductivity (ASCE 1996).

deposits from the Quaternary, while lower values to the quaternary lacustrine clay. Moreover, the significant hydraulic conductivity in volcanic rocks may also be potentiated by the presence of fractures (see section 6.2.2).

Because of the high permeability that characterizes alluvial unit, most extraction wells are usually located in these zones and some of them in the lower parts of the mountainous ranges that surround the lacustrine unit and of the volcanic edifices of basaltic (or andesitic) composition (see also Figure 6-1).

Water extraction wells are also found in the lacustrine unit of low permeability and horizontal hydraulic conductivity; however, extraction depth in these cases usually reach higher depths where the water quality tends to decrease (Tortajada and Castelán 2003).

6.3.3 Lacustrine soils: properties and mechanical behaviour

The soils of Mexico City, encompassing from hard (basalts) to soft soils (clays), have unique properties. Physical characteristics of the soft soils are very important since most of the consolidation and consequent land settlement take place there.

The lacustrine sediments that characterize the Valley of Mexico subsoil's present complex mechanical and physics behaviour. Water contents higher than 400%, plasticity indexes exceeding 300% and compression indexes up to 10 can be identified in these sequences (Diaz-Rodriguez 2006). These intrinsic characteristics of the high compressible lacustrine clays make them highly deformable giving rise to foundation problems in the construction of high and massive buildings (Diaz-Rodriguez 2006).

Lacustrine soils are mainly affected by consolidation, a process whereby a decrease in soil volume occurs due to the expulsion of interstitial water (Carreón-Freyre et al. 2006). Two types of consolidation have been affecting the clay rich deposits of the Valley (Castillo-Guerrero 2012):

i)Natural consolidation: In this case the formation of the soils implied the consolidation of the clays due to their own weight, except for the *Costras Duras* that suffered a preconsolidation process due to dehydration or were dried by the sun. Presumable, in the zone of the Texcoco Lake, characterized by a presence of high salt content and affected by drought periods, the clays were more soft and compressible than in other regions of the Mexico Basin.

ii)Induced consolidation: the urban development of the lacustrine area of the Valley of Mexico have induced to a severe consolidation process in which the following factors influence:

- Construction and the development of cropping land areas during the prehispanic époque.
- Construction of tunnels and aqueducts (*tajos*) for the discharge of waste and storm waters that have produced the lowering of the piezometric levels, incrementing the thickness of the *Costra Superficial* and consolidating the upper layer of clays (see Figure 6-4).
- Groundwater extraction that have conduced to the progressively consolidation of the clays, from the lowest strata to the most superficial.
- Construction of modern urban structures.

The application of continuous loadings to the saturated soils of the Valley of Mexico has induced to a long term deformation due to consolidation. In general, the consolidation process consists of: primary consolidation (due to the pore water expulsion) and secondary consolidation (due to the viscoelastic deformation of the soil particles).

Zeevaert (1986) established a theory of secondary consolidation and intergranular viscosity for solid highly compressible soils. He proposed four consolidation configurations for the Mexico City clays that are shown in Figure 6-7.

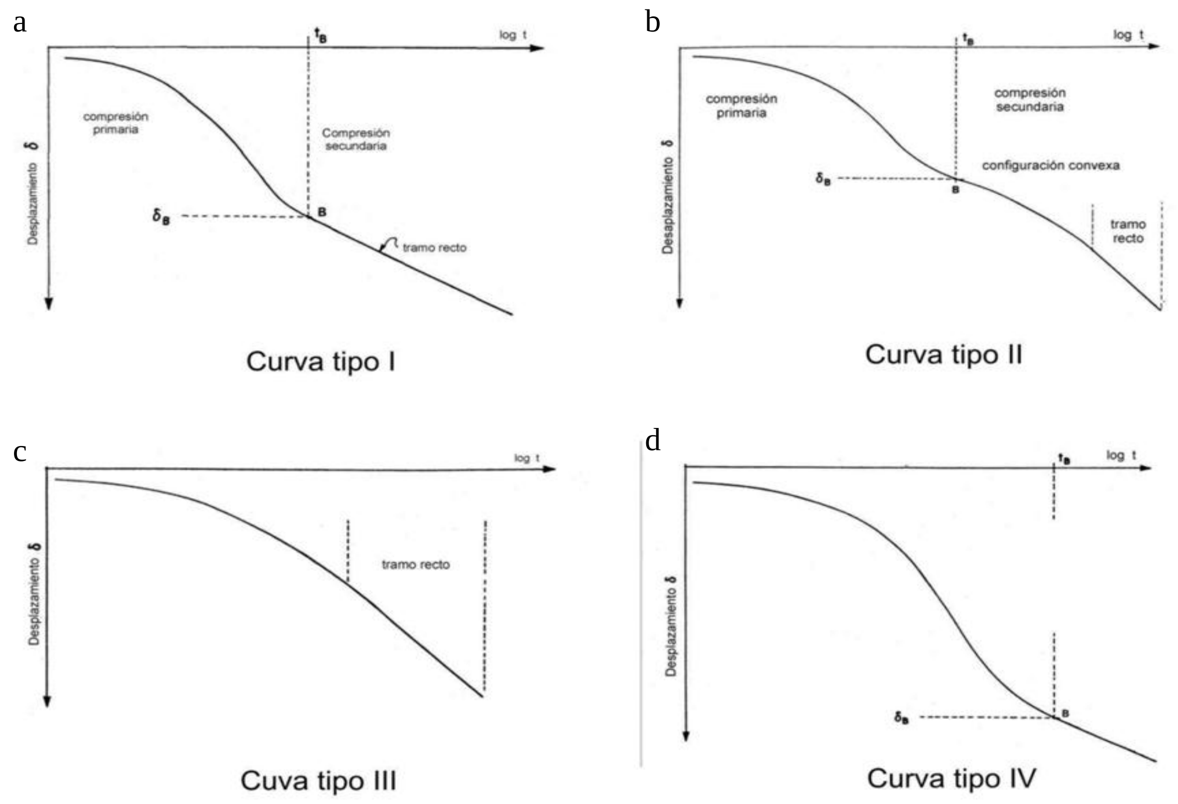

Figure 6-7 Consolidation curves according to Zeevaert (1986). a) Corresponds to the efforts lower than the yield stress σ_Y. b) The magnitude of the strains is lower but near to σ_Y. After the primary consolidation, the secondary compression starts to manifest as a convex curve. c) Configuration III results from the application of strains that are equal to σ_Y; no break is observed. d) Curve IV corresponds to strains larger than the yield stress. In this case, the formation of a new structure (e.g. fractures) can take place due to the application of larger stresses (Diaz-Rodriguez 2006).

Inspection and analysis of deformation time series in the next chapters, indicate that the subsidence in some areas of the Valley of Mexico, effectively, follows some of the configurations proposed by Zeevaert (1986) (see also Chapter 8).

6.3.4 Piezometric evolution and pumping rates

The intensive groundwater withdrawal from the Valley of Mexico aquifer system has produced the lowering of the piezometric levels and led to subsidence due to the consolidation of the clayey deposits (Lesser and Cortéz 1998).

Originally, the Mexico City water supply was satisfied by natural springs. However, due to the intensive water demand, groundwater extraction wells started to be drilled, being in 1886 more than one thousand (Lesser and Cortéz 1998) and with an increasing number since then.

In the year 1870, water abstraction in the Mexico Basin was around 2 m^3/s, augmenting to 22 m^3/s in 1952 and reaching up to 59.3 m^3/s in 2007 (Burns 2009), exceeding the natural recharge.

The decline of the piezometric levels has started to manifest in 1930 when natural springs started to dry and exploitation depths increased, reaching up to (100-200) m (National Research Council et al. 1995).

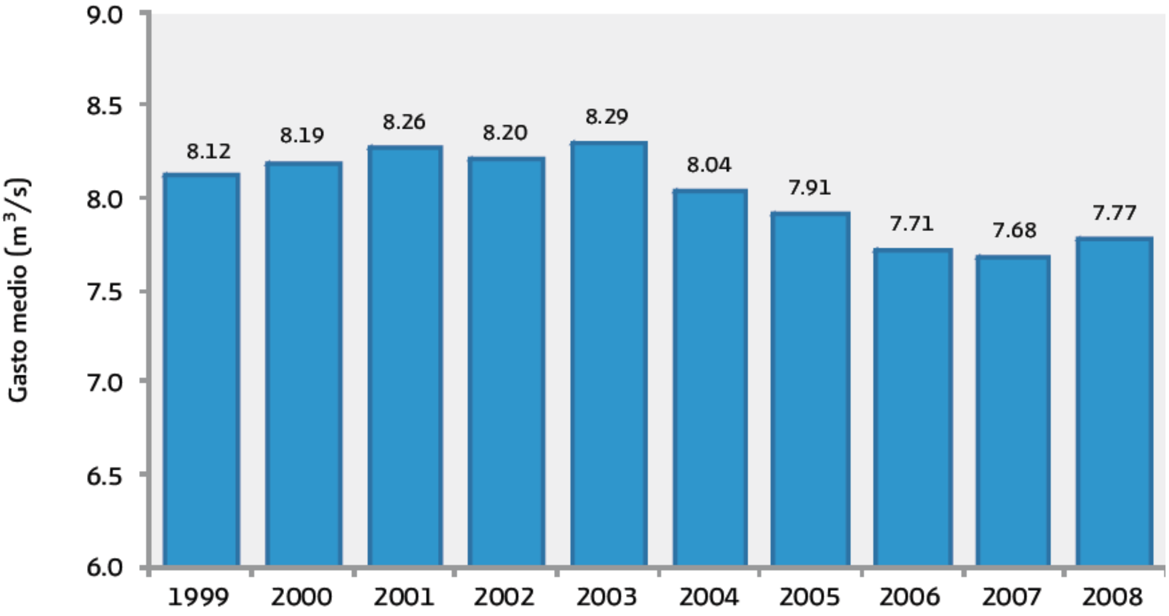

Figure 6-8 Evolution of the water supply provided by the PAI wells for the period 1999-2008 (from CONAGUA 2009)

The water supply to Mexico City became a severe issue and as a temporal solution the so called *Pozos de Accion Inmediata* (PAI) started to operate in 1974 aimed to reduce the overexploitation of the aquifers (CONAGUA 2009). They were expected to work until the 80's, but they continue functioning until now, becoming a paramount source of water supply for Mexico State and the Federal District (see Figure 6-8). At the present the PAI system comprises 218 wells distributed in 7 branches (see Figure 6-1). Moreover, to further reduce the pumping rates in Mexico City, water is imported from the Cutzamala and Lerma hydraulic systems (Burns 2009).

In general, most of the extraction wells are located in the transition areas between the lacustrine unit and the mountainous ranges and foothills (see Figure 6-1). A high density of wells are concentrated particularly to the west of Mexico City (Sierra de las Cruces) and to the east, in the Texcoco aquifer zone (see also Carrera-Hernandez and Gaskin 2007).

Several studies focused on the analysis of the evolution of the piezometric levels have been carried out over different areas of the Mexico Basin (e.g., Lesser 1992; Ortega Guerrero et al. 1993; Huizar Alvarez et al. 2001; Huizar Alvarez et al. 2003; Lesser and Posadas 2005). Yet, Carrera-Hernandez and Gaskin (2007) presented for the first time a complete study of the dynamics of the piezometric levels in entire Basin for the 1969-2001 period. On the other hand, the *Instituto Mexicano de Tecnologia del Agua* (IMTA) has performed an analysis for the entire Basin but concentrated on the water balance and estimation of the piezometric levels for the year 2001 (SEMARNAT and IMTA 2003).

According to Carrera-Hernandez and Gaskin (2007), an overall regional decrement of the potenciometric levels occurred during for the period 1969-2002. In Apan, however, the situation was different than in the rest of the Basin, being the water table for most of the monitoring wells almost constant for that period. The largest drawdown was found in Ecatepec (2.6 m/yr for the period 1975-2002; Carrera-Hernandez and Gaskin 2007).

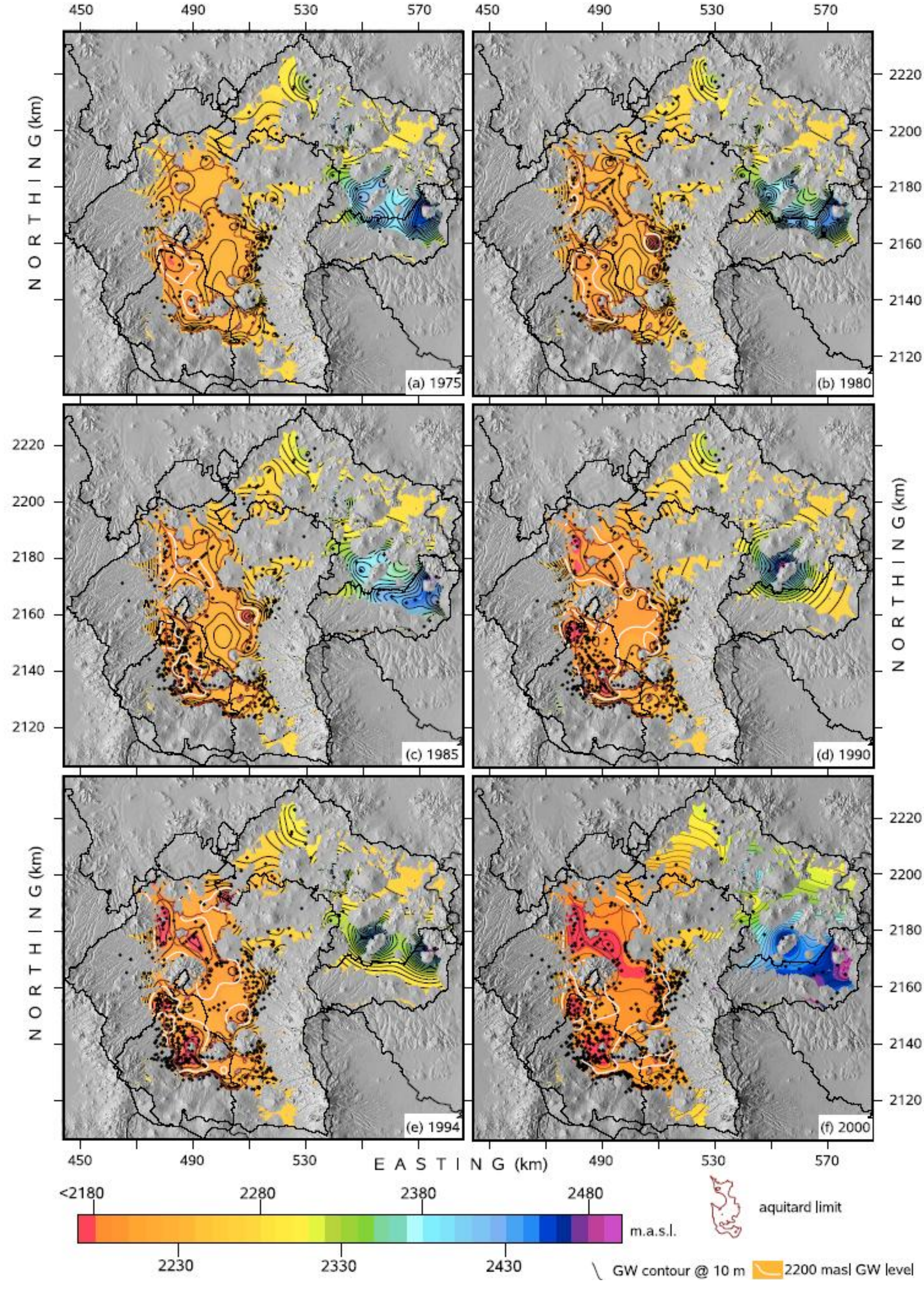

Figure 6-9 Evolution of the piezometric surface in the Mexico Basin for the period 1975-2000 (from Carrera-Hernandez and Gaskin 2007).

The map of the potentiometric surface evolution for the 1975-2000 period (Figure 6-9; Carrera-Hernandez and Gaskin 2007), indicates that the lowering mainly occurs in the Valley of Mexico. Furthermore, the development of some depression areas coincides with the location of the PAI wells; particularly the Reyes-Ecatepec, Teoloyucan and Tlahuac systems (see also Figure 6-1). The observed decline at these locations might be explained by exhaustive pumping rates (Figure 6-8). Notwithstanding, the dropping of the potenciometric surface does not always correlate with the extraction rates (Carrera-Hernandez and Gaskin 2007). For example, even though the extraction rates are large to the east of Sierra de Chichinautzin, the presence of high permeable rocks (see Figure 6-1 and Table 6-2) and important water infiltration through existing fractures during rainy seasons may compensate the volume of water extraction. However, the urban sprawl to this and other potential recharge areas (see Figure 6-2) impact negatively to the recharge capacity of the aquifer by preventing the water to infiltrate, reducing, as well, the capacity of auto regulation during the rainy periods.

Overall, water levels in the Basin are decreasing at rate of 1 m/yr (Burns 2009).This produces dehydration of the lacustrine clay, resulting in land subsidence and fracturing, main topics of analysis throughout this thesis (see Chapters 7 and 8).

6.4 Hydraulic situation

6.4.1 Water Balance and stress

Water extraction in all the aquifers of the Valley of Mexico exceeds the natural recharge, conducing to a regional groundwater deficit (Burns 2009). The values in Table 6-3 suggest an overexploitation of the entire Valley of Mexico aquifer system.

The largest deficit corresponds to the ZMCM aquifer, followed by that of Texcoco and the Cuautitlan-Pachuca systems; the lowest corresponds to the aquifer of Chalco-Amecameca (-16.36 hm^3/yr; CONAGUA 2009). Despite the proximity of the latter area to the Sierra Chichinautzin, a potential recharge zone, the replenishment is very low. The increasing urban spread over this area might have impacted negatively reducing the recharge capacity.

Aquifer Unit	Recharge	Natural Discharge Compromised	Concession of Water Volume	Mean water availability	Publication date (Diario Oficial de la Federacion)
ZMCM	279	0	1 248.58	-969.58	31-Ene-2003
Chalco-Amecameca	74	0	90.36	-16.36	31-Ene-2003
Texcoco	48.6	0	92.54	-43.94	31-Ene-2003
Cuautitlan-Pachuca	202.9	0	243.39	-40.49	31-Ene-2003

Table 6-3 Hydric Balance for the aquifers within the Valley of Mexico. Units are given in hm^3/yr (adapted from CONAGUA 2009).

Furthermore, the hydraulic stress (situation in which the water extractions exceed the 40% of the renewable resources; CONAGUA 2009) of 182 % causes deterioration of the aquifers quality and quantity. In addition, a mean water availability of 74 m^3 per inhabitant (CONAGUA 2009) suggests an absolute water scarcity.

The Valley of Mexico is enduring a severe hydric situation that requires urgent measures to mitigate the effects of groundwater depletion and to improve the groundwater management. Some endeavours to ameliorate this severe scenario are introduced in section 6.6.

6.4.2 Consequences of the water exploitation in the Valley of Mexico: general overview

The overexploitation of the aquifer of the Valley of Mexico has had several detrimental effects. Among them, the lowering of the piezometric levels has conducted to the loss of pore pressure, compaction of the lacustrine deposits, and the subsequent subsidence that has reached alarming values.

Water scarcity and the unsustainable exploitation of the superficial aquifer; have driven to the extraction of groundwater at greater depths, incrementing the drilling and water purification costs. Moreover, these procedures threaten the aquifers by infiltration of sewage water and other pollutants that could contaminate them.

Most springs and lagoons are almost dry and the groundwater resources notably reduced due to the extensive groundwater extraction practices. This situation forced the importation of water from outer Basins possibly transferring water related problems to those areas as well.

The indiscriminate groundwater extraction in the Valley of Mexico (and other areas) has not only economic and environmental repercussions, but also social and political consequences. Even though there is an important deficit of this vital resource, large volumes of water are wasted every day.

Most effects of the overexploitation are principally related to the subsidence. The natural river flow regimes have been modified due to the regional land sinking that alters the slopes. Besides, general infrastructure is severely affected by this and related soil fracturing.

In the following sections subsidence and its associated consequences are further addressed.

6.5 Subsidence

The Mexico City subsidence is a very serious but not a recent problem. Already in 1925, the sinking had been reported by Roberto Gayol, who associated it to the construction of the drainage system which at that moment consists of the Gran Canal del Desagüe and the Tunnel of Tesquisquiac (Figueroa-Vega 1984). However, the subsidence might have started since the pumping of the shallow aquifer in the late 1800s (Lesser and Cortéz 1998).

In 1945, the *Comision Impulsora y Coordinadora de la Investigacion Cientifica* began studies of the Mexico City's subsoil, and Dr. Nabor Carrillo linked for the first time, in 1947, the consolidation of the clays and consequent land subsidence to the exploitation of the aquifer. Later, other scientist such as Raul Marsal and Marcos Mazari confirmed the hypothesis of Dr. Carrillo (Figuero-Vega 1984; Santoyo 2007). Since then, many interdisciplinary studies have been performed to monitor, evaluate and understand the ground sinking problem in Mexico City. Investigations include the application of in situ measurement such as levelling (e.g., Lesser and Cortes 1998; Méndez et al. 2008b**)** and GPS campaigns (e.g., Cabral Cano et al. 2008), remote sensing techniques (e.g., Strozzi et al. 2003; Lopez-Quiroz et al. 2009 ; Yan et al. 2012 ; Chaussard et al. 2014; Siles et al. 2013) and combination of methods (Osmanoglu et al. 2010).

The present and future trends (e.g., increasing population and water demand) indicate that subsidence and its associated consequences may continue to impact the Valley of Mexico and other regions. Thus, the settlement phenomenon is still an important subject of study.

6.5.1 Causes

There are many mechanisms that can produce subsidence. Anthropogenic activities such as pumping of gas, oil and /or water from the underground are the main cause. The presence of active tectonic faults can also provoke land subsidence.

Dissolution of some materials such as sedimentary rocks or sulphates can produce the collapse of the underground channels or caves, conducing to land sinking. Another type of mechanism that can generate ground settlement is the decomposition of buried trash or underground debris (Kolh 2001).

Assuming a simple aquifer model of two aquitards (clay and silt) and one aquifer (sand and gravel), groundwater-related subsidence occurs when the water extraction from the aquifer unit induce a vertical drainage from the aquitard. The reduction of the pore pressure in the silty-clay beds, causes volume diminution (compaction), vertical and horizontal stresses leading to subsidence and soil fracturing (Huizar Alvarez et al. 2003; Carreón-Freyre et al. 2006).

In the Valley of Mexico the principal source of the land subsidence is the excessive water extraction from the aquifer underneath. However, the location of the Valley within the TMVB and the presence of the regional faults (see also Figure 6-5) might also contribute to the this process. Another component coming from the decomposition and displacement of buried trash, presumably adding to this process is considered in Chapter 7.

6.5.2 Evolution of the regional subsidence

Considering the first records, subsidence might have been impacted the Valley of Mexico for more than 150 years (Ovando-Shelley et al. 2013).

Levelling measurements for the period 1891-1895 indicate a subsidence rate of ~5 cm/yr in Mexico City, reaching up to 18 cm/yr for the period 1936-1944 (Lesser and Cortéz 1998).

Lesser and Cortéz (1998), showned that the pumping rates in the centre of the City experienced a drastic reduction from 1940 until the late 50s and the subsidence decreased up to ~8 m (see Lesser and Cortez 1998). Later, in the 70s, the extraction in the south of the Valley (Chalco-Xochimilco) triggered the sinking of this area.

For the period 1891-1994, the centre of Mexico City had subsided up to 10 m, from the centre to the international airport around (6-7) m and more than 6 m in the Chalco area (Lesser and Cortéz 1998). In Tlahuac, the ground surface sank ~5 m for the same period (Lesser and Cortéz 1998). These values were measured relative to an area outside the lacustrine unit.

In the year 1995, the zones critically affected by the subsidence were the Peñon del Marquez (40 cm/yr), Ecatepec (20 cm/yr) and Chalco (30 cm/yr) (Santoyo 2007). These observations are similar to the levelling results published by the GDF et al. (2012b) for the 1992-2007 period (see also Figure 7-20) .

The subsidence in Mexico City has notoriously influenced several urban infrastructure and historical monuments. Figure 6-10 shows an example of the ground surface settlement evolution for four well-known cases, from 1900 until 2010 (Auvinet et al. 2013). Note that subsidence of most structures presents four main phases:

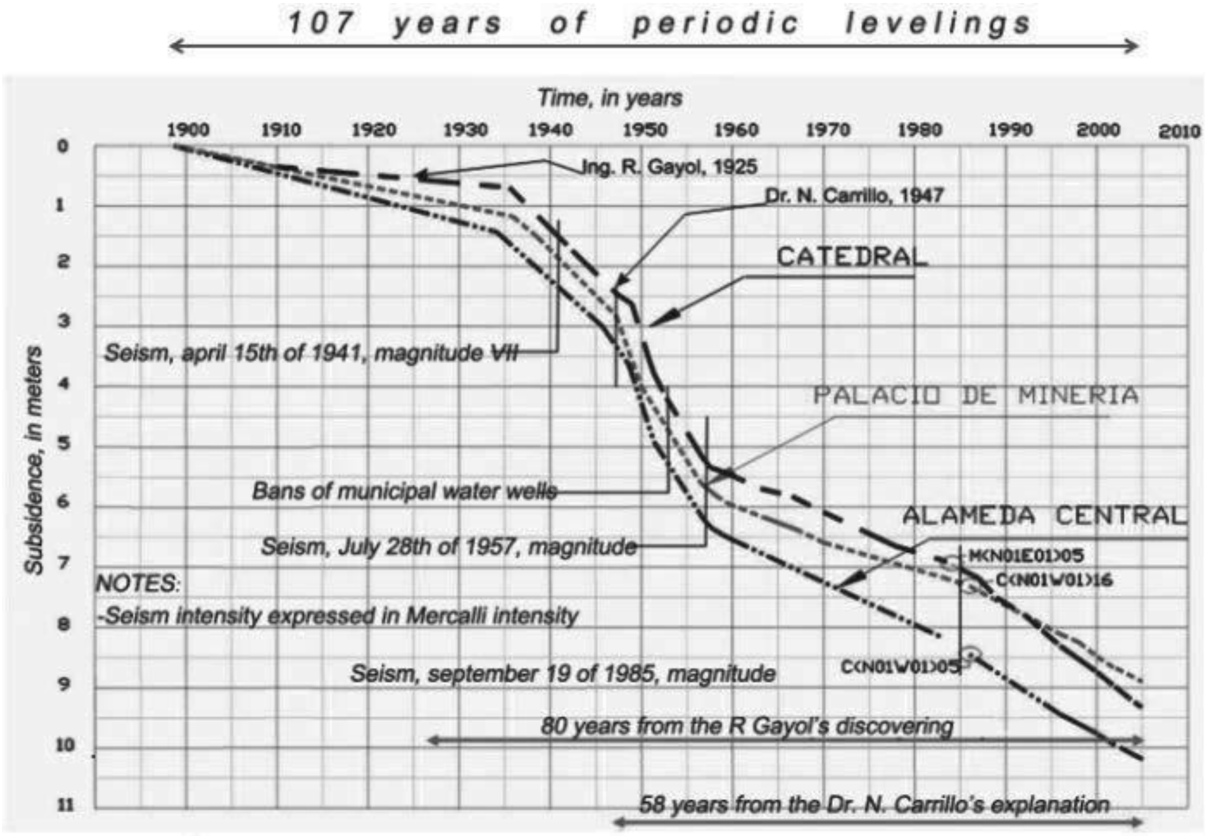

Figure 6-10 Subsidence evolution of three historic sites for the 1898-2005 period (from Auvinet et al. 2013).

- 1898-1937: the settlement is almost linear. Approximately average subsindence rates of 4 cm/yr.
- 1937-1947: subsidence is characterized by a linear behaviour, being the average ~16 cm/yr.
- 1947-1957: the mean subsidence is 29 cm/year, rapid subsidence characterized this period.
- 1957-2010: the subsidence during this period decrease and the average is ~6 cm/yr.

From the literature review, it was noticed that most of studies are concentrated on the south of the Valley, existing a few surveys performed on the north. Lesser and Cortéz (1998) suggested a mean subsidence in the north of Valley of ~6, 6 cm/yr for the period 1963-1993. A relatively new report (Auvinet et al. 2012) indicated subsidence rates between 5 and 7 cm/yr for the same area.

Even though there are some variations between the subsidence rates published due to different techniques, period of study and other sources of discrepancies, most settlement investigations (e.g., Lesser and Cortez 1998; Auvinet and Juarez 2011; Juarez et al. 2010; Cabral-Cano et al. 2008; Lopez-Quiroz et al. 2009; Cerca et al. 2012; Perez 2009) indicate similar maximum subsiding velocities ranging between 30-40 cm/yr.

Subsidence rates tend to be larger in the centre of the lacustrine plain, decreasing towards the mountainous ranges and the volcanic edifices, and correlate with the clay thickness spatial distribution (Lesser and Cortéz 1998; Auvinet and Juarez 2011; Cabral-Cano et al. 2008). Furthermore, subsidence rates decrease from the north to the south of the Valley following the direction of the clay thickness diminution, as shown in this study by means of the InSAR techniques (see results in Chapters 7 and 8).

It is important to emphasize that even if the groundwater extraction would cease, the subsidence may continue but with lower rates (Lesser and Cortéz 1998).

6.5.3 Consequences

Land subsidence in the Valley of Mexico has had several repercussions. Particularly, the fracturing process has become a severe problem affecting pipelines, aqueducts and civil infrastructure, threatening people's life as well.

Fractures can develop in the following areas:

- **Lacustrine Plain:** The clay deposits that constitute the lacustrine unit are characterized by crystallized and amorphous minerals that have a very complex behaviour (Carreon-Freyre 2010; Carreon-Freyre and Cerca 2006). Contrasting pumping rates and variation of the piezometric levels might differently modify the physical and mechanical properties of the sedimentary materials. In this case different tensional (vertical and horizontal) stresses might create weak plains and their propagation. Even if the pumping rates do not vary spatially, the heterogeneous configuration of the fluvio-lacustrine soils are subjected to different consolidation, producing soil cracking. Such is the case in Atzcaptozalco, located in the north western part of Mexico City (Auvinet 2010).

  The presence of buried geological structures such as grabens or horsts can also contribute to the generation of fractures (Figure 6-11). The geometry of depressed (or raised) blocks limited by normal (or inverse) faults filled by fine grain deposits subjected to non-uniform consolidation might conduce to the appearance of cracks. Moreover, active dynamics of these structures can produce differential (vertical and/or horizontal) movements compounding fissuring of the sedimentary sequences.

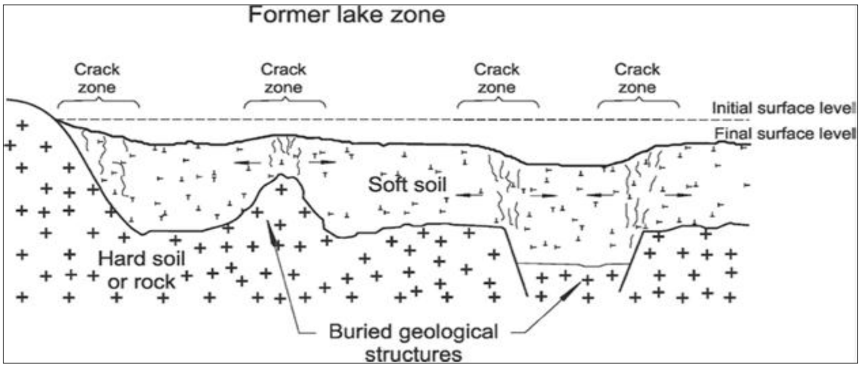

Figure 6-11 Cracks induced by geological buried structures (from Ovando-Shelley et al. 2012).

- **Transition zones**: The thickness of the clayey deposits decreases towards the edges of the lacustrine unit where the volcanic structures (mountainous ranges and cones) are found. In some of these areas the abrupt change of the compressible clay thickness combined with the regional subsidence, induce differential deformation producing fracturing (Figure 6-12). Differential subsidence in transition zone notably occurs in the areas of the Peñón de los Baños, Peñon del Marqués, Peñón Viejo, and Cerros del Xico and Tlapacoya in Chalco (Auvinet 2010).

Because soil fracturing can actually occurs as a consequence of any condition leading to large tensile stresses or extension strains in the soil (Auvinet 2010), other mechanisms that induce the creation and propagation of fractures need also to be evaluated (e.g. hydraulic fracturing due to water infiltration, injection of water, loading of soil surface). In the Peñon del Marquez, for example, the installation of infiltration wells may produce tensional stresses

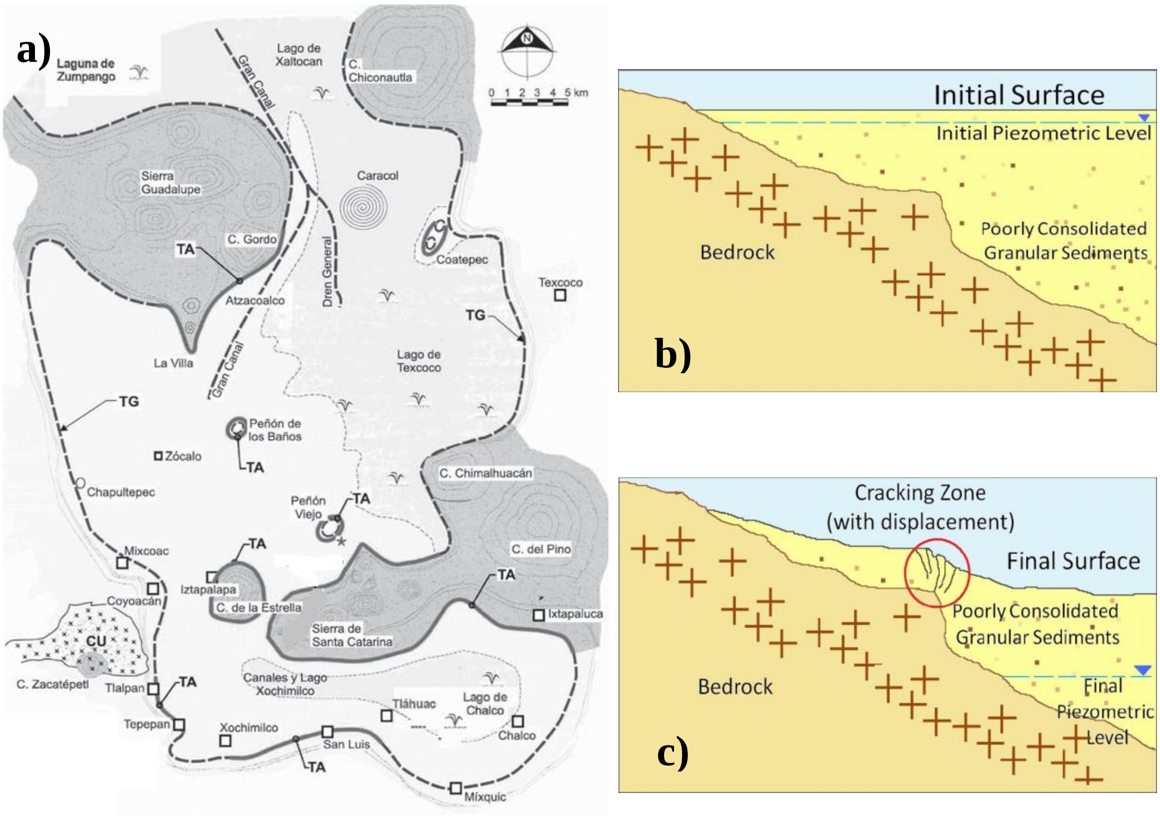

Figure 6-12 a) Prone to soil facturing areas in the Valley of Mexico (adapted from Ovando-Shelley et al. 2012). Grey full lines: sharp transition zone prone to fracturing. Dashed grey lines: smooth transition zones. In panels b-c cracking mechanism in abrupt transition areas is depicted (from Lermo et al. 2010). b) Thickness of compressible clay layers changes progressively. c) Thickness of compressible clay layers changes sharply over short distances. Differentials collapses occur in these zones. Note that the piezometric level decreases from b) to c), compounding differential subsidence and soil fracturing.

contributing to the fracturing process, also potentiated by a sliding mechanism (Cerca 2010; Cerca et al. 2012). See also section 7.6.

The regional subsidence together with the accelerated urban growth and periods of intensive rain made the current drainage system inefficient to cope with their normal tasks such as the discharge of sewage and storms water outside the Valley. Water discharge capacity of waterways such as the Gran Canal del Desagüe has been reduced due to gradual modification of the terrain slope as a consequence of subsidence (CONAGUA 2012) (see also Figure 6-14). This situation has increased the risk of flooding, which in turn might contribute to the propagation of discontinuities due water infiltration into existing earth fissures.

Besides, the water quality has been endangered by the percolation of the pollutants into the aquifer through the creation (or proliferation) of fractures that affect the clay rich deposits. Several water wells are near contamination sources such as waste deposal sites, located in areas prone to soil fracturing (e.g., area of Texcoco Lake). This equally threatens people’s health. Another consequence from the settlement evolution is the development of a lake in the middle of the Chalco plain (Ortiz-Zamora and Ortega-Guerrero 2010).

6.6 Measures to reduce the hydraulic problems in the Valley of Mexico

Water and wastewater management in the Valley of Mexico has turned into a major challenge. The quest of an integral solution for water problems in the Valley needs to consider social, economic and environmental variables as a whole. Solution to these problems is out of the scope of this thesis; however, general water policies applied by the Federal District and the Mexico State water organizations are here outlined and discussed.

Water importation from other basins

The Cutzamala and Lerma hydraulic systems have been operating since 1951 and 1982, respectively (CONAGUA 2009). Their main objective is to supply water to Mexico City and to reduce the overexploitation of the local aquifer. Even though part of the water supply is fulfilled by the importation from these outer basins, water scarcity and land subsidence prevail. Moreover, water-related problems started to manifest in those systems, especially in the Lerma basin. This situation motivated the reduction of the volume of water exported from this basin from 15 m^3/s to 5 m^3/s (Burns 2009).

Groundwater is imported from the Lerma Basin by an aqueduct, being first disinfected with chlorine and added to the same duct before the water is distributed in the ZMCM (National Research Council et al. 1995). It is important to highlight that an inadequate water treatment could have a mass repercussion on people’s health.

Another principal source of water supply is the PAI wells system (see Figure 6-1). Low-quality groundwater extracted from some of these wells also represents a danger for the consumers. A solution to this situation could be the implementation of new and costly purification systems, however, other problems such as the severe drawdown of the piezometric levels and subsidence would persist.

Water reuse (CONAGUA 2009)

The water reuse is an essential component of the integral water management. The wastewater produce in the metropolitan area of Mexico City is reused specially by the Valley of Tula (94%). On the other hand, the Valley of Mexico uses 4% of the wastewater mainly for irrigation of gardens and car washing. The remaining 2% is used by the industry in both Valleys. Values published by the CONAGUA (2009) indicate very low employment of treated wastewater; however, the utilization of advanced treatment techniques and improved maintenance of existing plants might be necessary before increasing its volume for public use.

Increment in the water cost

One strategy of the water authorities consists of incrementing the water tariff. The implementation of this strategy could help to create social consciousness about the rational water usage and to cover part of the cost involved in the maintenance and the construction of hydraulic infrastructure. Nevertheless, social inequity should be considered in the estimation of new and higher taxes that different social classes should pay (Carrera-Hernández 2007). The application of education programs oriented to the rational use of water should also be taken into account.

Artificial recharge

Artificial water recharge projects have been applied in many countries such as in France, Spain and United States. In Mexico, one method consists of the infiltration lagoons. This low-cost strategy has a high potential but in the long term because the clayey deposits act as an impermeable layer, preventing the water to easily seep into the aquifer.

An alternative procedure comprises the usage of rain water absorption wells. In Iztapalapa, several absorption wells of various depths operate to mitigate the flooding due to subsidence, helping also to restore the aquifer’s balance (Carreon-Freyre 2011; SACMEX 2012).

Treated waste and storm water injection through infiltration wells is also being evaluated and has been already applied in some areas (GDF et al. 2012a; Lesser and Asociados 1991; Lesser and Cortéz 1998).

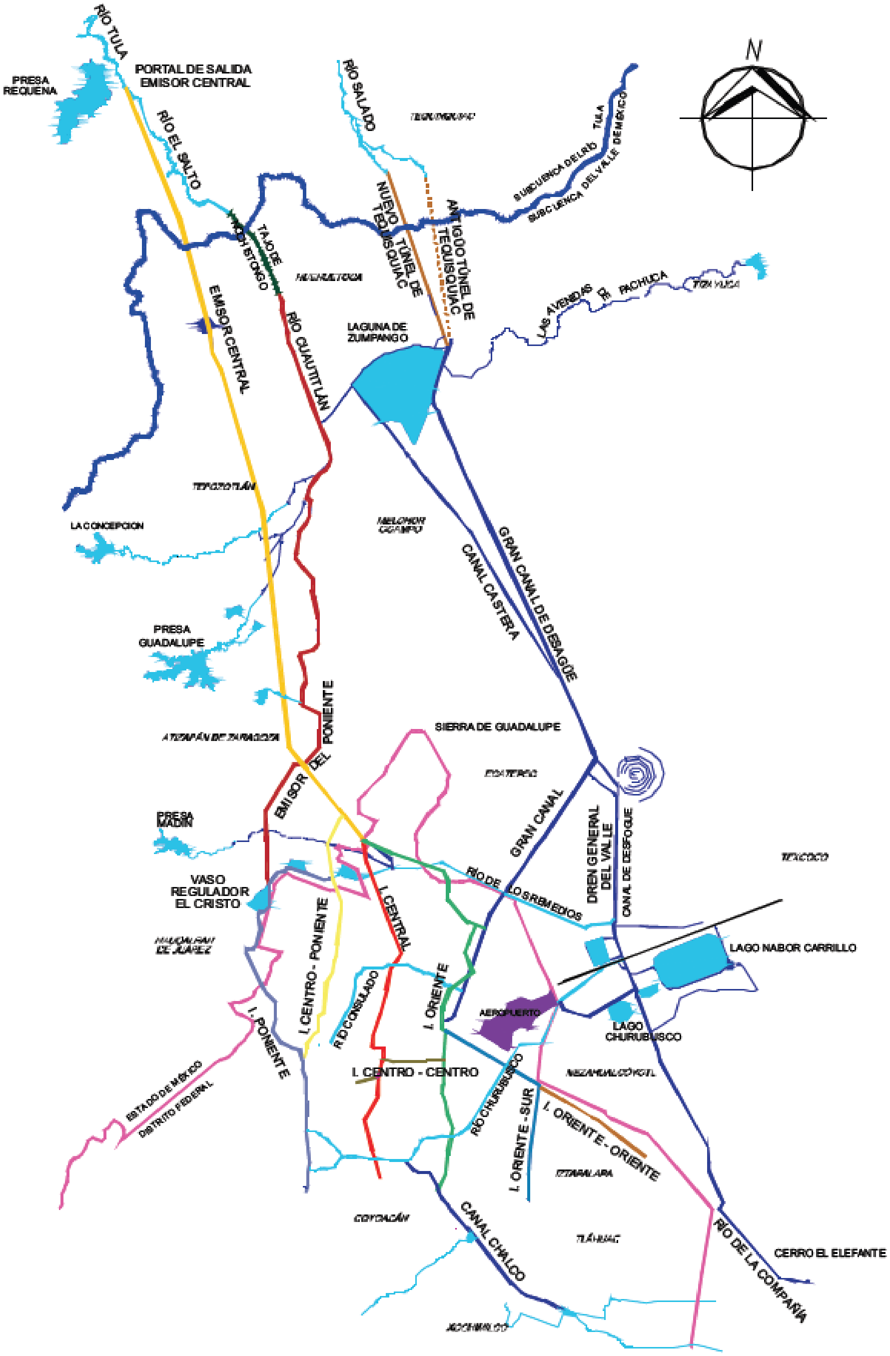

Figure 6-13 Main drainage system of the Valley of Mexico (CONAGUA 2009). The *SDP* is constituted by 9 main structures: Emisor Central, Interceptores, Central, Oriente, Oriente-Sur, Centro-Poniente; Poniente, Centro-Centro, Oriente-Oriente, Iztapalapa , Canal Nacional- Canal de Chalco, Obrero Mundial , Gran Canal, Indios verdes, Ermita and Cuautepec. Some structures of the old drainage system (and that still operate) are also displayed.

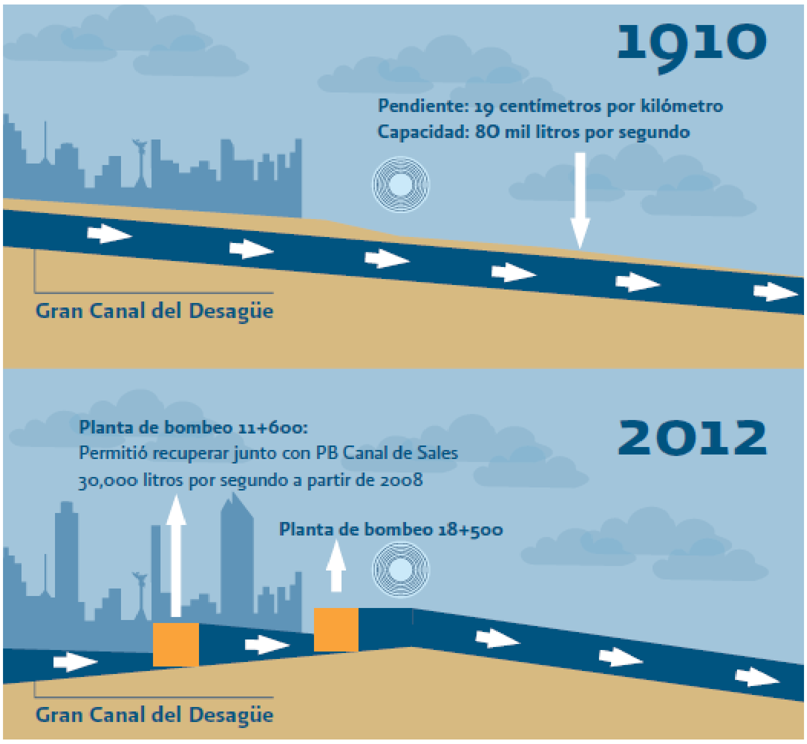

Figure 6-14 Slope alteration of the Gran Canal del Desagüe due to subsidence (from CONAGUA 2012). Its slope was reduced up to almost 100% and its water transportation capacity up to ~62%. A pamping station was installed in 2008 to improve its capacity.

Even though water absorption and injection methods can reduce the risk of inundations in certain areas, it needs a careful evaluation because the infiltration of inadequately treated waste or rain water can reduce the aquifer's water quality due to contamination.

Recharge by agriculture irrigation has been very successful in the Valley of Mexquital, where the removal of contaminants by plants, soils and open channels is highly efficient and with comparable results to those achieved in a secondary treatment plant (Jiménez and Chávez 2004). Notwithstanding, the extensive and uncontrolled urbanization over farming lands reduces the efficacy of this method in the Valley of Mexico. A better urban planning is required, to take advantage of this recharge method. Improvement of the vulnerability maps to ground ruptures in the area by the proposed methodology in Chapter 8 may meaningfully contribute to this task.

Hydraulic infrastructure: Drainage System

The water drainage system of the Valley of Mexico has historically comprised 4 main hydraulic structures: the Noschitongo cut (1629), the Tequixquiac tunnel (1900), the New tunnel of Tequixquiac (1955) and the Emisor Central (1975) (CONAGUA 2010).

The increasing urban growth and the evolution of the land settlement made this system inefficient to drainage the water surplus out of the Valley and thus, an improved hydraulic infrastructure is necessary. The current hydraulic system of the Valley of Mexico is composed by several channels, lakes and lagoons and the *Sistema de Drenaje Profundo* (SDP) (see Figure 6-13; CONAGUA 2009). The main objective of this system is to reduce the risk of flooding that affect directly the population and their goods.

The *SDP*, operating since 1975, is one of the most important drainage systems of Mexico City. It collects waste and storm waters of the City and other urban centres and transports them to the Hidalgo State by using profound channels (CONAGUA 2009).

Despite the efforts to improve the original drainage system of the Valley, the continuous regional subsidence, the differential deformation, the urban sprawl and abnormal periods of heavy rain, make it incapable to accomplish its objectives. The Gran Canal del Desagüe, part of the *SDP*, represents a well-known example of this situation. In 1915 its slope was 19 meters per kilometres while at the present is almost cero (Figure 6-14). Thus, the installation of water pumping stations to prevent the water from stagnation and to help its transportation to its final destination was required. Added to this, a failure in the Emisor Central may produce a catastrophic flood that can significantly affect the metropolitan area.

Because of the complications in the current hydraulic system, the construction of a new tunnel with a capacity to transport 315 m^3/s of water becomes indispensable. The *Tunel Emisor Oriente* with 62 km length is planned to cover the deficit of the drainage system by conducting the excess waste and pluvial water out of the Valley of Mexico, allowing, as well, the maintenance of the Gran Canal del Desagüe and reducing the risk of inundations, hence subsidence impact analysis on this structure is fundamental (see also Chapter 8). This system will work alternately with the *SDP* (CONAGUA 2012).

Discussion

Water related problems in the Valley of Mexico require the implementation of strategic measures to achieve an efficient water management and to mitigate the effects that stem from the irrational use of the water resources.

Ensure the water sustainability for the Valley of Mexico is a challenging task. The application of large-scale water projects such as planning and construction of a new drainage and wastewater system aimed to improve the water services, is ambitious and complex from the economic and the geologic point view. On the other hand, frequent problems such as broken water pipes produce important water leakages (35% of the distributed water; GDF et al. 2006), need first to be tackled more quickly and effectively. Moreover, a better control and registration of illegal wells is essential to improve the water management plan.

The *Secretaria del Medio Ambiente* (SMA) strongly recommends the responsible and rational use of fresh water and water reuse (e.g., collection and reuse of the water from the shower, correctly close taps, etc.). However, to make these pro-water measures succeed, the promotion and installation of a good water culture through educational programs should be first reinforced.

Besides, the protection of conservation and potential recharge areas by means of better urban planning needs to be considered among the water management actions. The superficial coverage of these areas by housing, concrete and asphalt has notably diminished the natural water infiltration towards the aquifers. Additional, water is more vulnerable to contamination and purification plants are necessary, adding extra costs to the hydraulic infrastructure.

The uncontrolled urbanization has also negatively impacted the natural flora and fauna of these regions. That is why an efficient water administration plan that includes the protection of preservation areas would also prevent the disappearance of local species.

The sizable volumes of water that are imported from the Cutzamala and Lerma Basins to supply the Mexico City demand, might partially solve the water scarcity problem. Nevertheless, this can result in overexploitation of the aquifers in those Basins leading to the lowering of water tables, settlement and water problems similar to those in the Valley of Mexico.

In conclusion, during the last years government and its local dependencies have made many efforts to improve the water supply and the drainage system, and have adopted some measures to protect the groundwater. Notwithstanding, some strategies already applied required further evaluation, and those proposed might need a better assessment before their implementation.

Chapter 7

Deformation study in southern Valley of Mexico by means of an open source MTI tool

The study of land subsidence in Valley of Mexico requires interdisciplinary research to monitor and understand its complex dynamics, as well as its associated hazards (e.g., soil fracturing and flooding). This is a regional phenomenon that evolves temporally and spatially; thus, surveying techniques that enable coverage in both dimensions (time and space) are particularly important. Consequently, the application of radar interferometric techniques results valuable.

Since the leap of this technique different algorithms to cope with the limitations of the conventional and D-InSAR mode have been developed. These methods involve the combination of multiple SAR images and their inversion to obtain the evolution of the phase delays through time. The PS (Ferretti et al. 2001) and the SBAS methods (Berardino et al. 2002) have notably improved the capacity of the original technique for measuring motion. Among these methods, StaMPS (Hooper 2008; Hooper et al. 2012; Hooper et al. 2007), represents powerful open source software for deformation applications because of its capability to identify pixels in low coherence areas and/or undergoing non-linear behaviour.

In this Chapter the capability of the StaMPS algorithm to measure the subsidence in the south of the Valley for the period 2002-2007 is evaluated, and its extension for selection of a suitable reference area for the time series inversion is explained. The temporal reference selection based on the analysis presented in Chapter 5 is applied and discussed. Moreover, a quantitative comparison with results from a previous and constrained SBAS analysis (López-Quiroz et al. 2009) over the same area is considered as part of the assessment, also evaluating the quality of the unwrapping. GPS (Cabral-Cano et al. 2008; Osmanoglu et al. 2010), PSI (Osmanoglu et al. 2010) and levelling information are also used in the appraisal. We stress that the assessment of the algorithm using existing and well-proven results is essential because the methodology for identification of fissure-prone areas depends on the correct estimation of the InSAR time series for their appropriate application.

Differently from other methods (e.g., Berardino et al. 2002; Lopez-Quiroz et al. 2009; Lauknes et al. 2011), StaMPS uses a priori full covariance matrix (i.e. observations are assumed to be correlated) constructed based on the noise information (see also Chapter 4 for details about inversion methods); however, the assumption that the weights are exactly known may not be proper. In addition, because the WLS method may be more sensible to outliers, the estimation of parameters can be negatively affected. Therefore, an analysis to evaluate how the ULS affect the results is also considered in this chapter. A WLS-SVD method for inversion of the phase ambiguities was also proposed and tested; notwithstanding, the results did not notably improve the quality of the outcomes as shown in section 7.5. In our subsidence study a presumable component from underground trash in decomposition is furthermore investigated in a particular garbage dump.

Among the hazards associated to the Mexico City land subsidence, soil fracturing represents one of the most destructive. In Section 7.6 a methodology that contributes to fault location and the understanding of its dynamic by exploiting the deformation time series is proposed. The method was applied to a particular area, El Peñon del Marqués, where subsidence and a sliding mechanism interact, but can be extended to other areas as well (see Chapter 8).

The chapter concludes with the extension and analysis of the time series for the period 2002-2010. Discrepancies with the period 2002-2007 are analysed considering the available records of pumping rates in certain areas.

7.1 Need of evaluation of a specific InSAR tool for measuring subsidence in the Valley of Mexico

Measuring and monitoring deformation by means of MTI techniques in Mexico City and areas with similar characteristics (great deformation gradients, large deformation, contrasting topography and loose of coherence due to changes in the scattering properties in the time) represent a challenge. Several InSAR, standard and multitemporal, algorithms have succeeded in the quantification of the subsidence in the south of the Valley (Yan et al. 2012; López-Quiroz et al. 2009; Osmanoglu et al. 2010; Chaussard et al. 2014). However, discrepancies in the subsidence magnitude have been observed in the results published until now that might arise from the application of different satellite data, period of study, unwrapping strategies, selection of the reference area, inversion methods and selection of parameters involved in the interferometric processing.

By comparing the standard InSAR results provided by Carnec et al. (2000), Strozzi and Wegmuller (1999), Strozzi et al. (2003) and Cabral-Cano et al. (2008), notable differences have been observed. These variations may be due to different SAR data, period of analysis, procedures used for coping with atmospheric delays, orbitals corrections, and the use of an imprecise DEM, which in turn might introduce significant inaccuracies in the subsidence rate estimation. MTI approaches applied over Mexico City have partially solved the limitations of the conventional method, producing more accurate results. Nevertheless, in the MTI results given by López-Quiroz et al. (2009), Osmanoglu et al. (2010), Yan et al. (2012) and Chaussard et al. (2014) discrepancies are noted as well. Furthermore, some of these MTI algorithms may fail to detect PS in some deforming areas (Lopez-Quiroz 2012), where the correlation is low, hence leading to loss of important information. Accordingly, the following questions propped out:

- Would an alternative algorithm such as StaMPS, applied for the first time in the proposed study area, be capable to produce same/similar results to the existing ones? What are the main sources of discrepancies?

- Could StaMPS detect points over non-coherent areas in the Valley of Mexico where other algorithms may fail?

- What can the flexibility of StaMPS to detect points undergoing non-steady deformation used for? What could this information unveil?

These issues and the known capabilities of StaMPS, motivated me to use it as the processing tool for this work, exploiting particularly the SBAS module to study subsidence and associated ground failures in the entire Valley of Mexico. The questions exposed above are developed throughout this and the following chapters. The evaluation of the proposed algorithm is performed by comparison with the constrained SBAS method developed by López-Quiroz et al. (2009). Same stack of ENVISAT data was used to avoid discrepancies due to different periods of analysis, focusing on the unwrapping, filtering and inversion methods; the source of differences are analysed in detail.

7.2 SAR data and InSAR processing

Thirty eight ENVISAT scenes operating in C-Band (wavelength 5.6 cm; frequency 5.3 GHz; Image mode IS2; VV polarization; descending orbits) were acquired for Mexico City. These images span the time interval between November 2002 and March 2007. A study area of about 60 x 60 km was selected from each SAR image (see Figure 7-1).

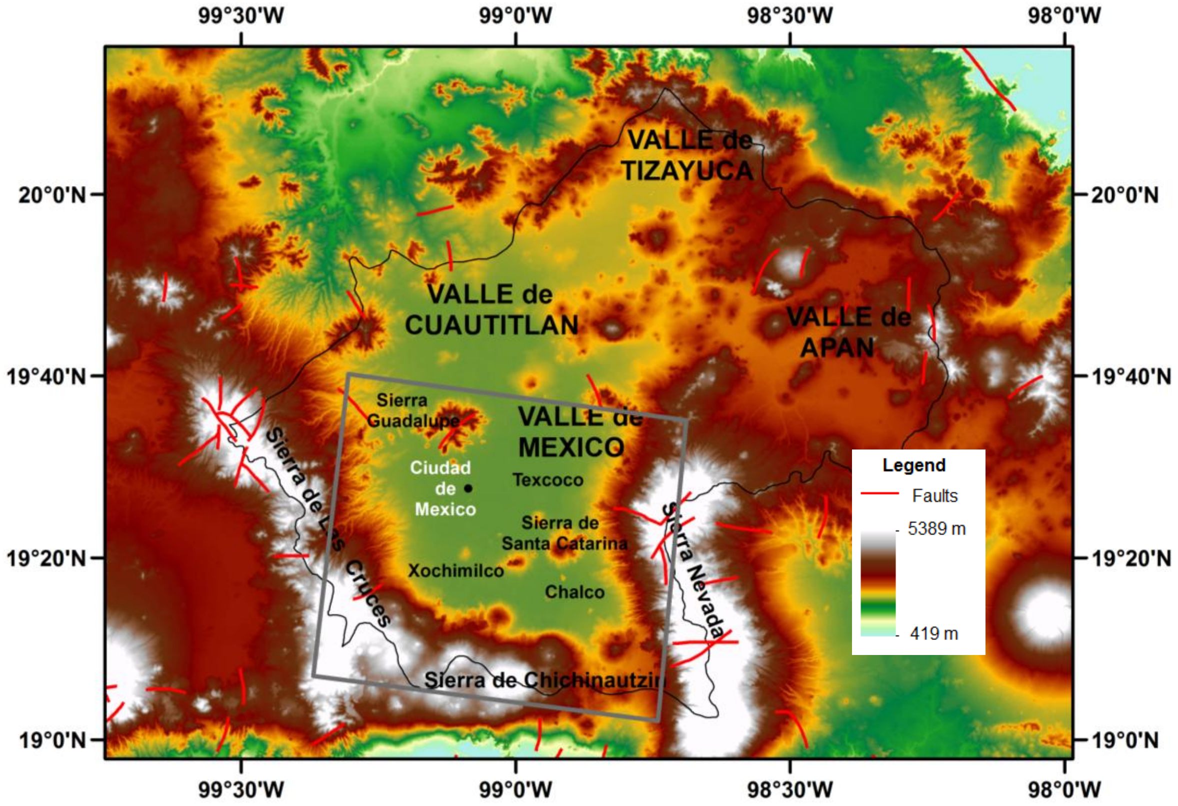

Figure 7-1 Location and topography of the Mexico Basin. The black line indicates the limits of Basin and the grey box the SBAS study area. Main fault systems (INEGI) are denoted by the red lines. Valleys, mountainous ranges, as well as approximate location of the lakes Texcoco, Chalco and Xochimilco are also represented. The elevation was derived from SRTM data.

To reduce the decorrelation between interferograms, initially we limited our analysis to pairs of images having temporal baselines lower than 350 days, perpendicular baselines smaller than 550 meters and coherence lower than 0.40. However, by using these parameters, some isolated clusters of images remained. To ensure that there was no missing connection in our network we decreased the minimum coherence value to 0.13. By using this criterion, 97 differential interferograms were constructed. However, noisy interferograms with larger perpendicular (> 400 meters) and temporal (> 300 days) baselines have negatively impacted the performance of the unwrapping. This and the inappropriate selection of the reference area led to results that were far from the expected values. Noisy interferograms were weeded from the processing and a new reference area was considered (see sections 5.5 and 7.3.2). Figures 7-2a and b show the perpendicular and temporal baselines of the selected SB interferograms, respectively.

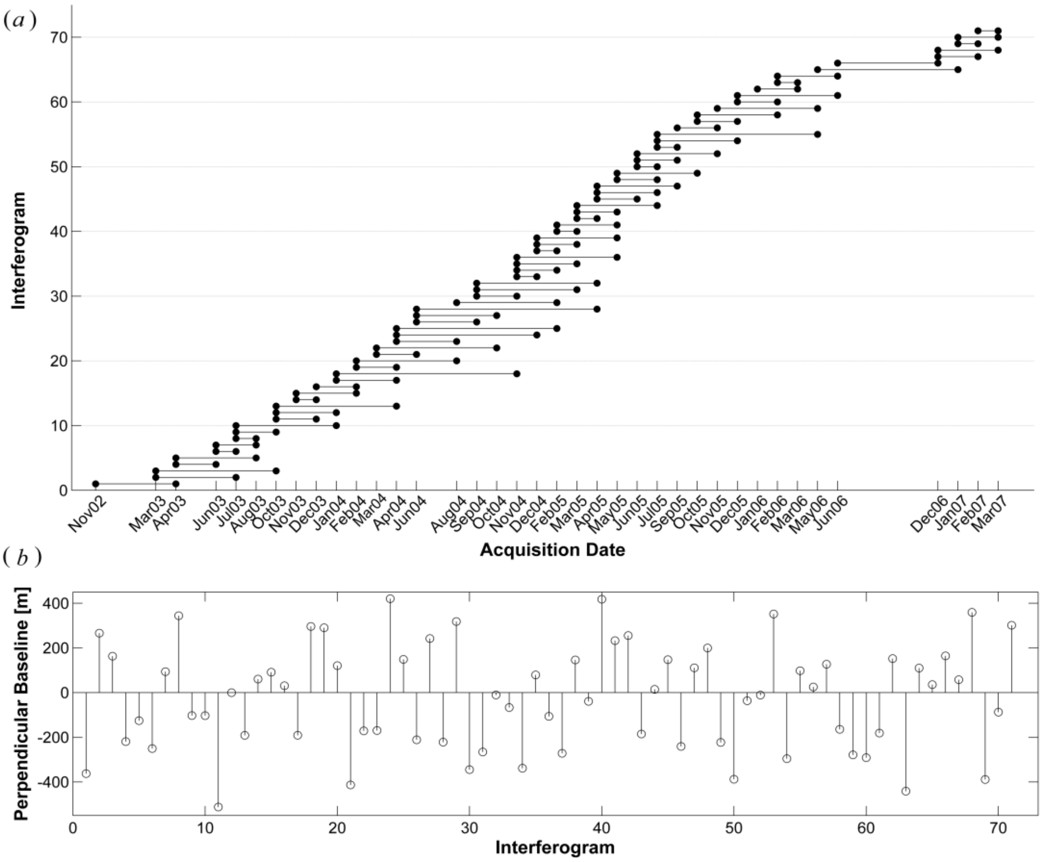

Figure 7-2 a) Temporal Baselines. b) Perpendicular baselines.

The ROI_PAC software (Rosen et al. 2004) was used for focusing the raw data (see Chapter 2) and the interferogram formation was carried out by the DORIS software (Kampes et al. (2003); see Chapter 3).

The following steps were performed in the interferometric processing (based on the preliminary concepts given in Chapter 3 and Chapter 5):

•**Coregistration**: All Single Look Complex (SLC) radar scenes were first coregistered to one “master” image. The image acquired on December 31, 2004 was selected as the master based on an error propagation analysis (see section 5.5). SLCs with baselines lower than 150 m were directly coregisterd to the master and those with larger baselines to the 4 closest images with smaller baseline. The fine coregistration was performed by using the oversample method, with an oversampling factor of 32 and a 64 by 64 window size. Cross correlations with coherence higher than 0.29 were initially selected.

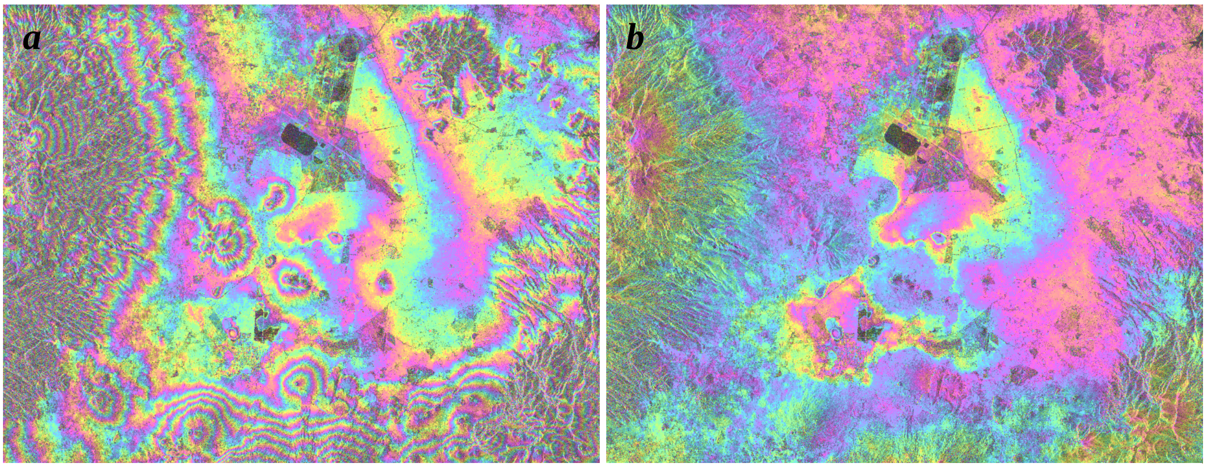

Figure 7-3 a) Example of interferogram affected by notable topographic effects. b) Same interferogram after topographic correction.

•**Resampling:** Once the alignment offsets had been estimated, the slaves were interpolated on the grid of the master using a 12 point raised cosine kernel.

•**Interferogram**: After resampling the pairs of images referenced to the coordinate system of the 31 December 2004 acquisition, interferograms were computed. We highlight that because no multi-looking was applied to the interferograms, the SNR was not improve, enabling, however, the identification of highly coherent pixels over time that may contain important information about the deformation.

•**Correction of Orbital Effects:** Orbital effects were diminished by using precise orbits from the Delft Institute for Earth-Oriented Space Research (DEOS) (Scharroo *et al.* 1998). The flat earth correction was carried out by modelling the reference phase for the full scene using a polynomial of degree 3. Precise orbits were used for estimation of the parallel baseline.

•**Topographic correction:** Subtraction of topographic fringes from each interferogram was performed using the 3-arc second SRTM DEM, version 4 (Farr et al. 2007) (see Figure 7-3).

•**Filtering:** Azimuth and range filtering was applied to further reduce the geometric decorrelation affecting the differential interferograms. The non-linear adaptive spatial filtering developed by Goldstein and Werner (1998) was used to increase the SNR. A 128 by 128 window size and a coherence-dependent filtering parameter a =0.2 were employed. By using these values the phase noise was smoothed without falling into an aggressive filtering. Because the SB interferograms were selected in order to reduce decorrelation, they presented in general a good coherence, as seen can be seen in Figure 7-4.

The deformation component of the signal was evaluated in the LOS direction. However, a 3D interpretation of the deformation field vector can be carried out by combining InSAR results and information coming from Global Navegation Satellite System (GNSS) measurements. Earlier works (Cabral-Cano et al. 2008; López-Quiroz et al. 2009; Osmanoglu et al. 2010 ; Yan et al. 2012 ; Chaussard et al. 2014) stated that the vertical component of the displacement plays the main role in Mexico City. Thus, the mean LOS velocities (v_{LOS}) can be converted into vertical subsidence v_V using the following expression $v_V = v_{LOS} / \cos\theta$, where θ represents the look angle (see Chapter 1).

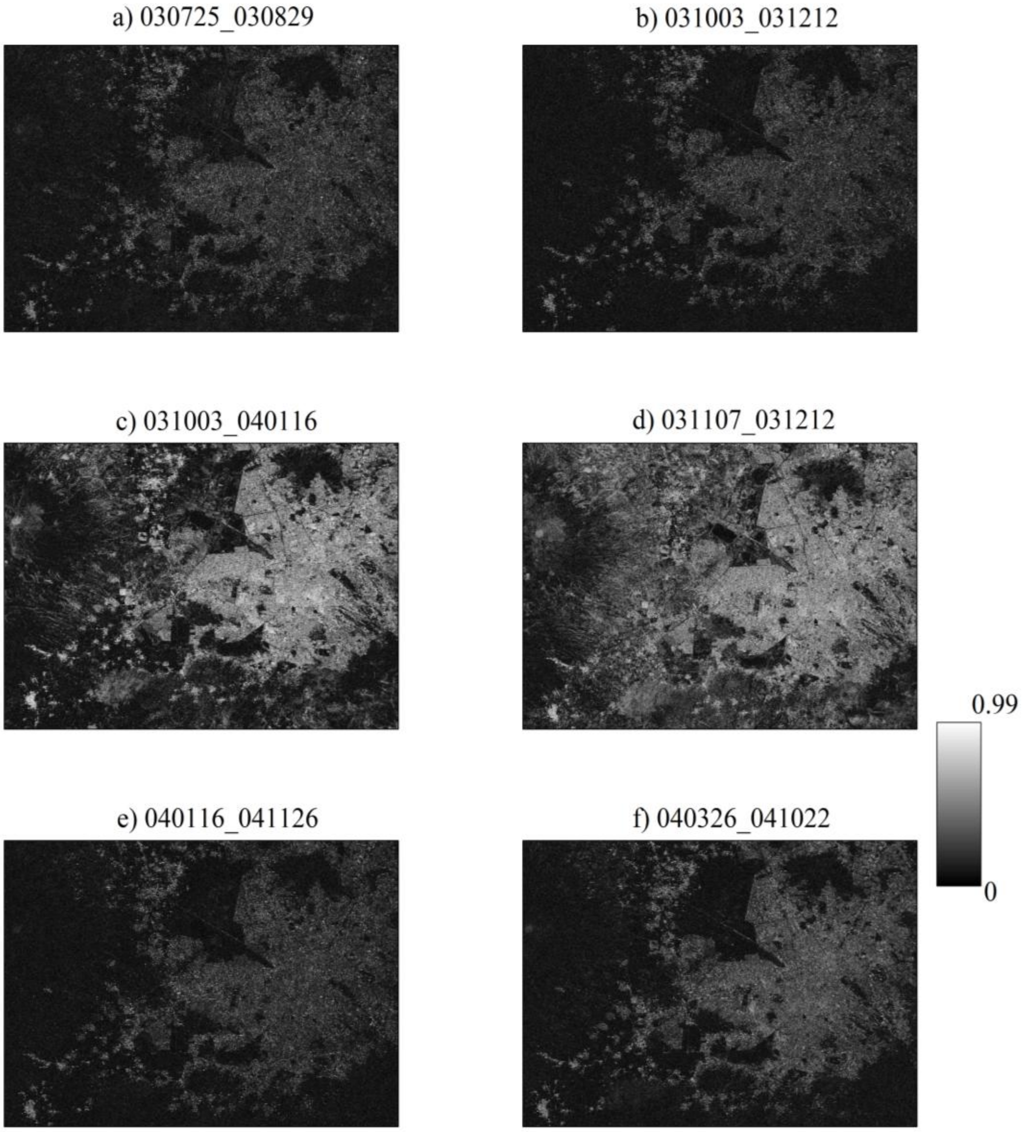

Figure 7-4 Coherence maps for different interferograms. Interferograms with larger perpendicular baselines (e.g., b: 512 m) present a lower coherence while those with shorter perpendicular baseline (e.g., c: 0.3 m) a better correlation. Interferograms spanning the wet season, albeit their relatively short temporal baseline, present less correlation (e.g., f: 105 days; 171 m). Probable in these cases the atmospheric artefacts increase the decorrelation. The length of the perpendicular baseline must also be taken into account (e.g. a: 35 days; 344 m). Note that interferograms with larger perpendicular and temporal baselines are critically affected by decorrelation (e.g., e: 315 days, 296 m). On the other hand, those spanning the dry season, with short temporal and perpendicular baselines present a good quality in the sense of coherence (e.g., d: 35 days, 61 m).

7.2.1 Justification of the master selection

Before the SB interferograms are formed, they need to be coregistered to a common master. We seek a reference acquisition that minimizes the sum of decorrelation from different sources (see also section 3.3.4). Usually, the acquisition that reduces the temporal decorrelation and that corresponds to the middle of the period of study is considered as a first criterion. Nevertheless, reduction of the Doppler and spatial baselines need also to be analysed. Here, the processing was performed for three different reference dates and the master image was selected based on an error propagation analysis (see also Chapter 5).

Thinking about geodetic networks, the error propagation was observed to occur similarly to an open traverse, where the azimuth must be measured at a certain position such that the error propagation is optimized, i.e. minimum position error in the last (or first) point of a network. For analysing how the errors propagate when using different temporal references, we considered the covariance matrix of the estimated parameters (i.e. cumulated phase delays) computed as

$$\Sigma_{\phi} = \left(\mathbf{G}\,\Sigma_{\varsigma}\,\mathbf{G}\right)^{-1}, \tag{7.1}$$

where **G** is the design matrix and Σ_{ζ} is the covariance matrix of the SB interferograms, which is estimated from the phase noise information.

Figure 7-5 shows the propagation of uncertainties for three reference times:

a) November 22, 2002
b) December 31, 2004.
c) March 17, 2007.

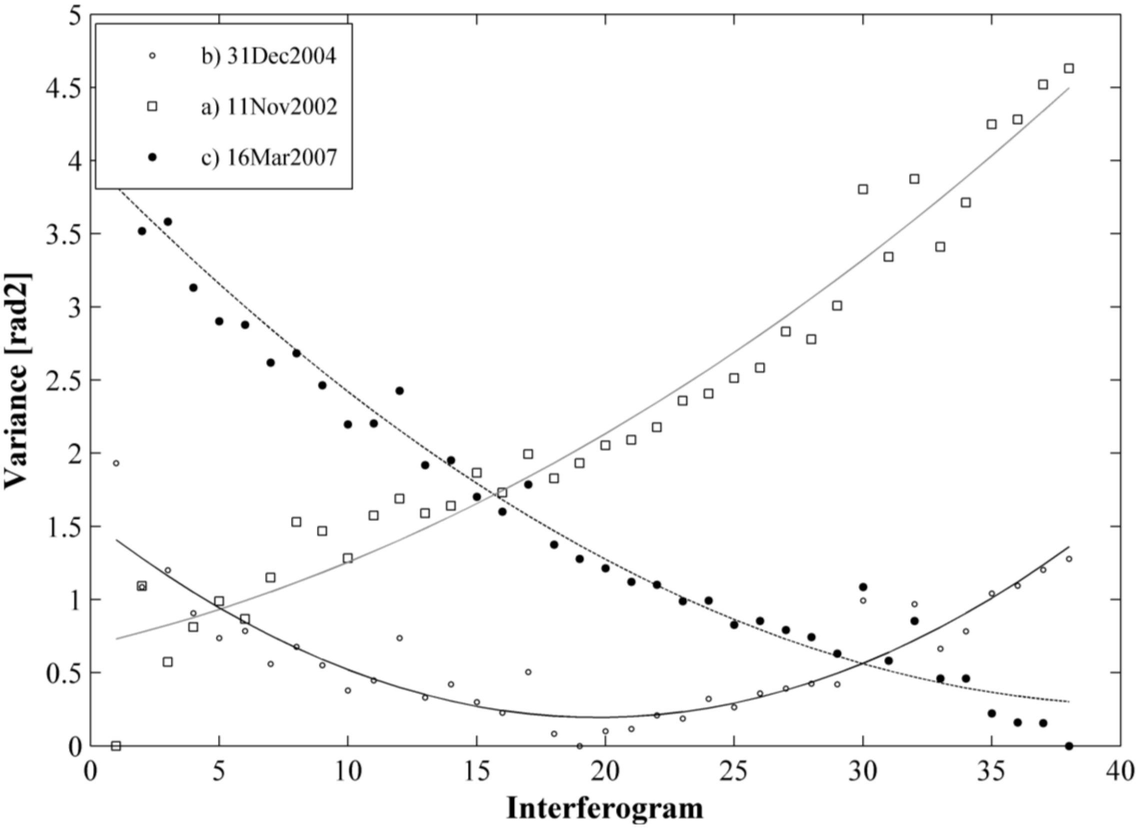

Figure 7-5 Error propagation by using three reference times: a) November 22, 2002, b) December 31, 2004 and c) March 16, 2007. The data were fitted with a quadratic function denoted by full black, dashed and grey lines, for cases a), b) and c), respectively.

Note that the error propagation for the three cases is fitted with a quadratic polynomial. The variance increases quadratically with the time from the first acquisition in (a), while in the third case (c), it decreases towards the March 2007 reference. A maximum error of 4.7 rad^2 was found in both cases, corresponding to the last and first acquisition dates, respectively.

In the present analysis, the variances for each mean incremental phase σ_{ϕ} are, in general, smaller when selecting the image from December 2004 as the reference compared to the values obtained when processing with the November 2002 or the March 2007 acquisitions (maximum variance ~1.3 rad; see Figure 7-5). Consequently, the present analysis suggests that by selecting the 31 December 2004 image, approximately corresponding to the middle of the study period, the magnitude of the variances in the interferometric system are reduced i.e. a more precise estimation of the cumulated phase delays is achieved (see also Chapter 5).

7.2.2 Small Baseline processing

The SBAS method of StaMPS was described in detail in Chapter 5. In this section important parameters used in the current SBAS processing are given and discussed.

Pixel Selection: the initial selection of candidate pixels is based on the amplitude difference dispersion index $D_{\Delta A}$ (Hooper 2008). Due to large data size, we divided the test area into 20 patches, first selecting pixels with $D_{\Delta A}$ higher than 0.58. In our case, the usage of a greater value conduced to computational issues related to memory limitations. Even though, the division of the area into more patches is possible, this may affect the unwrapping processing at the edges of neighbouring patches. Lower values of $D_{\Delta A}$ prevent from the selection of pixels in some areas of interest (e.g., areas experiencing non-steady deformation). Thus, this parameter was selected so that SDFP pixels over areas of particular interest were included in the processing, but attempting to avoid memory limitations as well.
Once the amplitude-based selection was performed, SDFP pixels with noise standard deviation lower than 0.80 were finally considered for further processing. For the estimation of the uncorrelated part of the look angle error, an initial maximum DEM error of 8 m was used (see also Chapter 5).

Tuned of parameters (unwrapping and filtering windows): StaMPS was run using different parameters before selecting those that gave optimum results, which were assessed by comparing with the previous SBAS subsidence field presented by López-Quiroz et al. (2009), whose results are in good agreement with GPS measurements (Cabral-Cano et al. 2008). After several tests, unwrapping windows of 190 days and 90 m in time and space, respectively, were selected, and the spatially correlated noise (atmosphere and orbits) was filtered using a 250 days-window.

Spatially-correlated look angle error (SCLA): Interferograms with larger perpendicular baseline tend to be more affected by topographic errors (Hanssen 2003). Although residuals of the topographic phase are estimated and subtracted during the SBAS processing, they may remain in the phase of some interferograms (particularly those with large $B_{\perp}$) biasing the final time series and conducing to misinterpretation of results. A preliminary inspection of the interferograms with larger perpendicular baselines indicated that some of them presented a component that apparently correlated with the baseline length. These interferograms were weeded from the estimation and correction of the SCLA.

7.3 Results

7.3.1 Global SBAS results for the 2002-2007 period

More than 64000 SDFPs were identified for the studied surface with a mean point density of 21 SDFPpixel/km^2. The density of the SDFP pixels decreases in vegetated areas and in places where there is a notable decorrelation due to changes in the scattering mechanisms. These changes were caused by the transition of some areas from rural to urban or the presence of flooding during the study period.

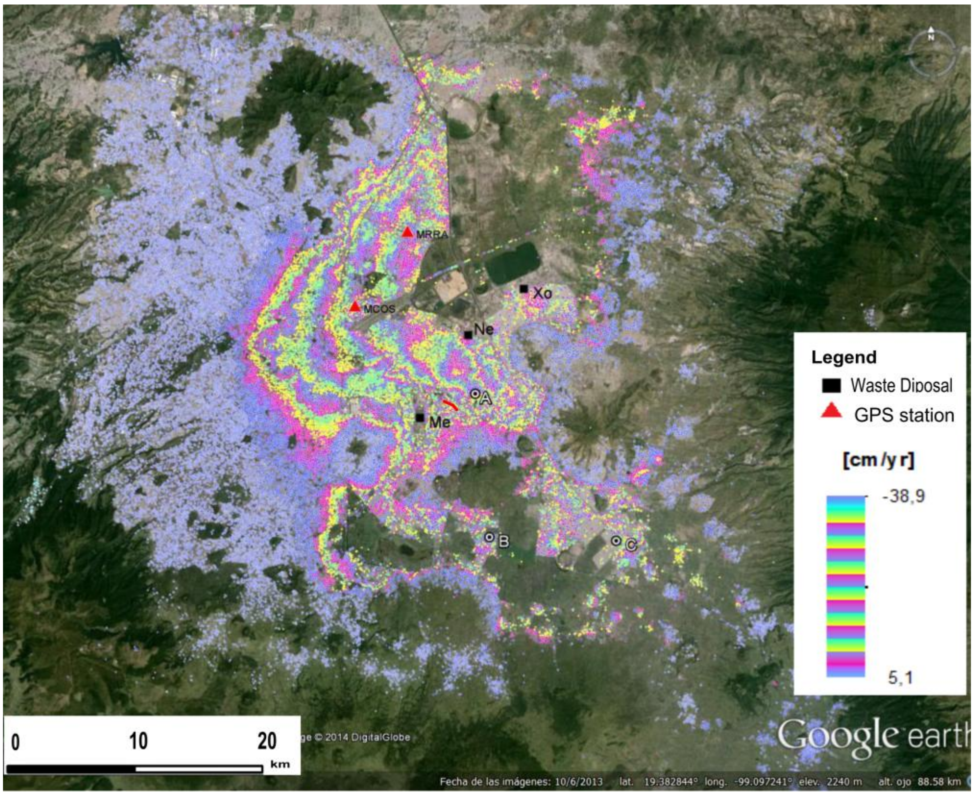

Figure 7-6 Average subsidence deformation rates in Mexico City for the period 2002-2007 obtained by means of the adjusted StaMPS SBAS approach. The subsidence map is overlaid on Google Earth imagery. The black rectangular symbols indicate the deposal sites coinciding with areas affected by large subsidence rates (Me: Meyehualco, Ne:Neza II, Xo: Tlatel Xochitenco). Time series for selected SDFP pixels (A, B, C) are shown in Figure 7-7. GPS stations are denoted by black triangles.

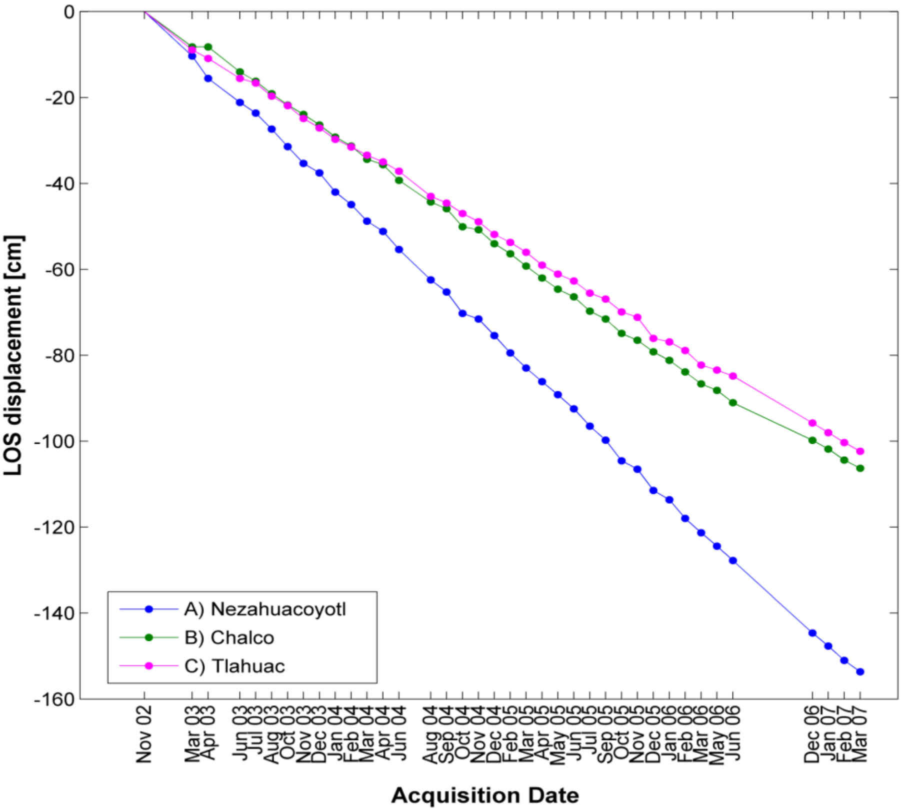

Figure 7-7 Time series measured at points located in high subsiding areas: Nezahualcóyotl (blue), Tláhuac (rose) and Chalco (green).

Figure 7-6 shows the average subsidence deformation map for the period 2002-2007 overlaid on Google Earth imagery. Time series for sectors with higher deformation rates

(Nezahualcóyotl, Chalco and Tláhuac) are depicted in Figure 7-7. They were rescaled to the first acquisition date (i.e. November 22, 2002), although the master database was the image acquired on December 2004. We observe almost linear temporal behaviour of the displacement; however, as reported by other MTI studies (e.g., López-Quiroz et al. 2009, Yan et al. 2012), there are areas experiencing non-linear deformation some of which coincide with regions affected by differential subsidence.

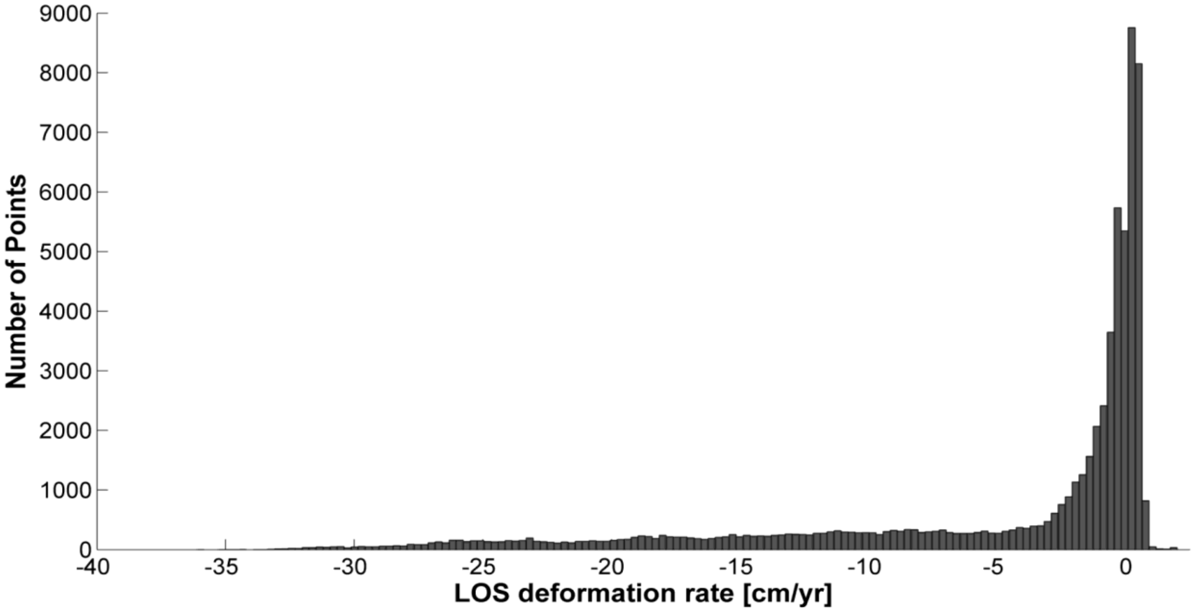

Figure 7-8 ENVISAT histograms of the measured SDFPs subsidence rates in LOS direction.

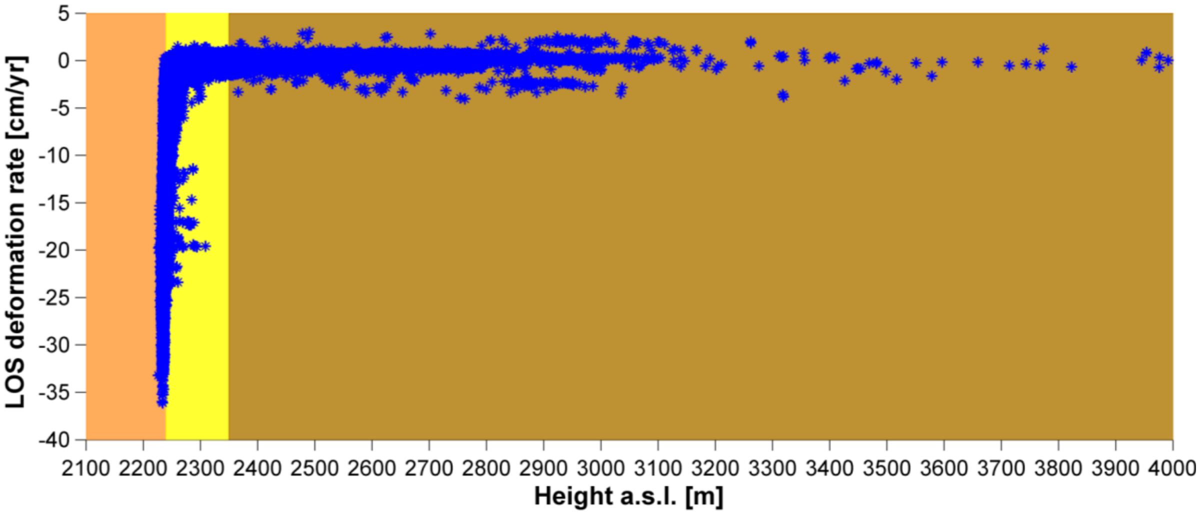

Figure 7-9 Comparison of the LOS deformation rates with the elevation for each SDFP. The different colours correspond to the three main geological units (GDF 2004). From left to right: Lacustrine deposits (Orange), Transitional deposits (Yellow) and Footfills (Brown).

The histogram in Figure 7-8 shows the distribution of the deformation rates. 70% of the samples correspond to negative values and the remaining 30% belong to positive values, confirming a prevailing sinking in the area. In general, two groups of points with different behaviour can be distinguished. The first group is constituted by points that are subsiding and which coincide with the lacustrine and transition areas, while the second corresponds to the stable-phase points located on the lower part of the volcano flanks surrounding the city. This can also be observed in Figure 7-9, which shows the velocity rates versus the height, and the limits of the three main geological units of the region (Gobierno del Distrito Federal 2004). Note that, in general, all the points corresponding to the lacustrine and the transition units have the largest deformation velocities. Points located in higher sectors exhibit in general no displacement and coincide with the expected non-deforming area. This also agrees with the results of levelling surveys (Lesser and Cortéz 1998). On the other hand, points in elevated regions “moving” towards the satellite could indicate uplifting due to groundwater recharge or suggest that the far field velocities need to be better determined (López-Quiroz et al. 2009).

7.3.2 *Analysis and justification of the reference area selection*

To estimate the unknown phase increments ϕ, the unwrapped phases of the SB interferograms must be adjusted relative to an area where no deformation is expected before the interferometric system (5.17) is inverted (see Chapter 5). According to the geological information (see Chapter 6) and to a preliminary deformation analysis on the area, the mountainous region (> 2250 m.a.s.l.) surrounding the lacustrine unit can be considered to be approximately stable. Figure 7-10 depicts the mean LOS velocities versus the height of the SDFP pixels considering different elevation ranges. Most of the deformation, as expected, occurs in the lacustrine area decreasing, in general, with the increasing elevation (see Figure 7-10a).

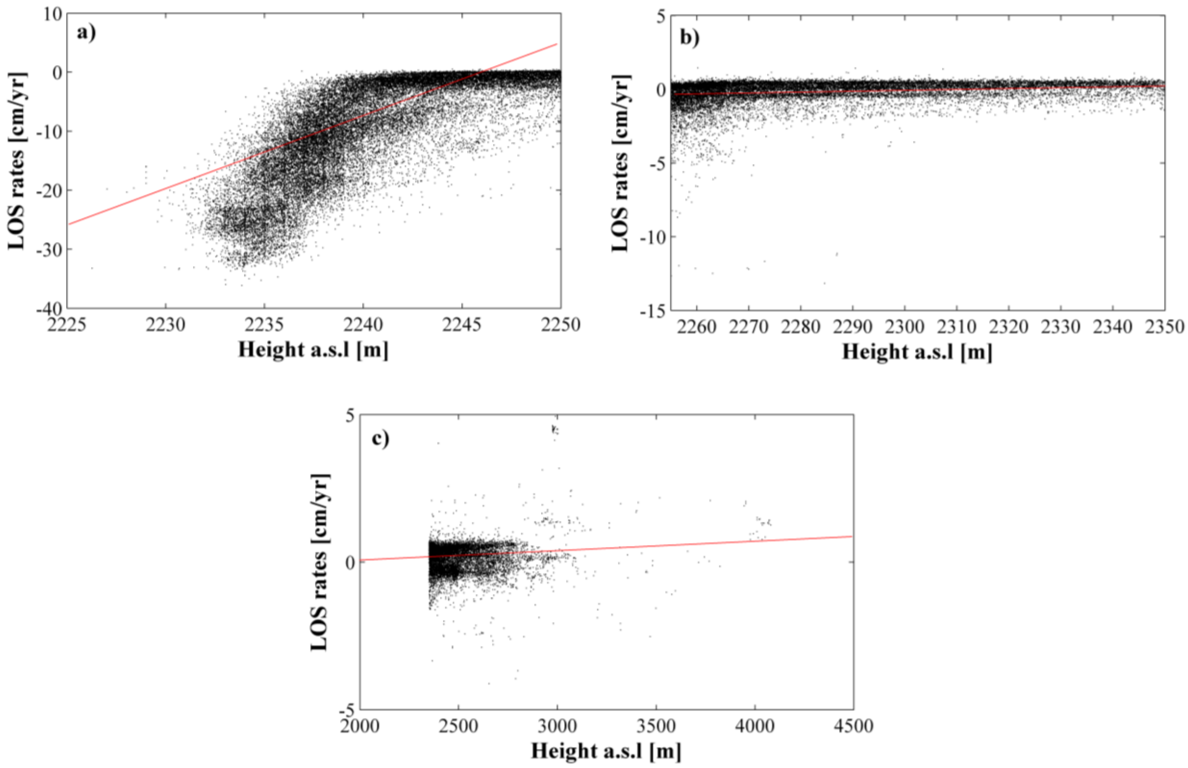

Figure 7-10 LOS displacement versus elevation: a) < 2250 m (mainly compressible deposits) b) > 2250 m and < 2350 m (mainly alluvial deposits) and c) > 2250 m (primarily incompressible deposits).

Overall, points more than 2250 m high experience no deformation (see Figure 7-10b and c), except for some located in alluvial deposits and where there is a large concentration of extraction wells (see Figure 6-1). SDFP pixels located at higher elevations (> ~2350 m; see

Figure 7-10c) might be affected by important atmospheric delays that could bias the final deformation time series. However, most of the points above 2250 meters elevation present almost no displacement, thus the average reference phase is approximately zero. One must take into account that atmospheric and other noise contributions that mask the signal of interest (i.e. deformation) are filtered after the estimation of the phase delays time series. Because undesirable signal from the reference phase propagates and affect the quality of the results, the selection of a suitable spatial reference before the inversion of the unwrapped phase delays is paramount.

Because StaMPS limits the selection of the reference area to rectangular and circular patches, the algorithm was extended to approximately include as the spatial reference the *Lomas* unit surrounding the silty-clay lacustrine plain (see also Chapter 6). Figure 7-11 shows the location of the pixels over the non-deforming region selected by the adapted algorithm. We observe that the selected reference pixels mainly coincide with the hard rock unit of basaltic and vulcanite composition where no deformation is expected.

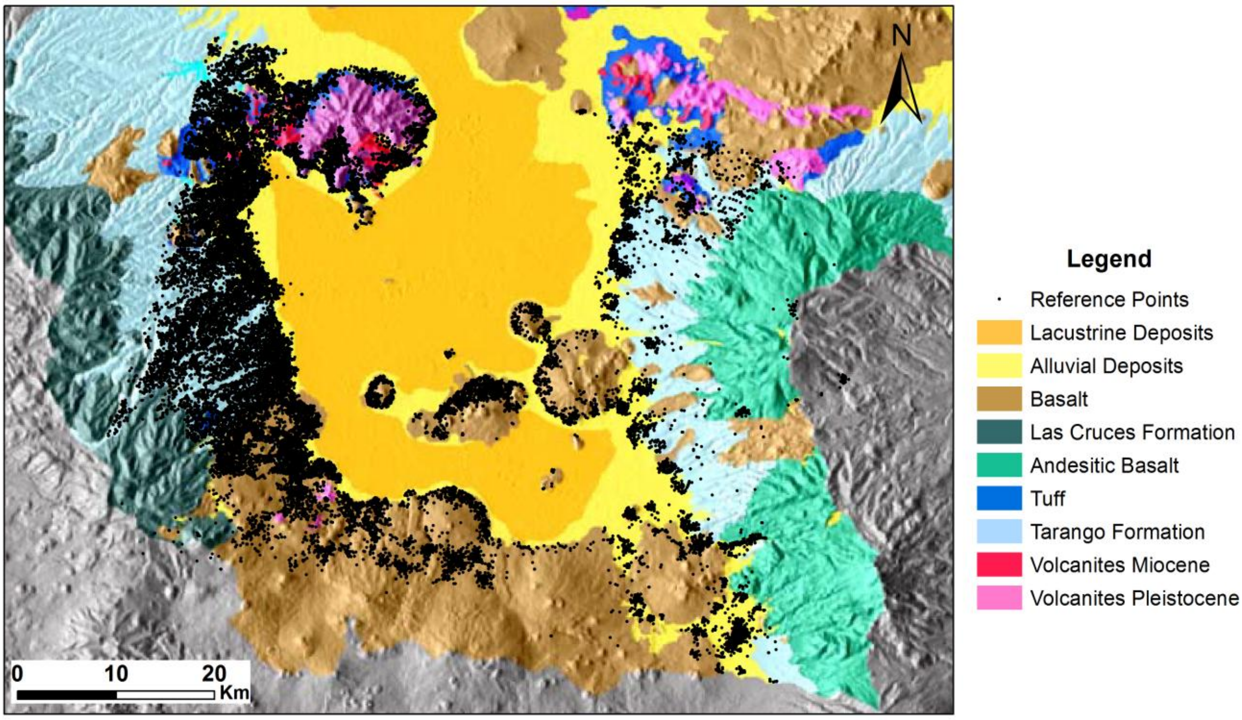

Figure 7-11 Main hydrogeological units and SRTM elevation adapted from Carrera-Hernandez and Gaskin (2007). 1) Alluvial sediments or aquifer layer (Yellow). 2) Lacustrine sediments or aquitard layer (Orange) partially covering the aquifer. 3) Basalt and vulcanites (Brown and other colours). The black dots indicate the location of the selected reference points after adjusting the StaMPS algorithm.

In order to evaluate how the reference area influences the final results, we compared the deformation maps using as reference:

a) average of all the points (default selection)
b) based on the geological information

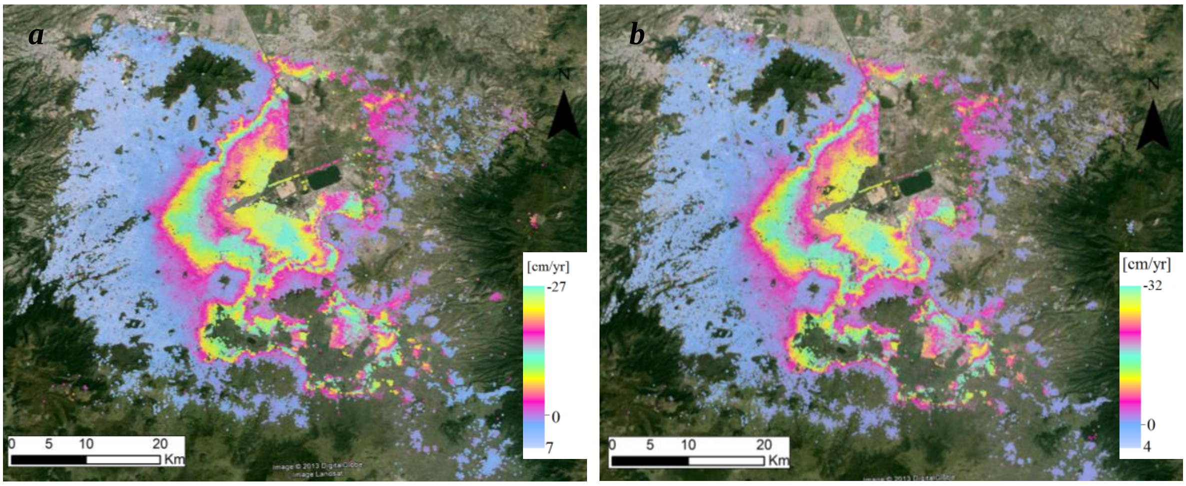

Figure 7-12 LOS displacement maps using two spatial references: a) entire area, and b) based on geological information.

Figures 7-12*a* and *b* show the results using different reference areas. Note that the average deformation rates in case *a* are lower than in *b*. This occurs because the relative veolcities in *a* refer to the entire area of study (i.e. mean velocities calculated using all SDFP pixels) including both non-deforming and deforming points. LOS velocities in Figure 7-12*a* ranging from 7 to 27 cm/yr suggest that in the computation of the mean reference phase, the number of subsiding points prevails over those experiencing no motion or a relative uplifting. On the other hand, LOS displacement rates in Figure 7-12*b*, estimated relative to the expected non-deforming areas (see Figure 7-11), shows results comparable to previous publications (e.g., Cabral-Cano et al. 2008; López-Quiroz et al. 2009; Yan et al. 2012. The current analysis indicates that StaMPS requires not only a temporal (see section 5.5 and 7.2.1) but also an appropriate spatial reference for the time series inversion. This has also been stated by Sousa et al. (2011).

7.3.3 Analysis of deformation in trash deposal areas

Some of the areas affected by high subsidence rates coincide with the location of former waste deposals. In these cases, the compaction and decomposition of the buried trash could have contributed to the subsidence observed in the ground surface. The process of compaction and decomposition of the solid waste is usually gradual, over a period of several years but may appear overnight (Kolh 2001). This could have produced the apparition of ground ruptures that have affected some areas where deposal sites were located.

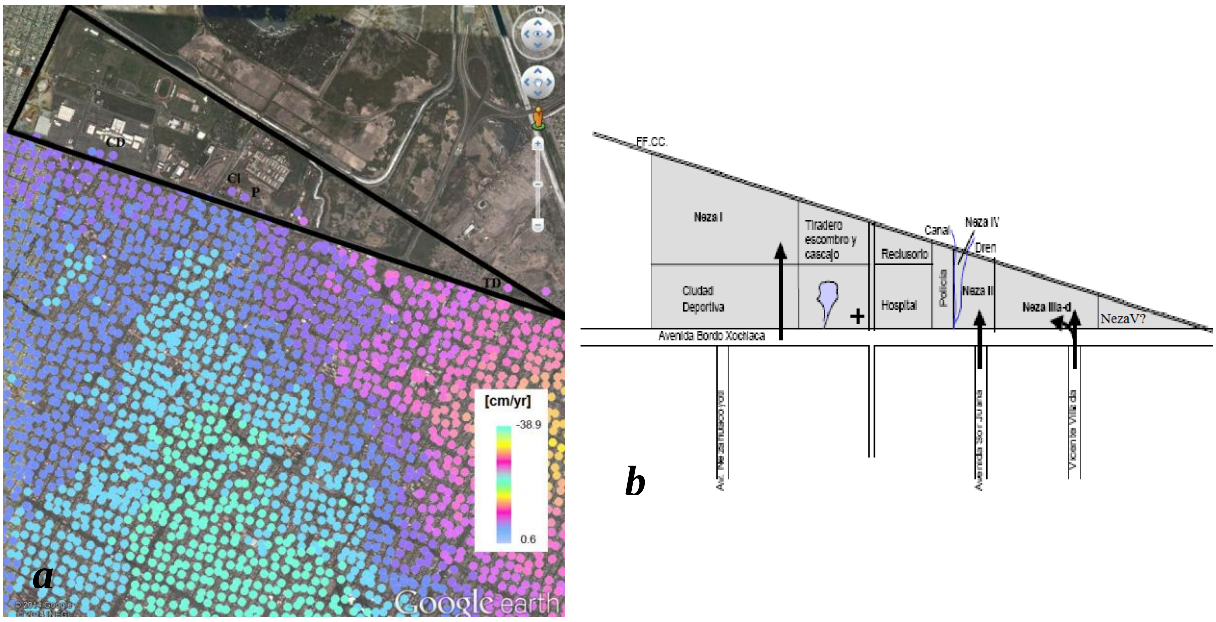

Figure 7-13 *a*) Zoom on the SBAS LOS map over the former disposal site Bordo Xochiaca indicated by the black triangle. Time series for selected SDFPs (CD: Ciudad Deportiva, Cl: Clinica, P: Police Station and TD: Trash Deposal Neza V) are shown in Figure 7-14.*b*) Bordo Xochiaca Triangle (modified from Gonzales Taobada 2008). This area is constituted by the following deposal sites: Neza I (transformed into landfill in 1999), Neza II, Neza III and Neza IV (illegal). Within the Neza III, four sub deposal sites from which one is illegal (Neza IIId) can be found. A fifth illegal dump (NezaV?), which is not recognized by the local government, is also part of the Bordo Xochiaca Triangle.

Particularly, the former trash dump Bordo Xochiaca in Nezahuacóyotl (see Figure 7-6 and Figure 7-13*a*) requires a continuous monitoring due the presence of important civil infrastructure that have been constructed on it (a church, a hospital, a police station and a sport centre). This deposal site is constituted by several units (see Figure 7-13*b*). The unit Neza I, has existed for more than 30 years, receiving around 1500 ton/day of garbage. In 1999, the local government decided to transform it into a landfill area. Advanced sanitation techniques and engineering methods were used for that purpose (Gonzales Taobada 2008). Moreover, ventilators were installed to enable the freedom of biogas (especially methane). Even though this section of the Bordo has been re-modelled, the remaining sites did not receive the same treatment. The yet existing disposals, either legal or illegal, have not been studied in detailed and apparently there are not concrete plans for reducing the effects of these hazardous areas that also affect the surrounding communities. Quick and efficient measures need to be taken since several explosions have already been reported for these areas, such as for example the 2010 crack that affected around 400 homes located in the proximity of this disposal site. This situation also endangers the groundwater quality due to percolation of pollutants through existing and possible new fractures in the area.

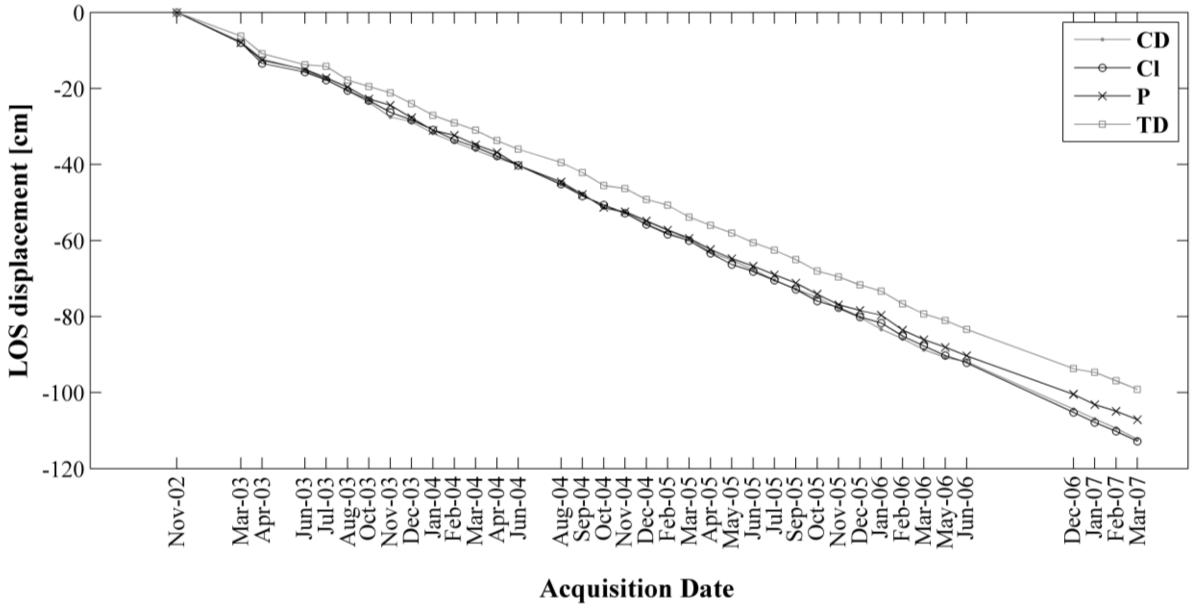

Figure 7-14 LOS displacements of selected SDFPs in Figure 7-13*a*. CD, Cl and P correspond to structures located on the former Bordo Xochiaca while TD is one of its remaining part that continue working as an illegal dump.

Figure 7-14 shows the time series of the SDFP pixels at the location of the civil infrastructures constructed on the former deposal site; most pixels experience important subsidence rates (~26 cm/yr). The time series indicate that structures located in the urbanized area of the former dump are undergoing a more rapid subsidence compared to the rates found in Neza V, a remaining illegal dump (see Figure 7-13*b*). Presumably, the weight of the buildings and the presence of the underneath buried trash in decomposition might conduce to a larger deformation. The spatial variation of clays thickness could also explain the observed rates; however, the clay thickness map (e.g., Méndez et al. 2010; Burns (2009)) suggests homogeneous distribution over this area. Nonetheless, a finer clay thickness resampling on this area is required for a better interpretation.

Unfortunately, SAR satellite images after the explosions and generation of the reported fractures in the area were not available to perform a more detailed evaluation of the component that might come from the trash decomposition process and displacement, contributing to the observed subsidence rates in the area. Meaningful information from ongoing SAR satellite such as TerraSAR-X, RADARSAT-2, COSMO-SkyMed or Sentinel-1 can be exploited to unveil the influence of this new element not taken before into account in the Mexico subsidence studies. In-situ measurement techniques such as Ground Penetrating Radar (GPR) can complement the analysis.

Moreover, important accumulation of gas methane in this area can also be monitored by analysing atmospheric anomalies using various SAR sensors and/or modes. Studies focused on the recovery of the gas methane result useful because of its usage for energy production (Chynowetha et al. 2001). Moreover, they can contribute to the improvement of local air quality and development of efficient public health programs.

Investigation of former disposal site areas in the Valley of Mexico are relevant because artificial recharge by treated wastewater infiltration are planned near them (Mendoza Archundia 2012; Huizar Álvarez 2011), threatening even more the water quality and thus people's health (see also Chapter 6).

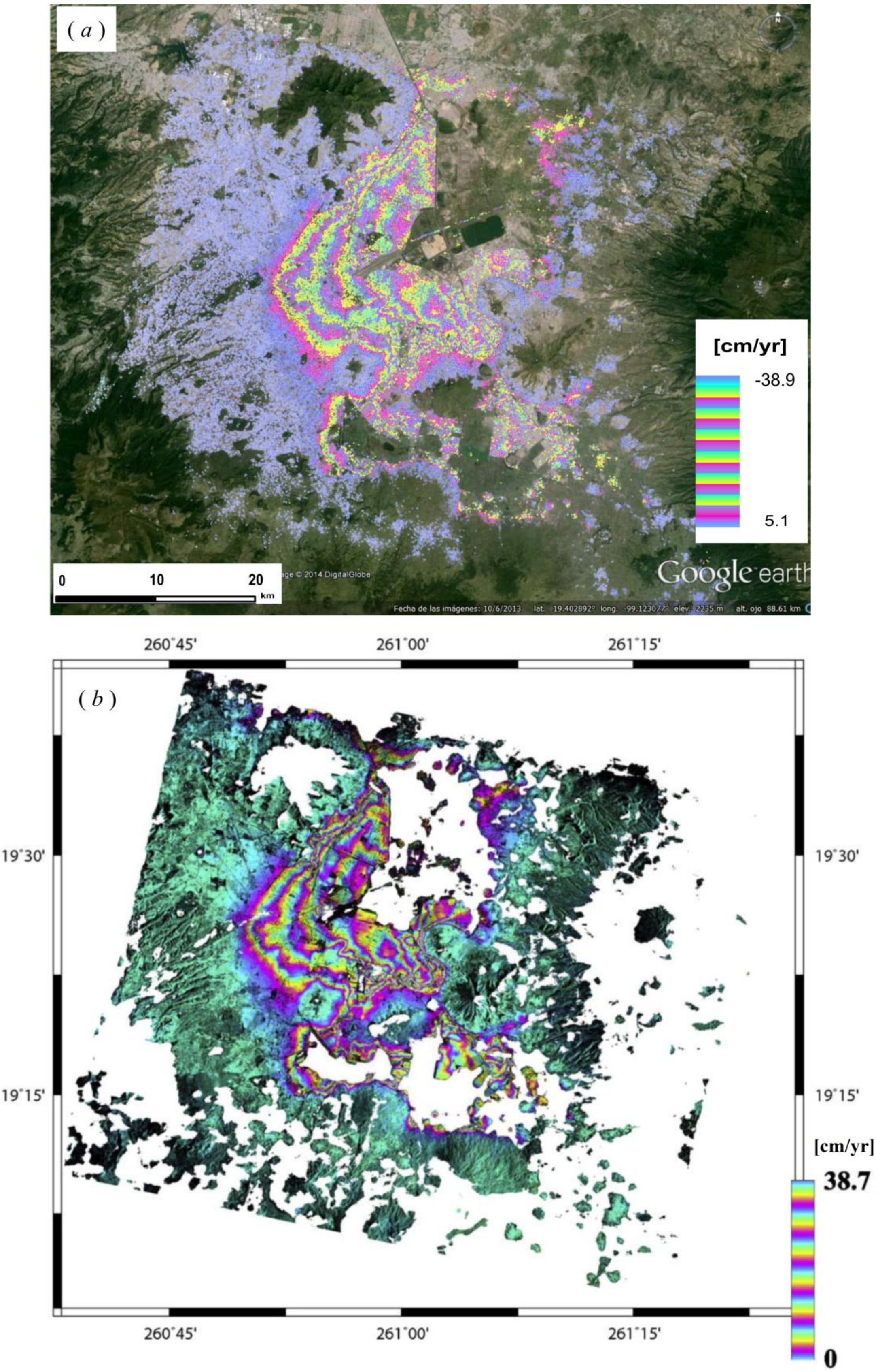

Figure 7-15 Average vertical subsidence rates for the period 2002-2007 from two SBAS approaches using similar colour scales:(*a*) StaMPS (this study), (*b*) López-Quiroz et al. (2009). The deformation patterns are quite comparable, even though there are some small discrepancies.

7.4 Algorithm assessment

This section aims to discuss the results obtained by the SBAS method from StaMPS. The values obtained have been compared with the results from a previous SBAS approach (López-Quiroz et al. 2009) and with existing GPS and PSI results on Mexico City. The present assessment is essential since the methodology for fracturing zonation presented in sections 7.6 and 8.3 is based on correct estimation of the InSAR time series. Levelling information for the 1994-2007 period is also considered in the appraisal of results.

7.4.1 Comparison with a previous SBAS approach

Figure 7-15*a* and *b* compares the subsidence rates from the current study, and the previous constraint SBAS analysis (López-Quiroz et al. 2009). The pattern and magnitude of the displacement are similar in both studies. However, some discrepancies occur due to the different master database, unwrapping methodologies and strategies for eliminating atmospheric effects, residual heights and other components that mask the deformation.

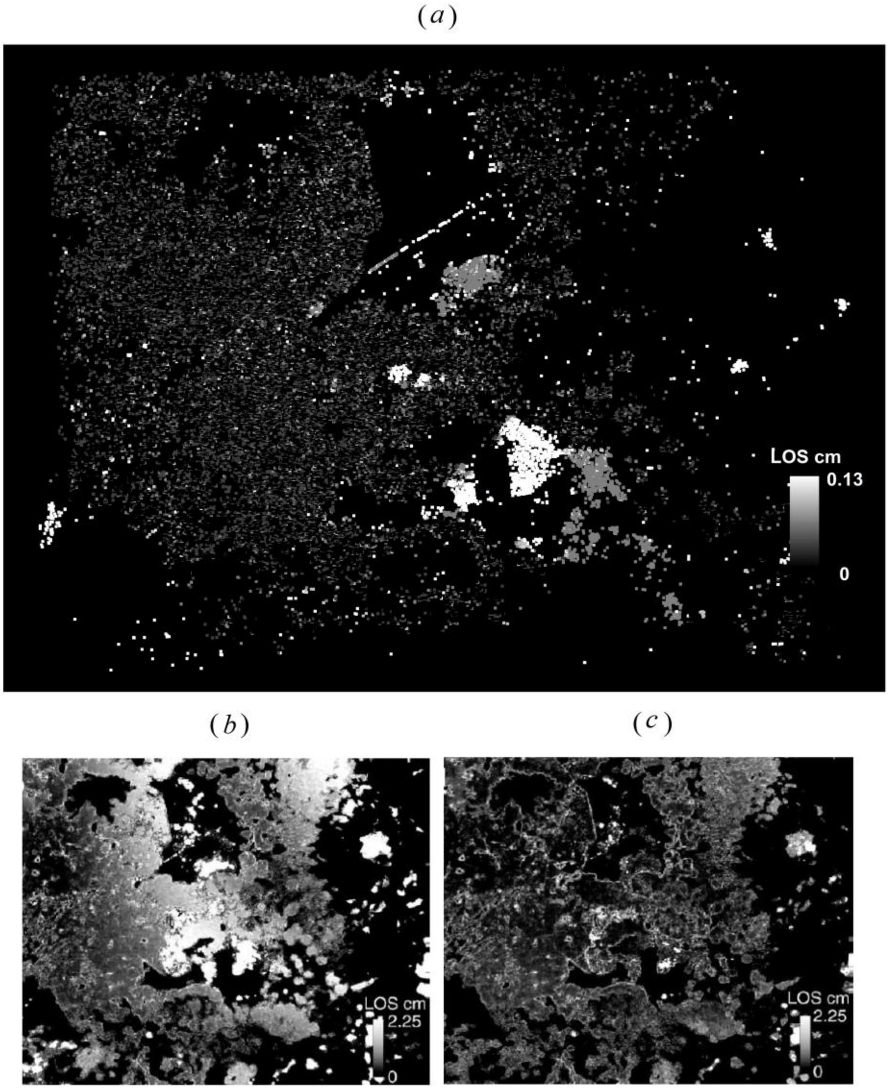

Figure 7-16 Map of the RMS between the observed unwrapped phase and the one reconstructed from the inversion system. (*a*) RMS for the SDFP pixels unwrapped with the 3D unwrapping method (Hooper 2010). In panels (*b*) and (*c*) RMS using the iterative unwrapping method developed by López-Quiroz et al. (2009), corresponding to the second and the third iteration, respectively.

Unwrapping

López-Quiroz et al. (2009) developed an iterative unwrapping method in the spatial domain to retrieve the unambiguous phase. Here, we applied a 3D unwrapping method (Hooper 2010) that profits from time information (see also section 3.4). In order to compare the performance of these unwrapping approaches the Root Mean Square (RMS) for each SDFP pixel was computed (Figures 16*a*-*c*). We observe that the locations of the unwrapping errors are similar in both studies and coincided with steeply sloped areas where geometric distortion may occur (see also Chapter 2) or where deformation gradients are high.

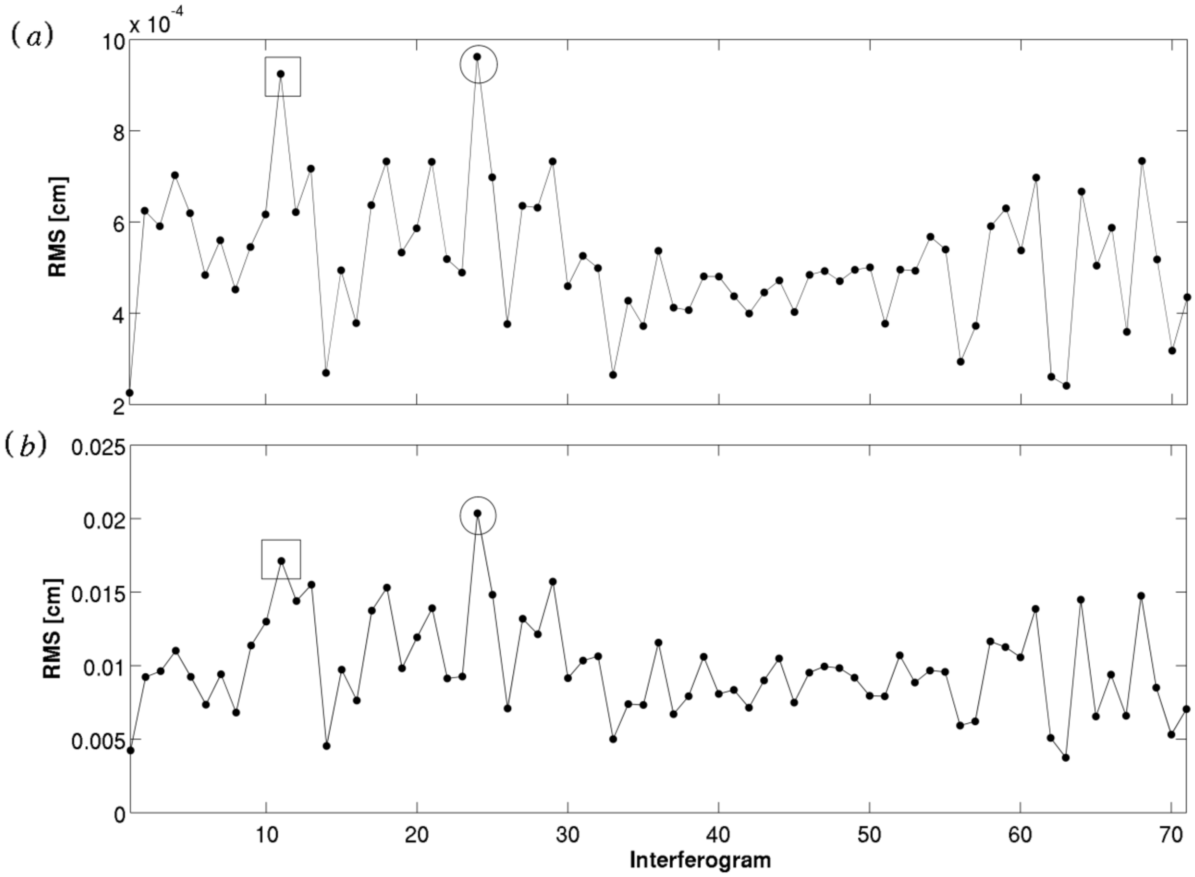

Figure 7-17 RMS values using: (*a*) all SDFPs and (*b*) SDFPs with residuals larger than interferograms with highest RMS are denoted by □ (interferogram 11) and ○ (interferogram 24).

Considering the magnitude of RMS, the unwrapping approach from StaMPS (Hooper 2010) has, in general, a better performance. Nevertheless, lower RMS values in this study (from 0 to 0.13 cm) can be explained by the lower number of pixels employed compared with the number used in SBAS analysis presented by López-Quiroz et al. (2009).

Figure 7-17*a* displays the global RMS estimated for each interferogram using the selected SDFP pixels. According to the RMS values interferogram 11 and interferogram 24 present inconsistencies due to unwrapping errors. In general, no clear correlation was observed between the magnitude of the RMS and the perpendicular or the temporal baselines (see also Figures 7-2*a*, *b*). Notwithstanding, interferogram 11, with the largest perpendicular baseline presented some unwrapping errors of systematic nature that might have mainly been induced by the spatially-correlated part of the look angle error which in turn is proportional to the perpendicular baseline. Additionally, the map of the residual phase for each interferogram was studied and the location of discrepancies identified; 96% of the SDFP pixels present residuals lower than π.

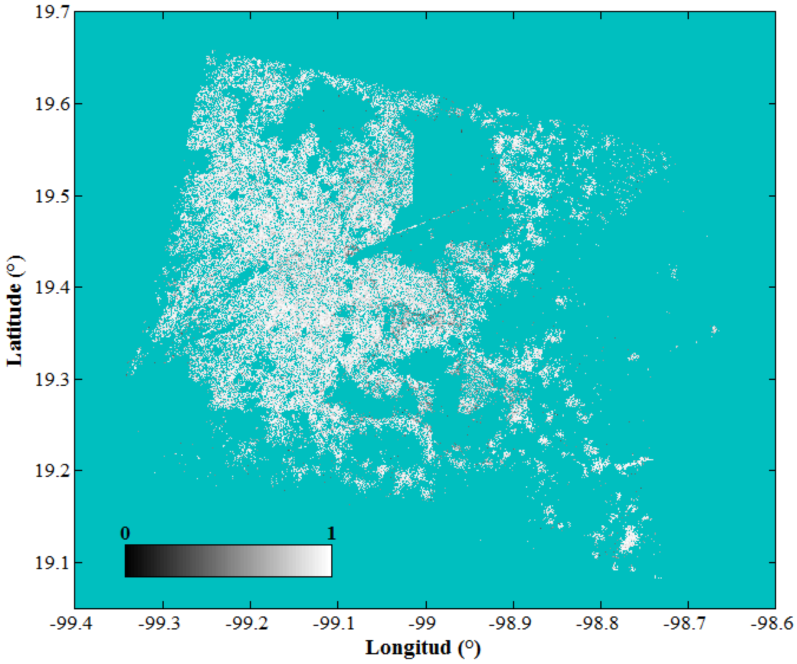

Figure 7-18 Mean coherence map.

Because most residuals used for the RMS computation were below π, some inconsistencies due to unwrapping errors could have been masked for certain interferograms. Therefore, a new RMS using pixels with residuals higher than half a phase cycle was estimated. Figure 7-17*b* depicts the RMS estimated using SDFP pixels for which unwrapping errors were detected. Note that the highest RMS errors still correspond to interferograms 24 and 11. In addition, we checked the SDFP coherence map to verify that low values did not induce unwrapping errors (see Figure 7-18). We noticed that even areas with high concentration of coherent points were affected by unwrapping errors. High deformations gradients or larger topographic errors made difficult the unwrapping in these areas conducing to errors in the unwrapped phase estimation, and thus larger RMS values.

Inversion

The inversion approaches are also different. Here, an unconstrained but WLS inversion was employed and a design matrix **G** with the same rank deficiency for all SDFP pixels was assumed. In constrast, López-Quiroz et al. (2009) applied the inversion to pixels having at least 35 valid interferograms out of 71 (see also Chapter 4). 42% of those pixels characterized by design matrices with different rank deficiencies were inverted using a constrained LS adjustment. For the remaining 58% (presenting no rank deficiencies), no constraints were imposed. ULS and WLS-SVD approaches were also proposed and evaluated for the study area (see section 7.5).

Atmospheric and other noise terms correction

In StaMPS temporal and spatial filtering is applied to the time series to extract the deformation signal. For that purpose, some components are assumed to be correlated spatially but not temporally, e.g., atmosphere and orbit components (see also Table 5-1).

Our study region is characterized by high humidity values and moisture contents which vary seasonally. Some interferograms comprising transition periods between the dry season (November - April) and the wet season (May - October) might have been affected by an inhomogeneous tropospheric effect (see also Chapter 3). Moreover, a large drought affecting the study area during the first half of 2005 could have intensified the difference in moisture content between seasons. In these cases, the atmospheric component might have been correlated temporally, in which case the assumption of its only spatial correlation would be inappropriate. We applied a window size (250 days) to filter the APS and other spatially correlated noise, attempting to keep most of the deformation (see Figure 7-19). The SBAS subsidence rate field presented by López-Quiroz et al. (2009) was taken into account to select the filtering window. However, lower deformation rates than expected were found in some areas suggesting that an appropriate window size for the entire area was not possible.

López-Quiroz et al. (2009), on the other hand, conducted the atmospheric stratified correction to the interferograms previous to the unwrapping. The method was successfully applied to eliminate the vertical atmospheric contribution outside the lacustrine unit. The turbulent contributions were considered as random phase.

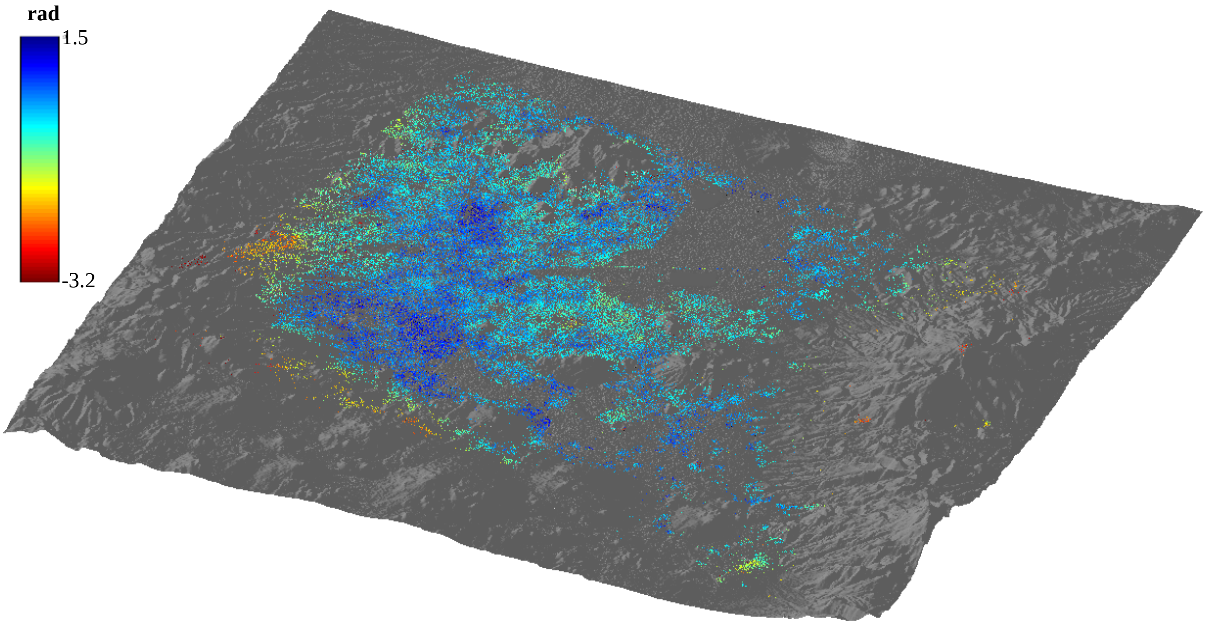

Figure 7-19 Master atmosphere and orbit error (AOE) overlaid on SRTM V4 shaded relief. The largest AOEs occur in the mountainous areas surrounding the lacustrine unit. Because precise orbits were used in the processing, the atmospheric delays might contribute the most to the AEO component. Some reference points might have been notably affected by the AEO error.

APS affecting the mountainous region which coincides with the location of the reference area might have been contributed to the discrepancies between the two SBAS methods over Mexico City (see Figure 7-19). This source of discrepancy could have been diminished by using the APS correction suggested by López-Quiroz et al. (2009) to reduce the vertical component. The remaining turbulent mixing component, affecting both flat and mountainous areas (Hanssen 2001), can be removed by using the collocation approach (Liu et al. 2011).

7.4.2 Comparison with GPS results at specific sites

Information of some continuous GPS stations (Cabral-Cano et al. 2008; Osmanoglu et al. 2010) located in Mexico City was used to validate our results. We selected two permanent GPS stations MOCS and MRRA, located within the lacustrine area (Gobierno del Distrito Federal 2004) and near Los Remedios and Oceania metro stations, respectively (see Figure 7-6). Unfortunately, we did not have access to precise coordinates, thus approximate coordinates were employed.

Site	GPS		PSI	Previous SBAS	SBAS_StaMPS	
	Vertical	LOS			LOS	Vertical
MOCS	-16.90	-14.91	-16.15	-16.18	-14.90	-16.13
MRRA	-25.60	-25.28	-25.44	-27.75	-25.60	-27.71

Table 7-1 Deformation rates [cm/yr] from different techniques measured at MOCS and MRRA GPS stations.

Table 7-1 compares deformation rates from different techniques used at the selected sites. Vertical GPS rates for the period 2004-2007 (Cabral-Cano et al. 2008) and the projection of GPS results to the LOS vector for the period 2005-2007 (Osmanoglu et al. 2010) are shown in Table 7-1. Discrepancies between PSI (Osmanoglu et al. 2010) and SBAS rates at the selected GPS locations are also depicted. Furthermore, the SBAS subsidence rates from López-Quiroz et al. (2009) spanning 2002-2007 are given, and results from StaMPS are expressed in LOS and converted into vertical motion. It is important to highlight that the PSI analysis (Osmanoglu et al. 2010), carried out for the period 2004-2006, assumes a linear model while in this study no deformation pattern was presupposed.

Overall, the deformation rates from StaMPS and the GPS measurements are in good agreement; however, differences up to 2 cm/yr were found. These differences might have been due to noise factors related to each technique and the different period of analysis (Osmanoglu et al. 2010). Lateral variability not taken into account when projecting LOS rates to the vertical may have also influenced the magnitude of discrepancies. This might have been the case for the MOCS GPS station which exhibits important horizontal motions (Cabral-Cano et al. 2008; Osmanoglu et al. 2010).

However, from the estimated mean StaMPS-GPS difference rates (-0.67 cm/yr and -0.16 mm/yr) we can conclude that there is a better consistency between our results and the GPS results obtained by Osmanoglu et al. (2010).

The mean difference between SBAS rates in this study and PSI rates (Osmanoglu et al. 2010) is 0.54 mm/yr. This value suggests some inconsistencies between the two methods that could mainly have been due to the assumption of a displacement model, different atmosphere correction procedures and the selection of the stable points.

On the other hand, the average difference between subsidence rates from the different SBAS approaches (this study and López-Quiroz et al. 2009) is almost negligible at the selected points: -0.05 cm/yr.

The GPS and InSAR rates from different approaches coincide with a high level. Notwithstanding, GPS measurements are restricted to a few locations while InSAR has a more extensive coverage. This advantage of the InSAR techniques over the GPS method allows more detailed information about the regional subsidence and makes it possible to find non-homogeneous displacements which may unveil valuable information, where GPS measurements are not available (see section 7.6).

7.4.3 Comparison with levelling results

Our InSAR results were further assessed from the comparison with levelling information. Levelling curves in Figure 7-20 were constructed from the levelling campaign carried out by the SACMEX between 1994 and 2007 (GDF et al. 2012b). The levelling map covers the south of the Valley of Mexico from the Sierra de Guadalupe until the Sierra de Chichinautzin.

For a better visual comparison between both methods, mean subsidence rate curves were constructed from the InSAR results. The LOS velocities, expressed in m/yr, were converted to vertical values (see section 7.2) and resampled using the Delaunay triangulation. The InSAR subsidence rate curves were then generated from the interpolated grid, masking topographic features and areas where few SDFP pixels were found.

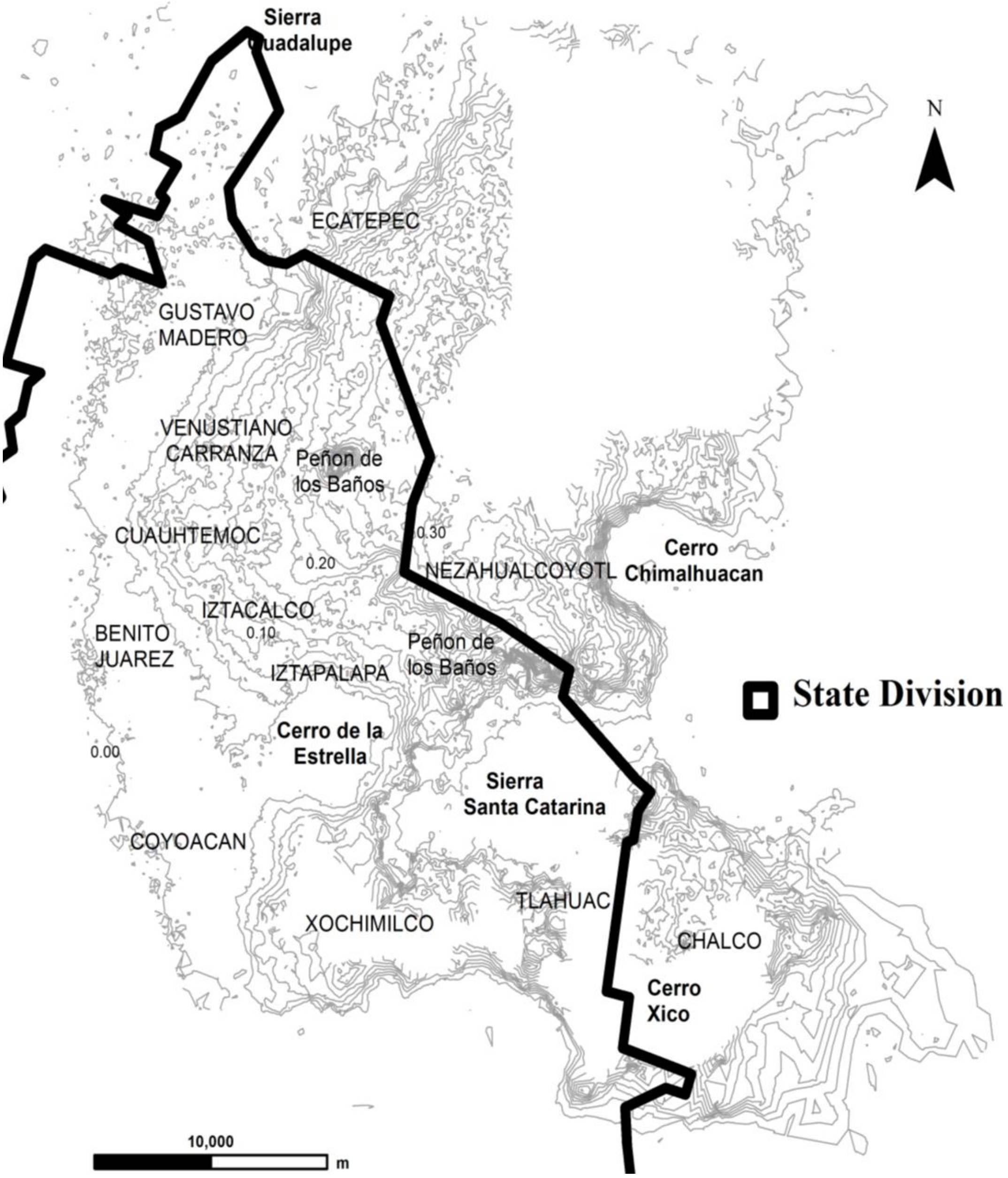

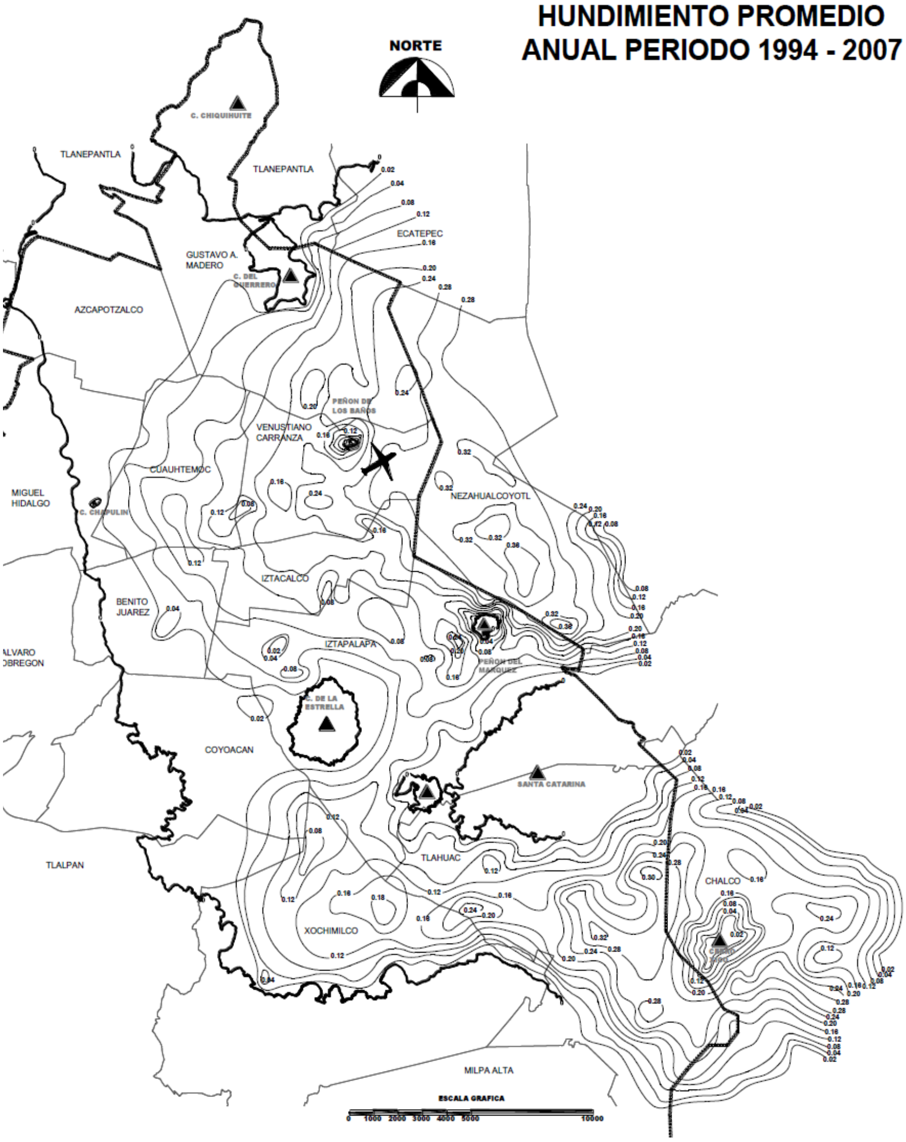

Figure 7-20 Top**:** InSAR subsidence rate contour lines obtained after interpolation, period 2002-2007. Bottom : annual subsidence rate map constructed from the levelling campaigns carried out by the Sistemas de Aguas de la Ciudad de Mexico (SACMEX) between 2002-2007 (GDF et al. 2012b)**.**

Both the InSAR and the levelling-based sinking velocity map exhibit highest deformation rates in Nezahuacoyotl, Chalco, Iztapalapa and Tlalhuac. The highest settlement (36.4 cm/yr) for the period 2002-2007 happens in Nezahuacoytl near the Calzada Ignacio Zaragoza Street, which connects Mexico City and Puebla. This value coincides to a good level with the one observed in the levelling map (~36 cm/yr).

Note that in both maps the displacement contour lines are concentric to the volcanic features of the Peñon del Marqués (~ 20 cm/yr according to both techniques) and Peñon de Los Baños (up to 24 cm/yr, levelling; up 26 cm/yr; InSAR); except in the Cerro Xico area (up to 20 cm/yr, levelling) where a few SDFP pixels were identified by the StaMPS algorithm. The high density of contour lines indicates high subsidence gradients in these areas, presumably due to important extraction rates (see also Carrera-Hernandez and Gaskin 2007), contrasting stratigraphy and soil fracturing processes. The same curves distribution can be observed around the Sierra de Santa Catarina, Cerro de la Estrella and Cerro Chimalhuacan where a presumably abrupt contact between sedimentary and volcanic sequence occurs (see also Figure 6-12). On the hand, a more spacing distribution of the contour lines in the centre of the plain suggest smoother subsidence spatial changes affecting this area, mainly characterized by the presence of clay-rich deposits (e.g., area of Iztacalco). Note that the linear subsidence behaviour observed in the latter areas might correspond to the presence of more homogeneous materials, opposed to the non-linear deformation observed near some volcano flanks or other zones where differential deformation may happen due to for example differential pumping rates or presence of heterogeneous materials.

In both maps, subsidence decreases towards the mountainous region (presence of more rigid material; see section 6.2) where no deformation is expected according to the geological information.

7.5 Evaluation of alternative inversion strategies

7.5.1 Unweight Least Squares

Different from some SBAS methods (e.g., López-Quiroz et al. 2009, Berardino et al. 2002), the StaMPS algorithm performs the inversion of the unwrapped phase delays using WLS. As already presented in Chapter 5, the weight matrix **P** is estimated from the noise phase information of each SB interferogram using expression (5.17). However, the algorithm was slightly modified to use the Unweight Least Squares (ULS) method, and impact on the quality of the results was evaluated.

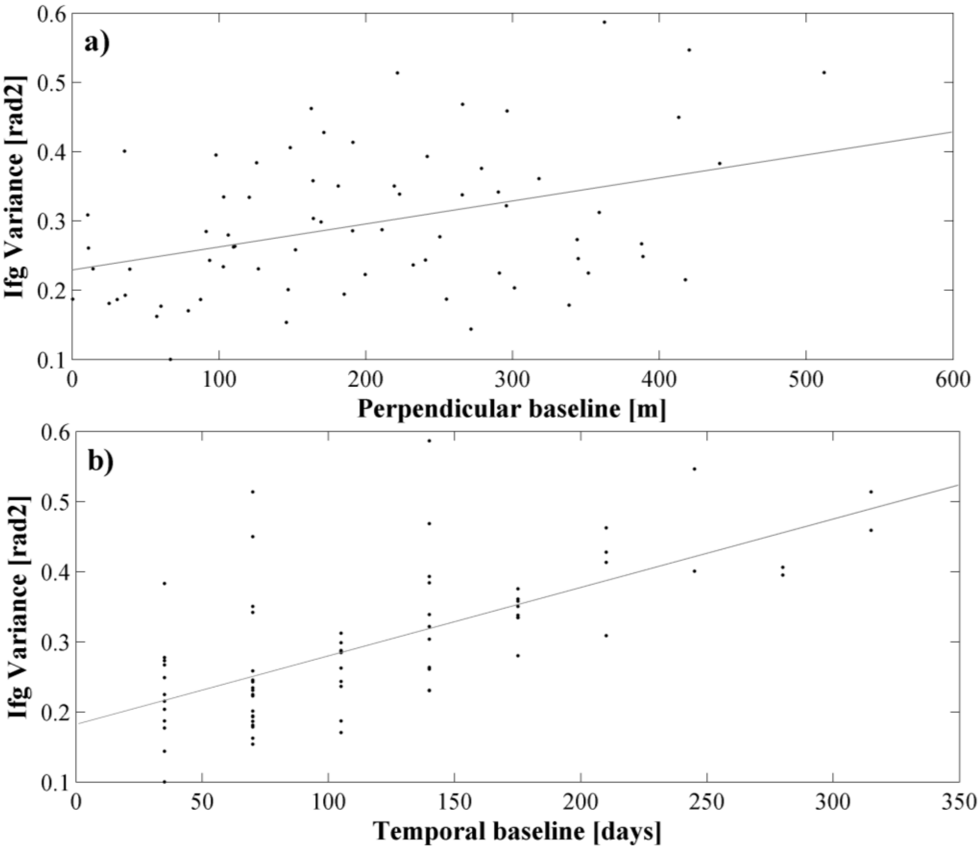

Figure 7-21 a) Phase noise variance of each SB interferograms versus the corresponding perpendicular baseline. Linear fit: grey line b) Comparison of the variances with the temporal baselines expressed in days. The grey line indicates the linear fit.

First, the priori covariance matrix $\boldsymbol{\Sigma}_n$ used in the WLS method was analysed. The decorrelation (i.e., noise) affecting the SB interferograms can be examined by inspection and comparison of each individual coherence map. Notwithstanding, it is also possible to evaluate the noise component affecting each interferogram by studying the correlation between the estimated noise variances and the perpendicular and temporal baselines. Figure 7-21a compares the noise variance of each interferogram with their perpendicular and temporal baselines. In both cases, a lineal model adjusts the data, indicating that the variances increment linearly with the baseline length. The latter confirms that, generally, interferograms with longer B_t and $B_\perp$ are more affected by decorrelation and that those with smaller variances receive more weight in the inversion system. Plots corresponding to the ULS, on the other hand, would correspond to a constant function, because all observations are considered equally precise ($\sigma_n^2=1$).

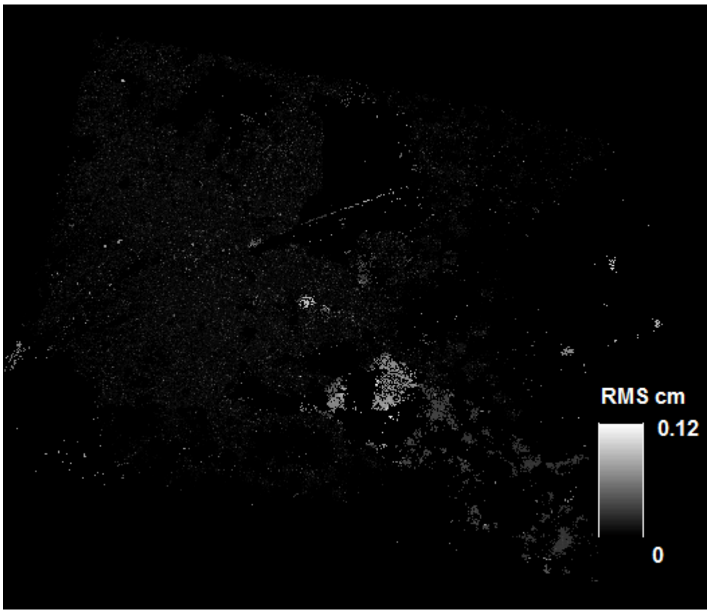

Figure 7-22 RMS map computed from the unwrapped inverted phases by the ULS.

Because we are interest on how the use of ULS influence the quality of the results, the system misclosure interferometric map and the global RMS for each interferogram were computed and compared with those obtained by WLS (see Figures 7-22, 7-23, respectively). Moreover, the error propagation in the time series obtained by each method was considered (Figure 7-23).

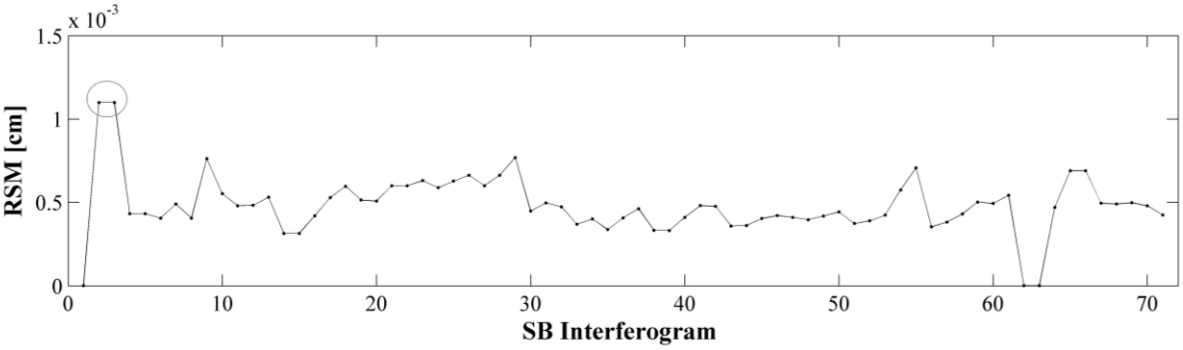

Figure 7-23 Misclosure for each SB interferogram after the ULS inversion. Interferograms 20030307-20031003 and 20030411-20030620 (denoted by the grey circle) present the largest RMS.

The RMS maps indicate same location of the unwrapping errors in both cases. Nevertheless, the magnitude of the RMS computed by using the phase delays estimated by the ULS are slightly lower than those obtained from the WLS inversion. From the inspection of the of RMS map one might assume that the WLS, presumable more sensitive to outliers than the ULS, may induce larger errors in the results. Nevertheless, from the examination of the variance of the estimated phase delay increments and the misclosure of the interferometric data (Figures 7-23, 7-24, respectively), the WLS optimizes the efficiency of the parameter estimation.

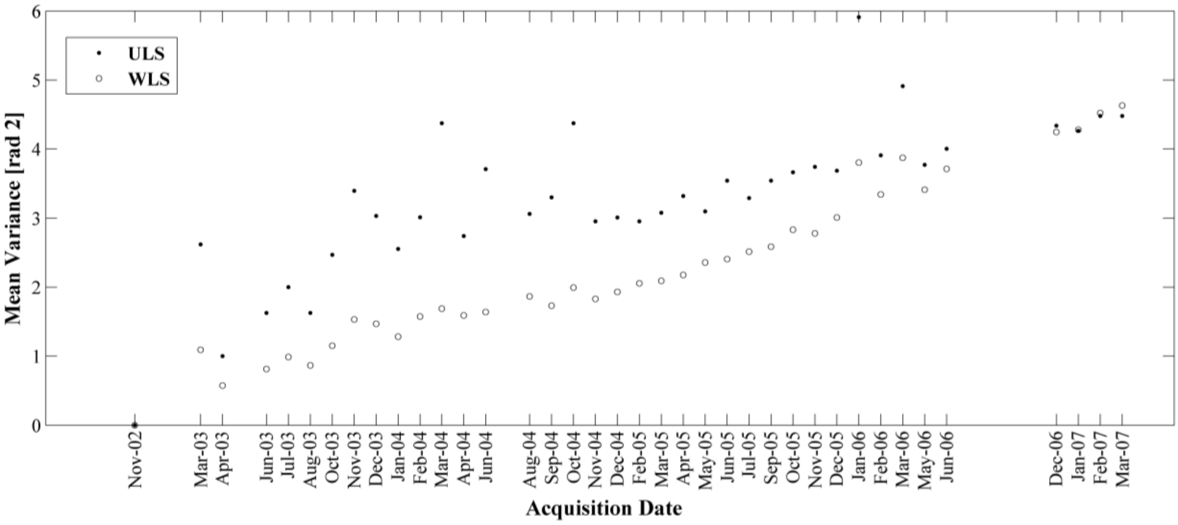

Figure 7-24 Mean variances of the phase delay increments estimated from both method: ULS and WLS. Note that the uncertainties are larger when inverting the interferometric system (5.17) with ULS.

We emphasize that even though the weighting of observations based on the noise information led to appropriate results in the present application, the selection of weights in other study cases should be carefully evaluated since they could have a negative impact in the parameter estimation.

7.5.2 SVD - WLS

As already presented in Chapter 4 and 5, most interferometric systems (5.17) are usually ill-conditioned. The design matrix **G** is generally rank deficient because there are groups of independent images that present no temporal or geometrical overlaps (Lopez-Quiroz et al. 2009). The rank deficiency problem can be solved by selecting a "control image" (see section 5.5) or by using inner constraints (see also Chapter 4).

However, as reported in the literature (e.g., Berardino et al. 2002; Lanari et al. 2004) the SVD represents an alternative regularization method to find the solution of the ill-posed interferometric system by using orthogonal transformations. López-Quiroz et al. (2009) have analysed the SVD, reporting that the incremental phase delays between chronological images are set to zero by this method, biasing the subsidence rates in Mexico City. Thus, they proposed the application of constrained LS to those pixels that present at least one critical link missing in the interferometric network (especially over non-urban areas where there is loss of coherence) and the SVD method to the remaining pixels (see Chapter 4). In the present work, on the other hand, the selected SDFP pixels have in general good coherence (most of them > 0.3) and they are assumed to have the same design matrix with the same rank defect. Therefore, we combine the WLS and SVD to determine if this combination could optimize the results.

By using the covariance matrix a priori the solution to the interferometric system (5.17) can be expressed as

$$\phi_{\mathrm{WLS}} = \left(\mathbf{G}^{\mathrm{T}}\mathbf{P}\mathbf{G}\right)^{-1}\mathbf{G}^{\mathrm{T}}\mathbf{P}\boldsymbol{\varsigma} \tag{7.2}$$

where ($\mathbf{G}^{\mathrm{T}}\mathbf{P}\mathbf{G}$) is solved by the SVD method and **P** is the weight matrix computed as the inverse of the covariance matrix known a priori and based on the noise information.

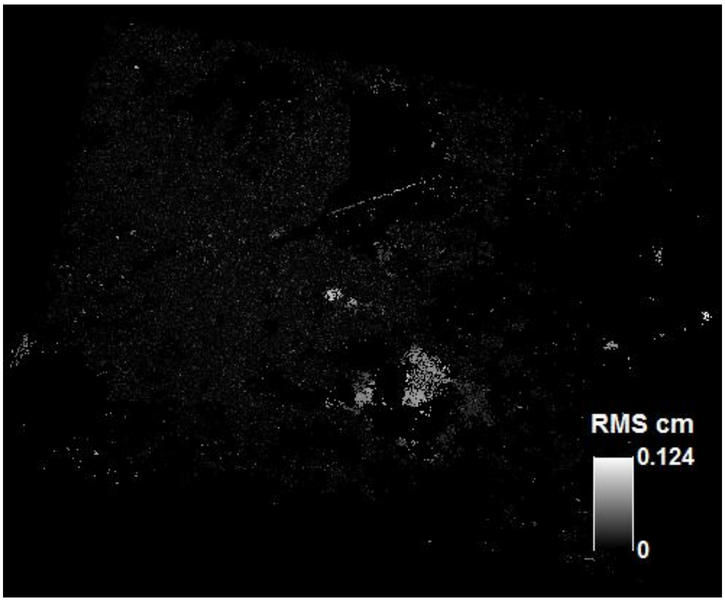

Figure 7-25 RMS map between the phase from each SB interferogram and the accumulated phase delays estimated by the SVD-WLS method.

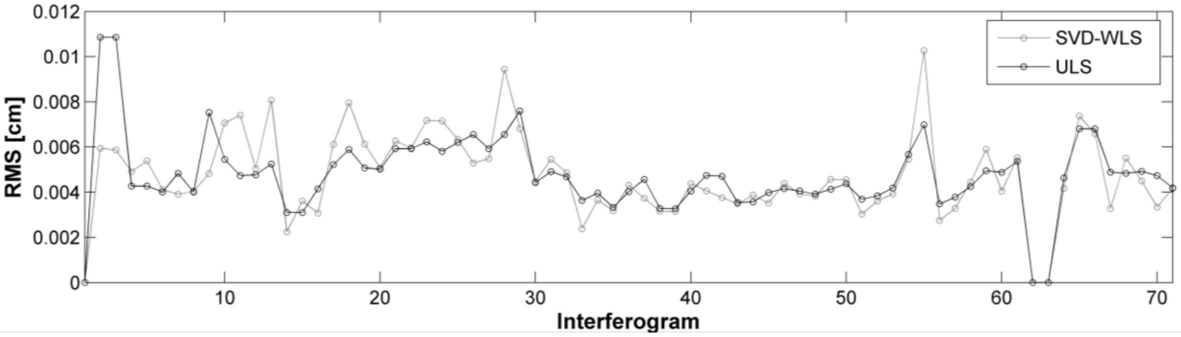

Figure 7-26 Comparison of misclosure of the interferometric data set using the ULS and SVD-WLS.

The RMS misclosure and global deviation map were computed and compared with the previous method (see Figures 7-25, 7-26). Plot in Figure 7-25 shows that location of the RMS values are similar to those in Figure 7-22; notwithstanding, larger values are obtained by the WLS-SVD method. Unwrapping errors still occur in areas where deformation gradients area high or in steep mountainous zones.

Although the WLS-SVD approach provided a more numerically stable solution, as seen from the results in Figures 7-25 and 7-26, the ill-posed nature of **G** may still compound the noise in the time series independently of the regularization method. The large condition numbers of **G** (>100) indicate that system (5.17) is very unstable and sensible to errors in the initial data (i.e. unwrapped phases). Moreover, roundoff errors might accrue in the calculation and the accuracy of the results may be potentially affected. In contrast, the use of $\mathbf{G}_{fr}$ full-rank (see section 5.5), characterized by a low condition number (29), produce a more stable solution of the target system.

We carried out some tests, as well, using iterative WLS trying to optimize the results from the covariance matrix of the observations. However, results were not notably improved. The results here presented suggest that more detailed analysis of the proposed method is required.

7.6 Non-linear deformation

Because many multi-temporal algorithms (e.g., Ferretti et al. 2001; Crosetto et al. 2003; Kampes 2005) use a lineal model of the deformation, they tend to fail to detect points undergoing nonlinear motion. StaMPS, however, has the flexibility to identify these points, proving in this way useful information for the understanding of complex subsidence behaviour and associated hazards.

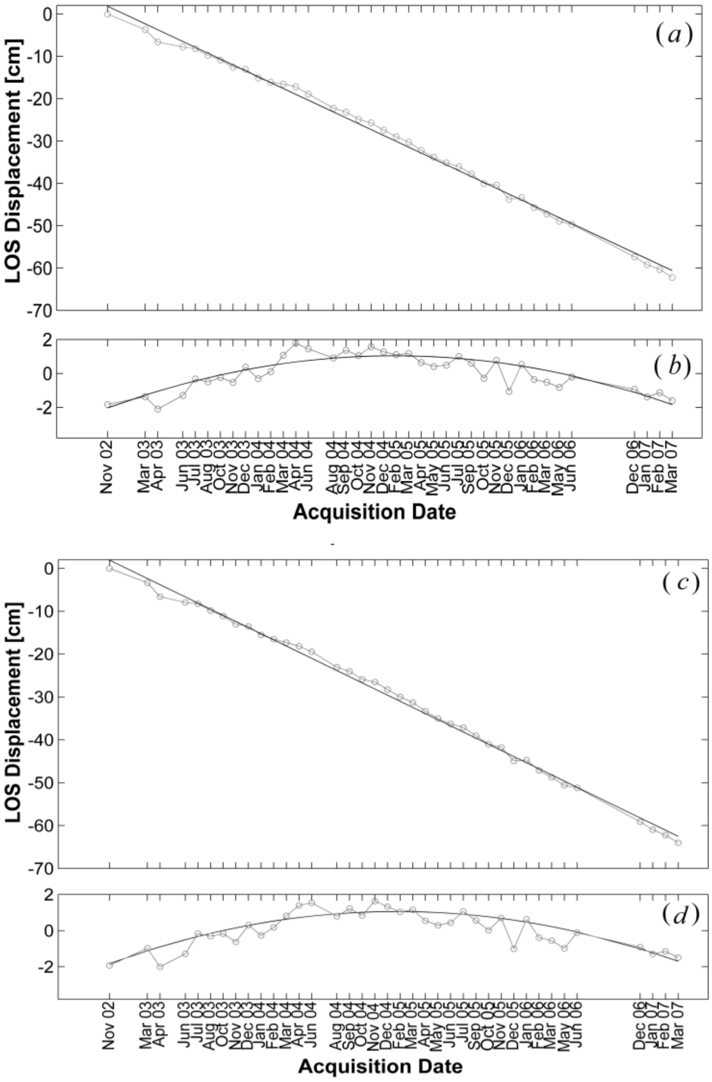

Figure 7-27 Examples of non-linear deformation affecting the area of El Peñon del Marqués. Panels (*a*) and (*c*) show subsidence rates presenting an almost linear behaviour. Linear fit: dark grey line. In panels (*b*) and (*d*), the residuals between the linear fit and the data points have been fitted with a quadratic polynomial (dark grey line).

Subsidence rates in Mexico City show almost perfect linear behaviour (see section 7.3); however, non-linear deformation was identified in some areas, as reported by previous studies (Lopez-Quiroz 2008; Lopez-Quiroz et al. 2010; Yan et al. 2012). Manual examination of the time series for the entire area was performed and the non-linear component was identified to be represented, in general, by a quadratic function, being in agreement with the existing reports (e.g., Lopez-Quiroz 2008; López-Quiroz et al. 2012). Plots in Figure 7-27 display examples of the detected non-linear component fitted with a quadratic polynomial function. The presence of highly heterogeneous stratigraphy (see Chapter 6) and the existing discontinuities may contribute to the observed non-linear behaviour in certain areas.

By integrating our InSAR results and the available geological information found in the literature (Cerca et al. 2010) a particular analysis over El Peñon del Marqués area, where non-steady deformation was observed, was performed. The methodology presented in this section can be extended to other areas presenting similar characteristics (see also Chapter 8).

This area is highly populated and represents a region of geological risk (SEDESOL 2011) due to the regional land subsidence and the presence of fractures (see Chapter 6). Existing fractures affecting this area might have been partly triggered by the installation of extraction wells around El Peñon, which were drilled in the late 1960s to supply water to Mexico City (Cerca et al. 2010). Fracturing could have been further intensified by infiltration wells that operated in the area since 2000 (Cerca et al. 2010; Cerca et al. 2012).

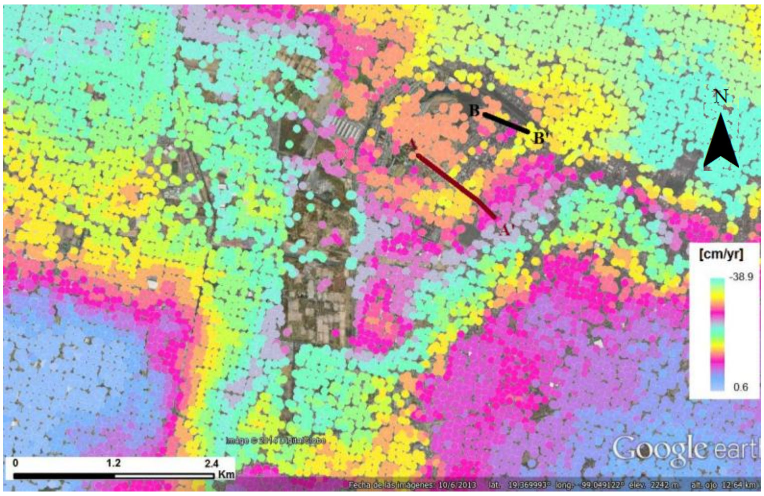

Figure 7-28 Zoom on the SBAS results over El Peñón del Marqués area. Red and black lines corresponds to the radargram of the Exploradores de Ejercito Oriente and the Diodoro Batalla Streets, respectively.

The present analysis was carried out along two main streets located in the surroundings of El Peñon del Marqués area (see Figure 7-28):

Street A: Exploradores de Ejercito Oriente

Street B: Diodoro Batalla

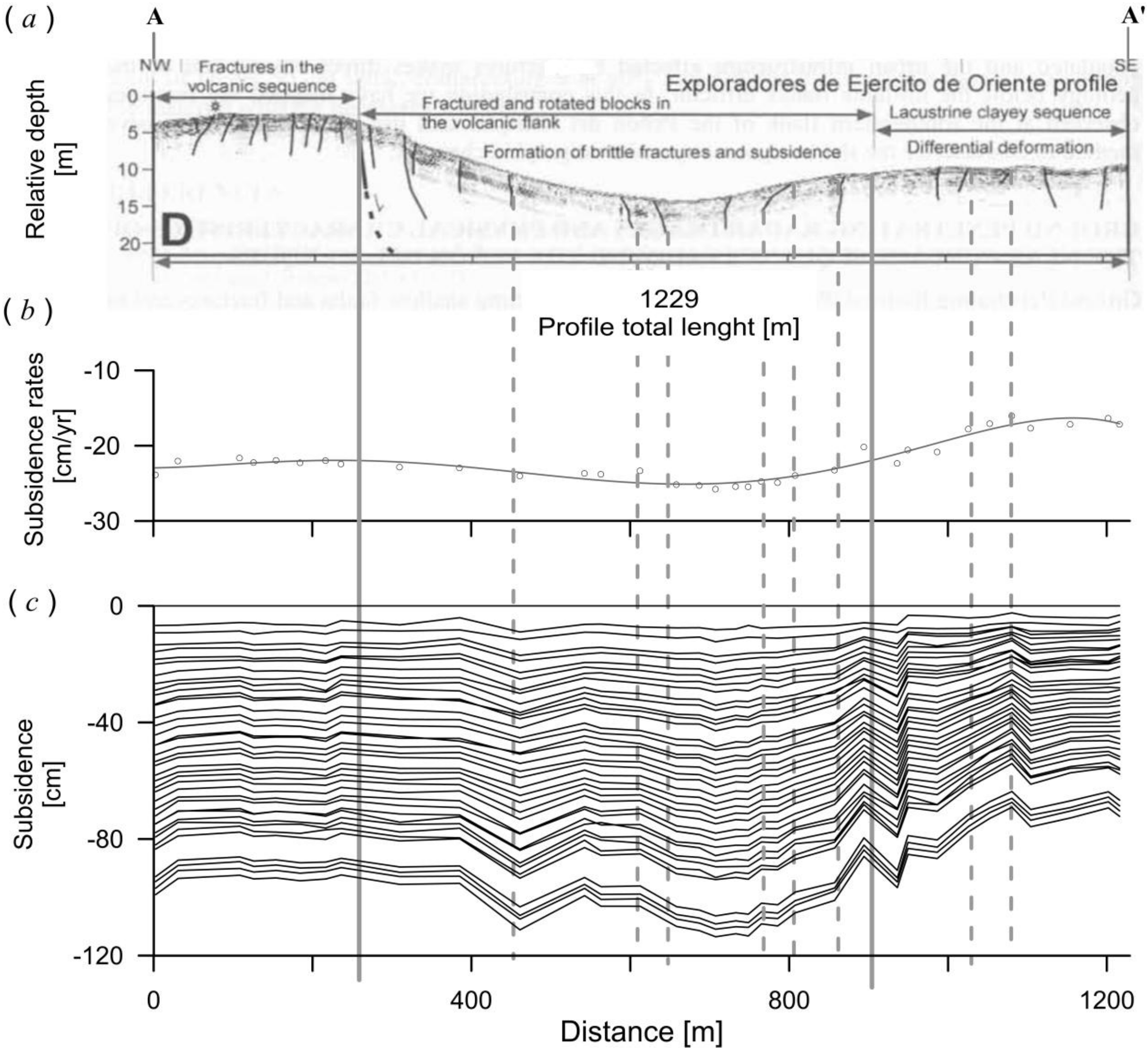

Figure 7-29 *a*) GPR radar profile along the Exploradores de Ejercito Oriente street showing the main geomorphologic and stratigraphic features of the zone (from Cerca et al. 2010). *b*) Average subsidence rate profile along the street. *c*) Subsidence evolution profile for the period 2002-2007. For correlation analysis between the three profiles, the structure locations observed in the radargram were projected to the profiles (*a*) and (*b*). The vertical grey lines indicate the projection of the main normal fault and the volcano-sedimentary contact. The dashed grey lines correspond to the projection of other structures.

A GPR profile collected with a 200 MHz antenna along these streets (Cerca et al. 2010) were used for interpretation and validation of the method (Figure 7-29*a*). The dynamic of the area was further analysed through a subsidence evolution profiles constructed from the times series obtained by StaMPS (Figures 7-29*c*, 7-30*c*). For the construction of the profiles buffers of 200 and 80 meters along streets A and B were employed, respectively. We evaluated the correlation between the geometry of deformation obtained by the GPR technique (Cerca et al. 2010) and the time series evolution along the profiles.

Figure 7-29*a* shows the profile of the average subsidence velocities along street A. Changes in the subsidence rates coincide significantly with the variations in the relative depth mapped in the radargram (Figure 7-29*a*). Homogeneous motion (~ 23 cm/yr) characterizes the footwall of the main normal fault, while the hanging wall presents more variable deformation rates, probably due to combined effect of the subsidence and a sliding mechanism acting on heterogeneous materials. Relative uplifting (16 cm/yr) with respect to the depression (SE part of the profile) can be explained by the slide of the volcanic flank (Cerca et al. 2010). The highest average deformation rates (up to 26 cm/yr) correspond to the depression area where rotated blocks and subsidence affect the volcanic sequence.

Note that most variations in the subsidence rates occur in the position of some brittle fractures and the volcano-sedimentary contact. The different mechanical behaviour between the lacustrine deposits and the volcanic sequence may manifest as jumps in the profile (see also Figure 6-12). Moreover, variations in the piezometric decline, differently affecting the compressible clay material and the pumice sequence could be associated to the observed behaviour.

The evolution profile suggests that the lateral flank displacement might have contributed to the appearance or propagation of tension fractures towards the SE direction.

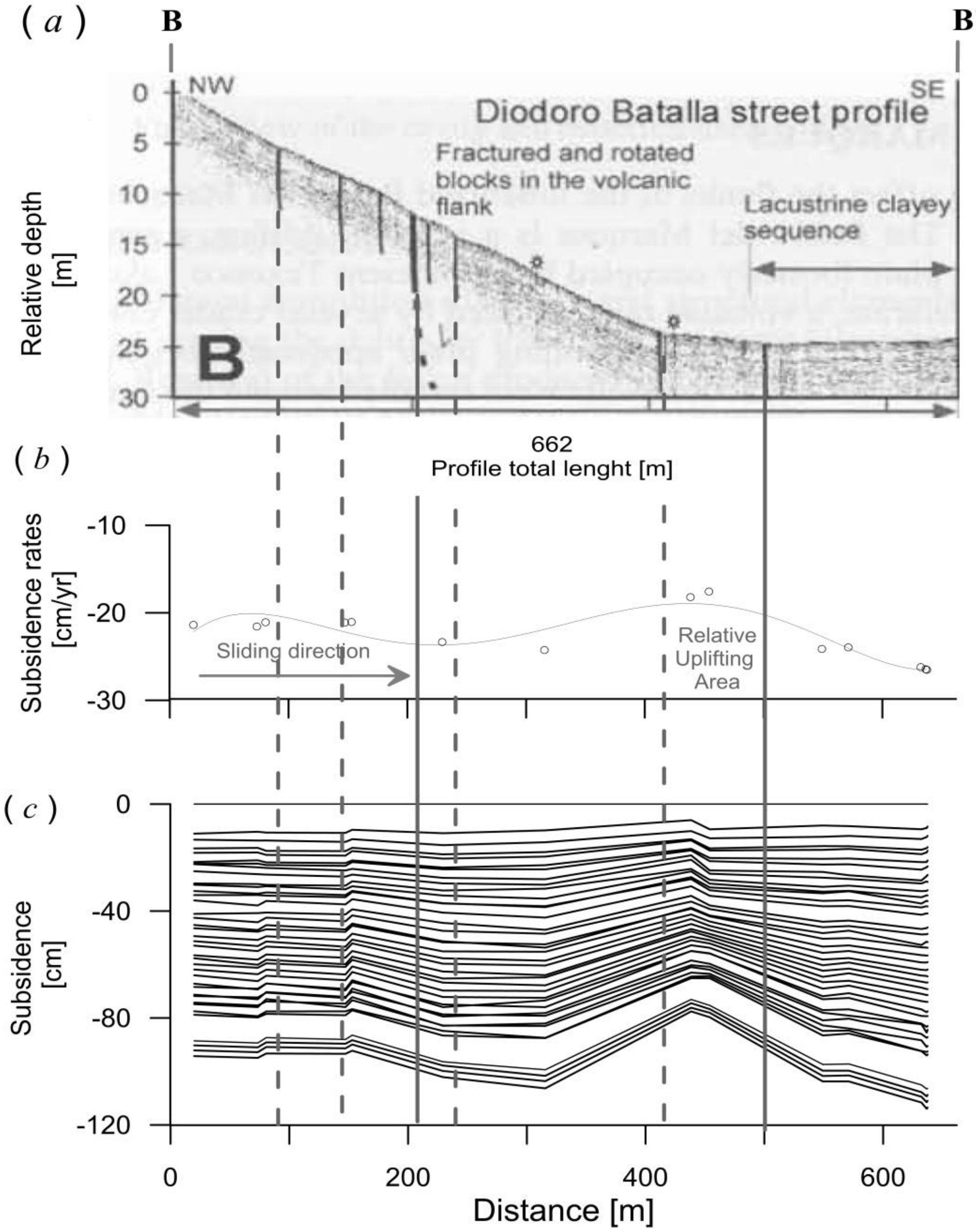

Figure 7-30 (*a*) GPR radar profile along the Diodoro Batalla street showing the main elements of the zone (from Cerca et al. 2010). (*b*) Average subsidence velocity profile along the street. (*c*) Subsidence profile evolution for the period 2002-2007. For correlation analysis between the three profiles, the structure locations observed in the radargram were projected to the profiles in (*a*) and (*b*). The vertical grey lines indicate the projection of the main normal fault and the volcano-sedimentary contact. The dashed grey lines correspond to the projection of other structures.

On the other hand, the velocity profile for the Diodoro Batalla Street indicates low correlation between the variations observed in the relative depth profile (Figure 7-30*a*) and the mean subsidence rate changes (Figure 7-30*b*). A continuous diminution of the relative depth with the length in the first 400 meters measured by the GPR antenna is displayed in the radargram (Figure 7-30*a*). Along the same segment the velocity profile indicates approximately constant subsidence velocities.

The deformation evolution profile in Figure 7-30*c* suggests that some ground displacement shifts coincide with the location of the fractures detected by the GPR technique. As already interpreted from Figure 7-29*c*, profile in Figure 7-30*c* denotes that the sliding block might be applying a tensional stress towards the SE direction of the section, inducing the protruding change observed at the location of the second infiltration well (~410 m; see Figure 7-30*a*).

Moreover, the generation of tensional stresses due to the water infiltration might also add to the tensional component producing the relative uplifting observed in the Diodoro Batalla profile, and the consequent creation and/or propagation of fractures. Besides, water may produce destabilization of the collapsible tuff material that characterized this area (Cerca et al. 2010; Cerca et al. 2012).

Note that the relative uplifting is more marked in Figure 7-29*c* than in Figure 7-30*c*. Presumably, a rotation component from the sliding mechanisms acting in south-north direction, towards the Diodoro Batalla street may induce more notable elevation in the latter area.

This interpretation reveals important information about the geodynamics of the area that could be used for geohazard assessment of civil infrastructure. Especially the location and behaviour of the actual faults have been detected through the present analysis based on time series InSAR.

In Chapter 8, a fracture identification methodology based on the modelling of the non-linear component is presented and applied to the northern Valley of Mexico.

7.7 Time series extension and interpretation until 2010

In this section we present the extension of the time series covering the period 2002-2010, after the proposed algorithm was assessed from the visual and qualitative comparison with previous results over Mexico City. Available pumping rates information are considered to explain the differences observed between this and the 2002-2007 study periods.

The selection of parameters was carried out following the criteria presented in section 7.2. Small temporal and perpendicular baselines were selected to reduce the geometrical decorrelation. 100 SB interferograms linking the available 52 SAR images for this period were constructed (see Figure 7-31).

The SDFP pixel selection was done by using a slightly higher value of the $D_{\Delta A}$ (0.6) and the weed standard deviation (0.9) to include a larger number of pixels in some areas of interest (e.g., important highways and railroads), attempting to avoid memory limitations and noisy pixels that could affect the quality of the unwrapping as well. For the latter, the misclosure map and the global RMS for each interferogram were evaluated.

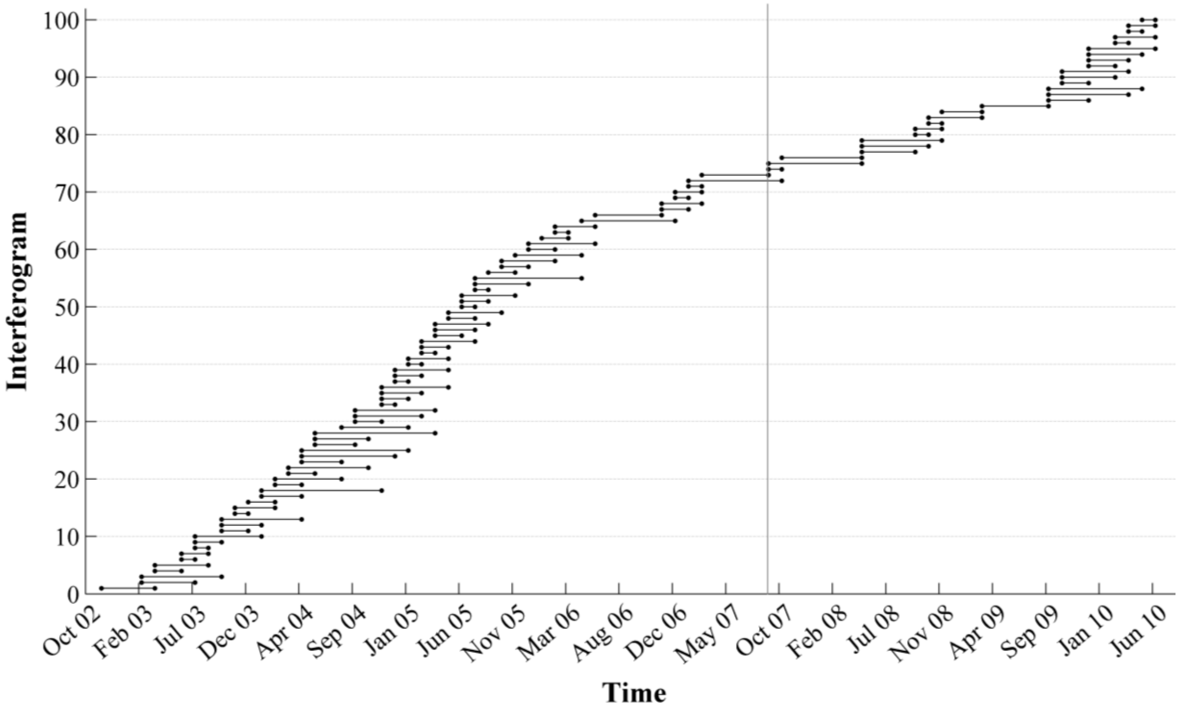

Figure 7-31 Set of interferogram generated from the 52 ENVISAT data set. The vertical grey line indicates the beginning of the extended period spanning from September 2007 to June 2010.

The retrieval of the time series was carried out using the WLS square method, proven that the use of a full phase noise covariance matrix in the WLS produce relatively better results than the ULS and the WLS-SVD methods.

7.7.1 Results and comparative analysis with previous study period

The StaMPS processing identified more than 85000 SDFP pixels in the study area, with a mean point density of 28 SDFP pixels/km^2 (~ 15% larger than the previous analysis). Figure 7-32*a* and b showing the LOS results for the periods 2002-2010 and 2002-2007, respectively, indicate almost no variation in the subsidence rates. Nevertheless, some differences observed between the present period of study and the previous (2002-2007) such as lower displacement rates and uplifts could be attributed to:

- Lower extraction rates during the period 2007-2010 (and previous years?) might have had a positive effect, indirectly helping to a slightly recovering of the groundwater levels (some other water policies might also have contributed; see also Chapter 6). A favourable dynamic response of the clay rich deposits in the sense of decrease of compaction rates in subsiding areas might have characterized this 3-year period.

- On the other hand, even though the RMS map suggests acceptable quality of the unwrapping outcomes, it could have happened that some noisy pixels, in fact, compromised the quality of the displacement map leading to the results observed (Figure 7-32a,b). Moreover, a larger number of reference points possibly affected by atmospheric effects can have bias the deformation rates. These two statements are discussed below.

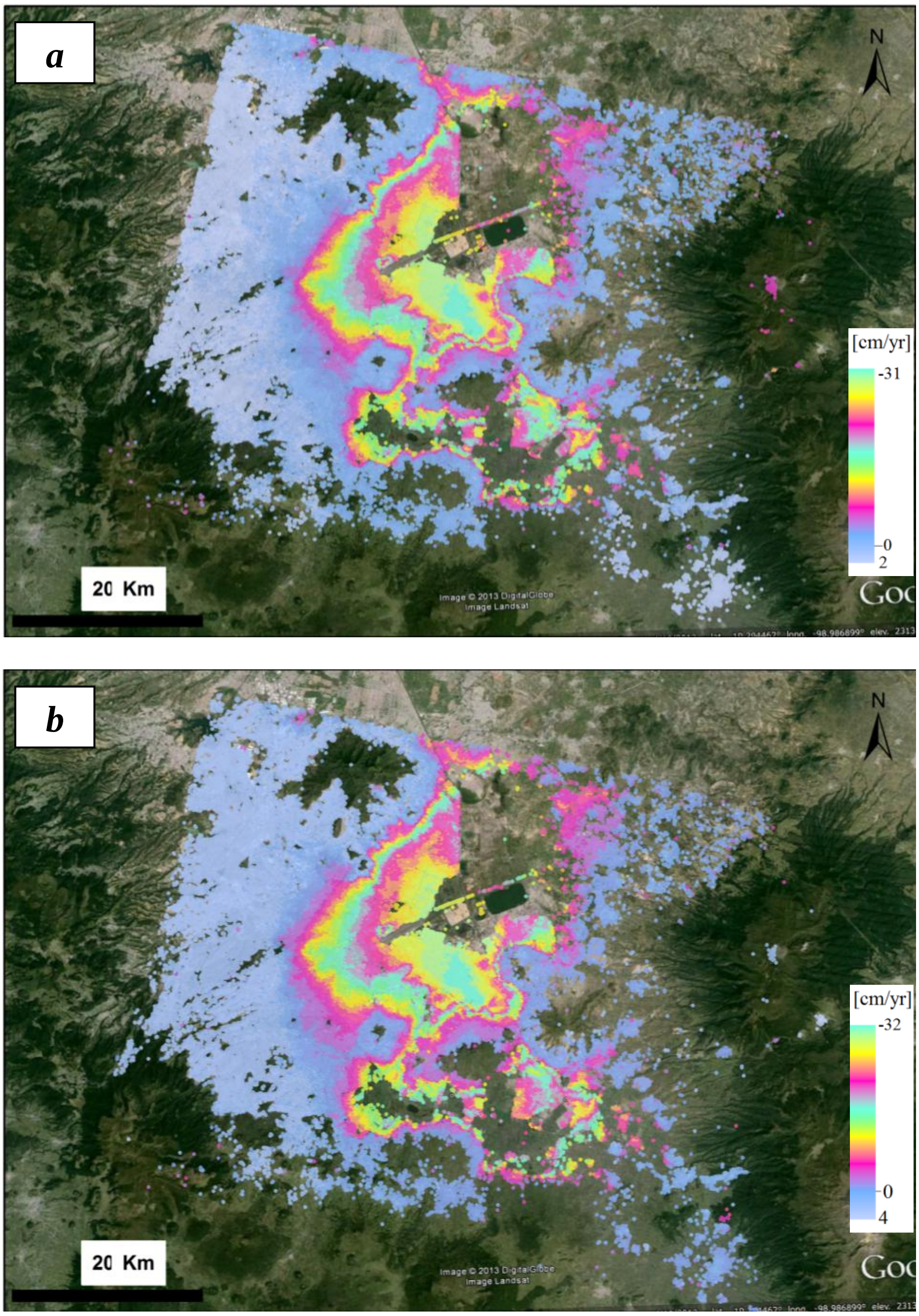

Figure 7-32 LOS displacement for two different study periods. *a*) 2002-2010 and *b*) 2002-2007. Note that there are slight differences between the two maps, and that the maximum average subsidence rate in *a* is slower than in *b***.**

Subsidence rates reduction due to decrease in the extraction rates?

Decreasing of groundwater pumpage and the application of pro-water policies such as artificial recharge and the protection of preservation soil (see Chapter 6) could contribute to the raising of the groundwater levels, delaying the compaction rates and thus the subsidence. Presumably, this could have manifested in the diminishing of the land settlement velocities for the period 2007-2010 as seen in Figure 7-32*a*. To evaluate the correlation between the pumping rates and slow down of the land subsidence, the groundwater abstraction of the PAI wells for the years 2005 (CONAGUA 2006), 2008 (CONAGUA 2009) and 2010 (Cytsa and MAV 2012) were considered (see Table 7-2).

PAI branch	**Extraction Rates (m3/s)**		
	2005	**2008**	**2010**
Reyes-Ecatepec	1.19	1.15	1.05
Tláhuac – Nezahualcóyotl	0.72	0.59	0.52
Mixquic – Santa Catarina	0.48	0.36	0.33
Texcoco – Peñón	0.63	0.61	0.58

Table 7-2 Evolution of the PAI groundwater rates for the 2005-2010 period; data from CONAGUA (2006), CONAGUA (2009) and Cytsa and MAV (2012) (see PAI location in Figure 6-1).

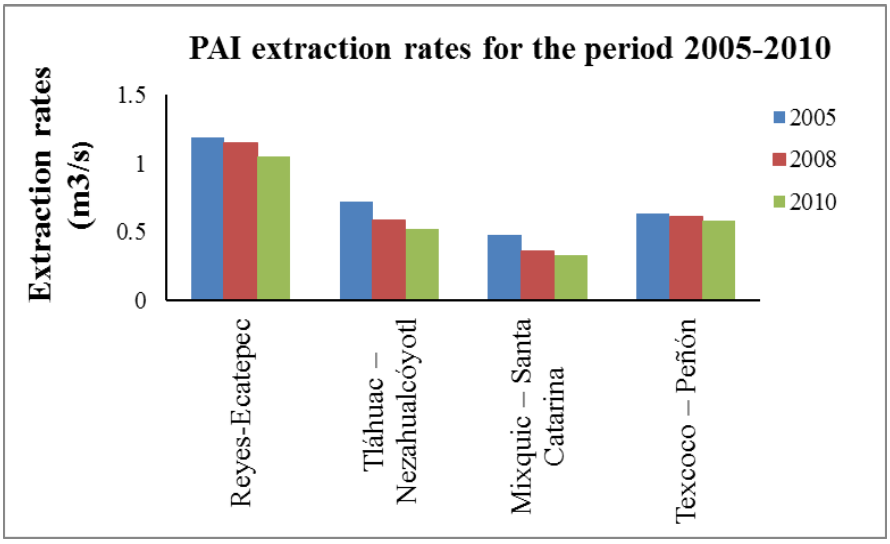

Figure 7-33 Evolution of the PAI branch extraction rates located in southern Valley of Mexico for the period 2005-2010. Note that all pumping rates decreased during that period (see also Table 7-2).

Table 7-2 and Figure 7-33 show the water extraction for the PAI wells located in the south of the Valley of Mexico. Highest extraction rates correspond to the Reyes-Ecatepec branch and the lowest to Mixquic-Santa Catarina. Extraction rates have decreased in all the PAI branches for the period 2005-2010, experiencing the Tlahuac-Nezahuacoyotl wells the highest diminution (~2 m^3/s from 2005 to 2010).

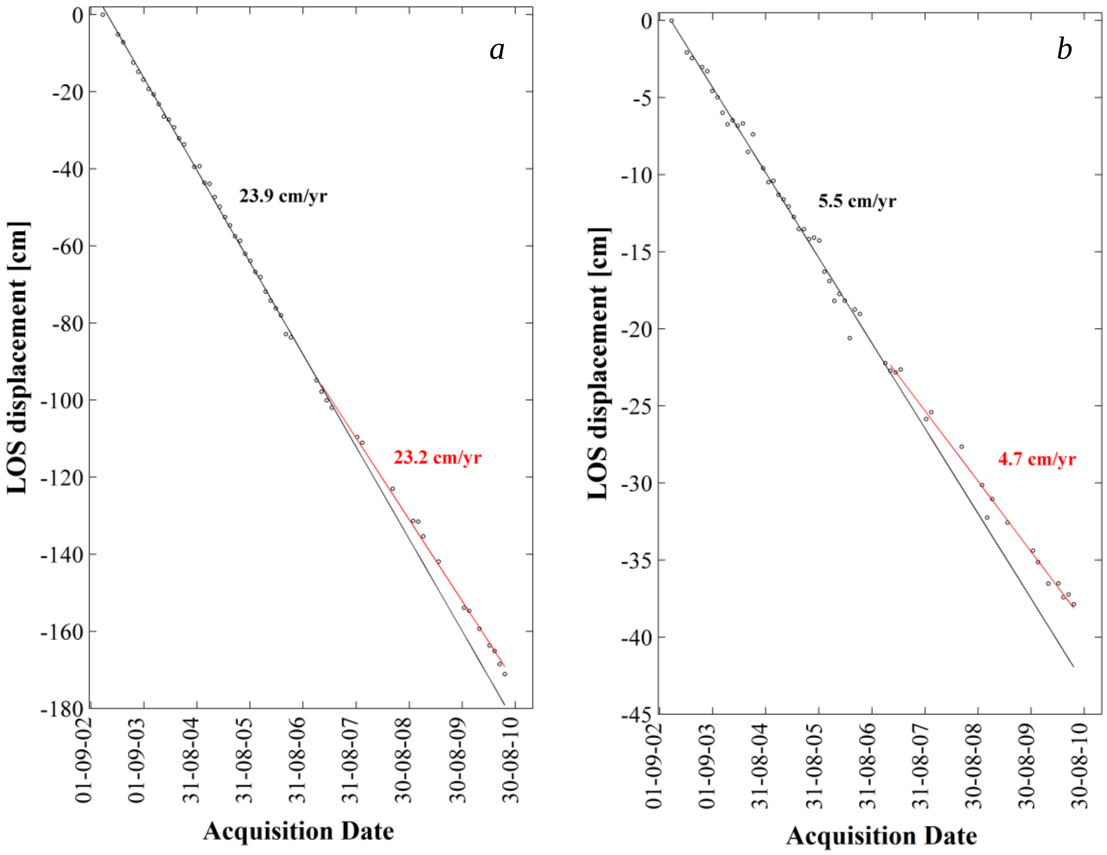

Figure 7-34 Time series for points near two PAI braches. *a*) Mixquic-Santa Catarina PAI branch and *b*) Los Reyes-Ecatepec. Note that the subsidence tends to decrease after 2007 corresponding to the decreasing extraction values observed in Figure 7-33 and Table 7-2. Black line represents the tendency for the period 2002-2007 and the red line for the period 2007-2010.

The observed decreasing extraction rates might have manifested in the reduction of the groundwater level decline, thus possibly slightly decelerating the rate of land subsidence in some areas. Figure 7-34Figures 7-34*a* and *b* show the time series for areas near the Mixquic-Santa Catarina and the Reyes-Ecatepec wells, respectively. Effectively, the time series corresponding to the later zones indicate a smaller tendency slope for the period 2007-2010, suggesting a retard in the sinking rates. However, to achieve more precise conclusions, detailed information about hydraulic parameters and other properties of the lacustrine deposits needs to be investigated to analyse their responses to the changes in the groundwater levels and the reduction of subsidence rates. Moreover, the current interpretation was performed over a local sector, but a more extended area needs to be included to evaluate the regional impact of a probable recovering of groundwater levels and the reduction of the land subsidence rates observed in the mean LOS displacement map.

Underestimation of the subsidence rate due to the inclusion of noisy pixels

Another source of discrepancies between the subsidence rates for the present period of analysis (2002-2010) and the previous one (2002-2007) could have been the inclusion of a larger number of noisy pixels that could have affected the quality of the unwrapping, and thus that of the displacement map.

The presence of a dense network of SDFP pixels with relatively high SNR can, in fact, improve the performance of the unwrapping. SNAPHU requires the resampling of the sparse data into a regular network, thus the use of a larger number of SDFP pixels might produce more reliable interpolation. However, the increment of noisy pixels in the network can impact the quality of the unwrapping solution due to errors associated to phase jumps. Consequently, the estimation of the phase-cycle ambiguities depends not only on the density of the phase-stable points selected but also on their quality in terms of decorrelation.

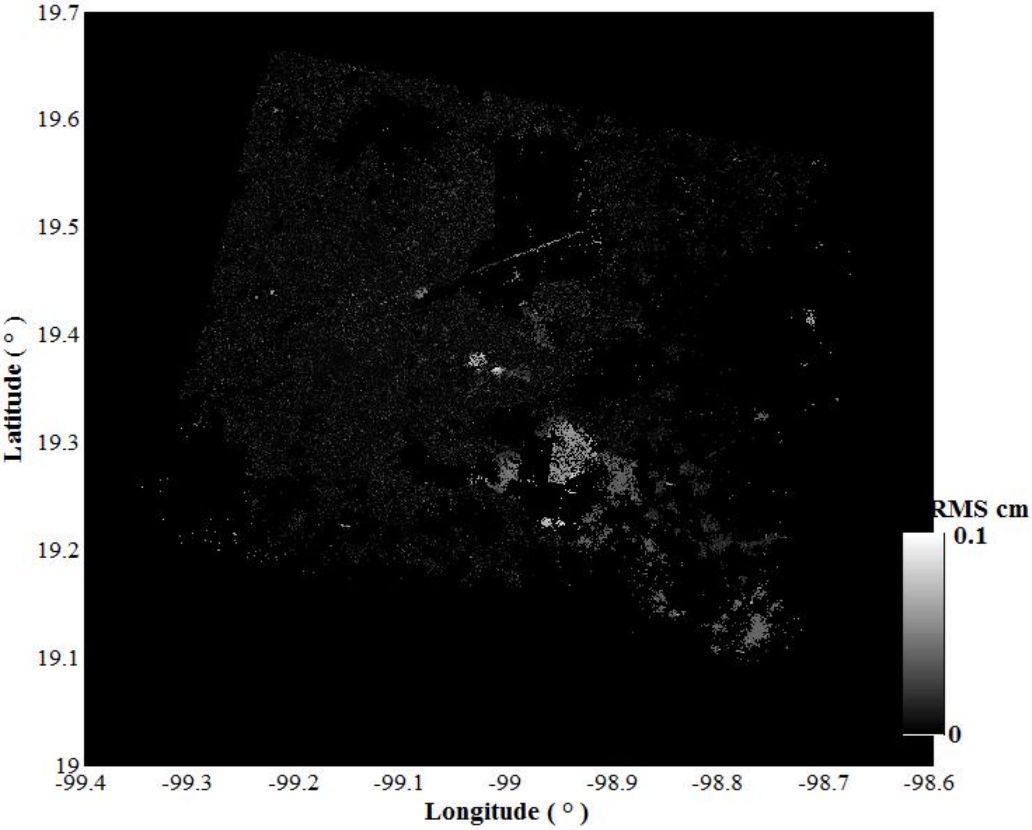

Figure 7-35 System misclosure map computed from the estimated phase delays for the 2002-2010 period.

The inspection of the map of residuals and the global RMS for each interferogram indicate that the inclusion of these points might not notably have affected the unwrapping performance, suggesting that the unwrapped phase delays are sound (see Figure 7-35). On the other hand, the inclusion of a larger number of noisy reference points located in the mountainous areas, affected by atmospheric effects and DEM residual errors, could have biased the deformation pattern provoking an under (or over) estimation of the phase delays (Usai 2001).

In conclusion, even though the InSAR results suggest a reduction of the subsidence for the 2007-2010 period, possibly induced by reduction in the water extraction rates, we do not discard that the inclusion of more noisy SDFP pixels in the present processing could have also influenced the observed results. Thus, a more detailed analysis and geo-hydrological data are required to achieve a more precise conclusion about the clayey deposits behaviour and their relation to the subsidence variation.

7.7.2 Evaluation of the subsidence effect on a main railroad line for the period 2002-2010

The metro is one of the main means of transportation in Mexico City and one with the highest usage frequency in the world (Montañes 2012). The system counts with 12 lines, has a total 195 stop stations and a longitude of 225.9 km. 184 stations are located in the Federal District and 11 in Mexico State.

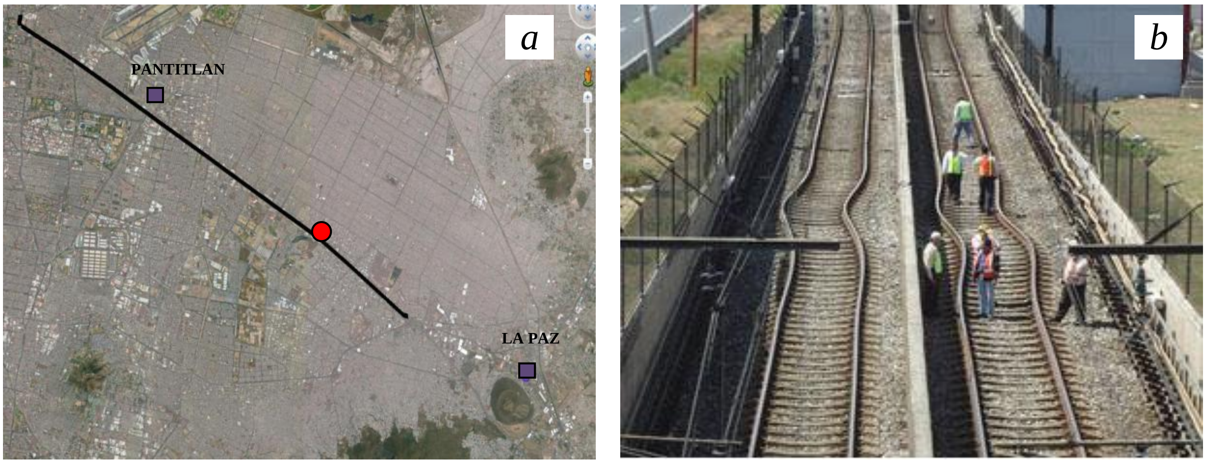

Figure 7-36 *a*) Location on Google Earth imagery of the Pantitlan and La Paz stations. The Calzada Zaragoza Street is denoted by the black line and the red dot indicates the approximate location of the deformation shown in *b*. *b*) Deformation of the railroad line A after the earthquake occurred in March 2012 (from Notimex (2012)) . The seismic movement reach up to a magnitude of 7.4 in the Richter scale.

The metro line A is one of the most important lines (~300000 users per year; STC 2014). It is located in the southeast part of the City and it is parallel to the crowded General Calzada Zaragoza street which connects Mexico City and Puebla (Figure 7-36*a*). Both infrastructures, very important for connection and transportation reasons, have been seriously affected by subsidence and associated soil fracturing (see Figure 7-36*b*). Several sinking and fissured points identified along the railroad have provoked the reduction of velocity from 70 to 40 km/h and the cancelation of services in several occasions. The Calzada Zaragosa has also suffered the repercussions of the overexploitation of the aquifer beneath the City such as the appearance in 2011 of a large ground rupture 2 meters long and wide affecting 10 cars. These events indicate that a monitoring system in this and other areas to prevent catastrophic consequences is necessary. In this context, InSAR techniques appear as a valuable tool for helping risk assessment for civil infrastructure.

Here, InSAR results are used to perform a deformation analysis along these structures for the period 2002-2010. For the present evaluation a profile along the metro line A from Pantitlan to La Paz was constructed (see Figure 7-37*a*). Points within a buffer of 10 meters to each side of the profile were plotted. Figure 7-37*b* shows that the highest subsidence rates occur within the first 7600 meters, comprising mainly lacustrine deposits. The sinking velocities decrease towards the Paz Station located near the Santa Catarina range of volcanic composition. The profile indicates a significant variability of the mean subsidence rates along the metro line that lead to the apparition and propagation of fissures affecting the railroad, the Calzada Zaragoza street and the near communities as well. Moreover, Carreon-Freyre (2011) reported the presence of fractures with E-W direction and aligned with this major street and characterized by important vertical movements.

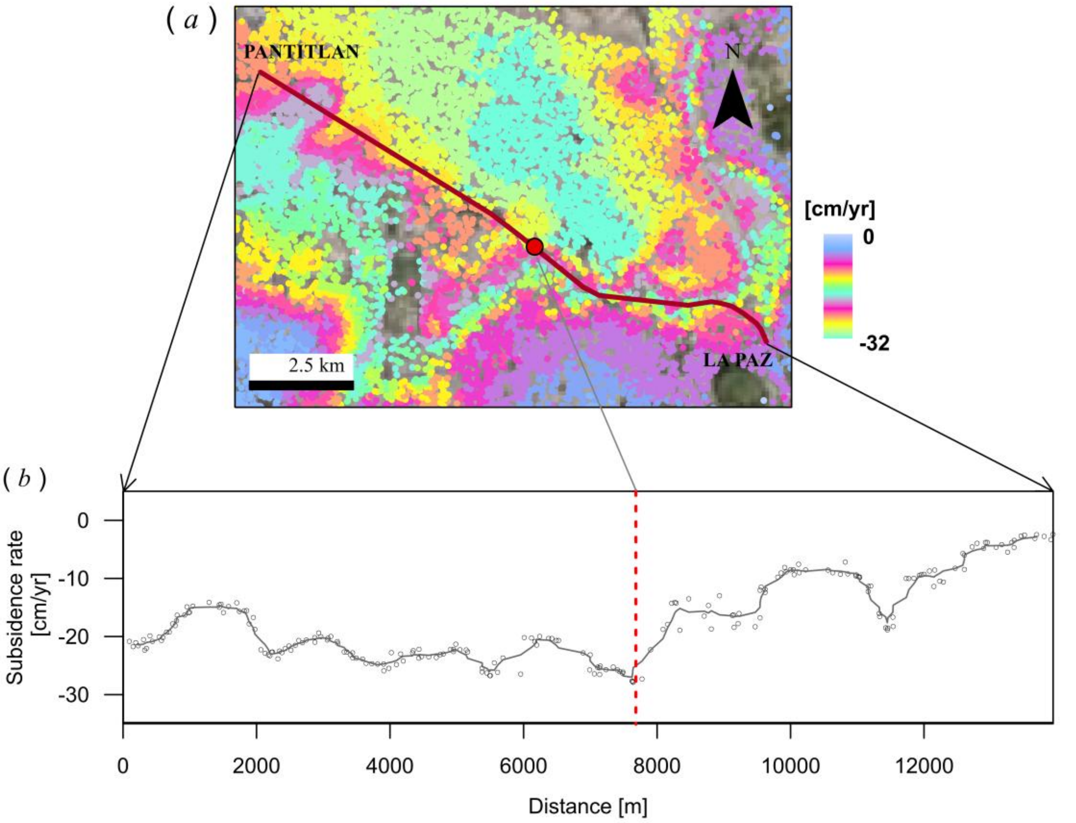

Figure 7-37 *a)* Profile along the metro line A from the Pantitlan to La Paz station (dark red line). The red dot indicates the approximate location of the deformation shown in Figure 7-36*b*. *b*) Velocity profile along the Pantitlan-La Paz segment of metro line A. The dotted red line indicates the area severely affected after the earthquake of 2012.

Considering the high daily traffic in the Calzada Zaragosa and frequency of usage of the metro A, a continuous surveillance of this zone is required. A critical failure in the transportation system due to soil cracking can put into risk thousands of lives. Furthermore, the active seismicity must be considered when assessing the geological risks of the area. In the year 2012 an earthquake of 7.4 in the Richter scale hit Mexico City and its surrounding, being the metro line A and the Calzada Zaragoza one of the most affected structures (see also Figure 7-36*b*). Note that the reported deformation have approximately occurred at the position where very contrasting deformation velocities are found in the profile displayed in Figure 7-36*b*, constructed from the InSAR velocities spanning the 2002-2010 period, before the occurrence of the quake.

This information can help to the evaluation of geotechnical and structural problems of the metro line A and the Calzada, and can complement the proposed re-levelling and rehabilitation Plan (STC 2013).

The use of new acquisitions from satellites such as TerraSAR-X can furthermore improve risk assessment in the area.

7.8 Conclusions

In this Chapter we demonstrate that the SBAS approach of StaMPS is capable of achieving overall subsidence rates (up to ~39 cm/yr) comparable to existing ones, and detecting essential non-linear deformation that could be used to aid risk assessment of ground failure in southern Mexico City. Some local differences between the SBAS methods (Lopez-Quiroz et al. 2009 and the one here explored) are mainly due to different unwrapping procedures and the correction of terms that obscure the deformation signal. Strategies from both approaches can be combined to improve the accuracy of deformation estimation. For example, the use of the stratified atmospheric correction before unwrapping implemented by López-Quiroz et al. (2009). Even though the 3D unwrapping algorithm (Hooper 2010) works, in general, correctly there are some areas where the Nyquist criterion is not fulfilled conducing to an underestimation of the subsidence. In this case, we can help the unwrapping by introducing information about the deformation behaviour estimated a priori, as proposed by López-Quiroz et al. (2009). This way, the number of fringes is reduced and the phase gradients are smoothed, making the unwrapping easier. By using this strategy and the third dimension (Hooper 2010) the performance of the unwrapping can be optimized.

We used an open-source adapted algorithm to produce deformation time series in southern Mexico City, which show an essentially lineal temporal behaviour. Results agree with previous multi-temporal investigations (López-Quiroz et al. 2009; Osmanoglu et al. 2010; Yan et al. 2012) and GPS results (Cabral-Cano et al. 2008; Osmanoglu et al. 2010). Non-linear deformation characterized by a quadratic function was identified in some areas where volcanic cones are located within the lacustrine unit (e.g., unstable area of El Peñon del Marqués). For the latter areas a methodology of analysis by exploiting the InSAR time series is proposed which can be effectively used for identification of faults and understanding of their dynamics (López-Quiroz et al. 2012).

It is well-known that the subsidence affecting the study region is mainly due to pressure loss in the clay-silt layers associated with excessive withdrawal. Nonetheless, contributions from other sources (e.g., compaction of buried trash) could also play an important role in the land settlement as shown in section 7.3.3.

The extended time series analysis covering the period 2007-2010 suggests lower subsidence rates than in the 2002-2007, which could be explained by reduction in the water pumping, presumably contributing to the recovering of the piezometric levels. However, a more in depth study is required to prove this hypothesis. By using velocity profiles, critical failure points were detected along local infractructure; similar methodology can be used to evaluate risk in other structures as well.

Chapter 8

Contribution to vulnerability maps in northern Valley of Mexico from InSAR

The Mexico Basin is part of the TMVB which is characterized by mountains of volcanic origin and by the common presence of faults and high seismic activity (Ovando-Shelley et al. 2013; see also Chapter 6). The intensive groundwater extraction practices together with the existing faults result in land subsidence. This is one of most harmful hazards critically impacting the Valley of Mexico. Subsidence and the associated phenomena cause damage in infrastructure and worsen the water quality which adversely affects people's life.

Many multidisciplinary studies have focused on the south of the ZMVM to measure, monitor and understand the subsidence problem (e.g., Ortega-Guerrero et al. 1999; Figueroa-Vega 1976; Carreon-Freyre and Cerca 2006; Cabral-Cano et al. 2008; López-Quiroz et al. 2009; Carreon-Freyre 2010; Cerca et al. 2012; Osmanoglu et al. 2010). However, a few studies have been performed in the north of the Valley where severe water-related problems, mainly due to the exhaustive withdrawal rates (and drawdown of piezometric levels at approximately 1.17 m/yr; Galindo Castillo et al. 2011), take place. Huizar Alvarez et al. (2003), for example, performed the simulation of groundwater flow in the Pachuca-Zumpango sub basin by means of a finite difference model. A relatively new geostatistical analysis (Galindo Castillo et al. 2011) in the Pachuca-Cuautitlan subbasin concentrate on determining areas where critical groundwater extraction occurs; accurate estimation of the hydraulic balance of the aquifer for the period 1999-2010 was included as well. The existing studies in the north of the Valley (e.g., Huizar Alvarez et al. 2003; Galindo Castillo et al. 2011; Neri-Ramírez et al. 2013) have principally focused on modelling of groundwater flow, estimation of water balance and sustainability of the aquifer; nonetheless, none of them have mapped and analysed in detail the subsidence in this area. In addition, knowledge of the spatial and temporal evolution of the subsidence is paramount to monitor the soil consolidation, define ground failure risk zones and mitigate effects.

Classical surveying techniques such as the GPS and levelling can measure the deformation with high accuracy. However, their spatial coverage is limited, representing an expensive solution. InSAR methods offer a new way to measure deformation at a regional scale with a relatively good accuracy comparable to that of the classical methods under ideal conditions (i.e., reduced height errors and atmospheric delays, high coherence). The MTI configurations (e.g., Ferretti et al. 2001; Berardino et al. 2002; Hooper et al. 2004) have been successfully applied to a number of applications for deformation monitoring (e.g., Perissin and Wang 2011; Hooper et al. 2012; Gourmelen et al. 2010; Perski et al. 2009; Herrera et al. 2009; Chen and Lin 2012; Engdahl and Hyyppä 2003).

In this chapter, a detailed analysis of the subsidence in northern Valley of Mexico based on the interferometric techniques is performed. The impact of the ground settlement is evaluated over main infrastructures and areas prone to fissuring are identified. For this purpose, a methodology for automatic detection and modelling of the non-steady component is proposed. Different fissure trigger mechanisms and their interaction are analysed in detail.

8.1 Preliminary D-InSAR survey of the northern Valley of Mexico

The conventional InSAR consists of the generation of an interferogram using a pair of SAR images. Even though, the method presents some limitations as emphasize previously (see Chapter 3), primarily due to the atmospheric delays and coherence loss, it is a useful tool for preliminary survey of areas affected by deformation.

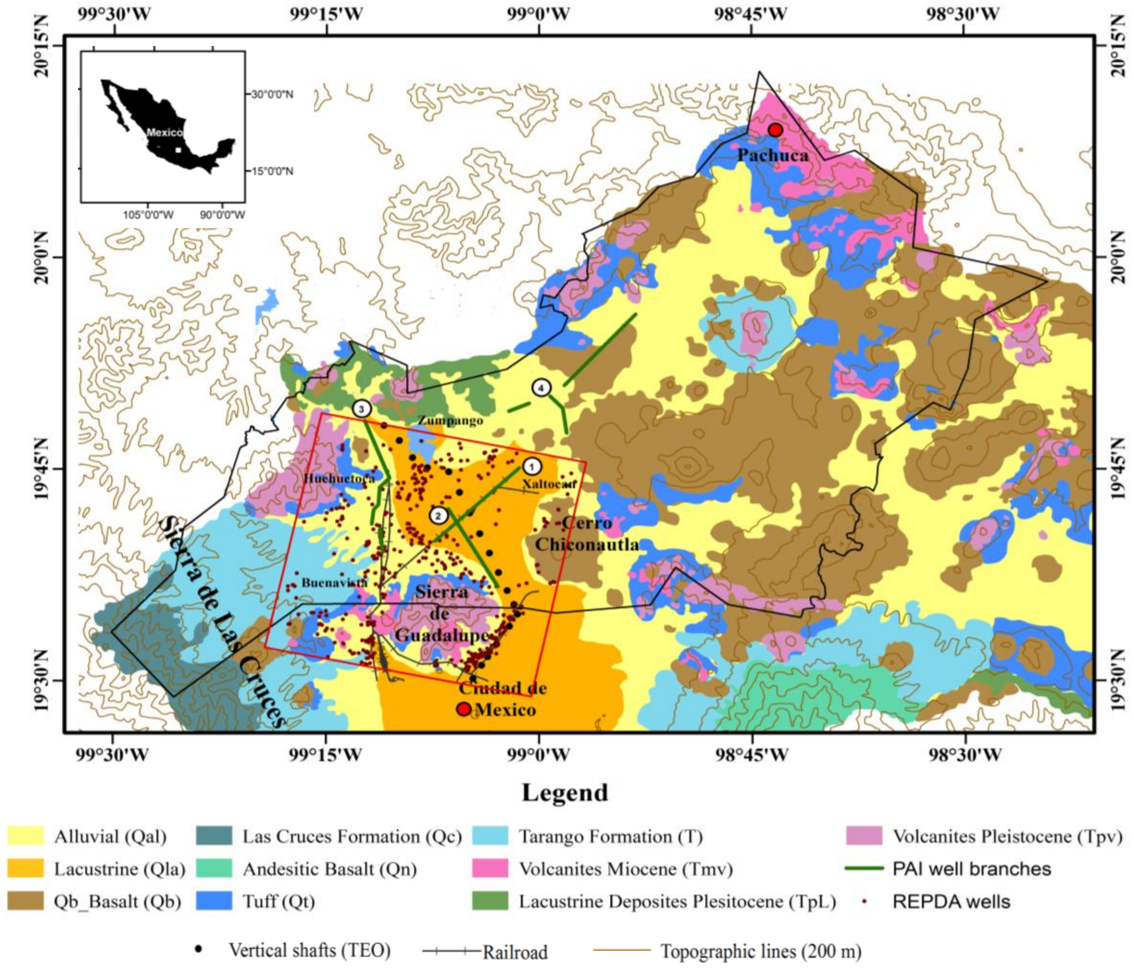

Figure 8-1 Geological map of Mexico Basin (based on Carrera-Hernandez and Gaskin 2007). The red box indicates our survey area, partly encompassing the Pachuca-Cautitlan subbasin (black Line). Geology is overlaid on the topographic map (INEGI), with main railroads of the area. Location of the TEO and wells within the study area are also represented. PAI brach wells depicted by the green lines are included (1: Los Reyes-Ferrocarril, 2: Los Reyes-Ecatepec, 3: Teoloyucan, 4: Tizayuca-Pachuca). The white rectangle in the small inset figure to the upper left outlines the area of research in Mexico.

The northern part of the Valley encompassing the Texcoco and the Cuautitlan-Pachuca subabsins (see Figure 8-1), was first examined using the D-InSAR technique to identify subsiding areas that are later subjected to a detailed multi-temporal analysis. In order to mitigate the effect of the components that reduce the potential of the conventional InSAR, pairs of images with small temporal and perpendicular baseline were selected.

8.1.1 SAR data and D-InSAR processing

For the present D-InSAR analysis we used a set of 10 radar images acquired by the ENVISAT (frequency 5.331 GHz) and ERS 1/2 (frequency 5.3 GHz) satellites. The scenes cover the period from 1995 to 2010 and correspond to descending orbits.

The conventional InSAR analysis was performed using the ROIPAC software (Rosen et al. 2004) including the conversion from raw images to SLCs (see Chapter 2).

Orbital effects in the ERS pair were reduced by using the precise orbits from the DEOS, and for the ENVISAT data set precise orbits provided by the European Space Agency (ESA) were employed.

Pair	Satellite	Dates	B_t [days]	B_{perp}[m]
A	ERS 2	29 Dic 1995 - 02 Feb 1996	35	125
B	ENVISAT	03 Nov 2003 - 12 dic 2003	35	63
C	ENVISAT	26 Nov 2004 - 31 Dic 2004	35	65
D	ENVISAT	01 Dic 2006 - 09 Feb 2007	35	54
E	ENVISAT	25 Nov 2009 - 05 Mar 2010	70	30

Table 8-1 Characteristics of the 5 differential Interferograms presented in Figure 8-2.

The traditional InSAR approach exploits two SAR images over a common area acquired at different times (Massonet and Feigl 1998). This technique uses the phase difference of the backscaterer signal to measure changes on the ground surface. The main steps involved are: co-registration, interferogram generation, removal of flat and topographic phase, filtering, unwrapping, conversion of unwrapped phase to range change and geocoding (see also Chapter 3).

For the current InSAR analysis 5 SAR pairs (1 from ERS and 4 ENVISAT) were chosen with temporal baselines < 105 days and perpendicular baseline < 150 m (see Table 8-1) to reduce geometric and temporal decorrelation. The interferometric pairs span the time interval between 1995 and 2010, and correspond to the dry season (November-April) to reduce the effect of atmospheric artifacts such as vapour content.

Raw images were processed at full resolution (i.e., 4 m and 20 m in azimuth and range, respectively). Once the SLCs images are obtained, a coarse coregistration process was performed to estimate the offsets from the orbits and the scene parameters (temporal and perpendicular baseline, and orbital offset in azimuth and range). Afterwards, a fine coregistration to align the slave and the master was carried out by using a first order affine transformation. As soon as the fine alignments were computed, the slave image was resampled on the master grid by a second order polynomial function. The interferogram was then computed by multiplying the complex master image by the conjugate of the complex slave. A multilooking ratio of 5:1 (approximately pixel size 20 m by 20 m) was applied to the interferogram and the rest of the products.

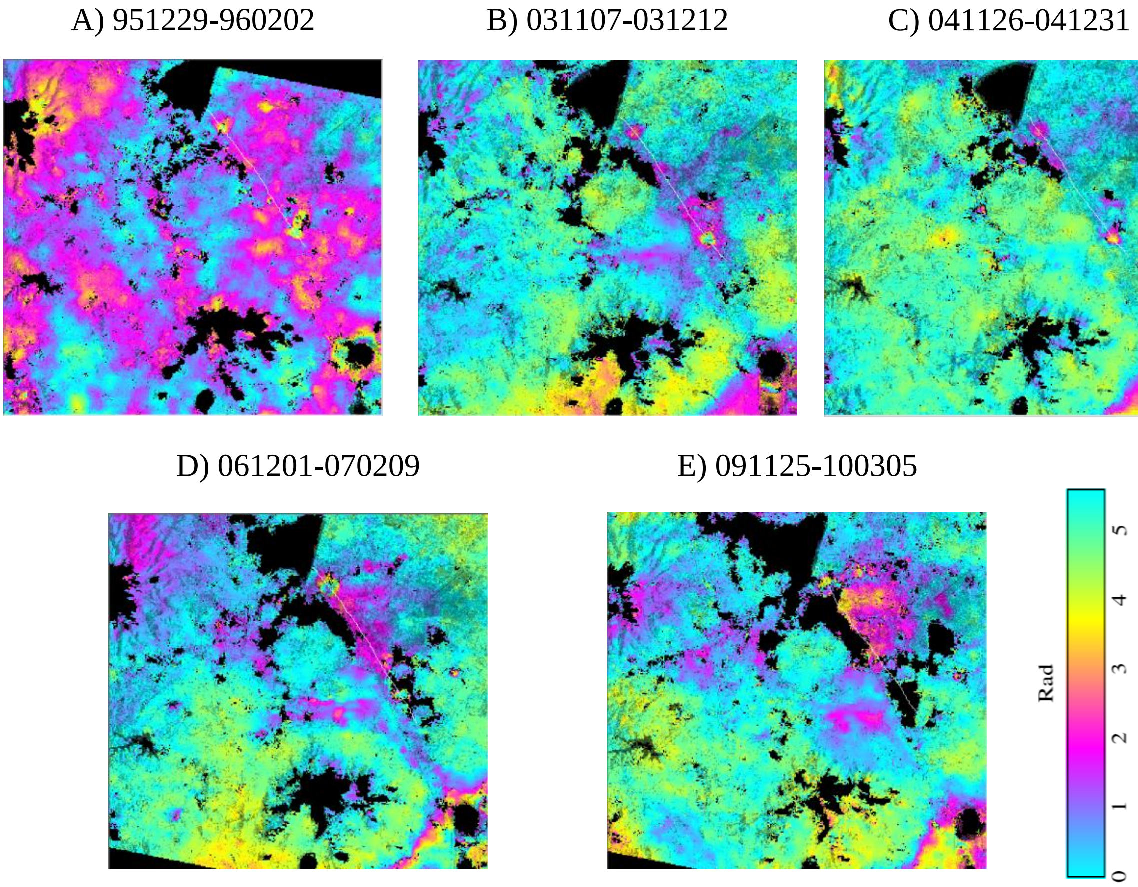
A) 951229-960202
B) 031107-031212
C) 041126-041231
D) 061201-070209
E) 091125-100305

Figure 8-2 Deformation evolution in northern Valley of Mexico between 1995-2010 using ERS 2 and ENVISAT data. Areas highly decorrelated or affected by topography are masked from the unwrapping (Black areas). The white line in each interferogram indicates the location of the corresponding profile shown in Figure 8-3.

A 90 m SRTM DEM version 4 (Farr et al. 2007), given by NASA, was used to reduce the topographic effects and a non-linear adaptive filtering (Gabriel and Goldstein 1988) and was applied to each differential interferogram to increase the SNR and improve the unwrapping, which was performed by using the branch-cut algorithm (Goldstein et al. 1988) provided by ROIPAC. High coherent points (> 0.85) were selected as the initial seed in the unwrapping and a magnitude of 0.2 was stablished for the connection of regions. Finally, the unwrapped phases can be converted to displacement values by multiplying by $\lambda/2\pi$ and geocoded from radar to geographic coordinates according to the DEM SRTM projection.

8.1.2 D-InSAR results and analysis

Figure 8-2 shows the results from the InSAR processing carried out by ROIPAC. The ERS-2 interferogram (Figure 8-2A) with the largest perpendicular baseline may have been affected by residual topographic errors that could have influenced the quality of the unwrapping. On the other hand, interferograms B, C, D and E were less sensible to this type of error due their low perpendicular baseline (< 70 m).

Lower coherent areas such as lakes, cropping lands and areas with sharp topography (e.g., Sierra de Guadalupe) were masked for the unwrapping. Note that the size of black areas, particularly those corresponding to cropping land, increases from 1995 to 2010; presumable some of them might have converted into more extensive and active agriculture zones, and that is why the SNR coming from these regions decreases with time.

Deformation mainly affects the lacustrine plain. Two clear circular patterns near the Zumpango Lake and Tecamac are observed in most of the interferograms and they coincide with the location of some water extraction wells (see Carrera-Hernandez and Gaskin 2007). The presence of these patterns may indicate local change in the hydraulic properties of the deposits. Note that the subsidence rates are lower than in the south of the Valley (particularly, the area corresponding to the Cautitlan-Pachuca subbasin; see also section 7.3). Probably the clay thickness distribution may have an effect on the contrasting rates observed between the north and the south of the Valley. The latter is analysed in detailed in section 8.2.

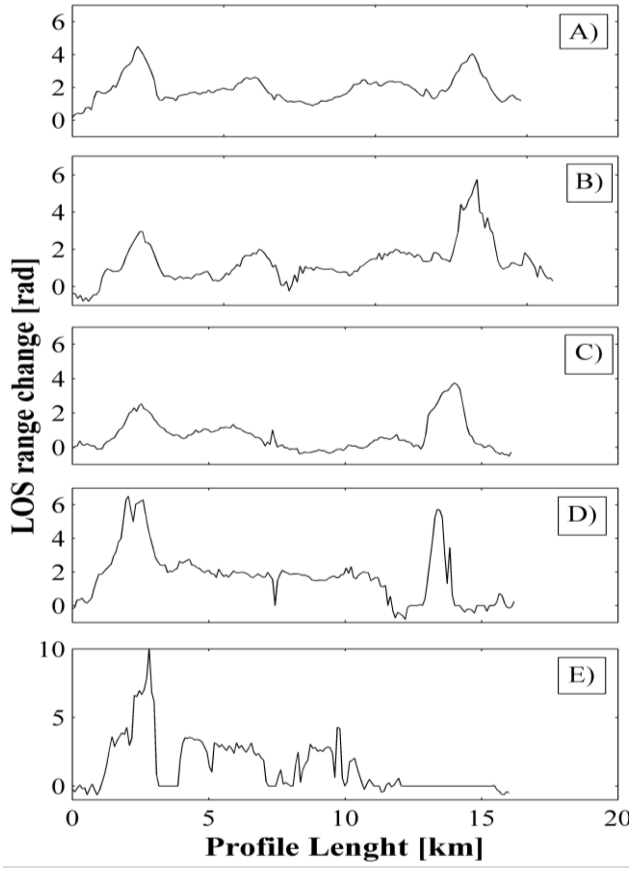

Figure 8-3 Profiles (white line) across individual interferogram in Figure 8-2. Each letter indicates the corresponding interferogram.

Several profiles were built for the different periods to perform a preliminar analysis of the spatial and temporal variation of deformation in the area. The sections correspond to the lacustrine area and traverse the circular subsidence patterns (Figure 8-2). The maximum displacement occurs near the Zumpango lake approximately at 2.5 km distance. Note that in profiles corresponding to 35 days (19951229-19960202, 20031107-20031212 and 20041126-20041231) the maximum displacement is smaller (average 5 rad) than in those spanning 70 days ($\phi_{20091225-20100305}$ ~7 rad; $\phi_{20061201-20070209}$ ~10 rad). The observed values suggest that the the deformation approximately follows a linear temporal behaviour. Nevertheless, it is important to highlight that atmospheric and topographic contributions might not be completely eliminated by the D-InSAR technique. Furthermore, the presence of these elements, especially those coming from local atmospheric heterogeneities, might have decreased the quality of the unwrapped phases and /or could have been wrongly added to the range deformation.

Albeit the limitations of the standard InSAR, the present analysis enables a first identification of areas affected by deformation and its temporal nature.

In order to overcome the constraints of the conventional InSAR technique, the exploitation of multiple interferograms is proposed (see section 8.2).

8.2 Role and need of a MTI analysis in northern Valley of Mexico

Some limitations of the conventional InSAR technique arise from the atmospheric delays and the reduction of the SNR due coherence loss. In the case of Mexico City, due to the high density of man-made structures the coherence is, in general, good particularly where the city is built and the deformation occurs. However, in the northern part of the Valley, where ~30% of the territory corresponds to vegetated and cropping lands, the standard InSAR particularly fails motion detection in the these areas. Moreover, its sparse temporal coverage does not provide enough information about the temporal evolution of the deformation, i.e. the number of highly coherent interferogram spanning a short period of time is limited and combination of images that produces optimal results for deformation studies is not always possible (Bechor 2006). The application of MTI methods such as PS, SBAS and/or their combination offers the possibility to partially overcome the restrictions of the standard approach, enabling the detection and measurement of deformation with sub-centimeter precision. Furthermore, if large data set with high repeated sampling is available, the time series methods provides better signal to noise separation (Bechor 2006).

In this section, the subsidence in the northern Valley of Mexico is analysed by means of the MTI technique. The SBAS method from StaMPS, already assessed in Chapter 7 is proposed for the investigation of this area. The methodology used is briefly described, global ERS and ENVISAT results are given and the impact of subsidence on local infrastructure is evaluated, analysing the cases of the drainage hydraulic project TEO and an existing railway. The proposed technique allowed a detailed monitoring and evaluation of the subsidence in the Cuautitlan-Pachuca subbasin, where a few in situ measurements were available. To our knowledge, no previous detailed time series InSAR studies have been conducted for subsidence evaluation in the entire northern Valley. Furthermore, the observed velocities gradients make possible the identification of possible soil cracking areas which are of high relevance for the generation and enhancement of vulnerability maps in the area. Urban planning, location of wastewater treatment plants and waste disposal sites can be aided by taken into account the information provided in this study. In addition, knowledge of prone to fissure areas is required for the recharge program planned to be implemented in the area (GDF et al. 2012a; Herrera Zaragoza 2012).

8.2.1 Methodology: SAR data and MTI processing

Over 50 radar images acquired by the ASAR (Advanced SAR) sensor on board the ENVISAT satellite, operating in C-band and 11 ERS 1/2 acquisitions were used on this study. The ERS images span the time interval between February 1999 and December 2000. Originally, 17 ERS 1/2 covering the period 1995-2000 were planned to be used. However, because the image from September 19, 1997 was corrupted (see Figure 8-4) it could not be used in the processing, and two periods of analysis (1995-1996 and 1999-2000) were considered to avoid high temporal and geometrical decorrelation that could affect the SBAS analysis. Since only 5 images were available for the first time interval (i.e. a very low temporal sampling), deformation using the ERS data was limited to the period 1999-2000, while the entire ENVISAT data set spanning 2002-2010 was employed.

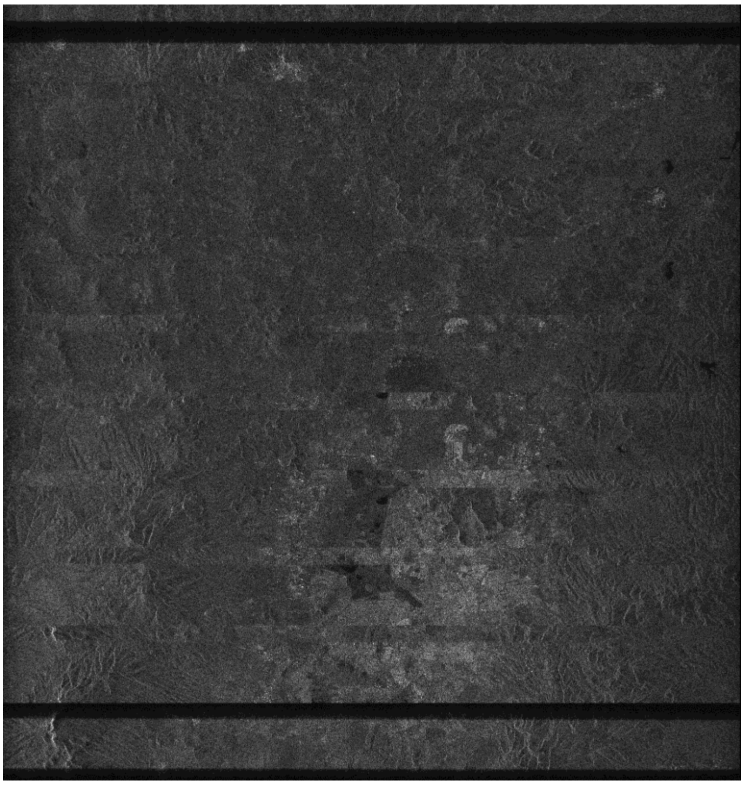

Figure 8-4 Corrupted ERS SAR acquisition from September 1997.

An area of about 30 x 30 km was cropped from all images, corresponding to the north part of the Valley of Mexico which includes part of the Texcoco and Cuautitlan-Pachuca subbasins.

The ROIPAC (Rosen et al. 2004) was used for focusing the raw data and get the SLC product, and the interferogram formation was carried out by DORIS (Kampes et al. 2003). Orbital effects in the ENVISAT and ERS interferometric pairs were diminished by using precise orbits provided by the ESA and from DEOS (Scharroo et al. 1998), respectively. Subtraction of topographic fringes from each interferogram was performed using a 3-arc second SRTM DEM, version 4 (Farr et al. 2007).

The MTI analysis was performed using the SBAS module of StaMPS, which was adapted for selection of an appropriate spatial reference for the present study (see also Chapter 7). This approach has been demonstrated to increase the mean pixel density, allowing a more reliable unwrapping, and thus more accurate deformation time series can be derived. It has the capability to find permanent scatterers where other algorithms fail such as in vegetated areas (Hooper et al. 2004). This flexibility becomes useful since subsidence in the study area also impacts agriculture crops.

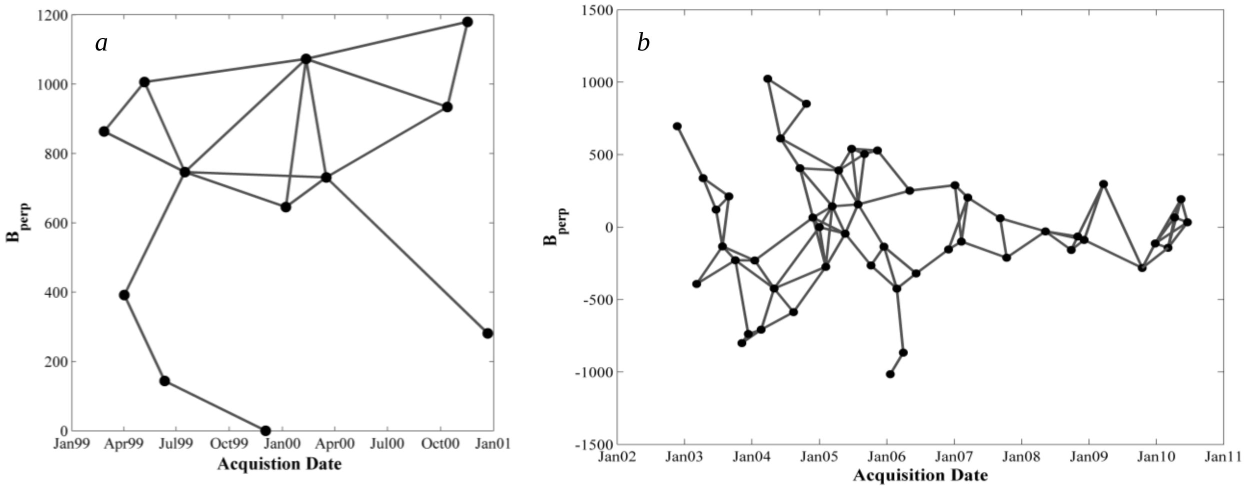

Figure 8-5 Perpendicular versus temporal baseline plots. Black dots represents the images used in the SBAS processing and the grey lines the SB interferograms. *a*) ERS SB interferograms (from February 1999 to December 2000). *b*) ENVISAT SB interferograms (from November 2002 to June 2010).

The SBAS analysis was applied to the set of available ERS and ENVISAT data. All ERS SLC radar scenes were first coregistered to the image from December 03, 1999 and the ENVISAT SCLs to the 12 December 2005 acquisition, taken into account the uncertainty analysis presented in Chapter 5. Note that in both cases the “master” image belongs to the dry season (November - April) to reduce possible atmospheric contributions. Since the available ERS and ENVISAT data does not overlapped in time, the used of an algorithm that combines both sets such as those proposed by Bonano et al. (2012), Pepe et al. (2005), Perissin et al. (2004) was discarded. Nevertheless, extension of the time series by employing for example forecasting methods for time series may be exploited in future work to overcome the non-overlapping obstacle.

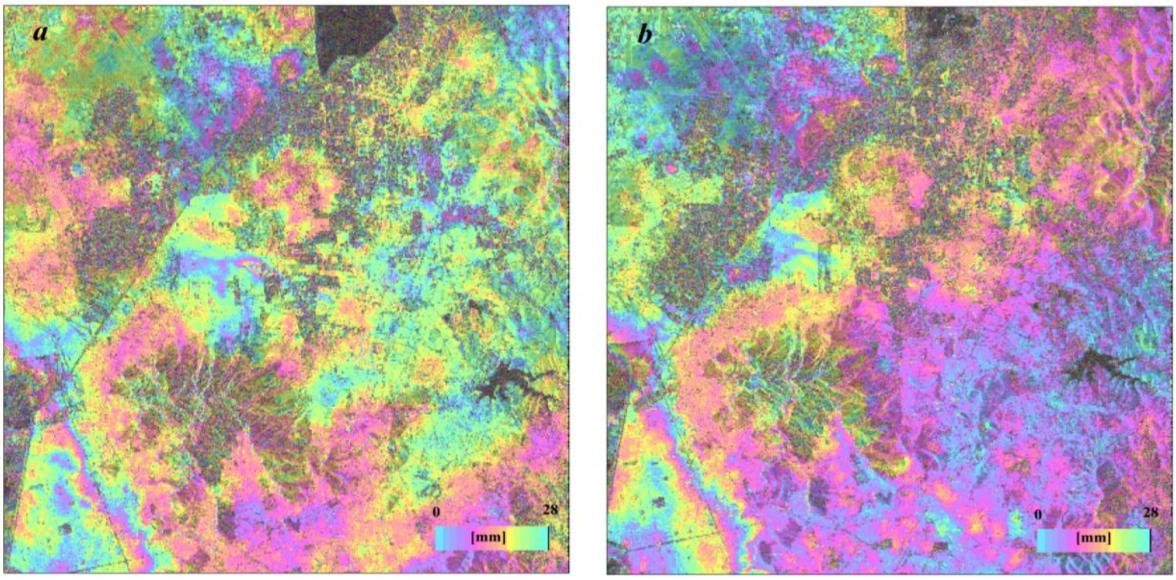

Figure 8-6 Example of SB interferograms with small temporal (70 days) and perpendicular baselines (<150 m), comprising the dry season. a) 20041231-20050311 ENVISAT interferogram. b) 20000107- 20000317 ERS interferogram. Their corresponding coherence map is compared in Figure 8-7.

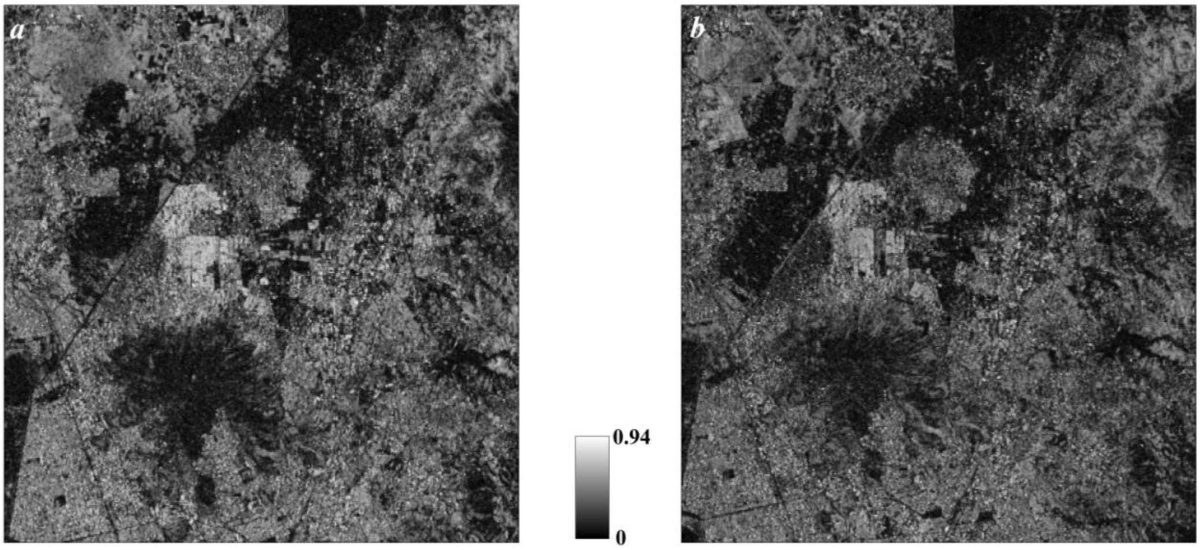

Figure 8-7 Coherence maps for SB interferograms displayed in Figure 8-6**.** *a*) ENVISAT *b*) ERS.

In order to reduce the geometrical and temporal decorrelation, interferograms with perpendicular baselines lower than 600 meters and temporal baselines lower than 350 days were constructed (see Figures 8-5a, b). A total number of 18 ERS and 98 ENVISAT interferograms that provide links between all the corresponding acquisitions were built. After flattening and topographic correction, spectral filtering was applied to the differential interferograms to further reduce the geometric decorrelation (see also Figure 8-6).

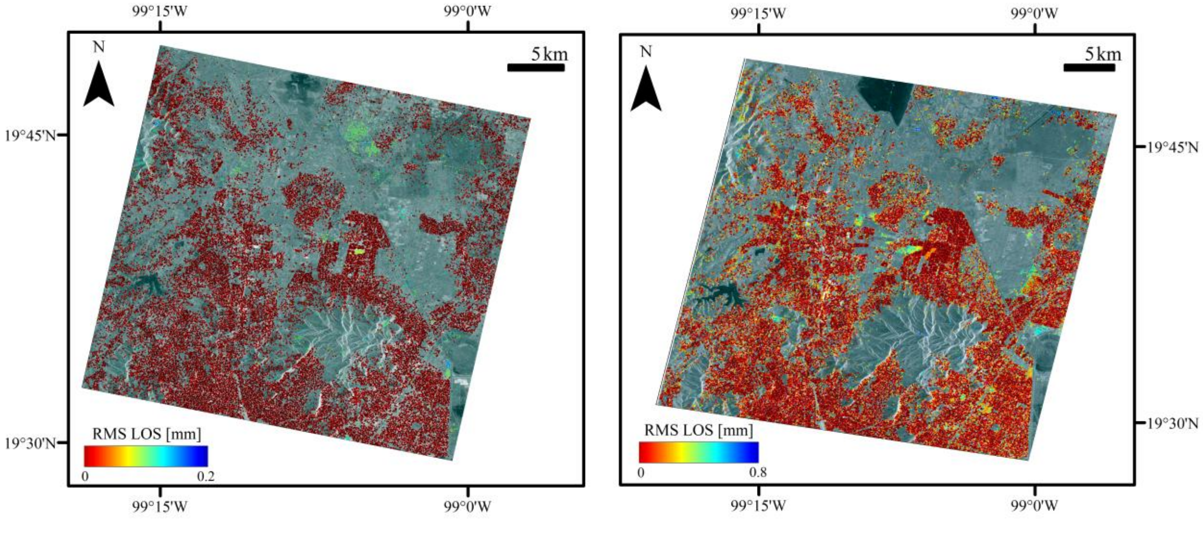

Figure 8-8 RMS maps overlaid on mean amplitude image, corresponding to: a) ERS data set from February 1999 to February 2000 and b) to ENVISAT data set from November 2002 to June 2010. Note that unwrapping errors in both cases occurs in low coherent areas (see also Figures 8-7*a* , *b*), where the deformation gradients are larger or in steep mountainous areas.

The study area was divided into several patches to overcome computational limitations during the SBAS procedure. Initially, SDFP pixels with $D_{\Delta A}$ larger than 0.62 were chosen. Afterwards, a phase stability analysis was performed and SDPFs with a standard noise deviation lower than 1.2 and 1.7 for the ENVISAT and ERS data sets, respectively, were selected for further processing. A larger standard noise deviation was chosen for the ERS to increase the number of selected pixels, particularly in some areas of interest (e.g., cropping land areas). Note that coherence maps in Figures 8-7a, b, indicate that a better correlation characterizes the ENVISAT interferogram; its slightly larger frequency might allow a better identification of certain SDFP pixels (e.g., those corresponding to manmade structures), but ERS may better identify those in vegetated areas.

The unambiguous phase was solved by a 3D unwrapping algorithm (Hooper 2010) which takes advantage of the temporal information (see Chapter 3). The method applies the SNAPHU algorithm for unwrapping the phase in space. For this, the irregular network of the SDFP pixels was first reduced to a regular grid (Shanker and Zebker 2010).

The time series are finally obtained by using the WLS method discussed in Chapter 5 and Chapter 7. In northern Valley of Mexico, the definition of the reference point or area based on in-situ measurements was not possible because to they were unavailable. Thus, the surface geology information (see Chapter 6) and a previous geotechnical study on the area (Juárez Camarena et al. 2010) were used to define the reference area (i.e., slopes of the mountains composed by rigid rocks and where no deformation is expected). This is critical for the correct estimation of the history of displacement and its interpretation.

As a complement to the SBAS analysis, the RMS misclosure map between the observed interferometric phase and the one reconstructed from the estimated phase delays was evaluated (Figures 8-8*a* and *b*). This allows the identification of locations where unwrapping errors occur and the evaluation of the quality of the final ERS and ENVISAT time series. The ENVISAT RMS map (maximum value 0.8 mm) indicates that larger unwrapping errors affected the ERS data (maximum value 0.2 mm); this can be explained by a larger number of noisy pixels or larger deformation gradients in the former case (ENVISAT). Nevertheless, both RMS map suggest a good performance of the unwrapping algorithm and reliable deformation time series.

Previous studies conducted in the Valley of Mexico basin (e.g., Cabral-Cano et al. 2008; López-Quiroz et al. 2009; Osmanoglu et al. 2010; Chaussard et al. 2014) suggest that the main component of the deformation is vertical. Thus, the mean LOS velocities (v_{LOS}) are converted into vertical subsidence v_V using the following expression $v_V = v_{LOS} / \cos\theta$, where θ represents the satellite look angle. Nevertheless, the contribution of the horizontal component in this are still needs further investigation by using terrestrial geodetic methods such as GPS or by combining descending and ascending orbits to reconstruct the 3D geometry of the deformation.

8.2.2 Global ERS and ENVISAT results

More than 55000 and 40000 SDFP pixels using the ENVISAT and ERS data set, respectively, were identified in the study area with a mean point density of 60 ENVISAT SDFP pixel/km^2 and 44 ERS SDFP pixel/km^2. Overall, the SDFP pixel density in both cases tends to be higher in urban areas and decreases in vegetated or in cropping land areas. The average ENVISAT and the ERS subsidence map overlaid in Google Imaginary is presented in Figures 8-9*a* and *b*.

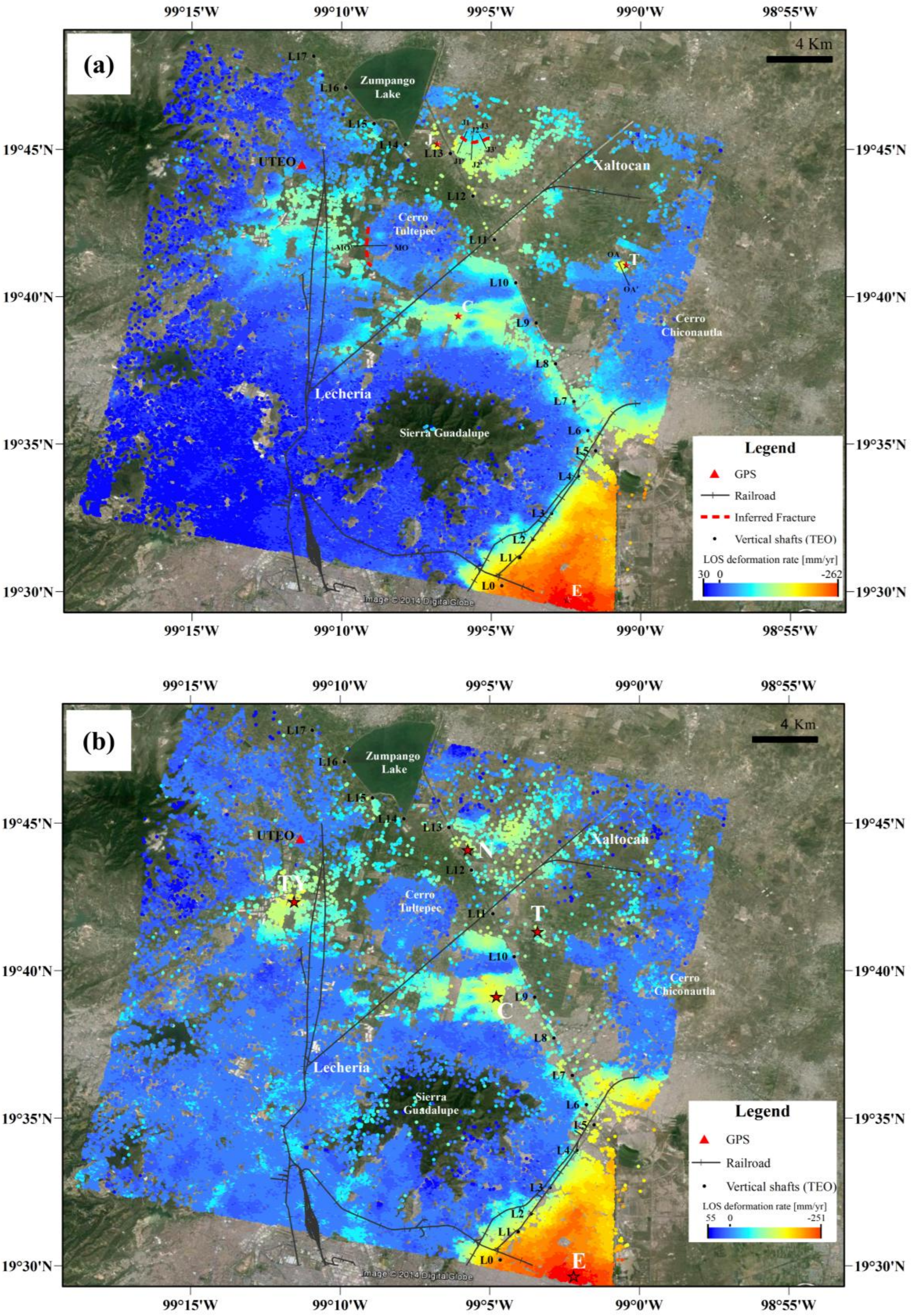

Figure 8-9 *a*) ENVISAT LOS displacement map for the period 2002-2010 . *b*) ERS LOS displacement map, period 1999-2000. Time series at different locations in the ENVISAT (E, T, J, C) and the ERS (E, T, C, TY, J) LOS maps are depicted in Figure 8-10*a* and *b*, respectively.

The subsidence rates tend to increase towards the centre of the subbasins where the thickness of clay-rich deposits is larger (Juárez Camarena et al. 2010). The times series of the areas impacted by the highest subsidence rates are shown in Figures 8-10*a* and *b*, being rescaled to the first acquisition date in each case, although the master database was the image from

December 1999 and December 2005 for the ERS and the ENVISAT, respectively. They suggest nearly constant rates of subsidence in almost all the locations over the approximately 11-year period spanned by the SAR acquisitions. However, non-linear behaviour was also identified in some deformation time series; the observed pattern is later used to develop a methodology to identified areas possibly influenced by fissures (see Chapter 8).

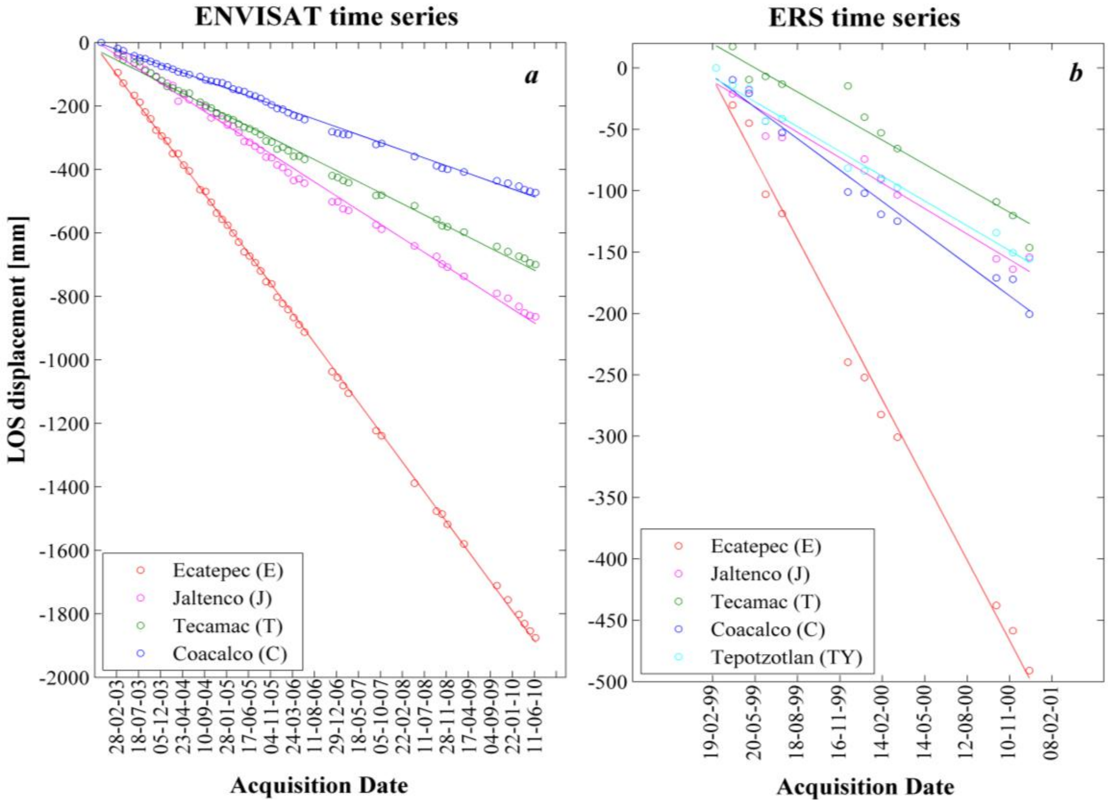

Figure 8-10 *a*) ENVISAT time series spanning from 2002-2010. *b*) ERS time series spanning from 1999 to 2000. Locations of points are shown in Figure 8-9.

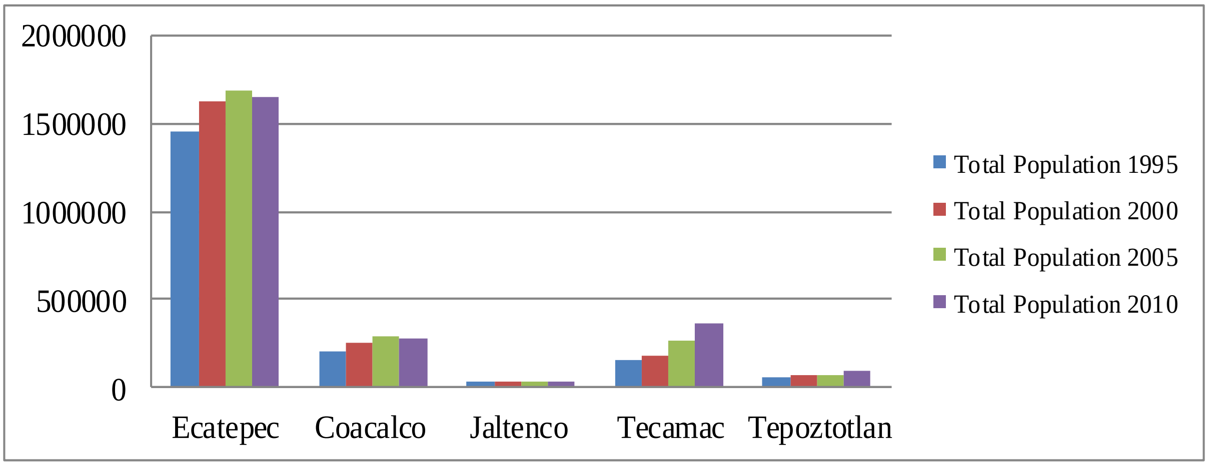

Figure 8-11 Population evolution from 1995 to 2010 (CONAPO 2010).

The ERS and ENVISAT mean LOS displacement maps reveal average increasing subsidence rates in northern Valley of Mexico for the approximately 11-year period of study. Moreover, they indicate that the largest subsidence rates have affected the localities of Ecatepec, Tecamac, Coacalco and Jaltenco. For the period 1999-2000, the municipality of Tepotzotlan was identified to be seriously impacted by subsidence (~ 70 mm/yr in LOS) (see

Figures 8-9*a* and *b*); however, for the 2002-2010 period the deformation rates decreased (~ 53 mm/yr in LOS), presumably due to a reduction in the extraction rates. The rapid subsidence rates observed in the these towns generally correlate with the population (see Figures 8-10 and 8-11), but also with the intensive water extraction intended for agriculture and cattle, such as in Jaltenco and in Tepotzotlan (Estrada Domínguez 2010; Vargas 2014).

Ecatepec, where the largest deformation occurs, is the highest populated city within the study area (see Figure 8-11). The increment of subsidence rates in Tecamac and Coacalco might also have been potentiated due to the demographic growth. Until 2000 the population in Coacalco was much larger than in Tecamac, corresponding to the observed mean deformation velocities which were higher in the first city for the 1999-2000 period. However, according to the plot in Figure 8-11, the difference in population between them decreased, and in 2010 population in Tecamac exceeded that of Coacalco by approximately 87000 people, possibly influencing the more rapid subsidence rates observed (see Figures 8-10 and 8-11). Note that the location of the maximum subsiding points in these cities differs for the two periods of study (see Figures 8-9*a*, *b*), indicating an important spatial evolution of land subsidence affecting new areas (or becoming more seriously in already subsiding areas).

Considerable settling velocities (up to 60 mm/yr and 40 mm/yr found in the LOS ENVISAT and ERS velocity maps, respectively) have also been detected in agricultural zones. Some subsiding areas are distributed as elongated patterns particularly those corresponding to the location of the PAI wells (see also Figure 8-1).

The overall increasing rural-to-urban migration in the area in the last years accompanied with an intensive growth in the water demand may have intensified the land settlement. Moreover, the water recharge progressively decreases due to the urban sprawl over potential groundwater recharge zones. Even though the decrease in the water levels for the study area is larger than in the south of the Valley (Carrera-Hernandez and Gaskin 2007), a lower presence of the fine-grain compressible deposits (silt and clay) in the northern area could explain the smaller subsidence rates noted.

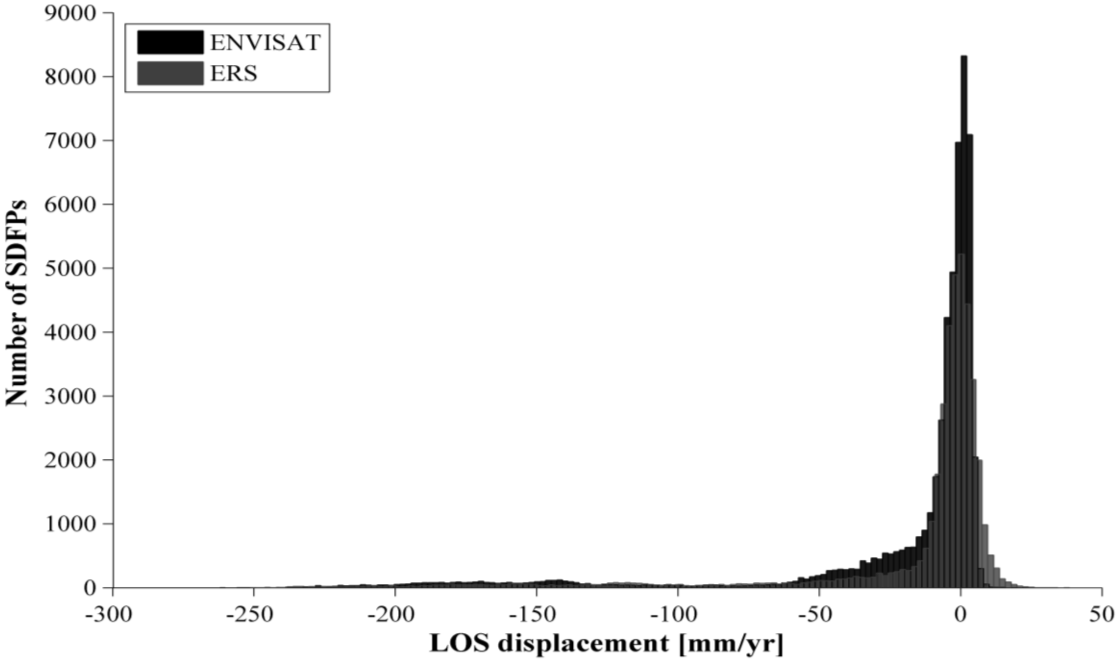

Figure 8-12 Histogram of LOS deformation rates observed in northern Valley of Mexico for two periods: 1999-2000 (ERS) and 2002-2010 (ENVISAT).

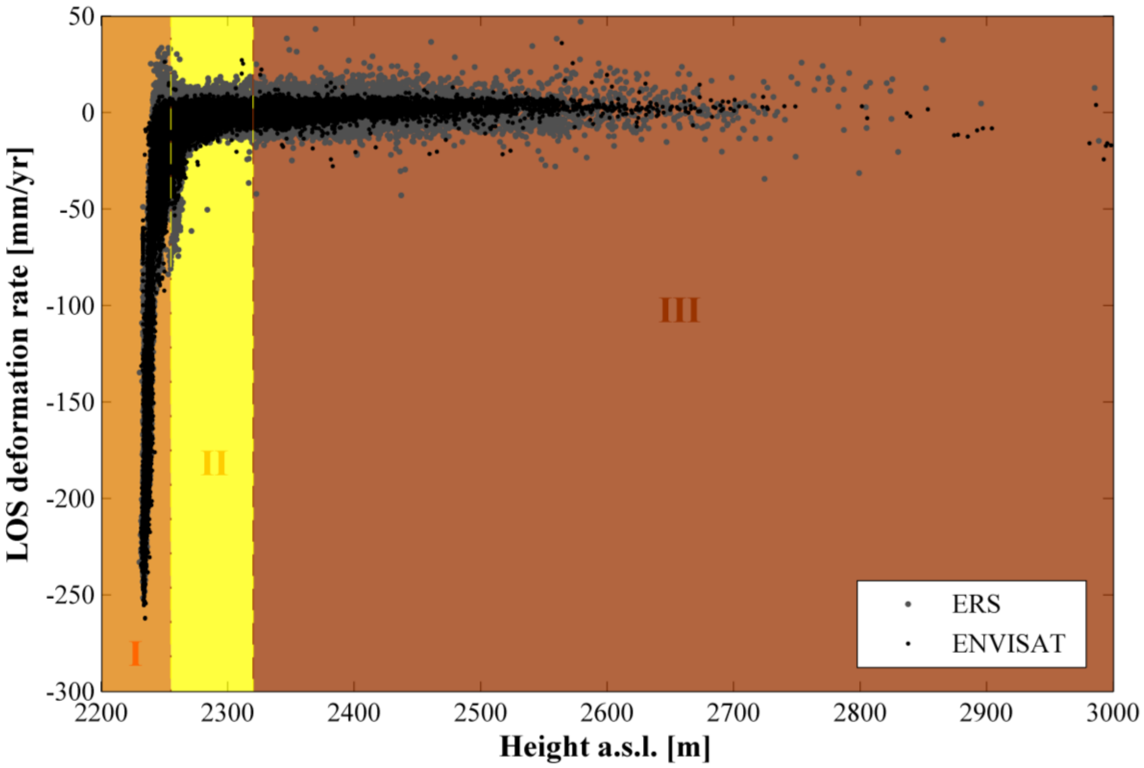

Figure 8-13 Elevation versus LOS range deformation for each SDFPs resulting from the ENVISAT and ERS data processing. The different colours indicate the approximate location of zone I (Orange; mainly lacustrine deposits), zone II (Yellow; mainly alluvial deposits) and zone III (Brown; Basalt and vulcanites) in northern Valley of Mexico based on height information and geology (see Chapter 6).

The histogram in Figure 8-12 presents the LOS deformation rates for all SDFP pixels for the ENVISAT and ERS data sets. In both cases most of the phase-stable pixels detected correspond to negative values while a small percentage correspond to positive or almost zero values, confirming subsidence in the study area. Furthermore, the number of pixels experiencing “uplift” is larger when performing the processing using the ERS data. The latter can be also seen in Figure 8-13 which compares the LOS deformation rates to the elevation of individual SDFP pixels. This graphic suggests that subsidence occurs principally in compressible deposits (alluvial and lacustrine) found at altitudes lower than ~2250 m.a.s.l. However, as stated in the previous chapter, some points at locations higher than 2250 m.a.s.l. display movements toward the satellite that can be interpreted as a consequence of the aquifer recharge, or suggest the need for a better estimation. The positive “movement” observed in higher areas (e.g., Sierra de Guadalupe, Sierra de Las Cruces) could also have been due to the atmospheric contribution. This factor should be considered in the analysis of the time series since some of these points might be included in the reference area, thus possibly biasing the entire subsidence pattern. Particularly in the ERS results this effect may manifest more notably than in the ENVISAT case, since a larger number of pixels, possibly be contaminated by atmospheric delay, is included as reference (see also Figure 8-13).

8.2.3 Impact on main infrastructure and soil fracturing: period 2002-2010

Considering the better temporal and spatial sampling over the region of interest provided by the ENVISAT data set in comparison to that of the ERS acquisitions, detailed analysis of important infrastructure and fracturing processes are carried out using the SBAS ENVISAT outcomes.

8.2.3.1 Subsidence at *Tunel Emisor Oriente*

The current drainage system capacity in Mexico City compared to that in 1975 has been reduced of about 30% while the population has doubled its size. The decrease of the drainage capacity has been mainly caused by the subsidence which has modified the channel- and tunnel-slopes preventing wastewater from going outside the Valley of Mexico (see Figure 6-14). To address this problem, the new drainage hydraulic project TEO (started on 2008 and still under construction) aims to avoid inundations in the Valley of Mexico during the rainy season by increasing twice the current wastewater conduction capacity (SEMARNAT 2008). This infrastructure is constituted mainly by a tunnel of 7.5 m diameter and around 62 km long. Furthermore, 24 shafts ranging within depths of 26-150 m are built in the TEO project for maintenance and construction of the tunnel. Therefore, the possible damages due to subsidence are highly relevant for this type of infrastructure.

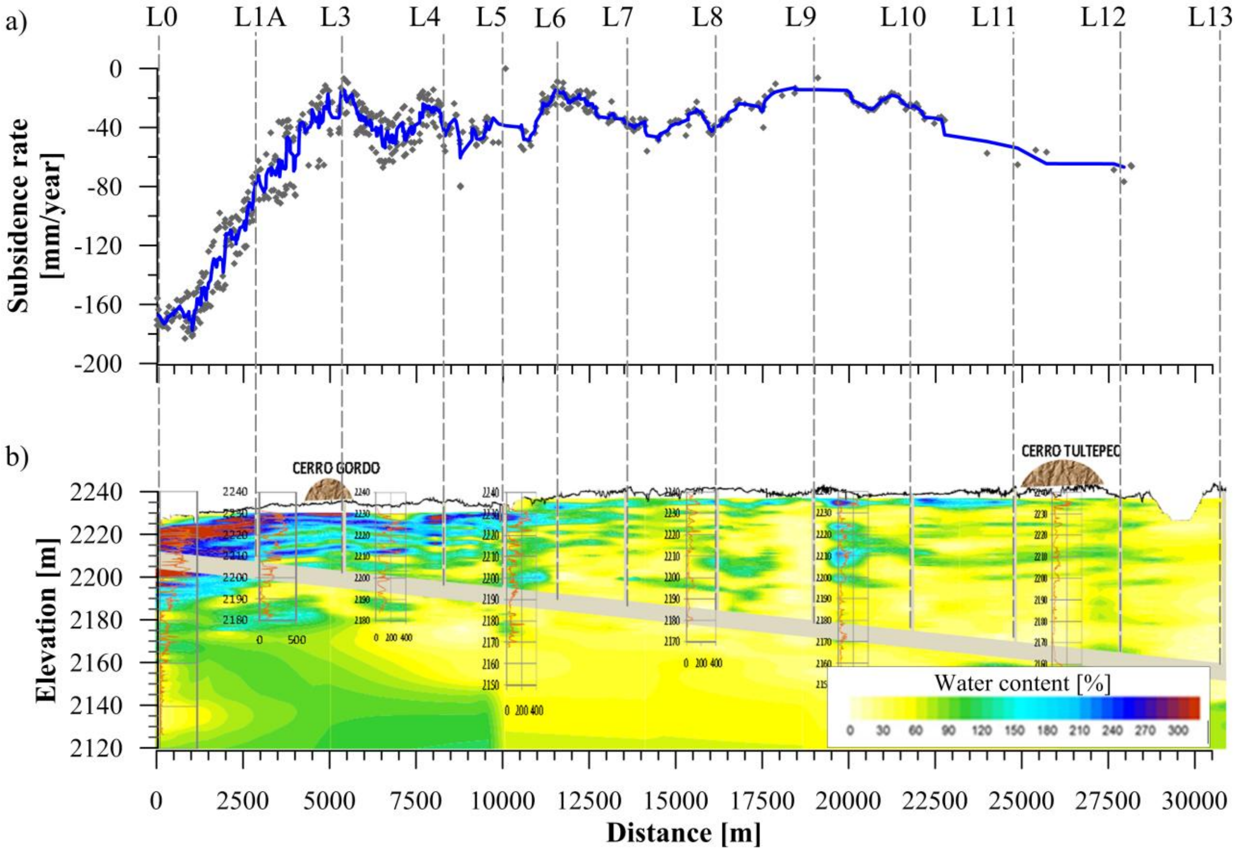

Figure 8-14 a) Subsidence velocity profile along the TEO segment between the shafts L0 and L13. The running average (with a 5 data-points window) is indicated by a blue line. b) Water model content adapted from Juárez Camarena et al. 2010)

The subsidence rates on the TEO based on the InSAR results are therefore analyzed particularly for the segment between the light-shafts L0 (-99.08°, 19.50°) and L13 (-99.11°, 19.75°).The largest subsidence is observed within the light-shafts L0 and L3 (with a distance ~5.4 km in between) where the maximum subsidence rate detected is approximately 185 mm/yr (Figure 8-14a). In Lesser and Cortéz (1998) a mean subsidence rate of 66 mm/yr (1963-1993) was found for the area where the L0-L4 shafts are located, while in the present study (2002-2010) the mean is of 77 mm/yr. Moreover, according to analyses of water content along the TEO (Figure 8-14b) the section between L0-L3 is located over an area with large water content (~150-320%; Juárez Camarena et al. 2010) where thicker clay deposits (see Lombardo 2011) may explain the larger subsidence observed in Figure 8-14.

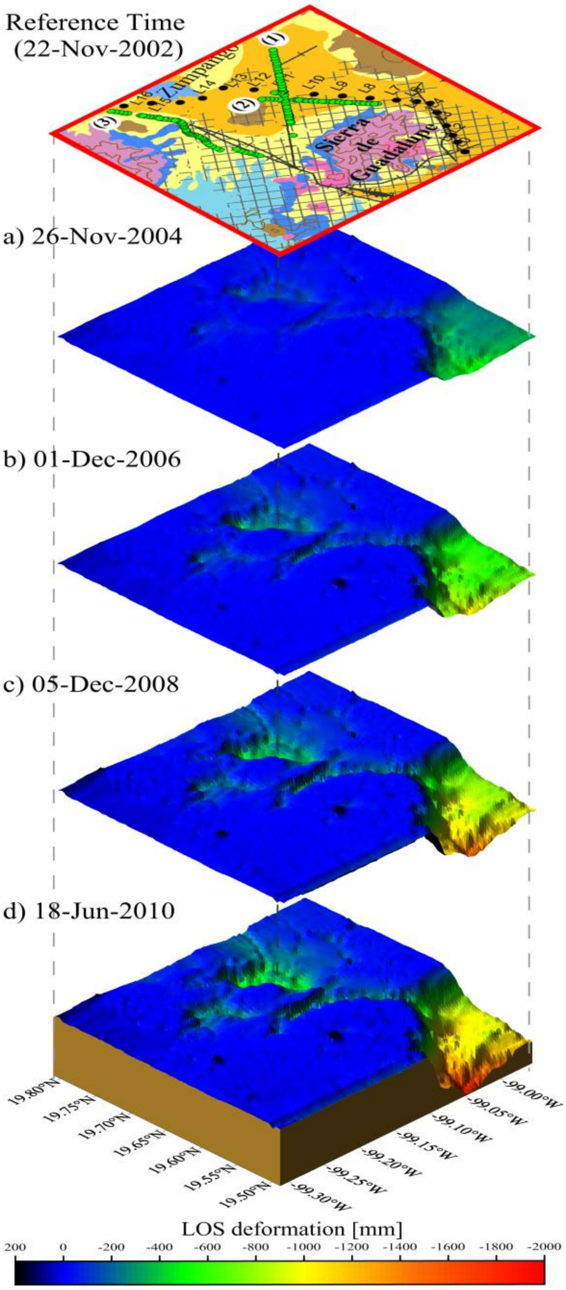

Figure 8-15 3D InSAR cumulative deformation every 2 years from 2002 to 2010. The subsidence is greater to the south of Sierra Guadalupe and lower to the north. Location of the PAI wells: (1) Los Reyes-Ferrocarril (2) Los Reyes-Ecatepec (3) Teoloyucan.

For the segment between the shafts L3 and L12 an average subsidence rate of 40 mm/yr is observed and a maximum up to 65 mm/yr, which is in agreement with values reported by Auvinet et al. (2012). The water content for this region (~0-200%; Juárez Camarena et al. 2010) is smaller than that of L0-L3, being the thickness of the clay deposits also smaller (see Lombardo 2011). Along the distance L3-L12 a battery of PAI wells with large extraction rates (103-135 l/s; Carrera-Hernandez and Gaskin 2007) are found and may induce the observed subsidence rates (see also Figure 8-15). However, thinner clay deposits

(Auvinet Guichard and Moises 2011) might explain the lower subsidence rates on section L3-L12 compared to those of section L0-L3, despite the pumping rates.

In conclusion, the change of subsidence rates along of the TEO seems to be influenced by the depth of clay deposits and water content that characterize the sub-basins where the TEO is located: a) Texcoco sub-basin (shafts L0-L4) and b) Cuatitlán-Pachuca sub-basin (shafts L5-L12). The constrasting cumulated subsidence in these sub-basins can be clearly observed in Figure 8-15.

8.2.3.2 Subsidence at railroad "Lechería-Xaltocan"

The development of a Suburban Railway system was planned by the beginning of the year 2000 to overcome the demand for urban transport in the ZMVM. This project was planned to take advantage of the 242 kms of existing railroads. The central line Buenavista-Cuautitlán-Huehuetoca is now operating, however, other railroads such as "Lechería-Xaltocan" might still be under consideration for urban usage.

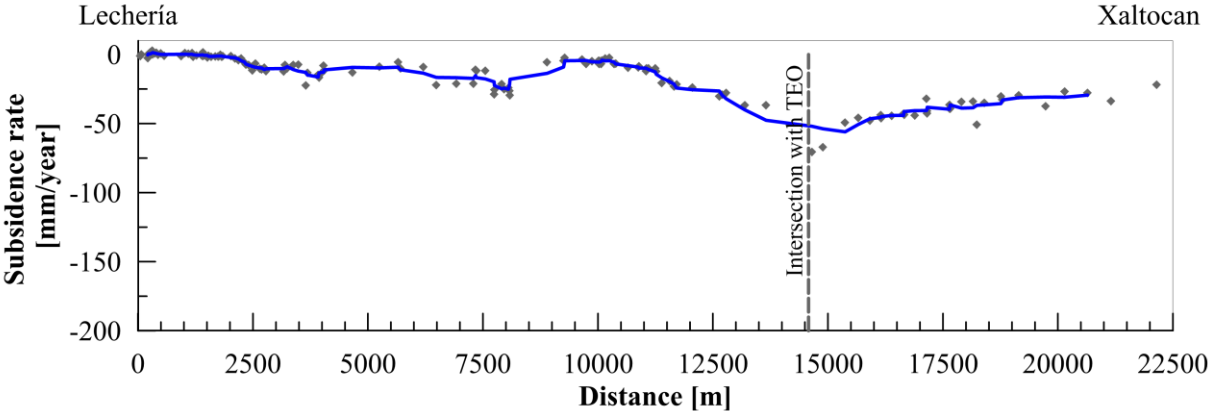

Figure 8-16 Subsidence velocity profile along the Lecheria-Xaltocan railroad. The blue line represents a running average line of the data (5 data-points window).

The subsidence along the railroad Lechería-Xaltocan is shown in Figure 8-16. The locations close to Lecheria (-99.18°, 19.61°) are found over the alluvial deposits (Qal) and smaller subsidence rates (< 20mm/yr) are observed in the first 10 km of the railway. Afterwards, the clay deposits (Qla) become more important and the subsidence increases up to 60 mm/yr. Maximum subsidence occurs close to the intersection of the railroad and the TEO affecting both infrastructures simultaneously, moreover, a concentration of PAI wells is also found on this area which might explain higher subsidence rates (see also Figure 8-15).

8.2.4 Differential deformation and ground rupture

The regional subsidence induced by the severe decline of the piezometric level has had numerous detrimental effects in the north of the Valley of Mexico and other mexican regions as well (e.g., Cigna et al. 2012; Chaussard et al. 2014). One of these effects includes the creation of earth fissures and cracks in the lacustrine deposits, representing a risk for infrastructure and for the population. The exhaustive exploitation of the aquifer causes a decline in the pore water pressure that leads to compaction, thus creating vertical and horizontal tension stresses that produce soil fracturing (Carreon-Freyre 2010).

In the study area, the apparition and/or propagation of soil failures have accentuated, critically damaging infrastructure and threatening people’s life. Velocity profiles have been constructed to locate fractures in certain areas; available records of soil cracking activity (Instituto de Proteccion Civil 2004) were used to support the present analysis.

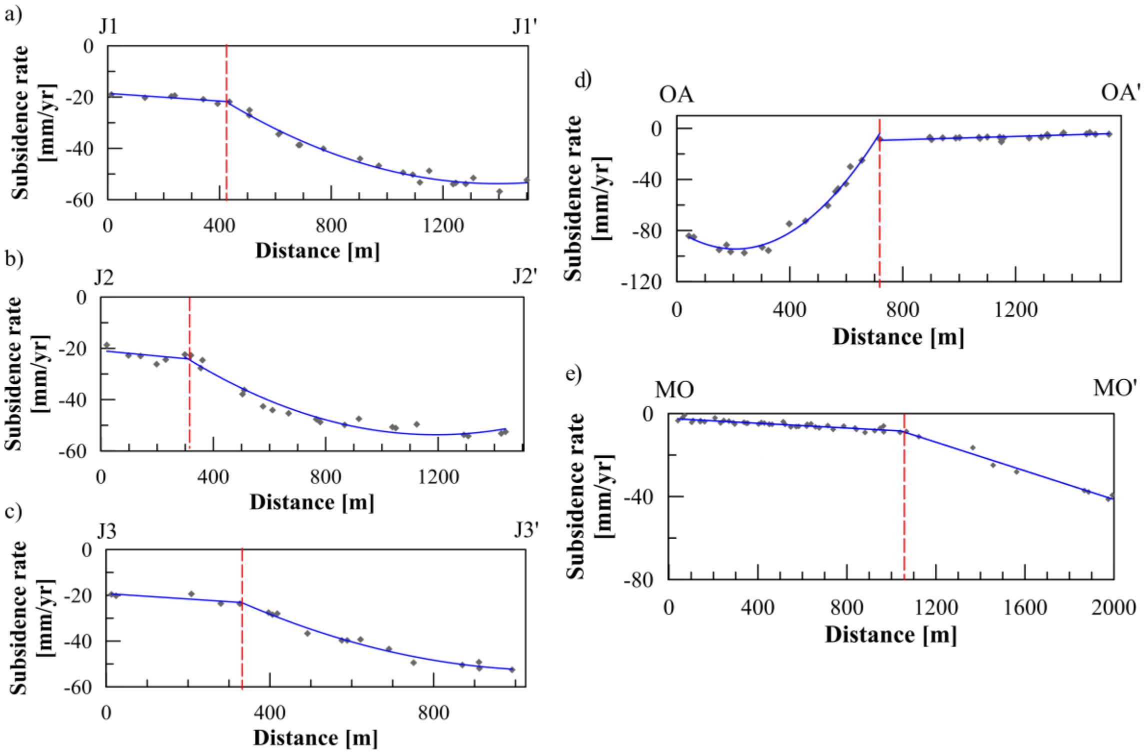

Figure 8-17 Subsidence velocity profiles across the mean LOS rate map shown in Figure 8-9*a*, corresponding to Jaltenco (a, b, c), Ojo de Agua, in Tecamac, (d) and Cuautitlan (e). The dashed red vertical lines represent the location of the inferred fractures. Blue line: velocity trend along the profile.

Our InSAR results indicate that a possible soil fracture can be defined in the locality of Jaltenco, where notable velocity gradients were distinguished in the average LOS deformation map (see Figure 8-9). This area coincides with the location of fissuring events reported by the Instituto de Proteccion Civil (2004). The larger water extraction (35 l/s; (CONAGUA/SIGA 2014) and subsidence rates (average 50 mm/yr) occur on the south side of the inferred fracture, while lower pumping (16 l/s; CONAGUA/SIGA 2014) and LOS mean velocities (average 24 mm/yr) affect its north part. The latter, suggests that the pumping rates correlate with the deformation velocities and that fracturing may be associated to different local tension stresses acting at both sides of the fracture. Moreover, different compressibility variations of the materials at both sides of the fracture (Qal and Qla, predominate in the north and south sides, respectively), might also add to the observed contrasting deformation velocities (see also Chapter 6). Several profiles shown in Figure 8-17 were examined to detect the changes in the deformation velocities and to map the fractures trace. According to the profiles the discontinuity might be associated with a normal fault dipping south with highest deformation rates on the hanging wall (see Figure 8-17a-c).

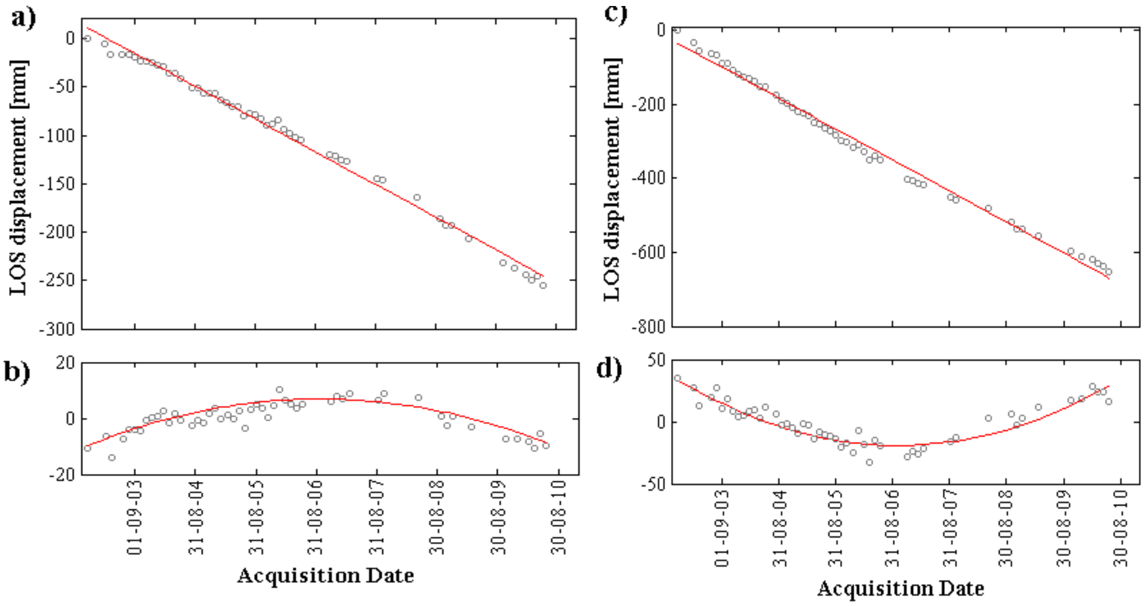

Figure 8-18 Examples of time series showing non-linear deformation. a) Estimated time series deformation and linear fit (red line). b) Residuals between the linear fit and the observations fitted with a quadratic function (red line). c) Time series adjusted with a linear fit (red line). d) Residuals obtained after linear adjustment of the observations in c). The red line represents the quadratic fit.

Soil fracturing has also been reported to affect the Ojo de Agua community (Instituto de Proteccion Civil 2004), which is located in Tecamac. Relatively high deformation rates were identified (up to 80 mm/yr) in this sector. The velocity profile across the area reveals the presence of a major discontinuity (Figure 8-17e). The velocities are larger in the lacustrine and alluvial sequences and decrease towards the Cerro Chiconautla of basaltic composition.

As in the south part of the basin (Siles et al. 2013), in some transition areas, soil fracturing might be associated to differential deformation due to the presence of inhomogeneous composition of materials (e.g., Figure 8-17d). A non-linear component was found to characterize the time series in some of the latter areas. Examples of the time series where non-steady deformation was found are shown in Figure 8-18. The observed behaviour could be explained by contrasting physical and mechanical properties of the materials that interact in volcanic-sedimentary contacts (see section 8.2), contrary to the centre of the lacustrine plain of mainly clay deposits and where the deformation tends to be approximately linear with time (see Figure 8-10).

Some fissures may appear due to water infiltration in rainy seasons or induced by buried geological structures such as grabens. Moreover, the presence of a major graben that links the Pachuca and Zumpango zones (Huizar Alvarez et al. 2003; Marin-Cordova et al. 2004), considered to be an active-transcurrent fault (De Cserna et al. 1988), might contribute to the displacements and associated soil fracturing.

More in depth studies involving geophysical and other in situ measurements are needed to better understand the fracture mechanisms that operate in the area. Moreover, since the fractures are irreversible and propagate once they are generated (Carreón-Freyre et al. 2011), a monitoring system would be useful in fracture-prone areas. As an aid to this purpose, a methodology based on the exploitation of the non-linear component was developed. This method is presented in the following section.

8.3 Methodology for detection of prone to soil fracturing areas

The subsidence in the Valley of Mexico in general presents linear behaviour through time. In some areas, however, non-linear deformation was identified, thanks to the flexibility of StaMPS to detect points undergoing non-steady motion.

In Chapter 7 this component was detected and analyzed in the Penon del Marqués area, where soil fracturing associated to regional subsidence and a sliding mechanism interact producing brittle deformation and destroying the urban and hydraulic infrastructure. Two temporal evolution profiles were constructed, interpreted and compared to the available results from a GPR exploration over the same area (Cerca et al. 2010; Cerca et al. 2012). Both analysis shows that this area, where a quadratic function described the time series (see section 7.6), effectively, is severally affected by fractures. The latter suggests that paramount information for geological risk assessment can be inferred by exploiting and evaluating the non-linear component identified in the time series InSAR. Previous studies (e.g., Cigna et al. 2011; Kim et al. 2010; Ishitsuka et al. 2014) have already profited from the anomalies found in the time series to characterize important events related to the aquifer's behaviour and complex geological proceses in other places.

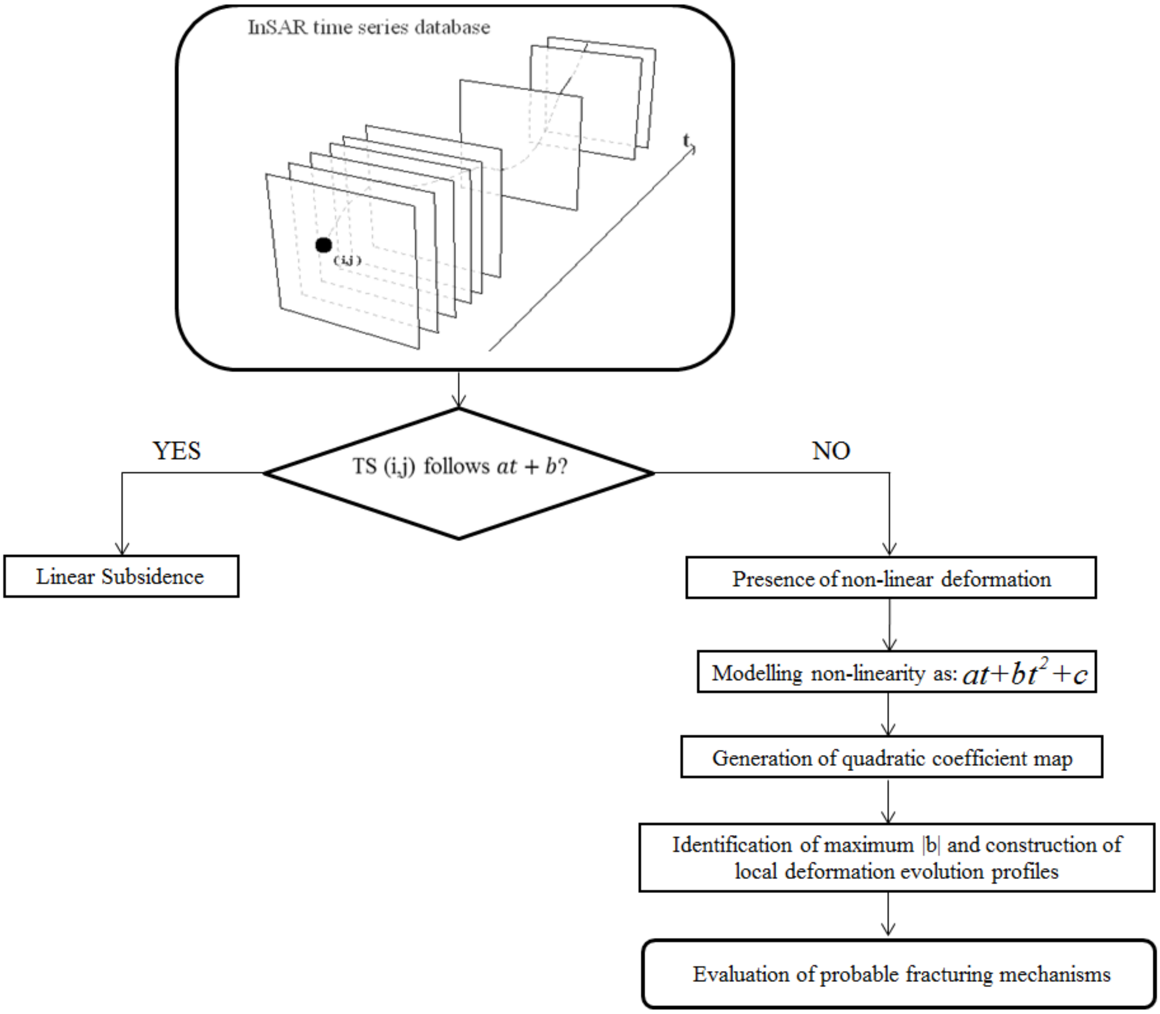

Figure 8-19 Flowchart of the methodology for identification of prone to soil fracturing areas.

As in the south of the Valley, in the north the subsidence is generally of linear nature, but non-steady motion was, as well, recognized in some particular areas where earth fissures occurs as presented in section 8.2.4.

The use of GPR would result very effective for detection and monitoring of prone to soil fracturing areas in northern Valley were a few related studies were performed. In fact, several campaigns were performed in the Valley of Mexico and other mexican zones showing its potential (e.g., Cerca et al. 2010; Cerca et al. 2012; Carreon-Freyre 2011; Cabral-Cano et al. 2010; Barajas-Nigoche et al. 2010). Nevertheless, since only local surveys can be performed by GPR, its usage would result timing and economic costly for a complete soil fracturing investigation over the region of interest. Moreover, the depth of penetration is limited by the presence of conductive clays or high conductivity pore fluid, and the GPR data interpretation requires a highly trained operator or investment in training.

In section 7.6, we verified that the usage of the non-linear information provided by the InSAR time series analysis and the construction of evolution deformation profiles can be used for the location of fractures and understanding of their dynamics. However, a complete, detailed and manual inspection of the times series to detect the non-linear component, in the entire area is not practical considering the density of SDFP pixels (more than 55000 for an area of around 900 km). Thus, a methodology for automatic detection of probable prone to fracturing areas in the northern Valley of Mexico was developed based on the modelling of the non-linear component and construction of deformation evolution profiles where notable acceleration or deceleration are identified. Figure 8-19 shows the flowchart diagram of the proposed methodology.

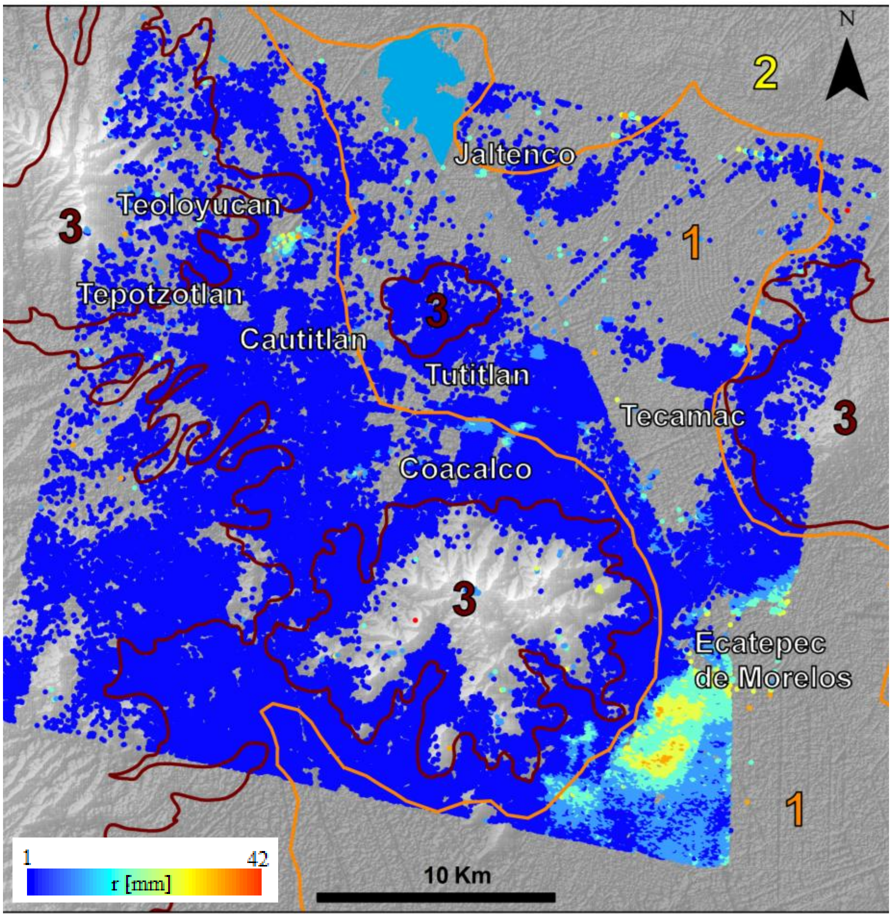

Figure 8-20 Map of residuals **r** indicating non-linear deforming areas overlaying SRTMV4 shaded topography.

The first step is to build a database with the cumulated displacement for the period of study. Afterwards, the time series of each SDFP pixel are analyzed to detect whether or not they adjust a linear model. The magnitude of the residuals between the linear model and the actual deformation behaviour inferred from the InSAR time series, are used to identify non-linear deforming areas (see Figure 8-20). Residuals are computed as (e.g., Lopez-Quiroz et al. 2010):

$$r = \sqrt{(1/M)\sum_{t=1}^{M}(\phi_t - \phi_t^{\text{mod}})^2} \tag{8.1}$$

where M is the number of images, ϕ_t the estimated phase delays and ϕ_t^{mod} the deformation modelled as *at*+*b*.

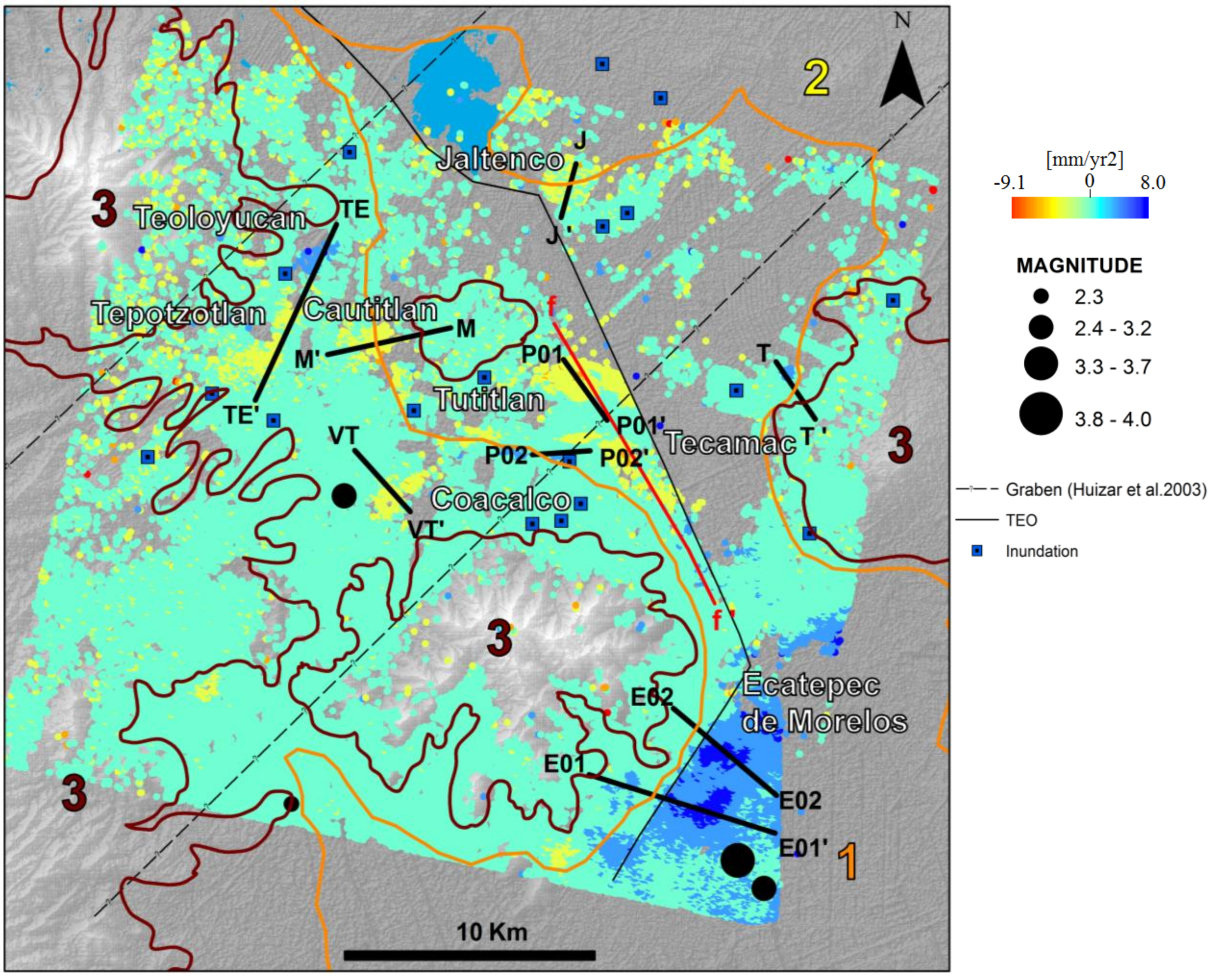

Figure 8-21 Quadratic coefficient map overlaid on SRTMV4 shaded topography. Main towns were the fracturing analysis was performed are labelled, and epicentres represented (INEGI). Surface geology contours are shown dark and light brown (1, 2 and 3 correspond to lacustrine, alluvial, and basalts and vulcanites, respectively). Black lines indicate profiles analysed in section 8.3.1. The geological cross section f-f' used in the discussion is also shown (adapted from Carrera-Hernandez and Gaskin 2007).

Finally, the non-linear deformation is modelled using a quadratic polynomial (based on preceding analysis; see sections 7.6 and 8.2.4) and a quadratic coefficient map is generated by for each SDFP pixel the term *b* from the following equation

$$at + bt^2 + c. \tag{8.2}$$

Figure 8-21 represents the acceleration and decelerating areas mapped from *b*. Previous inspection of the time series in some areas reported to be affected by soil fractures (generally in the transition zones; see Chapter 6) follow a quadratic function. The same was observed in the south of the Valley and described by existing studies (Yan et al. 2012; López-Quiroz et al. 2009; Lopez-Quiroz et al. 2010; Lopez-Quiroz et al. 2012). It is clear that assuming a quadratic function for areas presumable affected by ruptures might not always be correct (see also section 8.5), nevertheless, this first approximation of the non-linear component can be used as preliminary model for their identification as demonstrated in the analysis presented in section 7.6, where also GPR measurements were used for interpretation of the profiles and validation of the fracture location.

We emphasize that detailed geotechnical, geo-hydrological and geophysical information and other local surveys still necessary to prove the assumptions of quadratic deformation behaviour in areas subjected to the apparition or propagation of soil fractures.

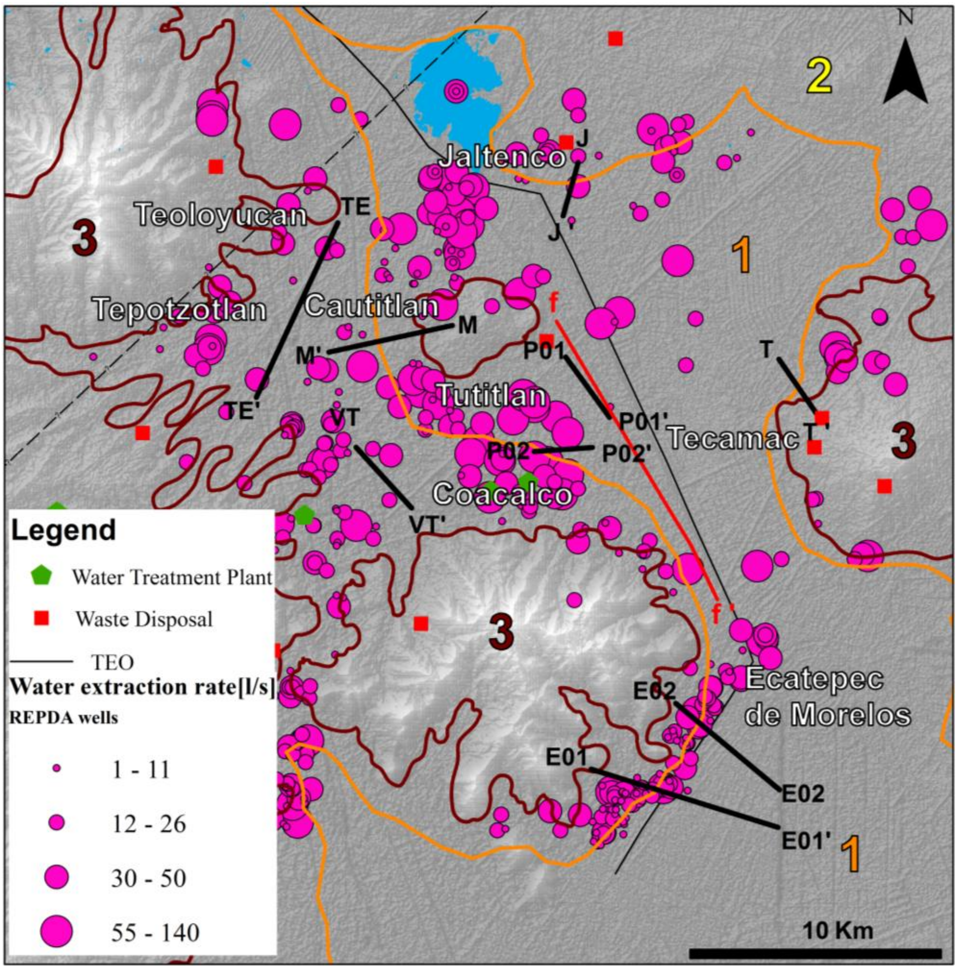

Figure 8-22 Water extraction rates in northern Valley of Mexico (CONAGUA/SIGA 2014). Sections for fracturing analysis are depicted by the black lines. Location of water treatment plants and waste disposal sites is considered in the analysis.

8.3.1 Evaluation of fissure mechanisms

Various information about inundations, soil use, reported earth fissures, geology, water extraction rates, seismic activity and the quadratic map are organized in a common database to identify probable mechanisms triggering fracture (see Figures 8-21 and 8-22). Furthermore, several temporal subsidence evolution profiles were constructed across areas presenting a significant acceleration (or deceleration), and analyzed together with the corresponsing quadratic component section.

The present evaluation reveals that, in general, there is a good correlation between location of higher magnitudes of the quadratic component and the apparition and/or propagation of soil fractures.

8.3.1.1 Ecatepec de Morelos

Figures 8-23*a* and *b* depict the subsidence evolution profile for the period 2002-2010 across Ecatepec de Morelos town which is seriously affected by subsidence and soil fracturing processes.

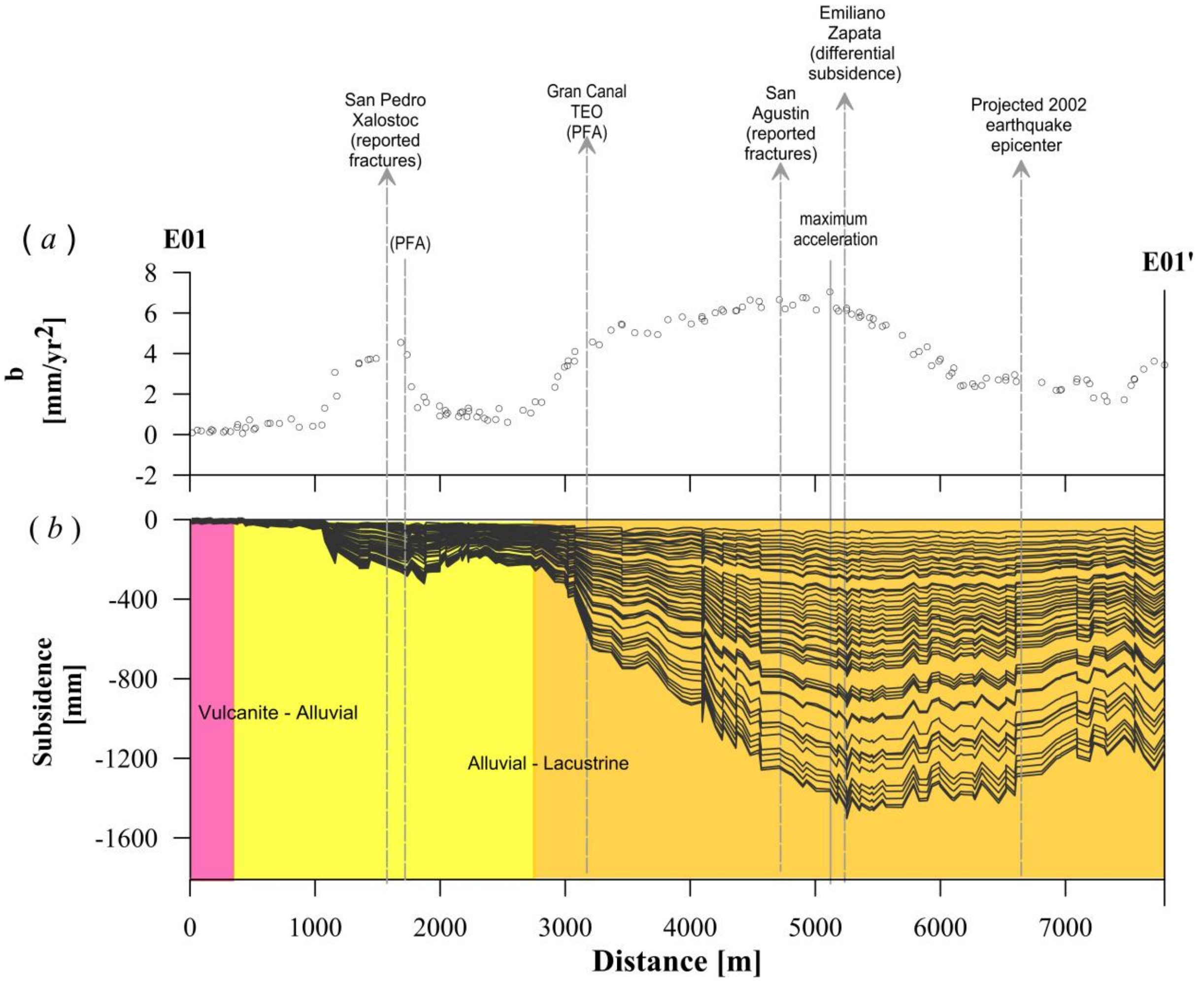

Figure 8-23 *a*) Quadratic coefficient ***b*** profile along E01-E01'.*b*) Temporal evolution profile of the deformation for the period 2002-2010 constructed from the estimated time series InSAR. The grey line indicates the maximum acceleration (or deceleration) and the dashed grey lines areas reported to be affected by fractures, as well as location of registered epicentres (INEGI) and important structures that the profiles crosses. Prone to soil fracturing areas inferred from the profiles are referred to as PFA. Transitions between different materials inferred from the surface geology information (Carrera-Hernandez and Gaskin 2007) are also represented.

Profile in Figure 8-23*a* indicates a good correlation between the location of higher quadratic coefficients along the profile and the probable apparition and/or propagation of fractures inferred from the evolution deformation profile (Figures 8-23 and 8-24). Soil cracking might occur where there is a meaningful displacement change such as at ~3000 meter-distance in the profile (Figure 8-23*b*), approximately coinciding with an acceleration peak (~5.5 mm/yr^2; see Figure 8-23*a*). Note that fracturing at this position happens near the Gran Canal and the TEO structures. Two other probable fractures may happen at ~1700- and 5200- meter distance, where abrupt changes in the magnitude of deformation takes place and where high values of the quadratic coefficient were found (4.5 mm/yr^2 and 7.0 mm/yr^2, respectively). Registered differential subsidence (Gobierno del Estado de Mexico and CAEM 2010) occured approximately at the position of maximum acceleration.

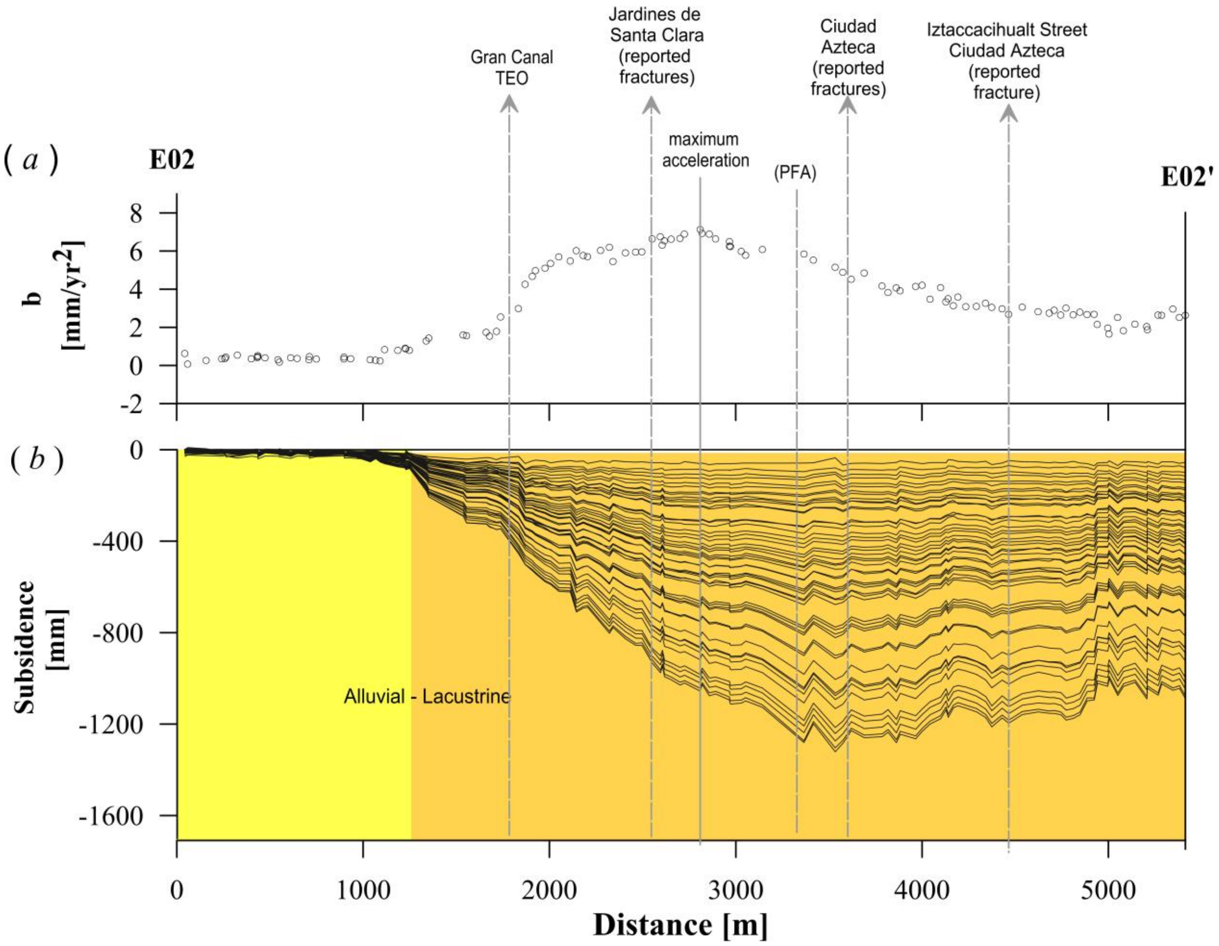

Figure 8-24 Same as Figure 5-23, the profile indicates probable fracturing near the maximum acceleration. Main hydraulic infrastructure (Gran Canal and TEO) are located near a soil fracturing prone area. Note that this and profile E01-E01' are cross an area of abrupt transition (Ovando-Shelley et al. (2012); see also Chapter 6).

Similarly, profiles in Figures 8-24*a* and *b*, suggest that a fracturing activity may develop approximately at 2800 meter near the location of maximum acceleration; contrasting displacement behaviour at this position is identified in the subsidence profile (see Figure 8-24*b*). Moreover, similarly to section E01-E01', sharp acceleration and subsidence displacement are observed near the Gran Canal del Desagüe and the TEO (~1800 meter-distance) (see also Ubaldo 2008). The Gran Canal del Desagüe have overflowed in several opportunities due to its inefficient water discharge capacity, provoking flooding and affecting villages (e.g., Alcaraz and Robles 2007; Servin and Quintero 2011).

Profile E01-E01' crosses several towns reported to be severely impacted by subsidence and differential deformation such as San Pedro Xalostoc, San Agustin and Emiliano Zapata (Gobierno del Estado de Mexico and CAEM 2010; Salinas and Nuñez 2009; Santiago 2014). Likewise, profile E02-E02' pass over Ciudad Azteca (H. Ayuntamiento de Ecatepec de Morelos et al. 2003) and other areas where the presence of soil fractures and differential subsidence were registered (Salvador 2009; Salinas Cesareo 2012).

Figure 8-25 Subsiding area in Ecatepec de Morelos. *a*) Sinkholes probably induced by water leakages in the drainage system, presumable provoked by the fracturing associated to subsidence (H. Ayuntamiento Constitucional de Ecatepec de Morelos 2011). *b*) Evidence of recent fracturing activity affecting a street (from "Grietas en Ecatepec" 2014).

Significant values of the quadratic component in Ecatepec de Morelos are located near a defined sharp transition zone (Ovando-Shelley et al. 2012) where earth fissuring activity was linked to regional subsidence and vertical differential compaction of heterogeneous materials (hard and soft soils) in the area (see also Chapter 6). Note that the dense concentration of wells of different pumping rates might lead to stresses (see also Figure 8-22), differently modifying the hydraulic properties of the materials.

Although the tensions provoked by the regional subsidence are the main mechanisms producing soil cracking in this area (Cerca et al. 2012), the medium to high seismic activity (GDF 2000) may need to be considered in the stress direction analysis. Besides, the penetration of water through existing discontinuity plains during the rainy seasons can produce hydraulic fracturing. The latter might be taken into account since frequently catastrophic flooding has affected Ecatepec de Morelos (Gobierno del Estado de Mexico and CAEM 2010; Salinas Cesareo 2014).

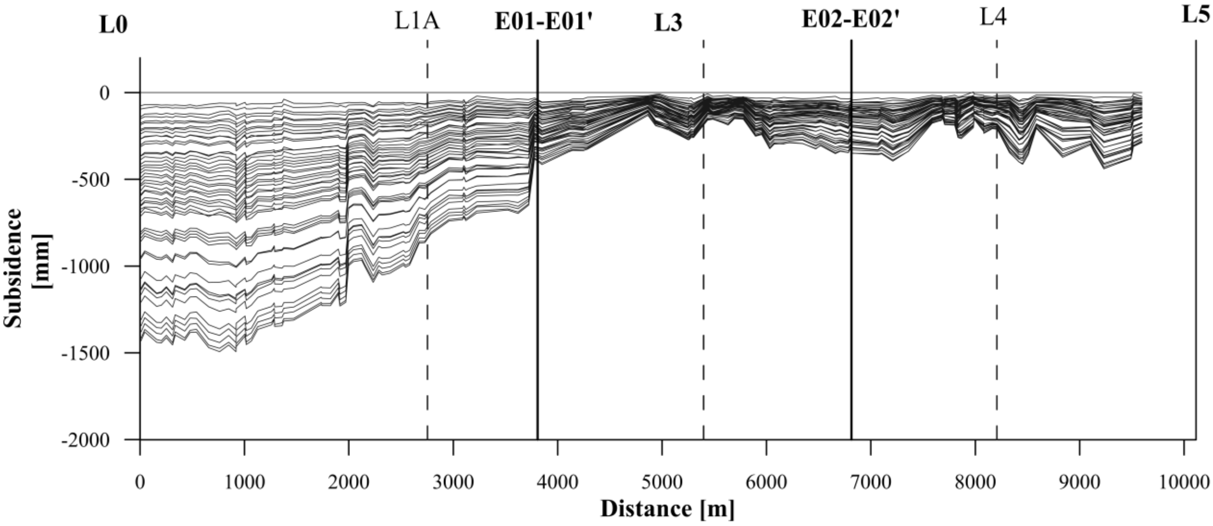

Figure 8-26 2002-2010 **s**ubsidence evolution profile along the TEO for the segment L0-L5. Sections plotted in Figures 8-25 and 8-24 are denoted by the thick black lines. Intermediate vertical shaft between L0 and L5 are indicated by the black dashed lines.

The presence of sudden soil collapse in the area was also reported (see Figure 8-25*a*) , mainly related to the water leakage in the drainage system, which are produced by subsidence and soil fracturing affecting hydraulic infrastructure (Méndez et al. 2008a).

Fracturing, its associated mechanisms and their dynamics need to be carefully evaluated since the TEO crosses the area under analysis and a failure in this structure can have catastrophic consequences (see also Figure 8-25*b*). Figure 8-26 indicates probable soil ruptures in the area near vertical shafts L1, L3 and the intersection with profile E01-E01'. Monitoring of this zone is furthermore paramount because the new Mexico City Airport is planned to be constructed near the potential fissure-prone site here studied.

8.3.1.2 Tecamac

Fracturing activity in this area was preliminary analysed in section 7.6. Here I present the quadratic component and the evolution profiles (Figures 8-27*a* and *b*, respectively), which indicate that the presence of a soil failures in this area correlates with the maximum acceleration observed.

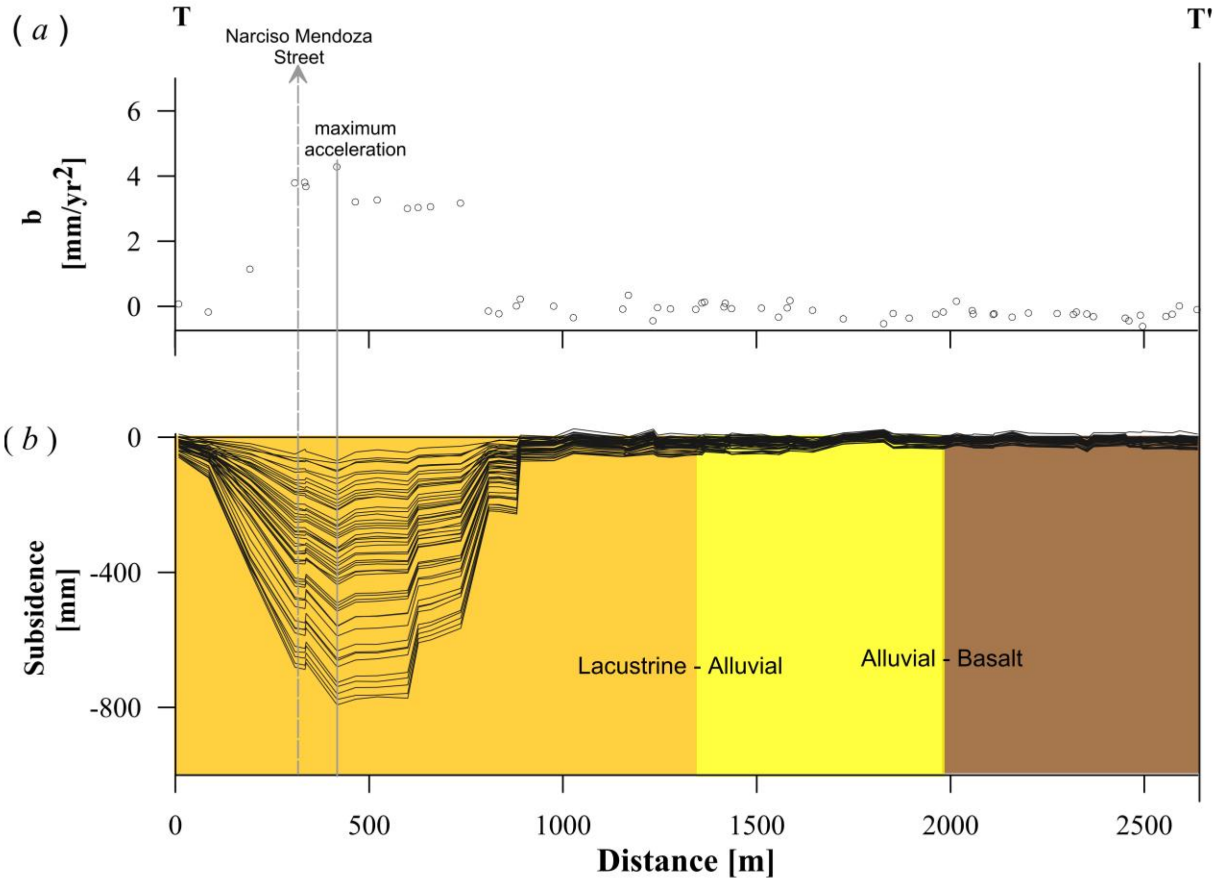

Figure 8-27 Ground settlement evolution constructed from the 2002-2010 deformation time series over the Ojo de Agua, located in Tecamac.

The prone to fracturing zone identified from the profiles is located close to the the Narciso Mendoza Street, where there area records of prominent subsidence and soil fractures (Gobierno del Estado de México and Ayuntamiento del Tecámac 2013). The phenomena impacted the fresh drinking water services and the drainage system (Gobierno del Estado de México and Ayuntamiento del Tecámac 2013). From the surface geology information no clear link between the fracturing process and transition between soft soil and hard materials is observed. Moreover, the cavity-liked shape in Figure 8-27*b* could imply the probable presence of an underground cavern (volcanic cones have been mapped in this area; Gobierno del Estado de México and Ayuntamiento del Tecámac 2013) or that a hollow have appeared due to water leaks in the beneath hydraulic system (Auvinet 2010; Méndez et al. 2008a).

Figure 8-28 Housing affected by ground fractures due to the extensive groundwater practices in Ojo de Agua, Tecamac (Salinas Cesareo 2009).

Notable acceleration has also been observed in other areas that could be associated to the spreading of fractures. In addition, earth fissures in certain areas were related to the intense groundwater extraction by wells at profound depths from where 1800 l/s of groundwater are extracted (see Figure 8-28; Salinas Cesareo 2009**)**. Based on this information, the main mechanism causing soil cracking in the later areas may be the subsidence associated to exhaustive groundwater practices which induce the lowering of groundwater levels, the subsequent consolidation and compaction of the clayey deposits.

The analysis of the occurence and propagation of fractures are very important since several extraction wells are installed in the area and also an artificial recharge program is planned to be implemented in Tecamac town near the Chiconautla hill and other areas as well (GDF et al. 2012a). Furthermore, since several of the groundwater extraction wells and planned recharge areas are located near trash sites, the appearance and spread of soil cracks (in depth and in longitude) can affect, even more, the water quality because hazardous pollutants can seep via them into the aquifer.

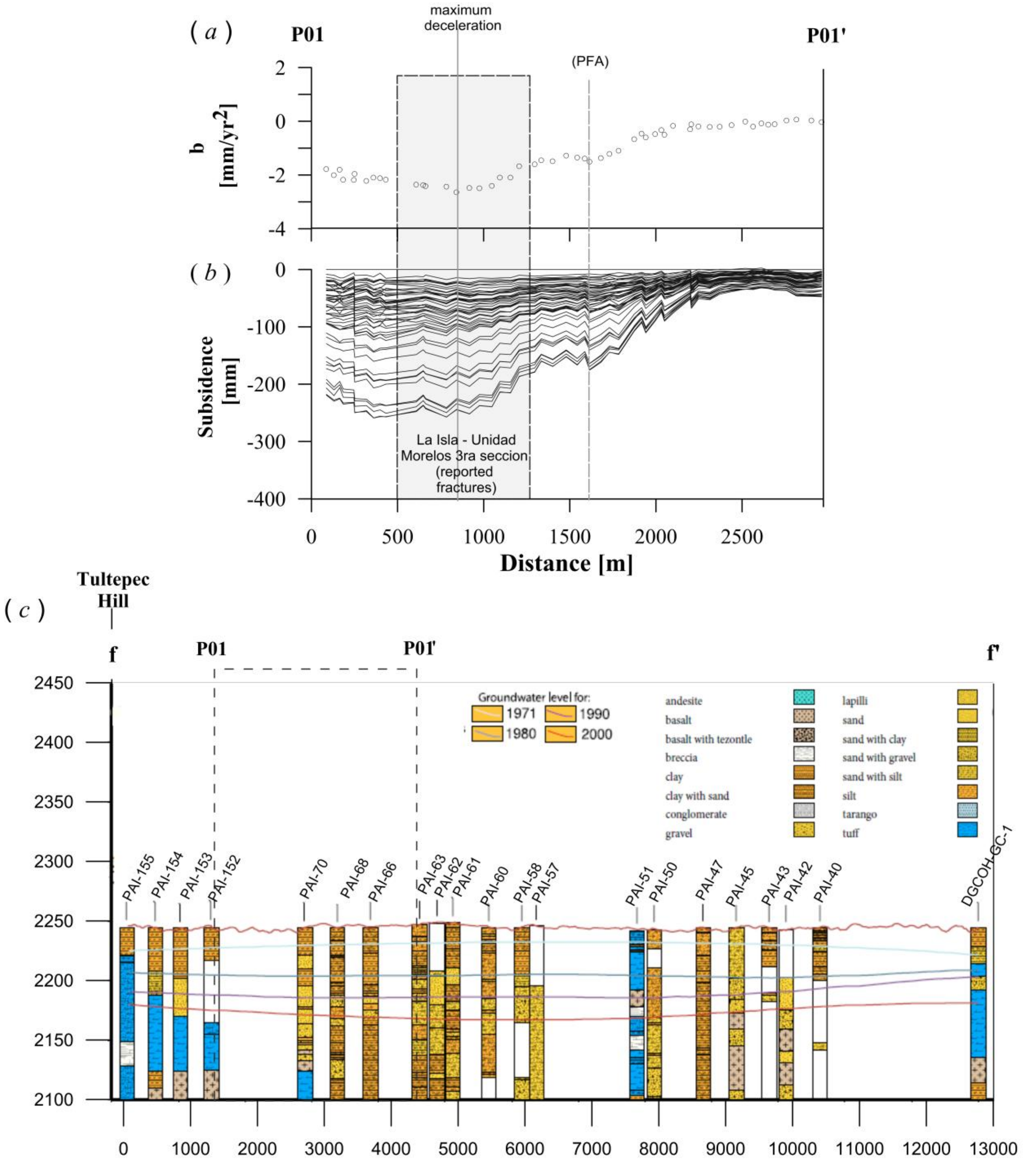

Figure 8-29 *a*) Quadratic coefficient and b) deformation profiles across San Pablo de la Salinas, Tutitlán. *c*) Geological cross section f–f' (adapted from Carrera-Hernández 2007) approximately comprising the P01-P01' profile. Groundwater level for 1971, 1980, 1990 and 2000 are also represented and the lithology is explained in the small inset figure in the upper right.

8.3.1.3 San Pablo de Las Salinas (Tultitlan)

Figures 8-29*a* and *b* compare the quadratic coefficient and the evolution deformation profiles for the 2002-2010 period across San Pablo de Las Salinas town located in the municipality of Tultitlan.

The maximum magnitude of the quadratic component (-2.6 mm/yr^2) occurs at ~ 840 meters-distance and coincides with the steep deformation change observed in Figure 8-29*b*. Another possible fissure may develop at approximatley1600 meter-distance, where a notable variation in *b* is distinguished. Note that the profile (mainly) crosses lacustrine deposits; therefore, in this case, soil fracturing might not be caused by sharp transition between contrasting materials. Notwithstanding, a probable abrupt thickness change in basaltic-lacustrine contacts such as near the Tultepec hill could trigger the apparition of cracks due to differential deformation. The geological section in Figure 8-29*c* (Carrera-Hernández 2007) approximately describe the lithology along profile P01-P01': presence of lacustrine deposits that overlies or are inter-bedded with coarse materials (mainly sand and gravel) is observed. Towards the Tultepec Hill, particularly between the PAI-154 and PAI-155 wells, noticeable thickness variation of the clay-rich deposits can be distinguished. The mechanism depicted in Figure 8-30 can be acting there producing a discontinuity surface.

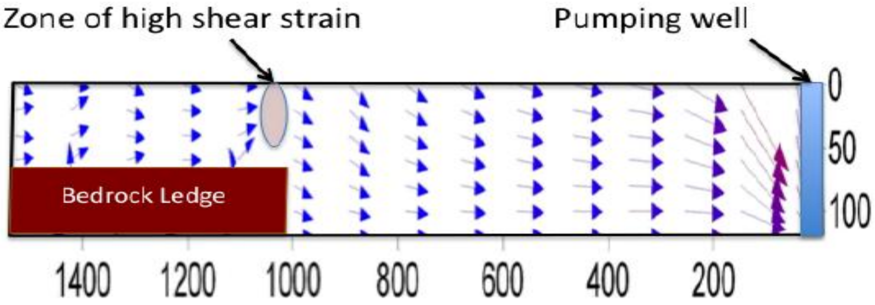

Figure 8-30 Representation of the mechanism that can produce fracturing in the Tultpec Hill area (from Burbey 2010). Relative horizontal displacement from the pumping wells might produce a strain gradient near the bedrock (or rigid materials such as basalts) contributing to failure.

The extreme abstraction rates (REPDA and PAI wells up ~103 l/s and 135-158 l/s, respectively; see also Carrera-Hernandez and Gaskin 2007) may have reduced the pore spaces size and number, leading to the compaction of soil, the consequent subsidence and associated soil fracturing in the area. Different responses to groundwater decline of the materials near the Tultepec Hill can lead to differential deformation, hence producing ground failures. Continuous compaction of the lacustrine deposits surrounding by rocky soils reduce their thickness (Ovando-Shelley et al. 2012), thus compounding the cracking (see also Chapter 6).

Figure 8-31 School located in Unidad Morelos Tercera Seccion affected by the 2012 seismic movement, with epicentre in Guerrero and a magnitude of ~7.4 in the Ritcher Scale. Subsidence and fracturing have been reported for the area (Núñez López 2012).

Housing structures in several villages of the San Pablo de las Salinas town have suffered the effects of subsidence and soil cracking (Salinas Cesareo 2012). Moreover, the seismic activity can generate or exacerbate the propagation of fissures (see Figure 8-31; Núñez López 2012).

Note that soil fracturing detected from Profile P01-P01' occurs near La Isla and Unidad Morelos Tercera Seccion (see rectangular area in Figure 8-29*b*) where many buildings were affected by fissures after a seismic movement occurred in 2012. Nevertheless, in order to determine the link between seismicity and soil cracking, detailed geophysical measurements are required to perform a more precise analysis of the stresses acting in the area. This would allow identifying the role of the mechanisms or how they interact in the soil fracturing process.

As in the previous case, the location of waste disposal sites (see Figure 8-22) close to zones affected by soil fractures can lead to serious environmental issues due to risk of groundwater contamination.

8.3.1.4 Coacalco

The map of quadratic coefficient *b* (see Figure 8-21) indicates that notable accelerated motion occurs in the municipality of Coacalco. Acceleration and subsidence evolution profiles were constructed and its relation to soil fracturing is studied, as well as possible triggering mechanisms (see Figures 8-32*a* and *b*).

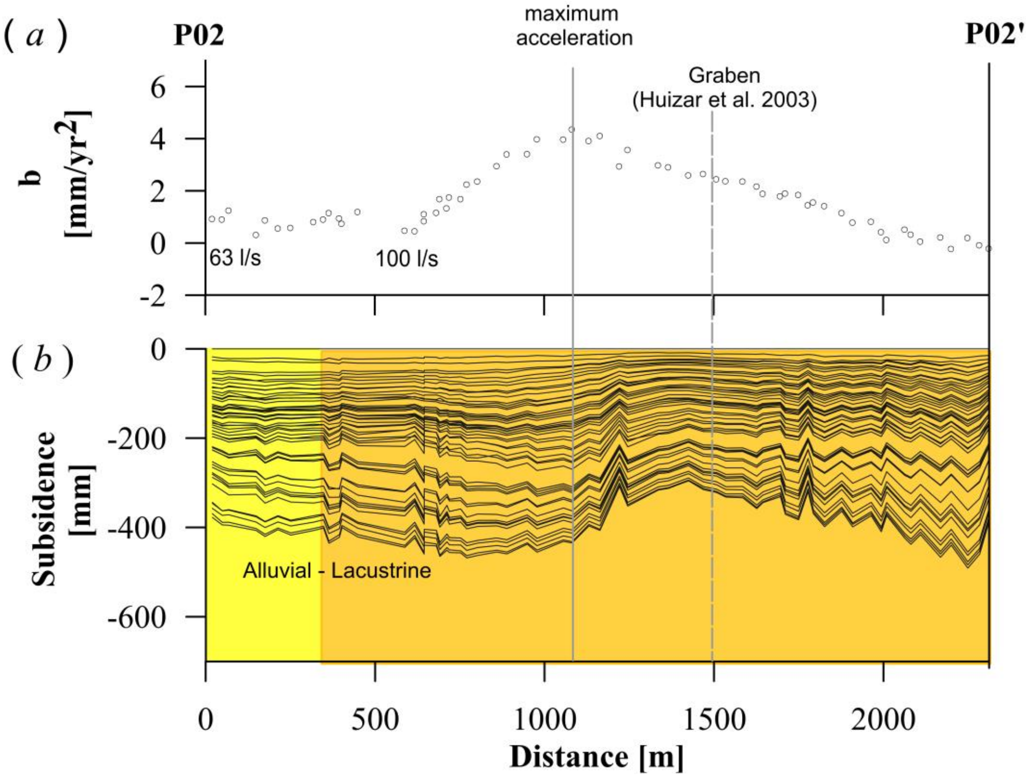

Figure 8-32 Quadratic coefficient (*a*) and evolution deformation profile (*b*) across Coacalco. The maximum acceleration coincides approximately with the inferred soil fracture from *b*).

The change observed in the displacement profile in Figure 8-32b indicates a probable soil fracture development at approximately 1100 meter-distance. This variation coincide with the location of the maximum acceleration (~4.3 mm/yr^2) observed in Figure 8-32a. In fact, this area was reported to be seriously influenced by subsidence and soil failures (see Figure 8-33; Salinas Cesareo 2007b). Sewage system, roadways and urban structure have been impacted by these phenomena (Ayuntamiento Constitucional de Coacalco de Berriozabal 2006; Salinas Cesareo 2007b; Toluca 2010).

Figure 8-33 Fracturing affecting a house in Coacalco (from Salinas Cesareo 2007b).

Different pumping rates inducing differential effective stresses in the compressible deposits, and the presence of heterogeneous materials that react differently to these conditions might be an important soil fracturing factor in the area. For example, in the contact between the lacustrine unit (consisting predominately of clay) and the alluvial deposits (conglomerate gravel, sand, silt, clay and tuff; see also Huizar et al. 2003) different responses of these materials to pumpage may manifest as a slight displacement jump in profile P02-P02’ (Figure 8-32*b*; see also Table 6-2). However, to performed a more comprehensive investigation precise knowledge of the local materials and their hydraulic and mechanical properties is needed. Note that the presence of a buried graben reported by Huizar Alvarez et al. (2003), located near the maximum acceleration and where ground rupture may occur (Figure 8-32*b*), could contribute to the subsidence and associated fissuring processes.

8.3.1.5 Tultitlan: profile VT-VT‘

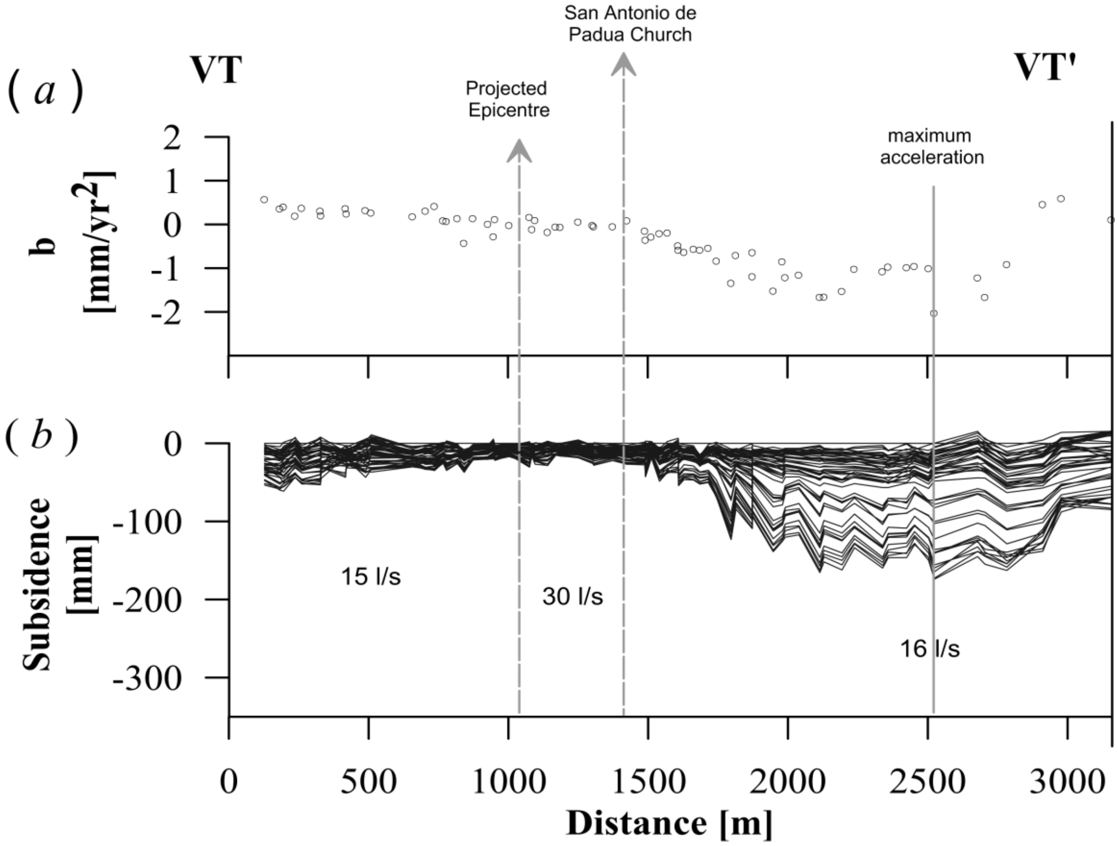

Figure 8-34 Soil fracturing analysis in Tutitlan *a*) Quadratic coefficient. b) Subsidence evolution profile.

Spatial distribution of the quadratic coefficient *b* and evolution of the deformation along the profile VT1-VT1’ are displayed in Figures 8-34*a* and *b*, respectively. The profile crosses an area constituted mainly by alluvial deposits and dispersive soils that are easily eroded in the presence of water (Ayuntamiento de Tutitlán 2006). The latter condition promotes the generation of fissures that potentiated by overloads from buildings, provoke sinking (Ayuntamiento de Tutitlán 2006). A soil fracture prone area can be distinguished at approximately 2500 meter-distance, corresponding to the maximum deceleration observed in Figure 8-34*a* (~-2 mm/yr^2).

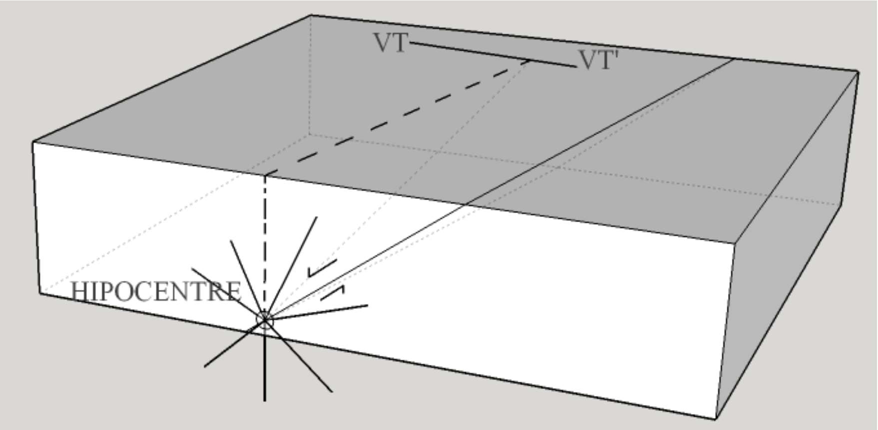

Figure 8-35 Cartoon in 3D dimension representing a probable soil fracture mechanism acting in the area. Profile VT-VT’ is located near the graben (Huizar et al. 2003). The discontinuity plain may dip a certain angle (exaggerated in the figure). The hypothetical location of the hypocentre of the 2004 earthquake (INEGI) is projected to the profile. A stress component coming from this event could have presumably exacerbated soil fracturing in the area.

Due to the lack of data about the area, the causes of soil fracturing are difficult to identify. However, relatively recent seismic activity in 2004 (epicentres located in Tutitlan at ~1400 meters far away from profile, magnitude of 2.8) and in 2012 (epicentre in Guerrero State with a magnitude 7.8 in the Ritcher scale) could have induced the reactivation of buried structure (Huizar Alvarez et al. 2003; Marin-Cordova et al. 2004; see also Chapter 6), thus provoking soil fracturing. Figure 8-35 shows a model of the mechanism that could trigger or contribute to the soil fracturing in this area. Huizar Alvarez et al. (2003) proposed a graben structure limited by normal faults with a fault plain dipping approximately 90°; however, the faulting plain could dip another angle. Normal faulting may interact with the regional subsidence induced by extreme overexploitation of the local aquifer (large number wells are distinguished in Figure 8-22).

The soil fracturing analysis in this area is very important because the extension of a metro line is planned there (see section 8.2.3.2). In addition, records of chromium contamination near the inferred ground rupture indicate that the presence of fractures may compromise the water quality of the Cuautitlan-Pachuca aquifer, hence peoples' health (see also Cruz Gonzales 2009; SEMARNAT 2012).

8.3.1.6 Teoloyucan-Tepotzotlan

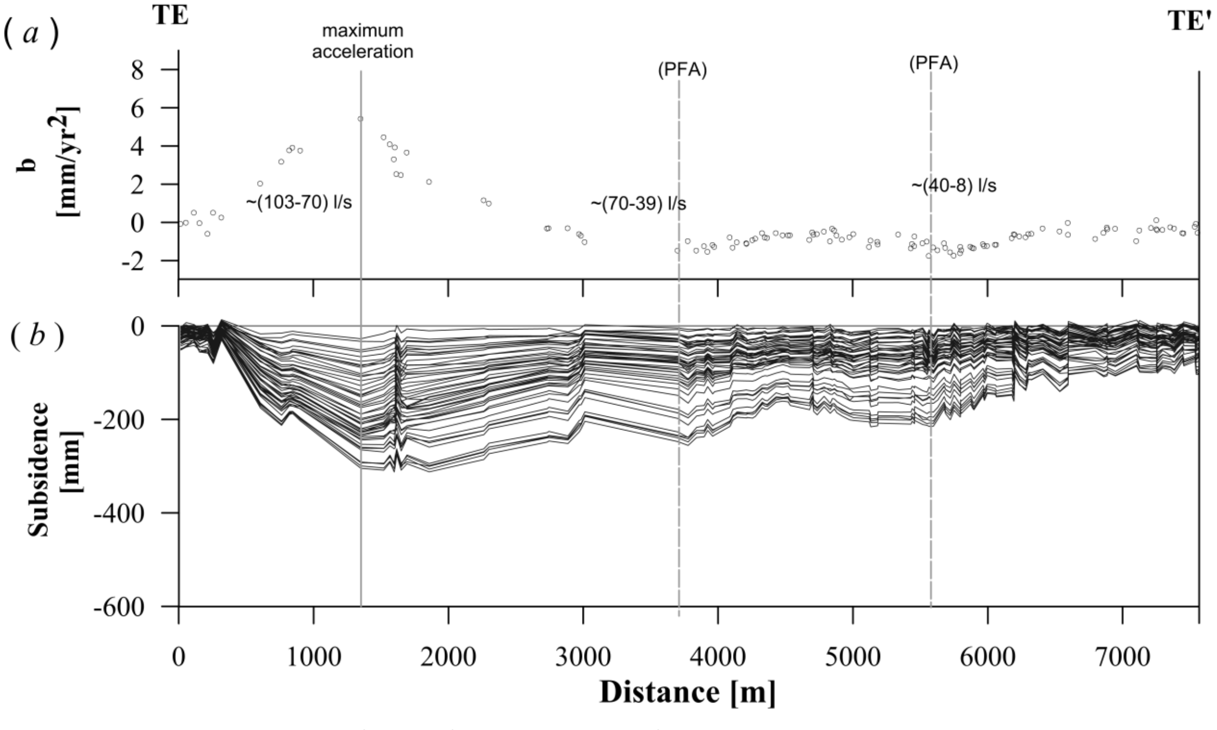

Figure 8-36 *a*) Quadratic component profile. *b*) Deformation evolution profile period 2002-2010 across Tepotzotlan and Teoloyucan. Three probable prone to fracturing areas are detected. The highest extraction rates in the area led to subsidence and associated soil fracturing. Hydraulic fracturing due to flooding and water infiltration into exiting discontinuities may compound soil cracking.

Figure 8-21 reveals a maximum acceleration (5.42 mm/yr^2) near the Teoloyucan PAI branch (see also Figure 8-1), and profiles in Figures 8-36*a* and *b* confirm the correlation between this observation and the presence of a possible soil fracture at 1350 meter-distance. The profile crosses an area mainly characterized by alluvial materials (e.g., sand, gravel), which are less compressible than the lacustrine deposits (mainly clay and silt). Note that the higher extraction rates (103-70 l/s; see also Carrera-Hernandez and Gaskin 2007) approximately correlate with the location of the main inferred soil fracture. Areas less prone to soil cracking areas have been identified at 3700 and 5600 m of the profile where minor extraction rates, 70-39 l/s and 39-8 l/s, respectively, are registered (see also Carrera-Hernandez and Gaskin 2007). The quadratic coefficient **b** at these positions reaches up to -1.5 mm/yr^2 and -1.8 mm/yr^2, respectively. Differential water extraction rates and different response of various materials with different physical, mechanical and hydraulic properties in the area may produce local differential deformation. Moreover, the non-homogeneous spatial pumping rates distribution lead to complex and different stress-strain behaviours within short distances, making several areas prone to soil fracturing. Actually, this area has been reported to be affected by subsidence and fissures that impacted several communities and railroads (SEMARNAT et al. 2008).

Considering the medium-level seismicity of the area (Ayuntamiento de Tepotzotlán and Gobierno del Estado de México 2003), a stress component from this source may need to be considered in the soil fissuring analysis (see also Chapter 6).

On the other hand, the presence of collapsible soil (Ayuntamiento de Teoloyucan 2004, 2013; Ayuntamiento de Tepotzotlán and Gobierno del Estado de México 2003) and frequent flooding may interact with the differential settlement intensifying the propagation of soil fractures; water penetrates into the existing discontinuities, generating tensile stresses.

8.3.1.7 Cuautitlan: profile M-M‘

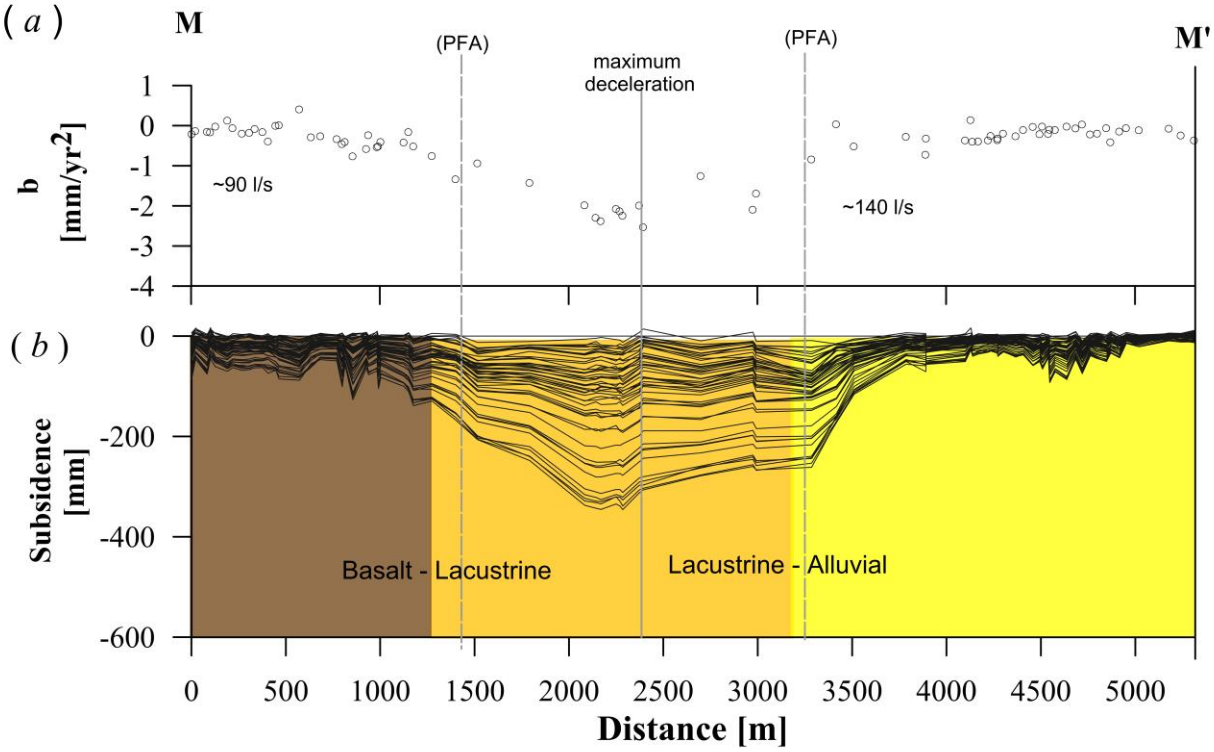

Figure 8-37 Quadratic coefficient (*a*) and evolution deformation profile (*b*) across Cuautitlan. The maximum deceleration coincides approximately with the fracture inferred from *b*).

Profile M-M’ in Figure 8-37 crosses urban and cropping areas. The maximum deceleration along the quadratic coefficient profile (see Figure 8-37*a*) occurs at ~2400 meter-distance, where notable displacement change occurs (see Figure 8-37*b*). The maximum extraction rates found in the Tultepec Hill of basaltic composition was 90 l/s, with wells that reach up to 300 m in depth (CONAGUA/SIGA 2014). In the alluvial area the maximum pumping rate near the profile is 150 l/s, and wells reach up to 150 m in depth (CONAGUA/SIGA 2014). The regional subsidence and the contrasting extraction rates causing differential stresses responses of the materials involved can produce earth fissures in this area. Most groundwater extractions by the REPDA wells are destined to cattle and agriculture uses. Some railroads near the area of maximum magnitude of the quadratic coefficient present cracks (see Figure 8-38).

Figure 8-38 Example of street impacted by fracturing near the maximum deceleration detected in Figure 8-37 (from Google Earth database).

Other soil cracking prone areas may develop at ~1400 and ~3200 meter-distance of the deformation evolution profile (Figure 8-37*b*), coinciding approximately with the transition between different materials (according to the surface geology information) and where larger decelerations are detected.

8.3.1.8 Jaltenco

Several rural and urban sectors of Jaltenco town located in the north of the study area, have been frequently reported to be impacted by ground ruptures (Instituto de Proteccion Civil 2004; Salinas Cesareo 2007a; Barrera Aguirre 2007)**.** Soil fracturing in this area impacts railroads, urban and hydraulic infrastructure (see Figure 8-39).

Figure 8-39 *a)* Cracks affecting a house in the locality of Jaltenco (Salinas Cesareo 2007). *b*) Picture of the Francisco Javier Mina street showing fracture evidence (from Instituto de Proteccion Civil 2004) . Profile J-J’ in Figure 8-40 crosses this street.

The analysis of velocity profiles in section 8.2.4 unveils high deformation gradients in Jaltenco. Here, the quadratic coefficient and the deformation evolution profiles displayed in Figures 8-40*a* and *b*, respectively, are evaluated to complement the study of this area. A maximum deceleration was identified at 950 meters of the profile J-J’ coinciding with the change in the displacement. This variation occurs relatively close to the alluvial-lacustrine transition, which needs to be taken into account when evaluating the responses of materials subjected to differential stresses, possibly triggered by contrasting pumping rates. Note that along profile J-J' (Figure 8-40*b*) the ground sinking distributiom is approximately homogeneous in the sector corresponding to the lacustrine deposits, where the extraction rate is 35 l/s. In contrast, land settlement on alluvial deposits results spatially more variable (see Figure 8-40*b*). Moreover, slower subsidence motion takes place in the section of alluvial deposits of higher permeability (~5; see Table 6-2) and compressibility, than in the Quaternary lacustrine plain.

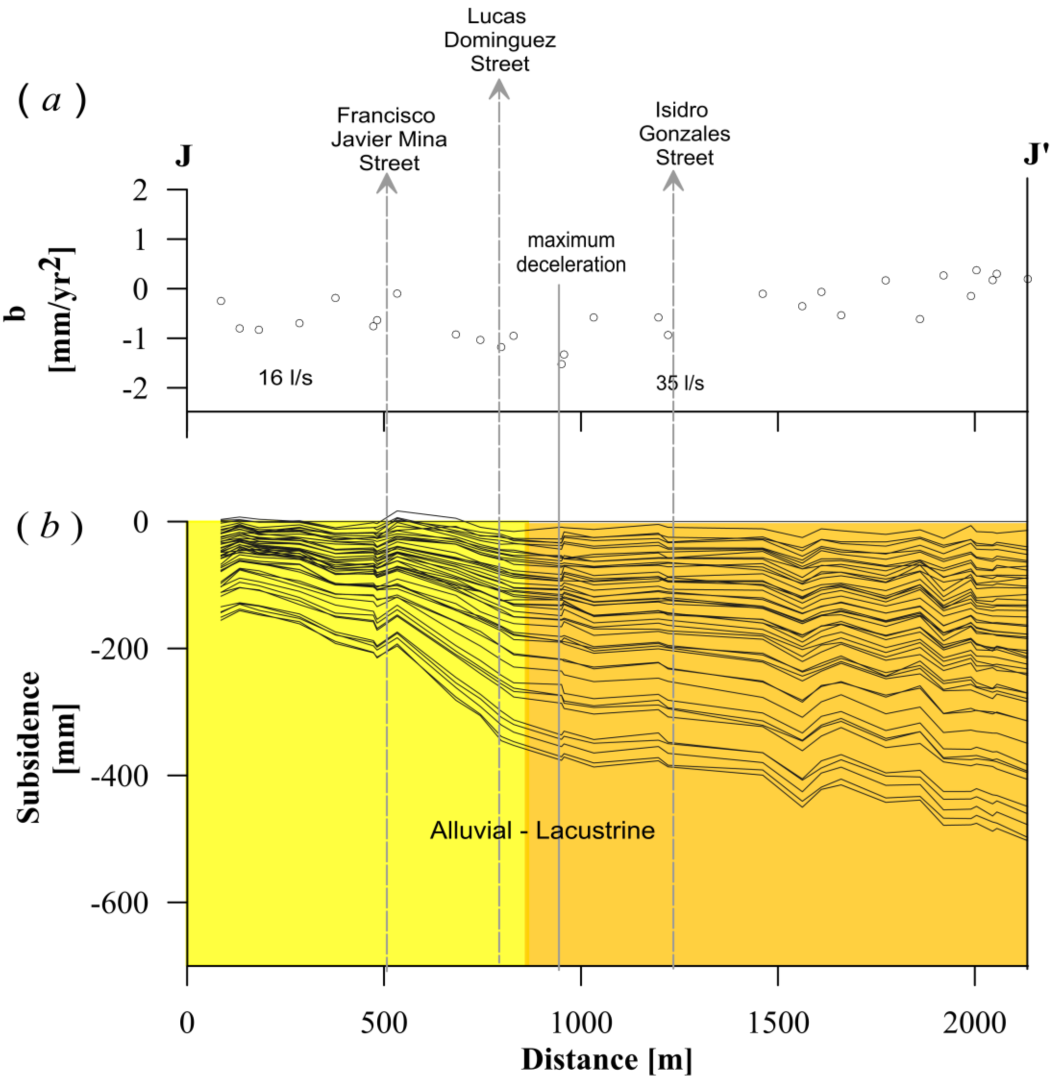

Figure 8-40 *a*) Profile J-J' across Jaltenco town where earth fissures have been registered (Instituto de Proteccion Civil 2004). Different extraction rates and responses from heterogeneous materials might induce the apparition of fractures in the area. Location of main streets affected by ground cracks is shown in panel *b*).

A ground rupture of approximate 3 km, affecting the area for more than 25 years (according to the Proteccion Civil Municipal), is represented in the profile; structures situated in the Francisco Javier Mina, Lucas Dominguez and Isidro Gonzales streets were notably damaged (Barrera Aguirre 2007). Observe that these streets (Lucas Dominguez and Isidro Gonzales) are located near the maximum magnitude of **b** (see Figure 8-40*a*).

Other mechanisms such as active seismicity and buried structures (Huizar Alvarez et al. 2003) that can contribute to soil fracturing (see also Figure 6-5) should not be precluded.

Records (Instituto de Proteccion Civil 2004) indicate that earth fissures frequently have manifested after intense rainfall, so hydraulic fracturing due to water infiltration into existing discontinuities also occurs. Nevertheless, the main ground cracking source acting in the zone may be the differential deformation.

Proximity of the TEO structure and waste disposal sites to this prone to soil fracturing area suggests that continuous monitoring is required.

8.4 Subsidence behaviour observed in expansive soils

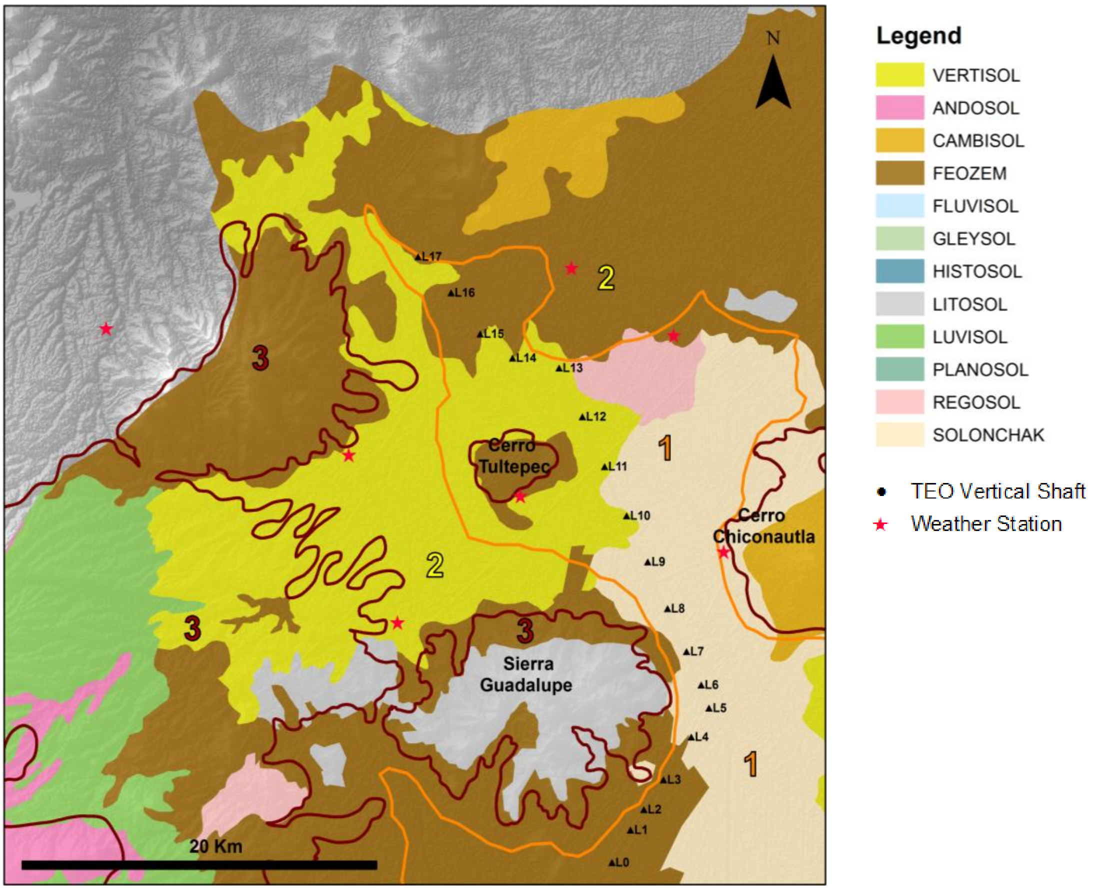

Figure 8-41 Land use map (based on INEGI 2013). Surface geology contours are shown dark and light brown (1, 2 and 3 correspond to lacustrine, alluvial, and basalts and vulcanites, respectively). The weather station near the Tultepec Hill (red star) and in vertisol soils was selected for the analysis presented in Figure 8-42.

Some areas of the region under study are located in vertisol soils (see Figure 8-41) which are characterized by expansive and collapsible behaviour when exposed to different moisture variations (Dirección General de Proteccion Civil and Ayuntamiento de Tultepec 2013; Gobierno del Estado de Mexico 2006, 2010, 2011; H.Ayuntamiento Constitucional de Coacalco de Berriozabal 2006). This type of soil presents very high content of clays, particularly montmorillonite, and tends to be very sticky when wet, and very hard when dry. Because they are subjected to drastic volumetric changes under variable humidity conditions they are not appropriate for agriculture uses. Moreover, these variations usually generate cracks that affect the drainage and wastewater system (Dirección General de Proteccion Civil and Ayuntamiento de Tultepec 2013).

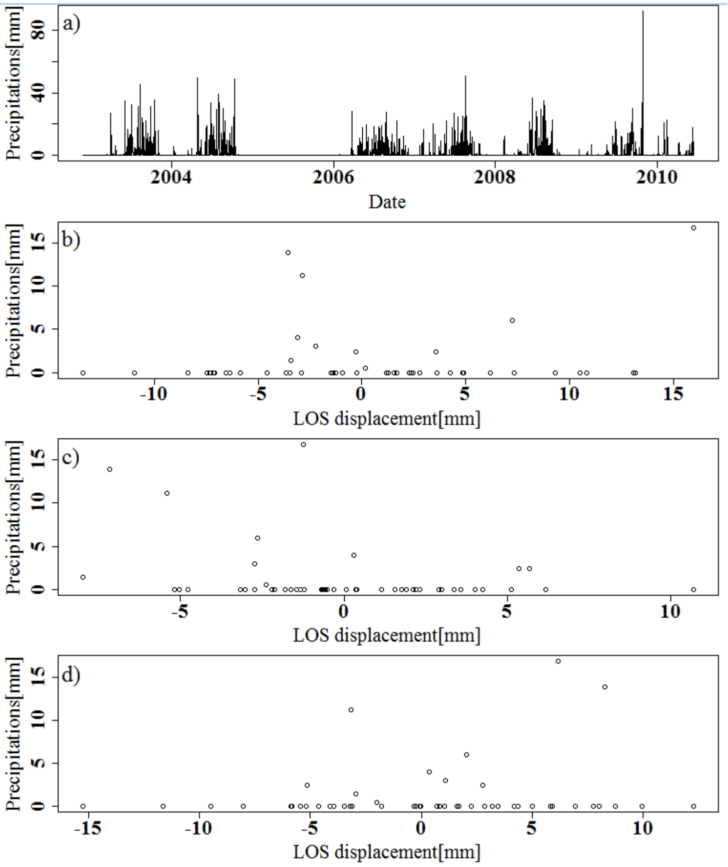

Figure 8-42 *a*) Precipitation for the period 2002-2010. 35-day resampled precipitation data and the residuales from the linear model where used, attempting to correlate possible seasonal variations of displacement and rain. Relation between the precipitation and displacement for three points near the weather station close to Tutlepec Hill (Figure 8-41) are shown in b, c and d (correlations b=0.20, c=-0.3 d= 0.2).

Thus, the deformation behaviour in these types of soil during rainy seasons was analysed. For this evaluation, precipitation data for the 2002-2010 period and SDFP pixels in cropping areas and near (~ 1400 meters away) the meteorological station close to Tultepec Hill (see Figure 8-41) were selected (water infiltration and volumetric changes, swelling and shrinkage may manifest better in cropping lands). Because the rain information was incomplete, resampling was necessary. Linear interpolation was employed to complete the precipitation time series (Figure 8-42a) and to correlate them with the InSAR displacements. Unfortunately, because the sampling of precipitation data for 2005 was very poor, the interpolation failed for that period. Figure 8-42*b*, *c* and *d* compare the residuals from the linear model (a possible seasonal component can be better distinguished) of three SDFP pixels and the precipitation data. In general, low correlation between residuals and the rainfall data was observed, suggesting that a probable expansion and/or compression of the vertisol soils during wet and dry seasons, respectively, cannot be clearly inferred from these data. Nevertheless, some apparent expansions were detected after heavy rainy days. Further rainfall information and a better temporal sampling are necessary to perform a more precise correlation analysis and interpretation.

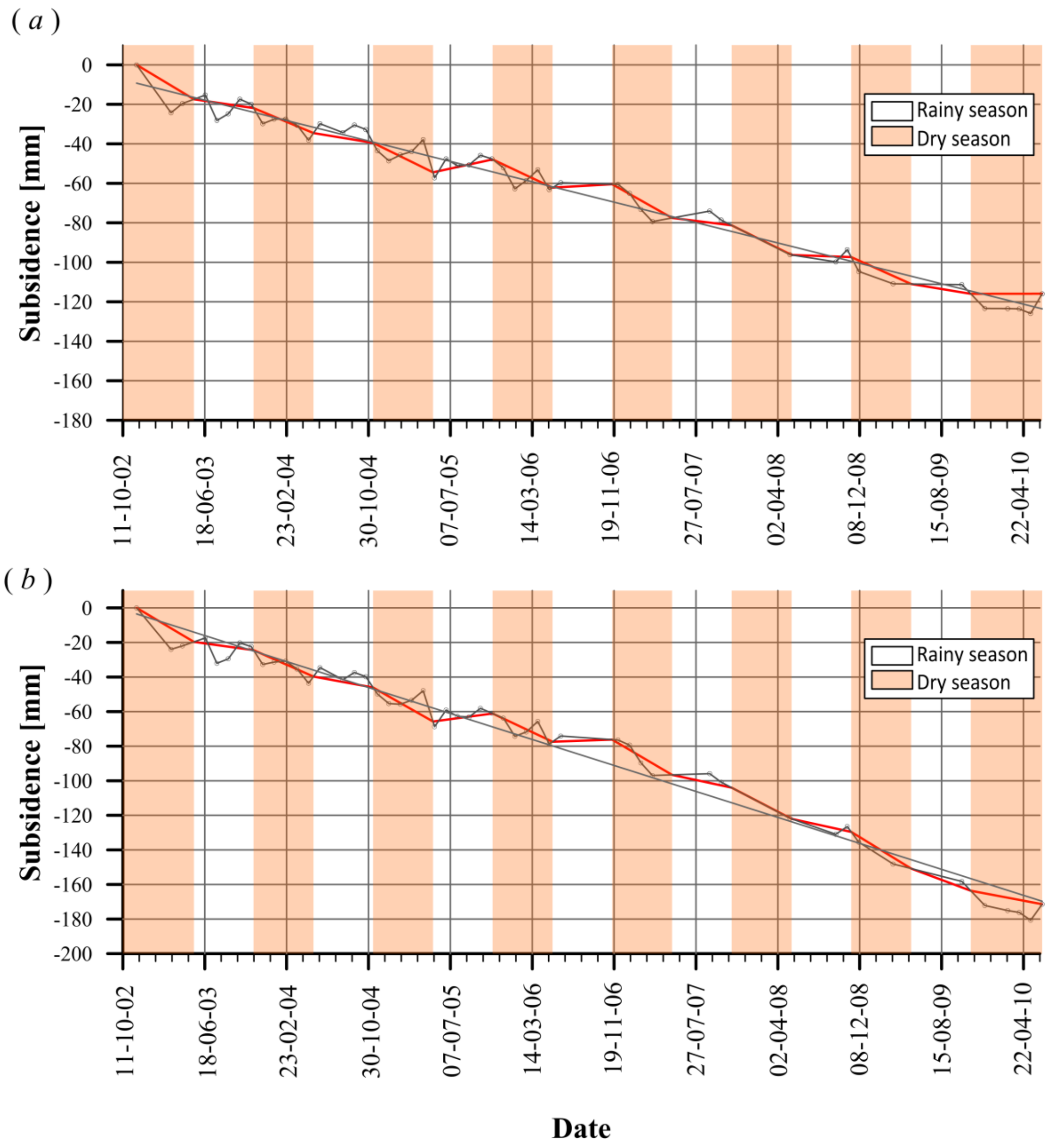

Figure 8-43 "Seasonal subsidence tendency" for the period 2002-2010. Note that, in general, the subsidence tends to increase at the end of the dry season. On the other hand, subsidence during the rainy seasons decreases or slightly varies. The small grey dots indicate the subsidence data and the grey line the linear subsidence tendency .Red line: "seasonal" subsidence trend.

Additionally, time series of points in vertisol soils were examined. In order to compare the variations of the subsidence between rainy (May-October) and wet seasons (November-April), a seasonal tendency for each period was estimated. Figures 8-43*a* and *b* show the time series for points located on vertisol soils, indicating the seasonal tendency. In both cases ~80% of the estimated seasonal slopes corresponding to the dry season (red lines in the orange shaded areas in Figures 8-43*a*,*b*) are larger than those estimated for the wet periods. These observations reveal that land subsidence may be more marked during the dry seasons, remaining approximately stable or slightly decreasing during the rainy season. Presumably, the relatively high water storage capacity of these type soils could locally counteract the sinking effect when periods of intensive rain occur, suggesting as well presence of elastic deformation. However, this hypothesis requires more precise measurements and knowledge of the mechanical and physical properties of these soils to better evaluate their responses.

8.5 Analysis over areas possibly experiencing secondary consolidation

The lacustrine soils of the Mexico Valley have a very complex behaviour and rare engineering properties (see also Chapter 6). The unusual pumping rates from the underlying aquifer system, have led to the compaction of the clay rich deposits and the regional subsidence. Moreover, differential deformation and soil fracturing severely deteriorate the urban infrastructure. Thus, the characterization of the clay rich deposits is a critical but challenging task for foundation engineering.

Because hydraulic behaviour and geo-mechanical properties of the Valley of Mexico clays evolve temporally and spatially (Ovando Shelley 2011), their continuous surveillance is required. Here some particular time series (Figure 8-44*a*), possibly indicating different consolidation phases are presented and interpreted.

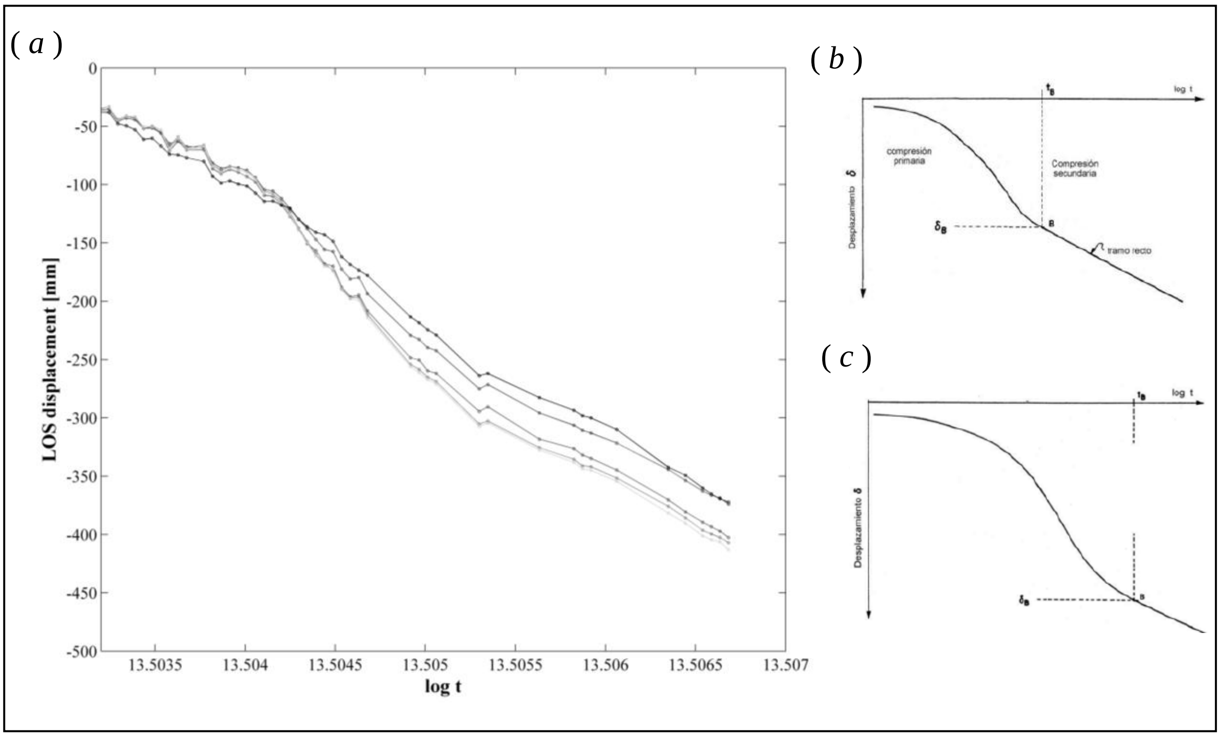

Figure 8-44 *a)* Examples of deformation time series approximately following the consolidation curves of the Mexico City clays described by Zeevert (1986). *b*) Consolidation curve type I. *c*) Consolidation curve type IV.

Non-linear deformation in many areas was found to (see Figure 8-20) fit a quadratic model (see sections 7.6 and 8.3); however, some time series such as those depicted in Figure 8-44*a* suggest the presence of particular and different behaviour. These special configurations approximately imitate those of the clay consolidation described by Zeevaert (1986) (Figures 8-44*b* and *c*). Apparently, ground sinking follows configurations of type I or IV (Zeevaert 1986; see also Chapter 6) that describe decoupled primary and second consolidation phases. The primary consolidation corresponds to the compression of soil controlled by the water flow resistance under induced gradients, while the secondary consolidation begins when the excessive pore water pressure approaches to zero.

Nevertheless, detailed in-situ and multidisciplinary research and tests are required for precise interpretation of the observed behaviour in the InSAR time series.

8.6 Comparison with GPS data

The subsidence rate measured at the UTEO GPS station (see Figure 8-9, Osmanoglu et al. 2010) was compared with our InSAR results. This station is located in the southwest part of the Zumpango lake and placed on tephra deposits. The GPS result at this site for the period 2004-2007 and processed in the ITRF-2000 reference frame was projected to the LOS vector following the procedure described by Osmanoglu et al. (2010). The approximate GPS_{LOS} rate obtained was -5.3 mm/yr, while the LOS mean velocity in this study is -5.8 mm/yr. These values suggest a good agreement between the two techniques; however, a denser network of the GPS stations should be used to perform a more accurate validation of the SBAS observations here presented.

8.7 Summary

A detailed subsidence analysis in northern Valley of Mexico for the 1999-2010 period by means of the SBAS method from StaMPS has been presented for the first time. The subsidence rates (up to 285 mm/yr) are higher to the south of Sierra de Guadalupe and lower to the north, and correlate with the spatial thickness reduction of the clay-rich deposits.

The largest subsidence rates occur in Ecatepec, Coacalco, Jaltenco and Tecamac correlating with the population and volumes of water extracted for agriculture and livestock uses. Ecatepec, where the largest piezometric drawdown is recorded (Carrera-Hernandez and Gaskin 2007), is undergoing the fastest ground motion.

The InSAR time series show remarkably linear deformation through time, however, as in the south of the Valley, a non-steady component was observed in some areas.

Subsidence affects important local infrastructure as observed in the study cases of the TEO and the railway Lechería-Xaltocan. Our InSAR results are in agreement with values reported by Lesser and Cortez (1998) and Auvinet et al. (2012). The TEO, which first kilometres are severely impacted by subsidence, is planned to improve the drainage system and reduce the risk of flooding. That is why evaluation of failure in this hydraulic structure is very important. Additionally, the analysis on the railway Lecheria-Xaltocan is useful for assessing the projects of the expansion of the urban transport system.

The obtained InSAR outcomes were used to develop a methodology based on non-linear deformation that can help to define areas possibly affected by ground ruptures. Actually, from existing reports, all the areas classify as "presumably subjected to soil failure" (based on the quadratic coefficient map), have been influenced by ground failures. Although the non-linear component does not always follow the quadratic model proposed, the information inferred from the current method (see section 8.3) can be used as a preliminary indicator of fissure-prone areas, thus improving the vulnerability maps. Outcomes from this research are essential for the present and future small- and large- scale projects such as the new Mexico City airport which is planned to be settled close to one of the hazardous areas identified (see section 8.3.1.1). Moreover, since several wastewater treatment plants and waste disposals are located near prone to ground rupture sites a continuous monitoring is necessary for risk mitigation of groundwater pollution.

The appearance of soil fractures may occur where the subsidence gradients are high. However, in order to understand better the stress-strain behaviour associated to fissuring, geological information, geophysical and other in-situ measurements have to be integrated in a common database.

Even though subsidence may not be reversible, its effects can be mitigated. For that purpose, techniques such as InSAR and GPS can be combined to provide paramount information that can be used for geotechnical hazard assessment, aiding a more efficient groundwater management and maintenance of existing and forthcoming local infrastructure.

Chapter 9

Summary and final conclusions

Radar remote sensing methods have notably developed during the last years. Among them InSAR techniques have radically changed the way of measuring earth processes, providing larger spatial coverage and results with a precision comparable to powerful surveying methods such as GPS or levelling. For example, subsidence in Mexico City has been almost completely mapped (except for some very low coherent areas) by using standard and MTI approaches. Nevertheless, discrepancies between existing results were observed motivating part of this investigation. Moreover, many studies have focused on the southern part of the Valley of Mexico; however, the northern sector, also experiencing important demographic growth and water related problems, needs to be further studied as demonstrated in this thesis.

In this work, a specific and adapted open source MTI software was proposed to measure subsidence in the entire Valley of Mexico and to characterize associated hazards, which seriously affect infrastructure and endanger the groundwater quality. Particularly, the SBAS mode was exploited to analyse deformation and related effects in the Valley.

In Chapter 7, the algorithm was assessed in detail over the southern part of the Valley by a quantitative comparison with previous results and by evaluating the quality of unwrapping from interferometric system misclosure maps (RMS maps). The approach was slightly modified to include a reference area selected on the basis of the surface geology (and geotechnical) information to correctly estimate the time series employed in the methodology for identification of areas prone to soil fracturing (section 7.6 and 8.3). The inversion strategy used in StaMPS was studied and results compared to those obtained by ULS and WLS-SVD, concluding that the WLS method from StaMPS with temporal reference selection based on the proposed uncertainty analysis provides relatively better results. However, the selection of the weight matrix needs to be carefully evaluated in other interferometric systems.

Until now causes of the subsidence in Mexico City have been mainly assigned to the extensive groundwater practices in the area; nevertheless, in some sectors where former disposal sites used to be located a component coming from buried trash in decomposition may also add to the deformation signal, as described in section 7.3.3.

Once the algorithm was proven to work correctly, the time series were extended to include the 2007-2010 period in the subsidence evolution study. Slightly lower subsidence rates than those for the period 2002-2007 were noted. The observed results were discussed attributed to small recovering of the groundwater levels that could have led to slower subsidence rates, or to the inclusion of larger number of noisy pixels that might have affected the quality of the unwrapping. A preliminary interpretation indicates that the first hypothesis could explain the rates obtained for the extended period. Unfortunately, detailed piezometric data and knowledge of mechanical and physical properties of the materials involved lacked to better evaluate their responses to variations in the groundwater levels and correlation with the ground settlement changes.

The 2002-2010 analysis on the southern part of the Valley indicate that the metro line A and the Calzada Zaragosa street are subjected to critical and very variable subsidence that produces important damages and high repair costs, posing, as well, a potential risk to their users.

Detailed conventional and multitemporal InSAR analysis in the northern part of the Valley of Mexico using the assessed algorithm was presented in Chapter 8, revealing important land sinking rates and its critical effect on meaningful infrastructure. ERS and ENVISAT time series for the periods 1999-2000 and 2002-2010, respectively, were produced and analysed. By exploiting the SBAS method, subsidence affecting both urban and non-urban areas was detected, capability normally reduced in the later areas when using the PSI method.

The methodology for fissuring zonation described in section 8.3, effectively identify ground rupture events where notable acceleration or deceleration occurs. Most ground failures would be triggered by differential subsidence, but other mechanisms may also intervene (e.g., active tectonics, stresses due to water infiltration). Furthermore, the presence of a graben structure could imply that part of the subsidence is controlled by existing faults. In Ecatepec de Morelos, large accelerations take place near important hydraulic infrastructure and in areas where challenging projects are planned (e.g., new Mexico Airport). Important findings for geological risk assessment can be achieved by complementing InSAR results with other survey techniques such as GPR, as demonstrated for southern Valley of Mexico (section 7.6).

Most areas studied have been experiencing significant demographic growth during the last decades, implying that improvement of fresh water services, sewage and drainage systems for urban and agriculture uses is indispensable. Hence, the identification, surveillance and forecast of soil fracture risk zones are important to prevent failures in future hydraulic systems or at least reduce related effects. Additionally, waste disposal sites and wastewater treatment plants were noticed to be located near the inferred fissuring areas. Accordingly, InSAR observations can be used to develop strategic water and waste management and planning. Critical spatial information for location of waste and water systems can be provided by exploiting the InSAR outcomes.

The particular analysis on expansive soils (vertisol) of the northern Valley suggested that subsidence rates tend to be larger during the dry seasons. Nevertheless, this study needs to be spatially extended and complemented with specific soils properties and meteorological data for a better interpretation. Extensive investigation of these soils is required for a better agriculture management, and better and safer cropping.

Subsidence in the entire Valley is essentially linear through time, but with a small quadratic component in certain areas. On the other hand, non-linearity observed in some deformation time series adjusts the consolidation configurations proposed by Zeevaert (1986). Characterization of the soft soils in underground engineering projects (e.g., Menache Varela 2010; Benamar and Zaldívar 2010), particularly the history of clay’s consolidation is paramount, thereby InSAR time series can also provide useful related information.

The extremely high rates of subsidence in the Valley of Mexico are constantly threatening city development and infrastructure. Moreover, if the population continues to grow at progressively higher rates, the pressure on water resources will increase, inducing a more severe consolidation of the aquitard and thus compounding the ground sinking problem and its consequences. In this scenario, InSAR appears as a valuable tool for improvement of urban planning and hazard assessment. Our methodology for regional identification of prone to soil fracturing zones results flexible and can be adapted to study other areas where anomalies observed in the InSAR time series follow a certain temporal pattern. Information obtained from this method is valuable to planners and public officials responsible for making decisions to mitigate risks.

Albeit the multi-disciplinary studies and efforts to attenuate water-related problems in Mexico Valley, it must be stressed that awareness-raising among its population is vital to reduce repercussions.

Future directions

Understanding the behaviour of the subsidence through time by using and combining geodetic satellite techniques and other in-situ measurements can aid the study of the complex strain-stress behaviour of aquifer systems not only in Mexico but also in other countries with similar water-related problematic.

Thus, the temporal extension of the deformation time series by using data from on-going SAR satellites such as TerraSAR-X, COSMO-SkyMed, Sentinel-1 can improve the present study. Moreover, the use of L-band can be exploited to increase the spatial sampling over agriculture areas negatively influenced by subsidence. Similarly, PSI and SBAS approaches can be combined to extract meaningful signal from targets with different scattering characteristics (Hooper 2008). This may enhance the methodology for identification of fissure-prone areas, improving the vulnerability maps and failure evaluation on important infrastructure. Moreover by using current SAR data, the monitoring of ground failure prone areas can be temporally extended and updated mapping achieved. Soil fracture trigger mechanisms need to be further studied; techniques such as GPR, GPS and levelling can support this investigation, particularly over the northern part of the Valley of Mexico, where only a few measurements were available.

Modelling of groundwater flow systems allows the analysis of hydrogeological conditions and prediction of transportation of pollutants (e.g., Bear and Cheng 2010). Moreover, by introducing the location of fractures (inferred from InSAR) into the groundwater models a better risk evaluation of contaminants and characterization of the aquifer dynamics and geometry can be accomplished. Information useful for recharge programs can also be derived.

Because subsidence may continue impacting the Valley, the development of a continuous surveillance system by integrating various methods and information represent a primordial need. Effective risk mitigation strategies can reduce repair and damage costs from land subsidence and associated hazards.

Bibliography

Adam, N., Kampes, B., & Eineder, M. (2004).Development of a scientific permanent scatterer system: Modifications for mixed ERS/ENVISAT time series.*Proceedings of the 2004 Envisat & ERS Symposium*.Salzburg, Austria.

Agram, P.S. (2010).Persistent Scatterer Interferometry in natural terrain. *PhD Thesis. California, USA.*

Agram, P.S., Jolivet, R., Riel, B., Lin, Y.N., Simons, M., Hetland, E., Doin, M.P., & Lassere, C. (2013). New Radar Interferometric Time Series Analysis Toolbox Released. *Eos Trans. AGU, 94*

Alcaraz, Y., & Robles, J. (2007).Desborda lluvia al recien entubado Gran Canal. Available online at http://www.eluniversal.com.mx/ciudad/85175.html

Alcocer Miranda, J. (2013).Un frágil e inestable sistema de transporte:La Cronica Available online at: http://www.cronica.com.mx/notas/2013/760978.html

Amelung, F., Galloway, D.L., Bell, J.W., Zebker, H.A., & Laczniak, R.J. (1999). Sensing the ups and downs of Las Vegas: InSAR reveals structural control of land subsidence and aquifer-system deformation. *Geology*, 483–486.

Armendariz Fierro, D. (2011).Parámetros de diseño geotécnico para la lumbrera 4 del túnel emisor oriente. *Thesis. D.F., Mexico.*

ASCE (1996). *Hydrology handbook, 2nd. Ed. Manuals and Reports on Engineering Practice No. 28*. USA: American Society of Civil Engineers

Attema, E., Snoeij, P., Davidson, M., Floury, N., Levrini, G., Rommen, B., & Rosich, B. (2008).The European GMES Sentinel-1 Radar Mission.*Geoscience and Remote Sensing Symposium, IGARSS 2008, Proceedings*. Boston, MA.

Auvinet , G. (2010).Soil fracturing induced by land subsidence.*Land Subsidence, Associated Hazards and the Role of Natural Resources Development (Proceedings of EISOLS 2010)*.Querétaro, Mexico

Auvinet , G., Comulada-Simpson, M., Maidl, U., Mendez, R., & Rangel, J.L. (2012). Tunel Emisor Oriente: Analsis, Diseño y Comportamiento. *Geotecnia, 223*, pp. 22-32.

Auvinet, G., Méndez, E., & Juárez, M. (2013).Soil Fracturing induced by Land Subsidence in Mexico City.*Proceedings of the 18th International Conference on Soil Mechanics and Geotechnical Engineering*.Paris, FRANCE

Auvinet Guichard, G., & Moises, J. (2011).Geotechnical characterization of Mexico City subsoil.*Proc., 14th Pan-American Conference on Soil Mechanics and Geotechnical Engineering*.Toronto, Ontario, Canada.

Ayuntamiento de Teoloyucan (2004).Plan municipal de desarrollo de Teoloyucan. Available online at: http://portal2.edomex.gob.mx/sedur/planes_de_desarrollo/planes_municipales/teoloyucan/index.htm

Ayuntamiento de Teoloyucan (2013).Plan de Desarrollo Municipal 2013-2015. Available online at: http://www.teoloyucan.gob.mx/transparencia/Plan_de%20Desarrollo_Municipal_2013-2015.pdf

Ayuntamiento de Tepotzotlán, & Gobierno del Estado de México (2003).Plan municipal de Desarrollo Urbano de Tepotzotlán. Available online at: http://seduv.edomexico.gob.mx/planes_municipales/Tepotzontlan/tepotzotlan%20mayo%202003.pdf

Ayuntamiento de Tutitlán (2006).Plan de Desarrollo Municipal 2006-2009. Available online at: http://ordenjuridicodemo.segob.gob.mx/Estatal/ESTADO%20DE%20MEXICO/Municipios/Tultitlan/Plan01.pdf

Bamler, R. (1992). A comparison of range-Doppler and wavenumber domain SAR focusing algorithms. *IEEE Transactions on Geoscience and Remote Sensing, 30*, 706 - 713

Barajas-Nigoche, L.D., Carreón-Freyre, D.C., Mata-Segura, J.L., Rivera-León, A., & Cafaggi-Félix, F. (2010).Geological and geophysical characterization of fracturing in granular deposits associated with land subsidence in San Luis Potosí City, Mexico.*Land Subsidence, Associated Hazards and the Role of Natural Resources Development (Proceedings of EISOLS 2010)*.Querétaro, Mexico.

Barbarrosa, S., & Farina, A. (1994). Space-time-frequency processing of synthetic aperture radar signals. *Aerospace and Electronic Systems, IEEE Transactions on, 30*, 341 – 358. DOI: 10.1109/7.272259

Barrera Aguirre, J.M. (2007).Afecta grieta de 3 kilómetros a casas de Jaltenco. Available online at http://www.eluniversal.com.mx/notas/436861.html

Batu, V. (1998). *Aquifer Hydraulics. A comprehensive guide to hydrogeologic data analysis*. United Stated of America: John Wiley & Sons,Inc.

Bear, J., & Cheng, A.H.-D. (2010). Modeling Groundwater Flow and Contaminant Transport: Springer Netherland

Bechor, N. (2006).Extending interferometric synthetic Aperture radar measurements from one to two dimensions. *PhD Thesis. California, USA.*

Benamar, I., & Zaldívar, D. (2010).Construcción de un túnel para Metro con escudo EPB en la zona de Lago de la ciudad de México.*XXV Reunión Nacional de Mecánica de Suelos e Ingeniería Geotécnica*.Acapulco, Mexico

Berardino, P., Fornaro, G., Lanari, R.a., & Santosti, E. (2002). A new algorithm for surface deformation monitoring based on small baseline differential SAR interferograms. *IEEE Transaction on Geoscience and Remote Sensing, 40*, 2375-2383.

Bonano, M., Manunta, M., Marsella, M., & Riccardo, L. (2012). Long-term ERS/ENVISAT deformation time-series generation at full spatial resolution via the extended SBAS technique. *International Journal of Remote Sensing, 33*, 4756-4783. DOI:10.1080/01431161.2011.638340

Broquetas, A., & Camps, A. (2000). Sensores Radar

Buckley, S.M. (2000). ROI_PAC Documentation. In P. Paul Rosen & P. Persaud (Eds.), *Radar Interferometry Measurement of Land Subsidence*. USA

Burbey, T.J. (2010).Mechanisms for earth fissure formation in heavily pumped basins.*Land Subsidence, Associated Hazards and the Role of Natural Resources Development (Proceedings of EISOLS 2010)*.Querétaro, Mexico.

Bürgmann, R., Schmidt, D., Nadeau, R.M., d'Alessio, M., Fielding, E., Manaker, D., McEvilly, T.V., & Murray, M.G. (2000). Earthquake potential along the Northern Hayward Fault, California. *Science, 289*, 1178–1182.

Burns, E. (2009). *Repensar la Cuenca. La gestión de ciclos del agua en el Valle de México*: Universidad Autónoma Metropolitana. Available online at: http://www.agua.org.mx/h2o/index.php?option=com_content&view=article&id=8232:libro-repensar-la-cuenca&catid=95&Itemid=110

Cabral-Cano, E., Dixon, T.H., Miralles-Wilhel, F., Sanchez-Zamora, O., & Carande, R.E. (2008). Space geodetic imaging of rapid ground subsidence in Mexico City. *Geological Society of America Bulletin, 120*, 1556-1566.

Camarillo, R., Maurer, F., & Ulacia, R. (2013).Lago Tlahuac-Xico.Regeneracion de un ecosistema hidrico urbano. *Master Thesis. Mexico. .*

Cao, Y.-G., Yan, L.-J., & Zheng, Z.-Z. (2009). Extraction of information on geology hazard from multi-polarization SAR images. *The International Archives of the Photogrammetry, Remote Sensing and Spatial Information Sciences, Vol. XXXVII. Part B4*, 1529-1532.

Carnec, C., Raucoules, D., Ledoux, E., Huré, A., & Rivera, A. (2000).Mapping and modelling of major urban subsidence on Mexico City from radar interferometry.*Int. Conf. Research and Application on Hydrogeological Disarray in the World, The Fragile Territory*.Rome, Italy

Carreon-Freyre, D. (2010).Land Subsidence Processes and associated ground fracturing in Central Mexico.*Land Subsidence, Associated Hazards and the Role of Natural Resources Development (Proceedings of EISOLS 2010)*.Queretaro, Mexico.

Carreon-Freyre, D. (2011). Identificación y caracterización de los diferentes tipos de fracturas que afectan el subsuelo de la delegación Iztapalapa del Distrito Federal. D.F., Mexico: Academia de Ingenieria A.C.

Carreon-Freyre, D., & Cerca, M. (2006). Delineating the near-surface geometry of the fracture system affecting the valley of Queretaro, Mexico: Correlation of GPR signatures and physical properties of sediments. *Near Surface Geophysics, EAGE, 4*, 49–55.

Carreón-Freyre, D., Cerca, M., Ochoa-Gonzales, H., Ortiz-Villasenor, I., Gámez-Gonzales, J., & Gutierrez-Calderón, R. (2011).Land Subsidence and ground fracturing affecting major cities of Central Mexico and related groundwater management.*Proceedings of the 14th Pan-American Conference on Soil Mechanics and Geotechnical Engineering*.Toronto, Canada

Carreón-Freyre, D., Hidalgo-Moreno, C., & Hernández-Marín, M. (2006). Mecanismos de fracturamiento de depósitos arcillosos en zonas urbanas. Caso de deformación diferencial en Chalco. *Boletín de la Sociedad Geológica Mexicana Número Especial de Geología Urbana 58*, 237- 250.

Carrera-Hernández, J.J. (2007).Spatio-temporal analysis of aquifer recharge and groundwater potentiometric levels in the Basin of Mexico through the development of a regional database and an open source tool for groundwater flow modelling. *PhD Thesis. Montreal, Canada*

Carrera-Hernandez, J.J., & Gaskin, S.J. (2007). The Basin of Mexico aquifer system: regional groundwater level dynamics and database development. *Hydrogeology Journal, 15*, 1577-1590.

Castillo-Guerrero, J.L. (2012).Interaccion suelo-estructura en suelos cohesivos totalmente saturados *Master Thesis. D.F., Mexico.*

Casu, F., Manzo, M., & Lanari, R. (2006). A quantitative assessment of the SBAS algorithm performance for surface deformation retrieval. *Remote Sens. Environ., 102*, 195-210.

Cavalie, O., Doin, M., Lasserre, C., & Briole, P. (2007). Ground motion measurement in the Lake Mead area, Nevada, by differential synthetic aperture radar interferometry time series analysis: probing the lithosphere rheological structure. *Journal of Geophysical Research, 112*

Cerca, M., Carreon-Freyre, D., & Gutierrez, R. (2010).Instability of the urbanized flank of El Peñón del Marques volcanic edifice and its relation to land subsidence in Mexico City.*Land Subsidence, Associated Hazards and the Role of Natural Resources Development (Proceedings of EISOLS 2010)*.Querétaro, Mexico.

Cerca, M., Carreón-Freyre, D., López-Quiroz, P., Ovando-Shelley, E., Doin, M.P., Gutierrez-Calderón, R., González-Hernández, M., Jimenez-Sánchez, A., & Blancas-Dominguez, D. (2012). Engineering geology approach to the effects of land subsidence in Mexico City. *Geological Society of America (GSA) Field Guide, 25*

Chan, Y.K., & Koo, V.C. (2008). An introduction to Synthetic aperture radar (SAR). *Progress In Electromagnetics Research*, *2*, 27–60.

Chaussard, E., Wdowinskia, S., Cabral-Cano, E., & Amelung, F. (2014). Land Subsidence in central Mexico detected by ALOS InSAR. *Remote Sens. Environ., 140*, 94-106. DOI: 10.1016/j.rse.2013.08.038

Chen, C.W. (2001).Statistical-cost network-flow approaches to two-dimensional phase unwrapping for radar interferometry. *PhD Thesis. California, USA.*

Chen, C.W., & Zebker, H. (2000). Network approaches to two-dimensional phase unwrapping: intractability and two new algorithms. *Journal of the Optical Society of America, 17*, 401-414.

Chen, F., & Lin, H. (2012). Surface deformation detected by the space-observed small baseline SAR interferometry over permafrost environment in Tibet Plateau, China. *The Cryosphere Discuss*, *6*, 4071–4099. doi:10.5194/tcd-6-4071-2012

Chen, V.C. (2011). *The micro Doppler effect in Radar*: ARTECH HOUSE

Chynowetha, P.D., Owensa, J.M., & Legrand, R. (2001). Renewable methane from anaerobic digestion of biomass. *Renewable Energy, 22*, 1-8. DOI: 10.1016/S0960-1481(00)00019-7

Cigna, F., Del Ventisette, C., Liguori, V., & Casagli, N. (2011). Advanced radar-interpretation of InSAR time series for mapping and characterization of geological processes. *Nat. Hazards Earth Syst. Sci., 11*, 865–881.

Cigna, F., Osmanoglu, B., Cabral-Cano, E., Dixon, T.H., Ávila-Olivera, J.A., Garduño-Monroy, V.H., DeMets, C., & Wdowinski, S. (2012). Monitoring land subsidence and its induced geological hazardwith Synthetic Aperture Radar Interferometry: A case study in Morelia, Mexico. *Remote Sensing of Environment, 117*, 146–161. http://dx.doi.org/10.1016/j.rse.2011.09.005

Cimino, J., Elachi, C., & Settle, M. (1986). SIR-B the second Shuttle Imaging Radar experiment. *IEEE Trans. Geosci. Remote Sens., GE-24*, 445–452.

Colesanti, C., Ferretti, A., Prati, C.a., & Rocca, F. (2003). Monitoring landslides and tectonic motions with the PS technique. *Eng. Geol., 68*, 3–14.

CONAGUA (2002a). Determinacion de la Disponibilidad de Agua en el Aquifero Zona Metropolitana de la Ciudad de Mexico Mexico, D.F.

CONAGUA (2002b).Determinación de la disponibilidad de agua en el acuífero Chalco-Amecameca, Estado de México. Available online at: http://www.conagua.gob.mx/conagua07/aguasubterranea/pdf/dr_1702.pdf

CONAGUA (2002c).Estudio Tecnico de Manejo y demanda de agua subterranea para el aquifero Chalco-Amecameca [Slide Presentation]. Available online at: www.cuencavalledemexico.com

CONAGUA (2006). Gasto medio suministrado por los ramales del PAI 2005. Mexico: Comision Nacional del Agua (CONAGUA)

CONAGUA (2009).Estadisticas del Agua de la Region Hidrologico-Administrativa XIII, Aguas de Mexico.Edicion 2009. Available online at: www.conagua.gob.mx/conagua07/noticias/ocavm-1-eaocavm2009.pdf

CONAGUA (2010).Comprendio del agua de la region Administrativa XIII. Edicion 2010. Available online at: www.conagua.gob.mx

CONAGUA (2012).Acciones de infraestructura de drenaje y abastecimiento de agua en el Valle de México 2007-2012. Available online at: www.conagua.gob.mex

CONAGUA, & OCAVM (2011).Proyecto de reglamento del uso del agua del acuífero de Texcoco [Slide Presentation]. D. Tecnica. Comision Nacional de Agua (CONAGUA), Organismo de Cuenca Aguas del Valle de México (OCAVM). Available online at: http://cuencavalledemexico.com/wp-content/uploads/2011/02/GEO-72-Reglamento-Acu%C3%ADfero-Texcoco.pdf

CONAGUA/SIGA (2014). Aprovechamientos Subterraneos por Estado. Mexico,: Comisión Nacional del Agua/Subgerencia de Informacion Geografica del Agua

Crosetto, M., Arnaud, A., Duro, J., Biescas, E., & Agudo , M. (2003).Deformation monitoring using remotely sensed radar interferometric data.*11th International FIG Symposium on Deformation Measurements, Geod. and Geod. Appl. Lab., Dep. of Civ. Eng.,Patras Univ.*Santorini, Italy.

Cruz Gonzales, V.H. (2009).Contaminacion de agua potable por cromo hexavalente. Caso de estudio: Colonia Lecheria, Municipio de Tutitlan, Estado de Mexico. *Master Thesis. D.F., Mexico.*

Curlander, J.C., & McDonough, R.N. (1991). *Synthetic aperture radar; Signal processing; Remote sensing* New York, USA: Wiley

Cytsa, & MAV (2012).Modelo de Marco Institucional para la Gestión de los Recursos Hídricos en el Valle de México. Creatividad y Tecnologia (Cytsa) & Miranda Aranda Velasco S.C (MAV). Banco Interamericano de Desarrollo. Available online at: http://www.agua.unam.mx/sacmex/assets/docs/IDBDOCS_GRH_ValleMexico.pdf

De Cserna, Z., De la Fuente-Duch, M., Palacios Nieto, M., Triay, L., Mitres Salazar, L.M., & Mota Palomino, R. (1988). Estructura geológica, gravimetría, sismicidad y relaciones neotectónicas regionales de la Cuenca de México. *Boletín 104. México, Instituto de Geología, UNAM, 71 p.*

Delacourt, C., Briole, P., & Achache, A. (1998). Tropospheric corrections of SAR interferograms with strong topography. Application to Etna. *Geophys. Res. Lett., 25*, 2849–2852.

Di Masso Cervera, N. (2007).Diseno del subsistema RF para el receptor SAR biestatico en Banda-C Sabrina Memoria. *Thesis of the Universitat Autonoma de Barcelona Barcelona, Spain.*

Diaz-Rodriguez, J.A. (2006). Los suelos lacustres de la Ciudad de Mexico *Rev. Int. de Desastres Naturales, Accidentes e Infraestructura Civil, 6*, pp.111-130.

Dierking , W., & Busche, T. (2006). Sea Ice Monitoring by L-Band SAR: An Assessment Based on Literature and Comparisons of JERS-1 and ERS-1 Imagery. *Geoscience and Remote Sensing, IEEE Transactions on, 44*, 957-970.

Dirección General de Proteccion Civil, & Ayuntamiento de Tultepec (2013).Altas de riesgo 2013-2015. Available online at: http://www.tultepec.gob.mx/pdf/ATLAS_TULTEPEC.pdf

DOF (2009).Acuerdo por el que se da a conocer la ubicacion geografica de 371 acuiferos del territorio nacional, se actualiza la disponibilidad media anual de agua subterranea de 282 acuiferos, y se modifica, para su mejor precision, la descripcion geografica de 202 acuiferos. Diario Oficial de la Federacion (DOF). Available online at:

Doin, M.P., Lasserre, C., Peltzer, G., Cavalie, O., & Doubre, C. (2009). Corrections of stratified tropospheric delays in SAR interferometry: validation with global atmospheric models. *J. Appl. Geophys., 69*, 35-50.

Eldhuset, K. (1996). An automatic ship and ship wake detection system for spaceborne SAR images in coastal regions. *IEEE Trans. Geosci. Remote Sens. , 34*, 1010–1019.

Engdahl, M., & Hyyppä, J. (2003). Land-Cover Classification Using Multitemporal ERS-1/2 InSAR Data. *EEE Transactions on Geoscience and Remote Sensing, 41*, 1620-1628.

Escobar Villagran, B.S. (2010).Análisis de la sobre-explotacion del Acuifero de Texcoco. *PhD Thesis. Montecillo, Mexico*

Escolero Fuentes, O., Martinez, S., Kralisch, S., & Perevochtchikova, M. (2009). Vulnerabilidad de las fuentes de abastecimiento de agua potable de la Ciudad de México en el contexto de cambio Climático. Informe Final. Mexico:

Estrada Domínguez, F. (2010). Jaltenco

Farr, T.G., and, & Kobrick, M. (2000). Shuttle radar topography mission produces a wealth of data. *Eos Trans. AGU 81*, 583–585.

Farr, T.G., Rosen, P.A., Caro, E., Crippen, R., Duren, R., Hensley, S., Kobrick, M., Paller, M., Rodriguez, E., Roth, L., Seal, D., Shaffer, S., Shimada, J., Umland, J., Werner, M., Oskin, M., Burbank, D., & Alsdorf, D. (2007). The shuttle radar topography mission. *Reviews of Geophysics, 45* http://dx.doi.org/10.1029/2005RG000183

Ferretti , A., Prati C, & F., R. (1999). Multibaseline InSAR DEM reconstruction: the wavelet approach. *IEEE Trans Geosci Remot Sen, 37*, 705–715.

Ferretti, A., Prati, C., & Rocca, F. (2001). Permanent scatterers in SAR interferometry. *IEEE Trans. Geosci. Remote Sens., 39*, 8–20.

Figueroa-Vega, F. (1984). Case history No. 9.8, Mexico, D.F., Mexico. Paris, France: United Nations Educational Scientific and Cultural Organization

Figueroa-Vega, G.E. (1976).Subsidence of the city of Mexico: a historical review.*Proceedings of the Second International Symposium on land Subidence, International Association of Hydrological Science*.Anaheim, California

Franceschetti, G., & Lanari, R. (1999). *Synthetic Aperture Radar Processing*. New York: CRC PRESS

Gabriel, A.K., & Goldstein, R.M. (1988). Crossed orbit interferometry: theory and experimental results from SIR-B. *International Journal of Remote Sensing, 9*, 857-872.

Gabriel, A.K., Goldstein, R.M., & Zebker, H.A. (1989). Mapping small elevation changes over large areas: differential radar interferometry. *Journal of Geophysical Research, 94*, 9183-9191.

Galindo Castillo, E., Otazo Sánchez, E.M., Gordillo Martínez, A.J., Santiago Arellano, I., González Ramírez, C.A., & Reyes Gutiérrez, L.R. (2011). Sobreexplotación del acuífero Cuautitlán-Pachuca:balance hídrico 1990-2010. *Avances en Impacto, Tecnologia y Toxicologia Ambiental*, 9-32.

GDF (2000). Zona Metropolitana del Valle de Mexico. Riesgos Geologicos. Mexico: Gobierno del Distrito Federal(GDF)

GDF, SERMANAT, & CONAGUA (2012a).Pruebas de recarga instantánea y a corto plazo (activa y pasiva), Proyecto piloto de recarga Artificial El Caracol. Gobierno del Distrito Federal (GDF), Secretaria de Medio Ambiente y Recursos Naturales (SERMANAT), Comision Nacional de Agua(CONAGUA). Available online at: http://cuencavalledemexico.com/wp-content/uploads/2012/05/GEO-81-Avances-SRA-Caracol.pdf

GDF, & SMA (2005). Informe Climatológico Ambiental del Valle de México 2005. Mexico:

GDF, & SMA (2006).Gestión ambiental del aire en el Distrito Federal. Avances y propuestas 2000-2006 Gobierno del Distrito Federal(GDF), Secretaria de Medio Ambiente(SMA). Available online at: http://www.sma.df.gob.mx/sma/download/archivos/gaa/gaa_avances_propuestas_2000_2006.pdf

GDF, SMA, & SACMEX (2012b).Programa de Gestion Integral de los Recursos Hidricos, Vision 20 años. Gobierno del Distrito Federal(GDF), Secretaria de medio Ambiente(SMA), Sistema de Aguas de la Ciudad de Mexico(SACMEX). Available online at: http://www.sacmex.df.gob.mx/img/home/vision.pdf

GDF, SMA, SOBSE, & SACMEX (2006).Programa de Manejo Sustentable del agua para la Ciudad de Mexico Gobierno del Distrito Federal(GDF), Secretaria de Medio Ambiente(SMA),Secretaria de Obras y Servicios(SOBSE),Sistema de Aguas de la Ciudad de Mexico(SACMEX). Available online at: www.sma.df.gob.mx

Geudtner, D., Winter, R.a., & Vachon, P.W. (1996).Flood monitoring using ERS-1 SAR interferometry coherence maps.*Geoscience and Remote Sensing Symposium on Remote Sensing for a Sustainable Future, IGARSS 1996, Proceedings*

Ghiglia, D.C., & Romero, L.A. (1994). Robust two-dimensional weighted and unweighted phase unwrapping that uses fast transforms and iterative methods. *Journal of the Optical Society of America, 11*, 107-117.

Gobierno del Distrito Federal (2004). *Reglamento de construcciones para el Distrito Federal (Mexico City Building Code)*. Mexico: Gaceta Oficial del Distrito Federal (GODF)

Gobierno del Estado de Mexico (2006).Programa de Desarrollo regional. Macro Region III Oriente. Region IV Cuautitlán Izcalli 2006-2011. Available online at: http://transparencia.edomex.gob.mx/coplademe/informacion/sectoriales/M%20III%20-%20R%20IV%20Cuautitlan%20Izcalli.pdf

Gobierno del Estado de Mexico (2010).Plan de Desarrollo Municipal 2009-2012.Cuautitlán Izcalli. Available online at:

Gobierno del Estado de Mexico (2011).Programa de Desarrollo Regional. Marcro Region III Oriente. Region XIV TULTITLÁN 2006-2011. Available online at: http://transparencia.edomex.gob.mx/coplademe/informacion/sectoriales/M%20III%20-%20R%20XIV%20Tultitlan.pdf

Gobierno del Estado de México, & Ayuntamiento del Tecámac (2013).Atlas de Riesgos Tecamac Available online at: http://www.google.de/url?sa=t&rct=j&q=&esrc=s&source=web&cd=1&ved=0CCMQFjAA&url=http%3A%2F%2Fwww.ipomex.org.mx%2Fipo%2Farchivos%2FdownloadAttach%2F303480.web%3Bjsessionid%3D7A8471EEF7CBED68D77A1017BE2E44B8&ei=UEAPVOGsDKW7ygPR74LADA&usg=AFQjCNG6D5Y9fgkrgvRbVbOrJnqnnIBUIA&sig2=1I2Sn1Y_zL0Mq16-_RUuZQ&bvm=bv.74649129,d.bGQ

Gobierno del Estado de Mexico, & CAEM (2010). Atlas de Inundaciones No.17. Municipio de Ecatepec de Morelos. Mexico: Gobierno del Estado de Mexico, Comision del Agua del Estado de Mexico

Goldstein, R.M., & Werner, C.L. (1998). Radar interferogram filtering for geophysical applications. *Geophysical Research Letters, 25*, 4035 – 4038.

Goldstein, R.M., Zebker, H.A., & Werner, C.L. (1988). Satellite radar interferometry: Two-dimensional phase unwrapping. *Radio Science, 23*, 713-720.

Gonzales Taobada, C. (2008).Comportamiento en el mercado inmobiliario al cambiar el uso de suelo de tiradero a centro comercial en Ciudad Nezahualcoyotl. *PhD Thesis. D.F., Mexico.*

Gourmelen, N., Amelung, F., & Lanari, R. (2010). Interferometric synthetic aperture radar–GPS integration: Interseismic strain accumulation across the Hunter Mountain fault in the eastern California shear zone. *Journal of Geophysical Research, 115* DOI: 10.1029/2009JB007064

Grafared, E.W. (1994). Optimization of Geodetic Networks. *Bolletino di Geodesia a Science Affini, 33*, 351-406

"Grietas en Ecatepec" (2014).Se empiezan a ver muchas grietas en Ecatepec. Available online at: http://reporterosenmovimiento.wordpress.com/2014/06/05/se-empiezan-a-ver-muchas-grietas-en-ecatepec/

H. Ayuntamiento Constitucional de Ecatepec de Morelos (2011).ATIENDE SAPASE BOQUETE EN SAN PEDRO XALOSTOC OCASIONADO POR LLUVIAS. Available online at: http://www.ecatepec.gob.mx/boletines/show.php?boletin=729

H. Ayuntamiento de Ecatepec de Morelos, GOBIERNO DEL ESTADO DE MEXICO, & SEDUVI (2003).PLAN MUNICIPAL DE DESARROLLO URBANO DE ECATEPEC H. Ayuntamiento de Ecatepec de Morelos, Gobierno del Estado de Mexico, Secretaria de Desarrollo Urbano y Vivienda,. Available online at: http://www.ecatepec.gob.mx/transparencia/Plan%20de%20Desarrollo%20Urbano%202003.pdf

H.Ayuntamiento Constitucional de Coacalco de Berriozabal (2006).Plan de Desarrollo Municipal 2003-2006. Available online at: http://www.ordenjuridico.gob.mx/Estatal/ESTADO%20DE%20MEXICO/Municipios/Coacalco%20de%20Berriozabal/COAPla1.pdf

Hanssen, R. (2003).Subsidence monitoring using contiguous and PS-INSAR: quality assessment based on precision and reliability.*Proceedings, 11th FIG Symposium on Deformation Measurements*.Santorini, Greece.

Hanssen, R.F. (2001). *Radar Interferometry Data Interpretation and Error Analysis*. The Netherlands: Kluwer Academic Publishers

Henderson, F.M., & Lewis, A.J. (1998). *Principles and applications of imaging radar Manual of Remote Sensing* New York, USA

Herrera, G., Fernandez, J.A., Tomas, R., Cooksley, G., & Mulas, J. (2009). Advanced interpretation of subsidence in Murcia (SE Spain) using A-DInSAR data—Modelling and validation. . *Natural Hazards Earth System Sciences, 9*, 647-661.

Herrera Zaragoza, L. (2012).Escenarios futuros del reuso de agua residual tratada a nivel terciario para abastecimiento publico-urbano en Ecatepec, Estado de Mexico. *Master Thesis San Luis Potosí, Mexico.*

Hetland, E.A., Muse, P., Simons, M., Lin, Y.N., Agram, P.S., & DiCaprio, C.J. (2012). Multiscale InSAR Time Series (MInTS) analysis of surface deformation. *J. Geophys. Res., 117* DOI:10.1029/2011JB008731

Hillman, A., Rolland, P., Chabot, M., Periard, R., Ledantec, P., & Martens, N. (2011).RADARSAT-2 Mission Operations status.*Geoscience and Remote Sensing Symposium, IGARSS 2011*.Vancouver, BC.

Holah, N., Baghdadi, N., Zribi, M., Bruand, A., & King, C. (2005). Potential of ASAR/ENVISAT for the characterization of soil surface parameters over bare agricultural fields. *Remote Sens. Environ., 96*, 78–86.

Hooper, A. (2008). A multi-temporal InSAR method incorporating both persistent scatterer and small baseline approaches. *Geophysical Research Letters, 35* doi:10.1029/2008GL034654.

Hooper, A. (2010).A statistical-cost approach to unwrapping the phase of insar time series.*Proceedings of the Advances in the Science and Applications of SAR Interferometry, ESA Fringe 2009,Workshop ESA*.Frascati, Italy.

Hooper, A., Bekaert, D., Spaans, K., & Arikan, M. (2012). Recent advances in SAR interferometry time series analysis for measuring crustal deformation. *Tectonophysics, 514-517*, 1-13. doi: 10.1016/j.tecto.2011.10.013

Hooper, A., Segall, P.a., & Zebker, H. (2007). Persistent scatterer InSAR for crustal deformation analysis, with application to Volcán Alcedo, Galápagos. *Journal of Geophysical Research, 112* doi:10.1029/2006JB004763.

Hooper, A., Zebker, H., Segall, P., & Kampes, B. (2004). A new method for measuring deformation on volcanoes and other natural terrains using InSAR persistent scatterers. *Geophys. Res. Lett., 31* doi:10.1029/2004GL021737

Huizar Alvarez, R. (1996). Hydrochemistry of the aquifers in the Río Las Avenidas basin, Pachuca, Hidalgo,Mexico. *Water, air and soil pollution, 96*, 185-201.

Huizar Álvarez, R. (1993). Simulacion matematica del sistema aquifero de Chalco-Amecameca, Mexico. *Geofisica International, 32*, 57-79.

Huizar Álvarez, R. (2011).Proyecto de recarga artificial del acuífero con aguas tratadas del modulo experimental de tratamiento terciario en la zona federal del lago de Texcoco. Available online at: http://cuencavalledemexico.com/wp-content/uploads/2012/05/GEO-78-Recarga-Artificial-Texcoco-IG-UNAM1.pdf

Huízar Álvarez, R., Campos, E., Oscar, M., Salazar, L.M., Alatriste, V., David, , Méndez, G., Teodoro, , & Juárez, S., Faustino (2001). Evaluación hidrogeológica de la subcuenca de Tecocomulco, Estados de Hidalgo, Puebla y Tlaxcala, México. *MéxicoRevista Mexicana de Ciencias Geológicas 18*

Huizar Alvarez, R., Hernandez, G., Carrillo-Martinez, M., Carrillo-Rivera, J.J., Hergt, T., & Ángeles, G. (2003). Geologic structure and groundwater flow in the Pachuca–Zumpango sub-basin, central Mexico. *Environmental Geology, 43*, 385-399. DOI:10.1007/s00254-002-0654-4.

INEGI (2013).Espacio y Datos de Mexico. Instituto Nacional de Estadisticas y Geografia (INEGI). Available online at: www.inegi.org.mx

Instituto de Proteccion Civil (2004). *Fracturamientos recientes en los municipios del Estado de Mexico. Cuaderno de investigacion 4*. Estado de Mexico, Mexico Available online at: http://portal2.edomex.gob.mx/dgproteccion_civil/prevencion/prevencion/cultura_proteccion_civil/trabajos_investigacion/groups/public/documents/edomex_archivo/dgproteccion_civil_pdf_ci4.pdf

Ishitsuka, K., Fukushima, Y., Tsuji, T., Yamada, Y., Matsuoka, T., & Giao, P.H. (2014). Natural surface rebound of the Bangkok plain and aquifer characterization by persistent scatterer interferometry. *Geochem. Geophys. Geosyst., 15*, 965–974. doi:10.1002/2013GC005154

Jacobs, A., Sandwell, D., Fialko, Y., and , & Sichoix, L. (2002). The 1999 (Mw 7.1) Hector Mine, California, earthquake: Near - field postseismic deformation from ERS interferometry. *Bull. Seism. Soc. Am. , 92*, 1433-1442.

Jiménez, B., & Chávez, A. (2004). Quality assessment of an aquifer recharge with wastewater for tis potential use as drinking source: “El Mezquital Valley” case. *Water Science and Technology, 50*, 269-276.

Jolivet, R., Grandin, R., Lasserre, C., Doin, M.P., & Peltzer, G. (2011). Systematic InSAR tropospheric phase delay corrections from global meteorological reanalysis data. *Geophysical Research Letters, 38*

Jordan, R.L. (1980). The Seasat—A synthetic aperture radar system. *IEEE J. Ocean. Eng., 5*, 154–164.

Jordan, R.L., Huneycutt, B.L., & Werner, M. (1991).The SIR-C/X-SAR synthetic aperture radar system.*Proceedings of the IEEE 1991*.

Juárez Camarena, M., Auvinet Guichard, G., Hernández Vizcarra, F., & Méndez Sánchez, E. (2010).Contribution to the geotechnical characterization of the subsoil of the north of Mexico basin.*XXV Reunión Nacional de Mecánica de Suelos e Ingeniería Geotécnica*.Acapulco, Mexico.

Kampes, B.M. (2005).Displacement parameter estimation using permanent scatterer interferometry. *PhD Thesis. Delft, Netherlands.*

Kampes, B.M., Hanssen, R.F., & Perski, Z. (2003).Radar Interferometry with Public Domain Tools.*Third International Workshop on ERS SAR Interferometry, `FRINGE03'*.Frascati, Italy

Kankaku, Y., Suzuki, S., & Osawa, Y. (2013).ALOS-2 mission and development status.*Geoscience and Remote Sensing Symposium, IGARSS 2013, Proceedings*.Melbourne, Australia.

Kerbaol, V., & Collard, F. (2005). SAR-derived coastal and marine applications: From research to operational products. *IEEE J. Ocean. Eng., 30*, 472–486.

Kim, D.-J., Kang, J., Yoon, B., Kim, Y., & Kim, Y. (2008).Observation of Crude Oil Spill off the West Coast of Korea Using TerraSAR-X, ENVISAT ASAR and ALOS PALSAR.*Geoscience and Remote Sensing Symposium , IGARSS 2008, Proceedings*.Boston, MA, USA.

Kim, S., Wdowinski, S., Dixon, T.H., Amelung, F., Kim, J.W., & Won, J. (2010). Measurements and predictions of subsidence induced by soil consolidation using persistent scatterer InSAR and a hyperbolic model. *Geophys. Res. Lett., 37* doi:10.1029/2009GL041644

Kolh, M.S. (2001). *Subsidence and sinkholes in east Tennessee. A field Guide to holes in the ground.State of Tennessee*. State of Tennessee Available online at: Available online at: https://www.tn.gov/environment/geology/docs/sink_hole.pdf (accessed on August 2013).

Krämer, R. (1989).Auf Kalman-Filtern basierende Phasen- und Parameter estimation zur Lösung der Phasen vieldeutigkeits problematik bei der Höhenmodellerstellung aus SAR-Interferogrammen. *PhD Thesis. Germany.*

Kurosu, T., Fujita, M., & Chiba, K. (1995). Monitoring of rice crop growth from space using ERS-1 C-band SAR. *IEEE Trans. Geosci. Remote Sens. , 33*, 1092–1096.

Lanari, R., Casu, F., Manzo, M., & Lundgren, P. (2007). Application of the SBAS-DInSAR technique to fault creep: A case study of the Hayward fault, California. *Remote Sens. Environ., 109*, 20–28. DOI:10.1029/2004GL021294.

Lanari, R., Mora, O., Manunta, M., Mallorqui, J., Berardino, P., & Sansosti, E. (2004). A small-baseline approach for investigating deformations on full-resolution differential SAR interferograms. *IEEE Transaction on Geoscience and Remote Sensing, 42*

Lauknes, T., Zebker, H., & Larsen, Y. (2011). InSAR deformation time series using an L1- Norm small-baseline approach *IEEE Transactions on Geoscience and Remote Sensing, 49*, 536–546.

Lermo, J., Ovando, E., & Espinosa, L. (2010).Microtremor measurements to detect zones of potential cracking in the Basin of México.*Land Subsidence, Associated Hazards and the Role of Natural Resources Development (Proceedings of EISOLS 2010)*.Querétaro, Mexico.

Lesser , J.M. (1992). Hidrología subterránea en el Valle de Mëxico. *Ingeniería Hidráulica en México, II*, pp.90-98.

Lesser, J.M., & Asociados, S.A. (1991). Recarga artificial de Agua Residual Tratada al Acuífero del Valle de México. Trabajo realizado para la DGCOH-DDF. *Ingeniería Hidráulica en México, Vol.IV, Num. 2*

Lesser, J.M., & Cortéz, M.A. (1998). El hundimiento del terreno en la Ciudad de Mexico y sus implicaciones en el sistema de drenaje. *Ingeniería Hidráulica en México, 13*, 13-18.

Lesser, J.M., & Posadas, D. (2005).Evolucion Piezometrica del Aquifero de la Ciudad de Mexico.*V Congreso de Aguas Subterraneas* Hermosillo,SONORA,Mexico

Leyva Suarez, E. (2010).Acuíferos semiconfinados y su modelación:aplicaciones al acuífero de la Zona Metropolitana de la Ciudad de México. *Master. Mexico, D.F.*

Li, F.K., & Goldstein, R.M. (1990). Studies of multibaseline spaceborne interferometric synthetic aperture radars. *Geoscience and Remote Sensing, IEEE Transactions on, 28*, 88-97.

Li, Z., Cross, P., Albert, P., Fischer, J., & Bennartz, R. (2006a). Assessment of the potential of meris near-infrared water vapour products to correct ASAR interferometric measurements. *International Journal of Remote Sensing 33* doi:10.1029/2005GL025299.

Li, Z., Fielding, E.J., Cross, P., & Muller, J.P. (2006b). Interferometric synthetic aperture radar atmospheric correction: medium resolution imaging spectrometer and advanced synthetic aperture radar integration. *Geophys. Res. Lett., 33* doi:10.1029/2005GL025299

Li, Z., Muller, J.P., Cross, P., & Fielding, E.J. (2005). Interferometric synthetic aperture radar (InSAR) atmospheric correction: GPS and Moderate Resolution Imaging Spectroradiometer (MODIS), and InSAR integration. . *J. Geophys. Res., 110* doi:10.1029/2004JB003446

Liu, G.L., Hao, H.D., & Tao, Q.X. (2010). Kalman filter phase unwrapping algorithm and comparison and analysis with other methods. *Geomatics and Information Science of Wuhan University, 35*, 1174-1178.

Liu, S., Hanssen, R., Hooper, A., Samiei-Esfahany, S., & Vanleijen, F. (2011).Separating non-linear deformation and atmospheric phase screen (APS) for InSAR time series analysis using least-squares collocation.*Proceedings of the Advances in the Science and Applications of SAR Interferometry, ESA Fringe 2009, Workshop ESA* Frascati, Italy.

Liu, S., Hanssen, R., & Mika, A. (2009).On the value of high-resolution weather models for atmospheric mitigation in SAR interferometry.*2009 IEEE Int. Geosci and Remote Sensing Symposium (IGARSS)*

Loffeld, O., Nies, H., Knedlik, S., & Wang, Y. (2008). Phase unwrapping for SAR interferometry-A data fusion approach by Kalman filtering. *IEEE Transactions on Geoscience and Remote Sensing, 46*, 47-58.

Löfgren, J.S., Björndahl, F., Moore, A.W., Webb, F.H., Fielding, E.J., & Fishbein, E.F. (2010).Tropospheric correction for InSAR using interpolated ECMWF data and GPS zenith total delay from the Southern California Integrated GPS Network.*Geoscience and Remote Sensing Symposium, IGARSS 2010 Proceedings* Honolulu, HI, USA.

Lombardo, A. (2011).Procedimientos de Construcción del Tunel emisor Oriente.*Jornada Tècnica de l'Aula Paymacotas "Túnels en Mèxic"*.Barcelona, Spain

Lopez-Quiroz, P. (2008).Séries temporelles de la subsidence de la ville de Mexico obtenues par interférométrie radar. *PhD Thesis Paris, France*

Lopez-Quiroz, P. (2012).Personal Communication

López-Quiroz, P., Doin, M., Carreon Freyre, D., & Cerca, M. (2012).Analysis of non linear land subsidence in Mexico city lacustrine plain (Abstract).*American Geophysical Union's 45th annual Fall Meeting*.San Franciso, California, USA

López-Quiroz, P., Doin, M.P., Tupin, F., Briole, P., and, & Nicolas, J.M. (2009). Time series analysis of Mexico City subsidence constrained by radar interferometry. *Journal of Applied Geophysics, 69*, 1–15. doi:10.1016/j.jappgeo.2009.02.006.

Lopez-Quiroz, P., Doin, M.P., Tupin, F., Briole, P., & Nicolas, J.M. (2010).Mexico City subsidence analysis assisted by InSAR.*Land Subsidence, Associated Hazards and the Role of Natural Resources Development (Proceedings of EISOLS 2010)*.Querétaro, Mexico.

Lyons, S., & Sandwell, D. (2003). Fault creep along the southern San Andreas from interferometric synthetic aperture radar, permanent scatterers and stacking. *Journal of Geophysical Research, 108*, 2047 – 2070. DOI10.1029/2002JB001831.

M.D. Pritt, J.S.S. (1994). Least-squares two-dimensional phase unwrapping using FFTs. *IEEE Transactions on Geoscience and Remote Sensing, 32*, 706-708.

Madsen, S.N. (1989). Estimating the Doppler centroid of SAR data. *IEEE Trans. Aerosp. Electron. Syst., 25*, 134-140.

Marin-Cordova, S., Campos-Enriquez, O., & Herrera-Moro-Castillo, M. (2004). Neotectonic related geological risk at dams in the Mexico Basin: Guadalupe dam. *Geofisica International 43*, pp. 435-443.

Massom, R., & Dan, L. (2006). *Polar Remote sensing*. Germany Springer Praxis. Available online at:

Massonet , D., & Feigl, K.L. (1998). Radar Interferometry and its Application to Changes in the Earth's surface. *Reviews of Geophysics 4*, 441-500.

Mathieu, R., Sbih, M., Viau, A., Anctil, F., Parent, L., & Boisvert, J. (2003). Relationships between Radarsat SAR data and surface moisture content of agricultural organic soils. *Int. J. Remote Sens., 24*, 5265–5281.

Menache Varela, A. (2010).Diseño geotécnico-estructural de dovelas para túneles en suelos blandos.*XXV Reunión Nacional de Mecánica de Suelos e Ingeniería Geotécnica*.Acapulco, Mexico.

Méndez, E., Auvinet, G., Juárez, M., & Matus, U. (2010).Caracterización geotécnica del subsuelo en el Circuito Interior.*XXV Reunión Nacional de Mecánica de Suelos e Ingeniería Geotécnica*.Acapulco, Mexico

Méndez, E., Auvinet, G., & Lermo, J. (2008a).Avances en la caracterización geotécnica del agrietamiento del subsuelo de la cuenca de México.*XXIV Reunión Nacional de Mecánica de Suelos e Ingeniería Geotécnica*.Aguascalientes, Mexico.

Méndez, E.S., Juárez, M.C., Pérez, C., D.,, & Auvinet, G. (2008b).Evolution of regional subsidence in Mexico Valley.*XXV Reunión Nacional de Mecánica de Suelos e Ingeniería Geotécnica*.Aguascalientes, Mexico

Mendoza Archundia, E. (2012).Caracterización hidrogeológica de la porción sureste de la planicie de Texcoco, México, para establecer sitos de recarga artificial al acuífero. *Master Thesis D.F., Mexico.*

Montañes, E. (2012).Los diez mejores metros del mundo ABC.es. Available online at: http://www.abc.es/estilo/viajes/20121125/abci-mejor-metro-mundo-201211222144.html

Moon, W.M., Staples, G., Kim, D.-J., Park, S.-E., & Park, K.-A. (2010).RADARSAT-2 and coastal applications: Surface wind, waterline, and intertidal flat roughness.*Proc. IEEE 2010*.

Mooser, F. (1975). *Historia geológica de la Cuenca de México, Memorias de las obras del Sistema de Drenaje Profundo del Distrito Federal*. Mexico, D.F.

Mooser, F., & Molina, C. (1993). Nuevo modelo hidrogeológico para la Cuenca de México. *Boletin del Centro de Investigación Sísmica Fundación Javier Barros Sierra, 3*, 68-84.

National Research Council, Academia Nacional de la Investigación Científica, A.C., & Academia Nacional de Ingeniería, A.C. (1995). Mexico City's Water Supply Washington, D.C. : NATIONAL ACADEMY PRESS

Neri-Ramírez, E., Rubiños-Panta, E.J., Palacios-Velez, O.L., Oropeza-Mota, J.L., Flores-Magdaleno, H., & Ocampo-Fletes, I. (2013). Evaluación de la sustentabilidad del acuífero cuautitlán-pachuca mediante el uso de la metodología mesmis. *Revista Chapingo. Serie Ciencias Forestales y del Ambiente, 19*, 273-285.

Ng, A.H.-M., Ge, L., Li, X., & Zhang, K. (2012). Monitoring ground deformation in Beijing, China with persistent SAR interferometry. *Journal of Geodesy, 86*, 375-392.

Niemeier, W. (2008). Datumsproblematik *Ausgleichungs-rechnung Statistiche Auswertenmethoden*. Berlin, Germany: De Gruyter

Notimex (2012).Un fuerte sismo sacude el centro y sur de México:CNNMéxico. Available online at: http://mexico.cnn.com/fotogalerias/2012/03/20/un-fuerte-sismo-sacude-el-centro-y-sur-de-mexico

Núñez Lópex, M.A. (2012).Daños en escuelas y edificios de Tultitlán a consecuencia del pasado sismo Available online at http://cronistadetultitlan.blogspot.de/2012/03/danos-en-escuelas-y-edificios-de.html

Onn, F., & Zebker, H.A. (2006). Correction for interferometric synthetic aperture radar atmospheric phase artifacts using time series of zenith wet delay observations from a GPS network. *Journal of Geophysical Research, 111*

Ortega-Guerrero, A., Cherry, J.A., & Rudolph, D.L. (1993). Large-Scale aquitard consolidation near Mexico City. *Groundwater, 31*, 708-718.

Ortega-Guerrero, A., Rudolph, D.L., & Cherry, J.A. (1999). Analysis of long-term land subsidence near Mexico City: Field investigations and predictive modeling. *Water Resources Research, 35*, 3327–3341.

Ortiz-Zamora, D., & Ortega-Guerrero, A. (2010). Evolution of long term land subsidence near Mexico City. Review, field investigations, and predictive simulations. *Water Resources Research, 46*, 1-15. DOI: 10.1029/2008WR007398

Osmanoglu, B., Dixon, T.H., Wdowinski, S., Cabral-Cano, E., & Jiang, Y. (2010). Mexico City Subsidence Observed with Persistent Scatterer InSAR. *International Journal of Applied Earth Observation and Geoinformation, 13*

Osmanoglu, B., Wdowinski, S., Dixon, T., & Biggs, J. (2009).InSAR phase unwrapping based on extended Kalman filtering.*Radar Conference 2009*.Pasadena, CA

Ovando-Shelley, E., Lermo-Samaniego, J., Auvinet, G., & Mendez-Sanchez, E. (2012). Microtremor measurements to identify zones of potential fissuring in the basin of Mexico. *Geofisica International*, 143-156.

Ovando-Shelley, E., Ossa, A., & Santoyo, E. (2013). Effects of regional subsidence and earthquakes on architectural monuments in Mexico City. *Boletín de la Sociedad Geológica Mexicana Número Especial de Geología Urbana, 65*, 157-167.

Ovando Shelley, E. (2011).Some geotechnical properties to characterize Mexico City Clay *Proceedings of the 14th Pan-American Conference on Soil Mechanics and Geotechnical Engineering*.Toronto, Ontario, Canada

Pan, B., & Gan, J. (2008).Error Analysis and Accuracy Assessment of InSAR Phase Unwrapping.*Proceedings of the 8th International Symposium on Spatial Accuracy Assessment in Natural Resources and Environmental Sciences*.Shangai, China

Pepe, A., Sansosti, E., Berardino , P., & Lanari, R. (2005). On the Generation of ERS/ENVISAT DInSAR Time-Series Via the SBAS Technique. *IEEE Geoscience and Remote Sensing Letters, 2*, 265-269.

Perez , D. (2010).Modelado del Hundimiento de la zona Lacustre del Valle de Mexico. Aspectos Estratigraficos y Piezometricos. *Mexico, D.F.*

Perissin, D., Prati, C., Rocca, F., & Ferretti, A. (2004).ERS-ENVISAT Permanent Scatterers.*Geoscience and Remote Sensing Symposium, IGARSS 2004 Proceedings*.

Perissin, D., & Wang, T. (2011). Time-series insar applications over urban areas in China. *IEEE J. Sel. Topics Appl. Earth Observ. Remote Sens. (JSTARS), 4*, 92-100.

Perski, Z., Hanssen, R., Wójcik, A., & Wojciechowski, T. (2009). InSAR analysis of terrain deformation near the Wieliczka Salt Mine, Poland. *Engineering Geology, 106*, 58–67. DOI: 10.1016/j.enggeo.2009.02.014

Pollitz, F., Wicks, C., & Thatcher, W. (2001). Mantle flow beneath a continental strike -slip fault: Postseismic deformation after the 1999 Hector Mine earthquake. *Science, 293*, 1814-1818.

Pritchard, M.E., & Simons, M. (2002). A satellite geodetic survey of large-scale deformation of volcanic centres in the central Andes. *Nature, 418*, 167 – 171.

Pritt, M.D. (1996). Phase unwrapping by means of multigrid techniques for interferometric SAR. *IEEE Transactions on Geoscience and Remote Sensing, IEEE Transactions on, 34*, 728-738.

Puysségur, B., Michel, R., & Avouac, J. (2007). ropospheric phase delay in interferometric synthetic aperture radar estimated from meteorological model and multispectral imagery *Journal of Geophysical Research, 112*

Rabus, B., Eineder, M., Roth, A., & Bamler, R. (2003). The shuttle radar topography mission—A new class of digital elevation models acquired by spaceborne radar. *ISPRS J. Photogramm., 57*, 241–262.

Raney, R.K. (1998). Radar Fundamentals: Technical Perspective. In H.a. Lewis (Ed.), *Principles and Applications of Imaging Radar, Manual of Remote Sensing* (pp. 9-130). New York, USA: Wiley Interscience

Raney, R.K., Luscombe, A.P., Langham, E.J., & Ahmed, S. (1991).RADARSAT.*Proceedings of the IEEE*.

Reale, D., Nitti, D.O., Peduto, D., Nutricato, R., Bovenga, F., & Fornaro, G. (2011). Postseismic deformation monitoring with the COSMO/SKYMED constellation. *IEEE Geosci. Remote Sens.Lett.*, *8*, 696–700.

Rodríguez-Castillo, R., & Rodríguez-Velázquez, I. (2006). Consecuencias sociales de un desastre inducido, subsidencia. *Boletín de la Sociedad Geológica Mexicana numero especial de Geologia Urbana LVIII*, 265-269.

Rodriguez, E., & Martin, J.M. (1992).Theory and design of interferometric synthetic aperture radars.*Radar and Signal Processing, IEE Proceedings F*.

Rosen, P., Hensley, S., Zebker, H., Webb, F.H., & Fielding, E.J. (1996). Surface deformation and coherence measurements of Kilauea Volcano, Hawaii, from SIR-C radar interferometry. *Journal of Geophysical Research* DOI: 10.1029/96JE01459

Rosen, P.A., Hensley, S., Peltzer, G., & Simons, M. (2004). Updated repeat orbit interferometry package released. *EOS Transactions - American Geophysical Union, 85*

Roth, A., Adam , N., Schwäbisch , M., Müschen , B., Böhm, C.a., & Lang, O. (1997).Observation of the effects of the subglacial volcano eruption underneath the Vatnajökull glacier in Iceland with ERS-SAR data.*3rd ERS Workshop*.Florence, Italy

Rufino, G., Moccia, A.a., & Esposito, S. (1996).DEM generation by means of ERS tandem data.*Proceedings of the Fringe '96 Workshop ERS SAR*.Zurich, Switzerland. .

Ryder, I.a., & Bürgmann, R. (2008). Spatial variations in slip deficit on the central San Andreas Fault from InSAR. *Geophys. J. Int.*, *175*, 837–852.

SACMEX (2012). El gran reto del agua en la Ciudad de México pasado, presente y prospectivas de solución para una de las ciudades más complejas del mundo. D.F., Mexico

Salinas Cesareo, J. (2007).Alerta en Jaltenco, Edomex, por grieta de 3 kilómetros en el subsuelo. Available online at http://www.jornada.unam.mx/2007/07/14/index.php?section=estados&article=028n1est

Salinas Cesareo, J. (2009).Perforación daña casas en Tecámac. Available online at http://www.jornada.unam.mx/2009/10/27/estados/031n3est

Salinas Cesareo, J. (2012).Exigen atender escuelas dañadas por el sismo en Ecatepec y Tultitlán. Available online at http://www.jornada.unam.mx/2012/03/29/estados/038n1est

Salinas Cesareo, J. (2014).Reportan inundaciones en avenidas, comercios y viviendas de Ecatepec. Available online at http://www.jornada.unam.mx/ultimas/2014/06/08/reportan-inundaciones-en-avenidas-comercios-y-viviendas-de-ecatepec-6300.html

Salinas, J., & Nuñez, M. (2009).Ecatepec: 520 viviendas dañadas y ocho destruidas por la tormenta. Available online at http://www.jornada.unam.mx/2009/11/02/estados/025n1est

Salvador, F. (2009).Temen habitantes por hundimiento de calle. Available online at http://www.especialistas.com.mx/saiweb/viewer.aspx?file=c8u0JHolyPzScjDD09MU1fsioM/OWrRZycFj6X4VsRjE1pLGJZISOdylwhYi8u6A&opcion=0&encrip=1

Sandwell, D.T., & Price, E.J. (1998). Phase gradient approach to stacking interferograms. *J. Geophys. Res.*, *103*, 30183–30204.

Santiago, M. (2014).Aparecen grietas en calles de Ecatepec. Available online at http://edomex.quadratin.com.mx/Aparecen-grietas-en-calles-de-Ecatepec/

Santoyo, E. (2007). Historia y Actualidad del hundimiento de la ciudad de Mexico. La construccion de un Pais. Mexico: CICM e IPN.

Scharroo, R., Visser, P.N.A.M., and , & Mets, G.J. (1998). Precise orbit determination and gravity field improvement for the ERS satellites. *Journal of Geophysical Research*, 8113–8127.

Schmidt, D.A., & Bürgmann, R. (2003). Time-dependent land uplift and subsidence in the Santa Clara valley, California, from a large interferometric synthetic aperture radar data set. *J. Geophys. Res.*, *108* doi:10.1029/2002JB002267.

SEDESOL (2011).Atlas de riesgos naturales de la delegación iztapalapa. Secretaria de Desarrollo Social del Gobierno Federal (SEDESOL). Available online at: http://www.normateca.sedesol.gob.mx/work/models/SEDESOL/Resource/2612/Atlas_Estados/09007_IZTAPALAPA/1_ATLAS_DE_RIESGOS.pdf

SEMARNAT (2008).Túnel Emisor Oriente duplicará la capacidad del drenaje profundo del Valle de México[Brochure]. Secretaria de Medio Ambiente y Recursos Naturales (SEMARNAT). Available online at: http://atl.org.mx/aguadf/images/docs/Folleto_El_Tunel_Emisor_Oriente.pdf

SEMARNAT (2012).Seguimiento a las acciones de contencion del riesgo, preparacion del sitio y la remediacion del predio ubicado en la Calle Francisco I. Madero No.30, Colonia Lecheria, Tutitlán, Estado de Mexico(Ex fábrica de Cromatos de Mexico). Secretaria de Medio Ambiente y Recursos Naturales (SEMARNAT).

Available online at: http://web2.semarnat.gob.mx/transparencia/Documents/LIBRO%20BLANCO%20CROMATOS.pdf

SEMARNAT, & IMTA (2003). Balance hidrico en la Cuenca de Mexico.Informe final 2003. Mexico:

SEMARNAT, SGPAI, & DGIRA (2008).Descarga de agua residual tratada sobre la margen izquierda del Río Hondo Tepozotlán, Municipio de Tepotzotlan, Estado de Mexico Secretaría de Medio Ambiente y Recursos Naturales(SEMARNAT), Subsecretaria de Gestion para la Proteccion Ambiental(SGPAI), Direccion General de Impacto y Riesgo Ambiental(DGIRA). Available online at: http://sinat.semarnat.gob.mx/dgiraDocs/documentos/mex/estudios/2008/15EM2008H0022.pdf

Servin, M., & Quintero, J. (2011).Se desborda el Gran Canal; 300 viviendas inundadas. Available online at http://www.jornada.unam.mx/2011/09/05/capital/033n1cap

Shanker, P., & Zebker, H. (2010). Edgelist phase unwrapping algorithm for time series InSAR analysis. *Journal of the Optical Society of America, 27*, 605–612.

Shimada, M., Tadono, T., & Rosenqvist, A. (2010).Advanced Land Observing Satellite (ALOS) and monitoring global environmental change.*Proc. IEEE 2010*

Siles, G., López-Quiroz, P., Niemeier, W., & Riedel, B. (2013).Subsidence rates estimation in Mexico City by means of an open-source algorithm for multitemporal interferometry (Poster).*Proceedings of 2nd Joint International Symposium on Deformation Monitoring (JISDM)*.Nottingham, U.K.

Siles, G., Niemeier, W., & Lopez-Quiroz, P. (2015).Wechselbeziehungen zwischen Grundwasser-entnahme, Bautätigkeit und Bodensenkungen -aufgezeigt am Beispiel Mexico City.*Geomonitoring Tagung 2015*.Clausthal, Germany

Simons, M., Fialko Y., a., & L., R. (2002). Coseismic deformation from the 1999 Mw 7.1 Hector Mine, California, earthquake as inferred from InSAR and GPS observations. *Bull. Seism. Soc. Am., 92*, 1390-1402.

Skriver, H., Schou, J., & Dierking, W. (2000). Mapping by airborne synthetic aperture radar (SAR). *International Archives of Photogrammetry and Remote Sensing, Vol. XXXIII, Part B1.*, 307-312.

Sousa, J.J., Hooper, A.J., Hanssen, R.F., & Bastos, L.C. (2011). Persistent scatterer InSAR: a comparison of methodologies based on a model of temporal deformation vs. spatial correlation selection criteria. *Remote Sens. Env., 115*, 2652-2663. DOI: 10.1016/j.rse.2011.05.021

Spellman, F.R. (2008). *The Science of the Water. Concepts and Applications.*: CRC Press

SSN (2011).Catalgo:Servicio Sismologico Nacional (SSN). Available online at: http://www.ssn.unam.mx/

STC (2013).El STC requiere mil 500 millones de pesos para renivelacion y rehabilitacion de trenes de la Linea A:Sistema de Transporte de Colectivo(STC). Available online at: http://www.metro.df.gob.mx/comunicados2/detalleComunicados.html?id_comunicado=863

STC (2014).Afluencia de estacion por linea 2014. Available online at: http://www.metro.df.gob.mx/

Strozzi, T., & Wegmuller, U. (1999).Land subsidence in Mexico City mapped by ERS differential SAR interferometry.*Geoscience and Remote Sensing Symposium, IGARSS 2000 Proceedings*.Hamburg, Germany

Strozzi, T., Wegmüller, U., Werner, C.L., Wiesmann, A.a., & Spreckles, V. (2003). JERS SAR interferometry for land subsidence monitoring. *IEEE Transaction on Geoscience and Remote Sensing, 41*, 1702-1708.

Taylor, C.J., & Alley, W.M. (2002). *Ground-water-level Monitoring and the Importance of Long-Term Water-Level Data*. Virginia, USA U.S. Geological Survey

Tomás, R., Márquez, Y., Lopez-Sanchez, J.M., Delgado, J., Blanco, P., Mallorqui, J., Martinez, M., Herrera, G., & Mulas, J. (2005). Mapping ground subsidence induced by aquifer overexploitation using advanced Differential SAR Interferometry: Vega Media of the Segura River (SE Spain) case study. *Remote Sensing Environment, 98*, 269-283.

Torre, A., & Capece, P. (2011).COSMO-SkyMed: The Advanced SAR Instrument.*Proceedings of the 5th International Conference on Recent Advances in Space Technologies (RASAT)*.Rome, Italy.

Tortajada, C., & Castelán, E. (2003). Water Management for a Megacity: Mexico City Metropolitan. *Ambio, 32*, 124-129.

Ubaldo, E. (2008).Metodologia para el analsis de riesgos ambientales. Impacto social en la poblacion del municipio de Ecatepec, Estado de Mexico *Master Thesis D.F., Mexico.*

Usai, S. (2001).A new approach for long term monitoring of deformations by differential SAR interferometry. *PhD Thesis Delft, The Netherlands.*

Usai, S. (2003). A least squares database approach for SAR interferometric data. *IEEE Transactions on Geoscience and Remote Sensing, 41*, 753-760. DOI:10.1109/TGRS.2003.810675

Usai, S., & Hanssen, R. (1997).Long time scale INSAR by means of high coherence features.*3rd ERS Symposium on Space at the service of our Environment*.Florence, Italy

Vachon, P.W., Krogstad, H.E., & Paterson, J.S. (1994). Airborne and spaceborne synthetic aperture radar observations of ocean waves. *Atmos. Ocean, 32*, 83–112.

Vargas, G.N. (2014).Enciclopedia de Los Municipios y Delegaciones de México.Estado de Mexico. Tepotzotlán. Available online at: http://www.inafed.gob.mx/work/enciclopedia/EMM15mexico/municipios/15095a.html

Vazquez, S., & Jaimes, P. (1989). Geologia de la Cuenca de Mexico *Revista Geofísica Internacional, 28*, 133-190.

Webley, P.W., Bingley, R.M., Dodson, A.H., Wadge, G., Waugh, S.J., & James, I.N. (2002). Atmospheric water vapour correction to InSAR surface motion measurements on mountains: results from a dense GPS network on Mount Etna. *Phy. Chem. Earth 27*, 363–370.

Wegmüller, U., Werner, C.L., Nüesch, D.a., & Borgeaud, M. (1995). Forest mapping using ERS repeat-pass SAR interferometry. *ESA Earth Observation Quarterly, 49*, pp. 4-7.

Werner, C., Wegmuller, U., Strozzi, T., & A. Wiesmann. A. (2003).Interferometric point target analysis for deformation mapping.*Geoscience and Remote Sensing Symposium, IGARSS 2003 Proceedings*.

Werninghaus, R., Buckreuss , S., & Pitz, W. (2007).TerraSAR-X Mission Status.*Geoscience and Remote Sensing Symposium, IGARSS 2007 Proceedings*.Barcelona, Spain

Wicks, C., Dzurisin, D., Ingebritsen, S., Thatcher, W., Lu, Z., & Iverson, J. (2002). Magmatic activity beneath the quiescent Three Sisters volcanic center, central Oregon Cascade Range, USA. *Geophysical Research Letters, 29*

Wiley, C. (1985). Synthetic Aperture Radars. A paradigm for technology evolution *IEEE Transactions on Aerospace and Electronic systems, VOL. AES-21*, 440-443

Williams, S., Bock, Y., & Fang, P. (1998). Integrated satellite interferometry: tropospheric noise, GPS estimates and implications for interferometric synthetic aperture radar products. *Journal of Geophysical Research, 103*

Yan, Y., Doin, M.P., López-Quiroz, P., Tupin, F., Fruneau, B., Pinel, V., & Trouvé, E. (2012). Mexico City Subsidence Measured by InSAR Time Series: Joint Analysis Using PS and SBAS Approaches. *IEEE Journal of selected topics in Applied Earth observations and Remote Sensing* doi: 10.1109/JSTARS.2012.2191146.

Zebker, H.A., & Goldstein, R.M. (1986). Topographic mapping from interferometric synthetic aperture radar observations. *Journal of Geophysical Research, 91*, 4993-4999.

Zebker, H.A., & Rosen, P. (1994).On the derivation of coseismic displacement fields using differential radar interferometry: the Launders earthquake.*Geoscience & Remote Sensing Symposium, IGARSS 1994 Proceedings*.Pasadena, CA, USA

Zebker, H.A., Rosen, P.A., & Hensley, S. (1997). Atmospheric effects in interferometric synthetic aperture radar surface deformation and topographic maps. *J. Geophys.Res., 102* 7547–7563.

Zebker, H.A., & Villasenor, J. (1992). Decorrelation in interferometric radar echoes. *IEEE Transactions on Geoscience and Remote Sensing, 30*, 950-959.

Zebker, H.A., Werner, C.L., Rosen, P.A.a., & Hensley, S. (1994). Accuracy of topographic maps derived from ERS-1 interferometric radar. *IEEE Transactions on Geoscience and Remote Sensing, 32*, 823-836.

Zeevaert, L. (1986). Consolidation in the intergranular viscosity of highly compressible soils. Philadelphia: American Society for Testing and Materials, ASTM STP 892

Zhong , L., Jixian , Z., Yonghong , Z.a., & Daniel , D. (2010). Monitoring and characterizing natural hazards with satellite InSAR imagery. *Annals of GIS, 16*, 55-66. 10.1080/19475681003700914